Helsinki University of Technology Radio Laboratory Publications
Teknillisen korkeakoulun Radiolaboratorion julkaisuja
Espoo, March 2004 REPORT S 264

MODELING OF INTERFACES AND LAYERS WITH THE FINITE-DIFFERENCE TIME-DOMAIN METHOD

Mikko Kärkkäinen

Dissertation for the degree of Doctor of Science in Technology to be presented with due permission for public examination and debate in Auditorium S2 at Helsinki University of Technology (Espoo, Finland) on the 22nd of March 2004, at 12 o'clock noon.

Helsinki University of Technology
Department of Electrical and Communications Engineering
Radio Laboratory

Teknillinen korkeakoulu
Sähkö- ja tietoliikennetekniikan osasto
Radiolaboratorio

Distribution:
Helsinki University of Technology
Radio Laboratory
P.O. Box 3000
FIN-02015 HUT
Tel. +358-9-451 5970
Fax. +358-9-451 2152

ISBN 951-22-6928-7
ISBN 951-22-6929-5 (pdf)
ISSN 1456-3835

Otamedia Oy
Espoo 2004

Author: Mikko Kärkkäinen

Title of thesis: Modeling of Interfaces and Layers with the Finite-Difference Time-Domain Method

Finnish title: Rajapintojen ja kerrosten mallintaminen FDTD-menetelmällä

Date: 22nd January, 2004 **Pages:** 154

Department: Department of Electrical and Communications Engineering

Chair: S-26 Radio Engineering

Supervisor: Professor Sergei Tretyakov

Instructor: Professor Sergei Tretyakov

Modeling of interfaces and layers with the finite-difference time-domain method (FDTD) is considered in this thesis. New numerical models are developed and verified.

A surface impedance boundary condition relates the tangential electric and magnetic fields on an interface between two materials. The exact surface impedance uniquely defines the electromagnetic fields outside the material. The material structure is removed from the computational space. The resulting computational savings are huge in electrically large problems, like the modeling of coated targets in military applications.

Using the surface impedance techniques in numerical methods is extremely reasonable when the reflection of electromagnetic fields from materials is difficult to compute directly. For example, if the wavelength inside the material under investigation is very small compared to the wavelength outside the material, the straightforward discretization of the fields inside the material is not a clever approach. The surface impedance boundary conditions may be utilized in such situations.

In this thesis, a higher-order FDTD-model of interfaces with metals and semiconductors is developed and verified [1]. As the most important new feature, the model takes arbitrary excitations into account in a general fashion using spatial derivatives on the interface. Novel techniques for modeling of dielectric layers on metal surfaces are also developed [2, 3]. Application of the surface impedance concept to derive analytical absorbing boundary conditions is also considered [4].

An alternative and original model for electrically thin dispersive layers is introduced [5]. Unusual electromagnetic properties of dispersive layers are numerically studied in the frequency range, where the real parts of material parameters are negative [6].

Applications of the surface impedance concept to modeling of antennas with artificial electromagnetic materials are presented with numerical results for prototype devices.

Keywords: FDTD, surface impedance boundary condition, dielectric layer, surface impedance, absorbing boundary condition, metamaterial

Preface

I want to thank my supervisor, Prof. Sergei Tretyakov for his encouraging supervision and optimistic attitude to new challenging research plans.

The comments of pre-examiners Jaakko Juntunen and Keith Whites and the suggestions of Sergei Tretyakov were valuable in polishing the manuscript to the final form.

I also want to express my gratitude to my wife Liisa and to my kids Emma and Anton, who have enriched my life in many ways.

Espoo, 22nd January, 2004

Mikko Kärkkäinen

Abbreviations

ABC	Absorbing Boundary Condition
ADE	Auxiliary Differential Equation
AMEST	Antenna Design, Measurement Techniques and Standardization
BW	Backward Wave (medium), Bandwidth
DNG	Double Negative (material)
EBG	Electromagnetic Bandgap
FDTD	Finite-Difference Time-Domain
FEM	Finite Element Method
MoM	Method of Moments
PDE	Partial Differential Equation
PEC	Perfect Electric Conductor
PMC	Perfect Magnetic Conductor
PML	Perfectly Matched Layer
SIBC	Surface Impedance Boundary Condition
TE_x	Transverse Electric with respect to x-axis
TM_z	Transverse Magnetic with respect to z-axis
UPML	Uniaxial Perfectly Matched Layer
VSWR	Voltage Standing Wave Ratio

List of Symbols

α, a, b	constants
B	susceptance
β, γ	variables
Γ	damping factor
c_0	the speed of light in vacuum
C	surface capacitance
δ	Dirac delta function (distribution), damping factor
Δx	spatial resolution of the FDTD mesh along x-axis
Δt	the discrete time increment in FDTD-method
D_t	first order differential operator with respect to time
$\mathbf{E}_t$	tangential electric field vector
$E_z\|_{i,j,k}$	z-component of electric field vector evaluated at spatial grid point i, j, k
$E_z\|^n$	z-component of electric field vector evaluated at time step n
ϵ_0	permittivity of vacuum
ϵ'	real part of permittivity
ϵ_r	relative permittivity
$\mathbf{H}_t$	tangential magnetic field vector
f	frequency of electromagnetic field

G	conductance
G	a partial differential operator
I_{inp}	input current
I_n	modified Bessel function of the first kind, of order n
j	imaginary unit
$\mathbf{J}_s$	surface current density
k	wavenumber
$\mathbf{k}$	wave vector of electromagnetic wave
L	inductance, surface inductance
$\mathcal{L}$	Laplace-transform operator
μ_0	permeability of vacuum
μ_∞	permeability in the limit $\omega \longrightarrow \infty$
$\overline{\overline{\mu}}$	permeability dyadic (a linear mapping from vectors to vectors)
$\mathbf{n}$	unit normal vector
ω	angular frequency of electromagnetic field
ω_0	resonant angular frequency, center frequency
p_1, q_1	constants
$\pi_{k=1}^{N}$	a product over indices 1 to N
r	radius, radial coordinate
R	resistance, reflection coefficient
s	Laplace-transform variable
S_{11}	input return loss parameter
σ	electric conductivity
$\sum_{k=1}^{n}$	summation over indices 1 to n

θ	angle (of incidence)
$\mathbf{u}_x$	unit vector along Cartesian coordinate axis x
U	a scalar function
V_{inp}	input voltage
η_0	wave impedance in free space
$\frac{\partial^k}{\partial x^k}$	k'th order derivative with respect to variable x
$\int_a^b$	integration from a to b
$*$	convolution (integral)
∇	gradient, a differential operator, a mapping from scalar fields to vector fields
∇_t	restriction of the gradient to a plane tangential to an interface
X	reactance
x, y, z	coordinate variables in Cartesian coordinate system
ξ, τ, u	integration variables
χ_m	magnetic susceptibility
Z_{in}	input impedance
Z_s	scalar surface impedance
$\overline{\overline{Z}}_s$	surface impedance operator
$\times$	cross product of two vectors
$\cdot$	dot product

List of Original Publications

The thesis is based on the following publications, written mainly by the author:

- M.K. Kärkkäinen, S.A. Tretyakov, Finite-difference time-domain model of interfaces with metals and semiconductors based on a higher-order surface impedance boundary condition, IEEE Trans. Antennas Propag., vol. 51, no. 9, Sept. 2003, pp. 2448–2455.
- M.K. Kärkkäinen, FDTD surface impedance models for electrically thick dispersive material coatings, Radio Science, vol. 38, no. 3, June 2003.
- M.K. Kärkkäinen, FDTD surface impedance model for coated conductors, accepted for publication in IEEE Trans. Electrom. Compat., 2003.
- M.K. Kärkkäinen, Subcell FDTD modeling of electrically thin dispersive layers, IEEE Trans. Microwave Theory and Tech., vol. 51, no. 6, June 2003, pp. 1774–1780.
- M.K. Kärkkäinen, S.A. Tretyakov, A class of analytical absorbing boundary conditions originating from the exact surface impedance boundary condition, IEEE Trans. Microwave Theory and Tech., vol. 51, no. 2, Feb. 2003, pp. 560–563.
- M.K. Kärkkäinen, Numerical study of wave propagation in uniaxially anisotropic Lorentzian backward wave slabs, Phys. Rev. E 68, 026602, Aug. 2003.

Contents

Chapter 1

Introduction

During the recent decades, the finite-difference time-domain method (FDTD) has been widely accepted as a reliable computational tool in numerical electromagnetics. The explicit nature of the time-stepping algorithm to solve Maxwell's equations conveniently enables the visualization of the electromagnetic fields inside the medium under investigation. This feature is a great benefit compared to frequency-domain methods, like the Method of Moments (MoM) or the Finite-Element Method (FEM). The division of the problem space into small cells can be a great advantage in the FDTD method when modeling small geometrical features. In some problems, however, the required spatial resolution may considerably increase the computational burden. Therefore, direct inclusion of the fine geometrical features of the structure under consideration into an FDTD-model by choosing a very small cell size is not a reasonable approach. In such problems, an equivalent local relation between the tangential electric and magnetic fields may sometimes be derived and used to reduce the number of cells in the discrete space. The computational savings are known to be remarkable in many problems.

In the frequency domain and in some simple problems, the quotient of the electric and the magnetic field on the material surface is called surface impedance. More generally, surface impedance is a linear operator, a tensor, mapping vectors to vectors. The surface impedance is inherently a frequency-domain concept. In the finite-difference time-domain method, we work in the time domain. Therefore, conversion from the frequency domain into the time domain must be accomplished for the surface impedance to be suitable for numerical analysis. Fourier-transform techniques can be utilized in this context.

The use of equivalent surface impedance boundary conditions allows us to remove the material under consideration from the computation space, thus enabling the use of the conventional coarse discretization outside the material body. This approach has been theoretically well known long time ago. The frequency-dependence of the impedance functions in the impedance boundary conditions represents a challenge for time-domain techniques. Hence, even if

an analytical impedance boundary condition is given, its implementation into finite-difference time-domain technique is often a non-trivial task.

In this thesis, contributions are made to FDTD modeling in the following three topics: 1) modeling of material interfaces, 2) modeling of electrically thin layers and 3) modeling of metamaterials. The major part of the thesis is devoted to modeling of material interfaces using impedance boundary conditions. Algorithms for conductors with and without material coatings are developed and verified in chapters 2,4 and 5. The surface impedance concept is also utilized in antenna applications in chapter 8, and to obtain absorbing boundary conditions in chapter 3. Regarding the second topic, a subcell model for frequency-dispersive coatings is developed in chapter 6. The proposed model generalizes several earlier models, which have been formulated for dielectric and conductive layers without frequency dispersion. The advantages of the proposed models as compared with some earlier models are demonstrated with numerical simulations. The third topic, modeling of metamaterials, is treated in chapter 7.

This thesis is mainly based on six papers: [1]–[6]. In the first paper, a higher-order FDTD model of interfaces with metals and semiconductors is developed. The model is based on higher-order surface impedance boundary conditions (SIBC). The model proposed in [1] is useful if an isotropic dielectric and conductive half-space is illuminated with an arbitrary excitation. Paper [2] introduces a new FDTD model for coated ideal conductors, and the model is extended for coatings on more general conductors in [3]. The models in [2]–[3] are very useful when simulating scattering from coated targets. A new subcell FDTD model for electrically thin dispersive layers is developed in [5] and applied to predict cut-off frequencies of a rectangular waveguide. The fifth paper [4] discusses the relation between surface impedance boundary conditions and absorbing boundary conditions (ABC). It is shown that the exact surface impedance boundary conditions provide a better starting point for deriving ABC's than the conventional Engquist-Majda equation. A class of analytical absorbing boundary conditions is derived where both the tangential electric and magnetic fields simultaneously appear.

Comparative discussion of the proposed models and known models is performed in every chapter, where new algorithms are formulated. The advantages of the proposed surface impedance models for interfaces with conductors and dielectric layers over many existing models ([7]–[14]) are discussed. The suggested FDTD model designed for modeling electrically thin layers represents an extension of the known models [15, 16, 17, 18, 19] to frequency-dispersive layers. The designed models are investigated with the conventional Yee algorithm [20], which has been popularized by Taflove [21, 22].

Metamaterials are materials that cannot be found or are not readily available in nature. A lot of research efforts have been recently put into the study of metamaterials because of their potentially revolutionary applications. They possess some unusual electromagnetic properties that are numerically stud-

ied in this thesis. Wave propagation, refraction and focusing phenomena in uniaxially anisotropic metamaterial slabs are numerically studied in paper [6]. Simulated results are presented and comparisons with theoretical results are made. In particular, the behavior of the evanescent waves in metamaterials is numerically studied in a novel way.

As a more practical part of the thesis, certain antennas with composite materials are investigated. This work has been done as a part of AMEST project, in co-operation with Nokia Research Center and the Technical Research Centre of Finland (VTT). The developed FDTD models for the AMEST project will be discussed in this thesis. Properties of some antennas will be numerically analyzed using the developed numerical models.

Chapter 2

Modeling Interfaces with Dielectric and Conducting Materials

Modeling material interfaces using the surface impedance technique is the topic of this chapter. Earlier models known from the literature are presented and a new higher-order model is introduced. The new model is numerically verified by comparing to analytical results.

2.1 Introduction to Known Models

Accurate FDTD modeling of metal and other conducting elements is a challenging task because the fields in these materials vary in space extremely quickly compared to surrounding air or dielectrics, demanding extremely dense meshes for accurate discretization of electromagnetic fields in metals. Usually, the conductivity of metal is assumed to be infinite (so that the fields inside metal elements are assumed to be zero) or a simple Leontovich surface impedance boundary condition (SIBC)

$$\mathbf{E}_t = Z(\omega)\mathbf{n} \times \mathbf{H}_t \tag{2.1}$$

is used, as in [7]–[8]. Here, index t denotes the tangential field components, $\mathbf{n}$ is the unit vector pointing outwards from the conducting body. In the frequency domain the surface impedance of an isotropic non-magnetic conductor in (2.1) reads

$$Z(\omega) = \frac{\eta_0}{\sqrt{\epsilon_{2,r} - j\frac{\sigma_2}{\omega\epsilon_0}}}. \tag{2.2}$$

The material parameters of the conductor are the relative permittivity $\epsilon_{2,r}$ and the conductivity σ_2. The wave impedance of free space is denoted by η_0. The use of surface impedances is very reasonable if the system contains conductive

parts. By using an appropriate SIBC, the volume of the conducting material can be eliminated from the computational space. The computational savings are discussed in [7], and it is clear that the surface impedance approach can tremendously reduce the computational burden.

Although the simple impedance boundary condition (2.1) allows to avoid calculation of fields inside conductors, its accuracy is limited due to the assumption that the waves inside metal propagate normally to the interface, whatever is the frequency or the source configuration and position. The Leontovich impedance boundary condition is valid if the fields outside the conductor vary very slowly in the direction along the surface as compared to the wavelength in metal. This condition can become invalid for instance in densely packed devices, where there are other conductors (e.g., wires or strips) near to the modeled interface, or where metal parts have complex geometry with sharp edges. Thus, more elaborate models are needed to model metal components in modern microwave devices.

Maloney and Smith showed in [7] with a couple of test problems that their FDTD model based on the simple impedance boundary condition is in good agreement with the exact results for large values of conductivity and a simple line source. However, it was found that for small conductivities the model proposed in [7] works not quite well. The same is true for the method proposed by Beggs *et al.* in [8]. Let us discuss the basics of Beggs' method, which is based on the Leontovich SIBC with the following high conductivity approximation:

$$\frac{\sigma}{\omega\epsilon_2} \gg 1, \tag{2.3}$$

where $\epsilon_2 = \epsilon_{2,r}\epsilon_0$ is the dielectric constant of the material half-space. Beggs *et al.* presented two SIBC-formulations. In the first one, the surface impedance is split into parts as

$$Z_s(\omega) = \sqrt{\frac{j\omega\mu_2}{\sigma_2}} = R_s(\omega) + j\omega L_s(\omega), \tag{2.4}$$

where the resistance, defined as $R_s(\omega) = \sqrt{\omega\mu_2/(2\sigma_2)}$ and the inductance $L_s(\omega) = \sqrt{\mu_2/(2\sigma_2\omega)}$ are evaluated at the desired frequency. Considering a two-dimensional TE$_y$-case, the SIBC on the boundary $z = 0$ is written as [8]

$$E_x(t) = R_s H_y(t) + L_s \frac{\partial}{\partial t} H_y(t). \tag{2.5}$$

This time-domain SIBC in then incorporated into the FDTD-algorithm by applying the Faraday-Maxwell law near the interface. Hence, the SIBC just modifies the usual update equation for H_y-component in Yee's algorithm. It should be noticed that a half-cell spatial error near the boundary is neglected in this procedure. This fact certainly reduces the accuracy of the model. Also, this model is valid at a *single* frequency only. A more useful model presented in [8] is a dispersive surface impedance implementation that is valid over a

wide frequency band. The underlying assumptions being the same, the SIBC in the frequency domain reads

$$E_x(\omega) = Z_s^{'}(\omega)\left[j\omega H_y(\omega)\right], \tag{2.6}$$

where the auxiliary quantity $Z_s^{'}$ is obtained from the actual surface impedance in the following manner:

$$Z_s^{'} = \frac{Z_s(\omega)}{j\omega}. \tag{2.7}$$

The time-domain equivalent of (2.6) can be obtained via inverse Fourier-transform operation as

$$E_x(t) = Z_s^{'}(t) * \frac{\partial}{\partial t} H_y(t). \tag{2.8}$$

The convolution is implemented recursively. A Laplace-transform pair

$$\mathcal{L}\left\{\frac{1}{\pi t}\right\} = \frac{1}{\sqrt{s}} \tag{2.9}$$

was utilized in [8] to obtain the time-domain equivalent of the frequency-domain surface impedance $Z_s(\omega)$. Again, the Faraday-Maxwell law is used to obtain the discretized form of the SIBC. For very large conductivities, the model properly reduces to the PEC boundary condition, as is easily seen from (2.8). In the limit $\sigma_2 \longrightarrow 0$, however, the discrete form of the model is equivalent to a perfect magnetic conductor (PMC) on the boundary, clearly an incorrect result. The reason for this is, of course, the high conductivity approximation. There is clearly a need for better SIBC models, although the most important application region lies in the higher conductivity regime.

Maloney and Smith created a better model by alleviating the high conductivity approximation. In their publication [7], they start from the Leontovich SIBC and assume that

$$\left|\epsilon_{2,r} - j\frac{\sigma_2}{\omega\epsilon_0}\right| \gg \sin^2(\theta_i). \tag{2.10}$$

With this assumption (θ_i is the angle of incidence), the surface impedance is of the form

$$Z_s(\omega) = \frac{\eta_0}{\sqrt{\epsilon_{2,r} - j\frac{\sigma_2}{\omega\epsilon_0}}}, \tag{2.11}$$

and the use of the Leontovich SIBC is justified. The surface impedance may be written in the Laplace domain using the substitution $s = j\omega$, where s is the Laplace domain variable. The exact inverse Laplace transform is known and the SIBC in the time-domain takes the form

$$\begin{aligned}\mathbf{E}_t(t) &= \frac{\eta_0}{\epsilon_{2,r}}\left\{\left[\mathbf{n}\times\mathbf{H}_t(t)\right] + \right. \\ &\left. \int_0^t \alpha e^{\alpha\tau}\left[I_1(\alpha\tau) + I_0(\alpha\tau)\right]\left[\mathbf{n}\times\mathbf{H}_t(t-\tau)\right]\, d\tau\right\},\end{aligned} \tag{2.12}$$

where $\alpha = -\sigma_2/(2\epsilon_2)$ and I_n is the Bessel function of the first kind and order n. Notice that again the SIBC in (2.12) is seen to reduce correctly to the PEC boundary condition in the limit $\sigma_2 \longrightarrow \infty$, since the integrand behaves as the Dirac delta function in this limit. It may be also noticed that if $\epsilon_2 = \epsilon_0$ and the limit $\sigma_2 \longrightarrow 0$ is taken, the result is quite reasonable, namely

$$\mathbf{E}_t = \eta_0 \left[\mathbf{n} \times \mathbf{H}_t\right]. \tag{2.13}$$

For the *normal* incidence, this means matching to the free space wave impedance η_0. Hence, an absorbing boundary condition should be obtained in this case. From the numerical point of view, interleaving of the field components in Yee's lattice forces us to make approximations. Maloney and Smith used the magnetic field component half-cell away from the boundary and half time step earlier in time to approximate the magnetic field on the boundary. Through many numerical examples, Maloney and Smith showed that their model works well for relatively large conductivities. However, for loss tangents (denoted here by p) smaller than $p \approx 1$, they reported increasing discrepancy with decreasing loss tangent. It will be later shown that the problems with the Maloney-Smith formulation can be considerably alleviated. First, a couple of other methods are briefly discussed.

Kellali *et al.* explored the possibility of inclusion of the angle of incidence in an FDTD SIBC model. Their formulation is valid for any *single* angle of incidence. Kellali *et al.* used the simple surface impedance which is correct only for the normal incidence in implementing the convolution product [9]. Kellali treated the horizontal and the vertical polarizations of the incident waves separately. Kellali's way of including the angle of incidence cannot be considered as a great generalization, since the incidence angle must be *a priori* known. In many practical problems, the incident wave is so complicated that a formulation which is valid only for a *single* angle of incidence cannot be applied. Kellali also used the idea of implementing the Leontovich SIBC in the time domain by fitting a series of exponential functions to the time domain surface impedance. This method allows the recursive evaluation of the convolution integral, being much more efficient than direct integration that should be done at every time step over the entire time history of the fields.

Oh and Schutt-Aine did not make the high conductivity approximation in [10], but the angle of incidence is not included into their implementation. Oh and Schutt-Aine used a series of first-order rational functions to approximate the impedance function in the Leontovich surface impedance relation. This formulation is again limited in the sense that the tangential variations of the fields on the interface are just neglected. Oh and Schutt-Aine wrote the impedance function of the Leontovich SIBC in the Laplace domain as

$$Z_c(s) = \eta \sqrt{\frac{\frac{s}{a}}{1 + \frac{s}{a}}} \tag{2.14}$$

and then used a normalized impedance function $Z_N(s')$ defined as

$$Z_N(s') = \frac{1}{\eta} Z_c(as') = \sqrt{\frac{s'}{1+s'}}. \tag{2.15}$$

The normalized impedance function can be approximated by

$$Z_N(s') = 1 - \sum_{i=1}^{L} \frac{C_i}{\omega_i + s'}, \tag{2.16}$$

where L denotes the number of first-order rational functions used in the approximation [10]. Now, the expression for the surface impedance boundary condition in the time domain can be written as [10]

$$\begin{aligned} \mathbf{E}_t(t) &= \mathcal{Z}_c(t) * \mathbf{n} \times \mathbf{H}_t(t) \\ &\approx \eta \left[\mathbf{n} \times \mathbf{H}_t(t)\right] - \eta \int_0^t \sum_{i=1}^{L} aC_i e^{a\omega_i(t-\tau)} \left[\mathbf{n} \times \mathbf{H}_t(\tau)\right]. \end{aligned} \tag{2.17}$$

This SIBC forms the basis of the discrete implementation, which is not considered here. Oh and Schutt-Aine reported quite good agreement with the exact results in one-dimensional example case, where the magnitude of a reflection coefficient from a half-space was calculated.

The use of rational approximations in the Laplace-domain seems a bit strange at first glance because the exact inverse Laplace transform of the Laplace-domain impedance function is known. Oh and Schutt-Aine showed in [10] that the maximum relative error of their approximation can be made very small, even if the number of terms in the approximation is quite acceptable. Their formulation has the advantage of eliminating the preprocessing time required for the exponential approximation of the time-domain impedance function. After all, the elimination of the preprocessing time can be regarded as a small improvement as compared to the previous models like [7].

More recently, Yuferev *et al.* used the perturbation theory in their SIBC implementation [11]. They used the high conductivity approximation, which is not made in this thesis. The numerical results presented in [11] do not indicate very good accuracy even for a relatively high conductivity of 1 S/m. Their model is designed to upgrade FDTD codes, where perfect electric conductor (PEC) boundary conditions have already been implemented. Yuferev starts with the general SIBC relating the tangential field components. It reads

$$\mathbf{E} = f(\mathbf{H}) \tag{2.18}$$

on the interface between the two media. The time-domain impedance function f is supposed to be known. In the one-dimensional example case, Yuferev *et al.* write the general SIBC of form (2.18) in discrete space as

$$E_i^n \approx f(H_{i-1/2}^{n-1/2}). \tag{2.19}$$

The boundary nodes are denoted by i. This approximation is then combined with the normal update equation for the tangential magnetic field. Yuferev assumes in [11] that the electric field on the interface is much smaller than inside the dielectric medium. This assumption implies that their formulation is not valid when the dielectric constant and the conductivity of the second medium are simultaneously small. The update equation for the magnetic field half cell away from the boundary was derived using the perturbation theory for the postulated small parameter relating the field components near the interface. Whenever the computational accuracy is appreciated, then Yuferev's method should be avoided, although results based on their model may have some engineering value.

Farahat *et al.* discuss the higher order SIBC in [12]. They use a more sophisticated version of the simple Leontovich SIBC which has the so called Mitzner's and Rytov's approximations included. The appropriate SIBC in TE_y configuration is of the form

$$E_t = T_1 * H_y - \frac{1}{R} T_2 * H_y - T_3 * \left(\frac{H_y}{8R^2} + \frac{1}{2} \frac{\partial^2 H_y}{\partial s^2} \right), \tag{2.20}$$

where $*$ denotes the convolution product, R is the local radius of curvature, s is the arc length and the time-dependent functions $T_i, \quad i = 1, 2, 3$ are written in the following form [12]:

$$\begin{aligned} T_1(t) &= \sqrt{\frac{\mu}{\epsilon}} \left[\delta(t) + \frac{\sigma}{2\epsilon} \left(I_1(\frac{\sigma t}{2\epsilon}) - I_0(\frac{\sigma t}{2\epsilon}) \right) e^{-\frac{\sigma t}{2\epsilon}} \right], \\ T_2(t) &= \frac{1}{\epsilon} e^{-\frac{\sigma t}{2\epsilon}}, \\ T_3(t) &= \frac{t}{\epsilon\sqrt{\epsilon\mu}} \left[I_0(\frac{\sigma t}{2\epsilon}) - I_1(\frac{\sigma t}{2\epsilon}) \right] e^{-\frac{\sigma t}{2\epsilon}}, \end{aligned} \tag{2.21}$$

where $I_n(t)$ is the modified Bessel function of order n and $\delta(t)$ is the Dirac delta function. The first term of (2.20) corresponds to the Leontovich SIBC. The functions T_2 and T_3 are related to the Mitzner's and Rytov's approximations, respectively. Contour-path method was used in [12] to account for the curvature of the cylindrical scatterer. They, however, neglect some spatial errors in the discretization which may actually deteriorate the expected accuracy resulting from the higher order formulation. Power series expansions were also used in their implementation, introducing an additional error source. It is not clear from the numerical examples presented in [12] whether their higher-order SIBC-model is accurate or not, because comparison to exact solution is omitted.

As discussed in this chapter, the proposed model is totally different from those presented in [11] and [12]. The proposed model is mathematically quite simple, because power series expansions or perturbation techniques are not needed. In what follows, it is shown that by starting with the exact operational surface impedance and by using a suitable rational approximation, the SIBC models proposed in [7]–[8] can be extended to be valid for small conductivities as well

(an absorbing boundary condition is obtained for negligible values of conductivity and no dielectric contrast). The inclusion of the angle of incidence in the model is performed in a quite general fashion by turning the tangential wavevector into a spatial derivative. Hence, the presented formulation is a good approximation for *all* angles of incidence.

In section 2.2, the exact surface impedance for modeling conductive half-spaces is presented and a rational approximation scheme is introduced. The FDTD-implementation of the surface impedance relation is discussed in section 2.3. In section 2.4, the proposed model is validated by comparing to the exact results. The results are compared with the results obtained using the Maloney-Smith method, since the proposed method is considered to be a natural higher-order extension of that method.

2.2 The Exact Surface Impedance Model

Consider a problem, where the solution space consists of a region of free space ($\epsilon_1 = \epsilon_0, \mu_1 = \mu_0, \sigma_1 = 0$) and another region of a conductor ($\epsilon_2 = \epsilon_{2,r}\epsilon_0, \mu_2 = \mu_0, \sigma_2 \neq 0$). The interface between these two regions is assumed to be planar. The problem geometry and the equivalent surface impedance model are shown in Figure 2.1.

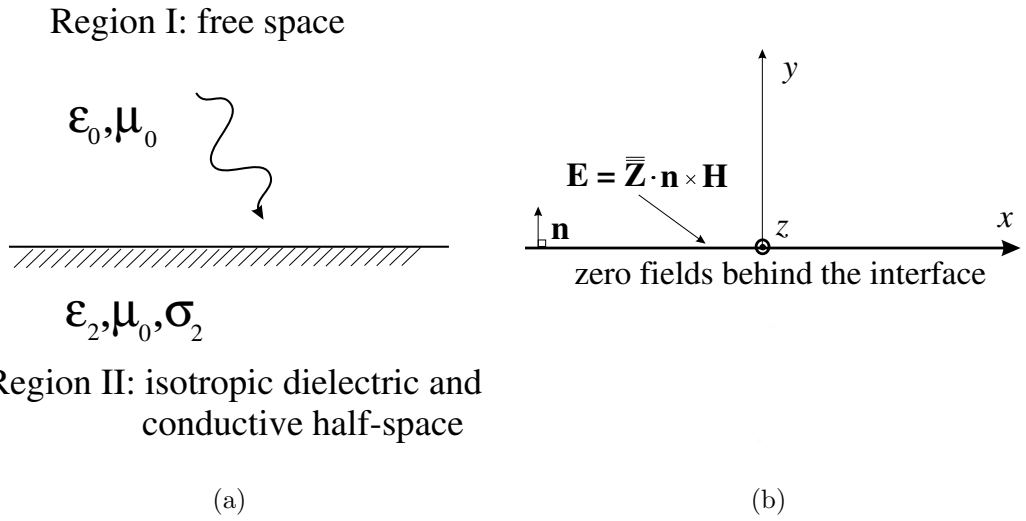

(a) (b)

Figure 2.1: (a) The interface between free space and isotropic dielectric and conductive half-space. (b) The equivalent surface impedance model.

The second medium can be modeled with the exact surface impedance operator which can be derived, for example, by using the equivalent circuit theory as in [23]. In the frequency domain the exact SIBC reads

$$\mathbf{E}_t = \overline{\overline{Z}}_s \cdot \mathbf{n} \times \mathbf{H}_t, \tag{2.22}$$

where the impedance operator is of the form

$$\overline{\overline{Z}}_s = Z(\omega)\frac{k\left(\overline{\overline{I}}_t + \frac{\nabla_t\nabla_t}{k^2}\right)}{\sqrt{k^2+\nabla_t^2}}. \tag{2.23}$$

Here, $\overline{\overline{I}}_t$ is the two-dimensional unit dyadic, and ∇_t is the two-dimensional gradient operator. Both operators are defined in the plane of the interface between the two media. The coefficient $Z(\omega)$ is the same as in the Leontovich boundary condition and it is given by (2.2). The exact surface impedance relation (2.22) simulates the conducting half space and it forms the basis of the subsequent derivations.

The difference in the starting point as compared to [7] is evident. In [7] the assumption

$$\left|\epsilon_{2,r} - j\frac{\sigma_2}{\omega\epsilon_0}\right| \gg \sin^2(\theta_i), \tag{2.24}$$

where θ_i is the angle of incidence was made to justify the use of Leontovich's surface impedance relation of the form

$$\mathbf{E}_t = Z_s(\omega)\mathbf{n}\times\mathbf{H}_t. \tag{2.25}$$

It is easily seen that the assumption (2.24) is not valid (for all angles of incidence) for small values of $\sigma_2/(\omega\epsilon_0)$ and for typical relative dielectric constants of conductors (usually they are close to unity).

2.3 An FDTD Implementation of the Surface Impedance

To keep the notations simpler, the derivation of the new method is done in two dimensions, and the three-dimensional case is briefly discussed later. Consider a two-dimensional problem of excitation of a conducting half space by TE-polarized sources. Let the interface be located at $y = 0$ with $\mathbf{n} = \mathbf{u}_y$ and let the currents of the sources flow in the z-direction. Thus, we have the field components H_x, H_y and E_z in a 2D FDTD lattice.

It is convenient to introduce the Laplace transform variable $s = j\omega$. In the Laplace-transformed domain, the scalar part of the surface impedance operator reads

$$Z(s) = \frac{\eta_0}{\sqrt{\epsilon_{2,r}}}\frac{\sqrt{s}}{\sqrt{s+\frac{\sigma_2}{\epsilon_2}}}. \tag{2.26}$$

The inverse Laplace transform of (2.26) is known to be

$$\mathcal{Z}(t) = \frac{\eta_0}{\sqrt{\epsilon_{2,r}}}\left[\alpha e^{\alpha t}(I_0(\alpha t)+I_1(\alpha t))u(t)+\delta(t)\right], \tag{2.27}$$

where $u(t)$ denotes the Heaviside unit step function, $\delta(t)$ is the Dirac delta distribution, and the constant $\alpha = -\sigma_2/2\epsilon_2$. Functions I_0 and I_1 are the modified Bessel functions of the first kind and of order zero and one, respectively.

The denominator of the expression in (2.23) is a pseudo-differential operator. Any practical use of this exact SIBC implies a rational approximation of the square root function in its expression. Let us introduce such an approximation of the function $\sqrt{1-x^2}$ on the interval $-1 \leq x \leq 1$ in the form

$$\sqrt{1-x^2} \approx \frac{a+bx^2}{1+dx^2}. \tag{2.28}$$

Different choices of the coefficients corresponding to different approximation schemes can be found in [24]. A good approximation of the square root in (2.28) is obtained by choosing $a = 0.99973$, $b = -0.80864$, $d = -0.31657$, corresponding to the so called Chebyshev on a subinterval approximation scheme. These parameters are used in the numerical simulations. Using the rational approximation of the form (2.28) in (2.22)–(2.23) and simplifying, we have the following equation for the phasor quantities:

$$\begin{aligned} \left(-a\epsilon_2\mu_0 s^2 - a\sigma_2\mu_0 s - b\frac{\partial^2}{\partial x^2}\right) E_z \;\; &= \\ -\frac{\eta_0}{\sqrt{\epsilon_{2,r}}} Z(s) \left(-\epsilon_2\mu_0 s^2 - \sigma_2\mu_0 s - d\frac{\partial^2}{\partial x^2}\right) H_x. & \end{aligned} \tag{2.29}$$

The dispersion relation for materials with conductivity σ_2 is $k^2 = -\epsilon_2\mu_0 s^2 - \sigma_2\mu_0 s$, and it was used in deriving (2.29). In contrast to the simple impedance boundary condition, this boundary condition contains tangential derivatives of both electric and magnetic fields thus taking into account field variations along the interface. Boundary conditions of this type are known as *higher-order impedance boundary conditions*.

Next, this equation will be transformed into the time domain. The product of two Fourier-transformed (or Laplace-transformed) quantities in the frequency domain corresponds to a convolution in the time domain. The Dirac delta function convolved with a smooth function $f(t)$ reproduces the function $f(t)$. Using the transform pair $s \leftrightarrow \partial/\partial t$ we obtain the desired SIBC in the time domain:

$$\begin{aligned} &-a\epsilon_2\mu_0\frac{\partial^2 E_z}{\partial t^2} - a\sigma_2\mu_0\frac{\partial E_z}{\partial t} - b\frac{\partial^2 E_z}{\partial x^2} \;\; = \\ &\frac{\eta_0}{\sqrt{\epsilon_{2,r}}}\left[\sigma_2\mu_0\frac{\partial H_x}{\partial t} + d\frac{\partial^2 H_x}{\partial x^2} + \epsilon_2\mu_0\frac{\partial^2 H_x}{\partial t^2}\right] + \frac{\eta_0}{\sqrt{\epsilon_{2,r}}} \cdot \\ &\int_0^t \alpha e^{\alpha\tau}(I_0(\alpha\tau) + I_1(\alpha\tau)) \cdot \\ &\left[\sigma_2\mu_0\frac{\partial H_x(t-\tau)}{\partial(t-\tau)} + d\frac{\partial^2 H_x(t-\tau)}{\partial x^2} + \epsilon_2\mu_0\frac{\partial^2 H_x(t-\tau)}{\partial(t-\tau)^2}\right] d\tau. \end{aligned} \tag{2.30}$$

By letting $\sigma_2 \to \infty$ and integrating once, we see that equation (2.30) reduces to $E_z = 0$ at the boundary, which is the boundary condition for a perfectly

conducting half-space. If we try to discretize equation (2.30) at $t = n\Delta t$, we find that the standard center difference scheme for $\partial^2 H_x/\partial t^2$ cannot be used. The reason is that the update equation is derived for E_z at time step $n+1$, but we do not know the value of H_x at this time step. This problem can be avoided, if we use the Maxwell equations and replace $\partial H_x/\partial t$ by $-\partial E_z/\mu_0 \partial y$. When this substitution is used under the convolution integral, we have to extract the electric field components at time step $n+1$ from under the integral and solve the resulting equation for E_z at time step $n+1$. As an example, consider the lattice boundary at $y = 0$. The discretization is done on that boundary at the grid position $(i, 0)$ at time step n. The update equation is then obtained for E_z located at $(i, 0)$ at time step $n+1$. No half-cell temporal or spatial differences are neglected. This is different from the implementation presented in [7] and [8], where the tangential magnetic field at the boundary was approximated by the nearest neighbor evaluated half time step earlier in time. The most important new feature of this method is inclusion of the pseudo-differential operator in the denominator of (2.23) by using a rational approximation. In the earlier FDTD models [7, 8, 10] that operator was just neglected.

It may be noticed that a straightforward discretization of $\partial E_z/\partial y$ using central differencing on the boundary is impossible because the fields behind the boundary surface are not defined. We have found that a third order accurate difference approximation for $\partial E_z/\partial y$ of the form

$$\left.\frac{\partial E_z}{\partial y}\right|_{i,0}^{n} \approx \frac{-11E_z\big|_{i,0}^{n} + 18E_z\big|_{i,1}^{n} - 9E_z\big|_{i,2}^{n} + 2E_z\big|_{i,3}^{n}}{6\Delta y} \tag{2.31}$$

works quite well. This scheme can be utilized in the discretization of $\partial^2 E_z/\partial y \partial t$ as well. A similar approach to approximate the normal derivative of the electric field was previously published by Lee *et al.* in [13], where the FDTD-modeling of thin PEC-backed sheets was discussed. The approximation of $\partial^2 E_z/\partial y \partial t$ was based on the use of a quadratic Lagrange interpolation polynomial. It can be shown that the use of the cubic Lagrange interpolation formula leads (after differentiation) to the approximation of form (2.31). To approximate the second order x-derivative of the tangential magnetic field on the boundary we evaluate the quadratic Lagrange interpolation polynomial for the fields at the boundary. The result is

$$\left.\frac{\partial^2 H_x}{\partial x^2}\right|_{i,0}^{n} \approx \frac{15\frac{\partial^2 H_x}{\partial x^2}\big|_{i,1/2}^{n} - 10\frac{\partial^2 H_x}{\partial x^2}\big|_{i,3/2}^{n} + 3\frac{\partial^2 H_x}{\partial x^2}\big|_{i,5/2}^{n}}{8}. \tag{2.32}$$

The problem of an efficient evaluation of the convolution integral is a common feature of the proposed methods and the methods in [7]–[8]. This is briefly discussed next. To discretize (2.30) the convolution integral is approximated as a sum of the form

$$\sum_{m=0}^{n-1} F(m) f(E_z|^{n-m}, H_x|^{n-m}), \tag{2.33}$$

where the function f refers to the part of the integrand that depends on the field components E_z and H_x at time steps $1 \dots n$. Assuming a piecewise linear behavior of $f(E_z, H_x)$, the coefficients $F(m)$ can be calculated as

$$F(m) = \int_{\max(0,m-1)}^{m+1} \alpha\Delta t \,(1 - |\xi - m|)\, e^{\alpha\Delta t\xi} \left[I_0(\alpha\Delta t\xi) + I_1(\alpha\Delta t\xi)\right] d\xi. \quad (2.34)$$

These coefficients are evaluated numerically in the beginning of FDTD simulations. For an efficient implementation, as discussed in [7] and in [8], the coefficients $F(m)$ can be obtained as a series of exponentials as

$$F(m) = \sum_{k=1}^{p} \beta_k e^{\hat{\gamma}_k m} = \sum_{k=1}^{p} \beta_k \gamma_k^m. \quad (2.35)$$

This is the so called Prony's method [28]. The summary of Prony's method with some practical hints for finding the coefficients β_k and γ_k can be found in the Appendix of [7] or in [8]. The numerical results in section 2.4 were calculated with $p = 13$. Essentially identical results were obtained with even smaller number of terms in the exponential approximation. Overall, the parameter p has a negligible effect on the results provided that it is about $p > 6$. Now, the integral in (2.30) at the grid position $x = i\Delta x$ may be expressed as a discrete sum in the form

$$\begin{aligned}
\sum_{m=0}^{n-1} F(m) f(E_z|_i^{n-m}, H_x|_i^{n-m}) &= F(0) f(E_z|_i^n, H_x|_i^n) \\
&+ \sum_{k=1}^{p} \sum_{m=1}^{n-1} \beta_k \gamma_k^m f(E_z|_i^{n-m}, H_x|_i^{n-m}) \\
&= F(0) f(E_z|_i^n, H_x|_i^n) + \sum_{k=1}^{p} G_k|_i^n, \quad (2.36)
\end{aligned}$$

where $G_k's$ at each position $x = i\Delta x$ satisfy a recursive relation of the form

$$\begin{aligned}
G_k|_i^1 &= 0 \ , k = 1, \dots, p \\
G_k|_i^n &= \gamma_k G_k|_i^{n-1} + \beta_k \gamma_k f(E_z|_i^{n-1}, H_x|_i^{n-1}) \ , k = 1, \dots, p. \quad (2.37)
\end{aligned}$$

After careful discretization of (2.30) with the described recursive convolution we obtain the final update equation for the electric field at the lattice boundary ($y = 0$):

$$\begin{aligned}
E_z|_{i,0}^{n+1} &= \frac{1}{A} \Big\{ -2a\epsilon_{2,r}\Delta y \left(-2E_z|_{i,0}^n + E_z|_{i,0}^{n-1}\right) + a\sigma_2\mu_0 c_0^2 \Delta t \Delta y E_z|_{i,0}^{n-1} \\
&- \frac{2b(c_0\Delta t)^2 \Delta y}{\Delta x^2} \left(E_z|_{i+1,0}^n - 2E_z|_{i,0}^n + E_z|_{i-1,0}^n\right) \quad (2.38) \\
&+ \frac{\eta_0\sigma_2(c_0\Delta t)^2(1 + F(0))}{3\sqrt{\epsilon_{2,r}}} \left(-11E_z|_{i,0}^n + 18E_z|_{i,1}^n - 9E_z|_{i,2}^n + 2E_z|_{i,3}^n\right) \\
&+ \frac{\sqrt{\epsilon_{2,r}} c_0 \Delta t(1 + F(0))}{6} \begin{bmatrix} 18E_z|_{i,1}^{n+1} - 9E_z|_{i,2}^{n+1} + 2E_z|_{i,3}^{n+1} + \\ 11E_z|_{i,0}^{n-1} - 18E_z|_{i,1}^{n-1} + 9E_z|_{i,2}^{n-1} - 2E_z|_{i,3}^{n-1} \end{bmatrix} \\
&- \frac{2\eta_0 d(c_0\Delta t)^2 \Delta y(1 + F(0))}{\sqrt{\epsilon_{2,r}}} \frac{\partial^2 H_x}{\partial x^2}\bigg|_{i,0}^n - \frac{2\eta_0(c_0\Delta t)^2 \Delta y}{\sqrt{\epsilon_{2,r}}} \sum_{k=1}^{p} G_k|_i^n \Big\},
\end{aligned}$$

where $\partial^2 H_x/\partial x^2$ is discretized according to (2.32) and the coefficient A is defined as

$$A = 2a\epsilon_{2,r}\Delta y + \frac{11}{6}\sqrt{\epsilon_{2,r}}c_0\Delta t(1+F(0)) + a\sigma_2\mu_0 c_0^2\Delta t\Delta y. \tag{2.39}$$

In the three-dimensional case, the numerator of (2.23) does not simplify as in two dimensions. Thus, the resulting SIBC is more complicated to discretize, although the square root may be approximated in a similar fashion as in two dimensions. It turns out that the resulting SIBC is a fourth-order PDE.

2.4 Validation of the Model

The method is validated by calculating the reflected fields and the total fields on the interface in the presence of a line current $I(t)$ radiating over a half-space. The exact solution for this problem in time domain can be calculated using numerical integrations. Let a line current source be located at $(x, y) = (0, y_s)$ and the interface be at $y = 0$. The analytical expression for the reflected electric field in the Fourier domain at the position $(x_0, 0)$ is of the form [7]

$$E_z^r(\omega, x) = -\frac{\mu_0\omega}{2\pi}I(\omega)\int_0^\infty R(\omega,\xi)\frac{1}{\sqrt{1-\xi^2}}e^{-j\frac{\omega y_s}{c_0}\sqrt{1-\xi^2}}\cos\frac{\omega x_0\xi}{c_0}\,d\xi, \tag{2.40}$$

where the reflection coefficient R is

$$R(\omega,\xi) = \frac{\sqrt{1-\xi^2} - \sqrt{\epsilon_{2,r} - j\frac{\sigma_2}{\omega\epsilon_0} - \xi^2}}{\sqrt{1-\xi^2} + \sqrt{\epsilon_{2,r} - j\frac{\sigma_2}{\omega\epsilon_0} - \xi^2}}. \tag{2.41}$$

The total electric field on the interface is

$$E_z^t(\omega, x) = -\frac{\mu_0\omega}{2\pi}I(\omega)\int_0^\infty \frac{1+R(\omega,\xi)}{\sqrt{1-\xi^2}}e^{-j\frac{\omega y_s}{c_0}\sqrt{1-\xi^2}}\cos\frac{\omega x_0\xi}{c_0}\,d\xi. \tag{2.42}$$

The numerical results are shown in the time domain. To enable a comparison, the reflected and the total waveforms have to be transformed into the time domain. This is performed by numerical integration after suitable transformations of variables to facilitate the convergence of the integrals in (2.40) and (2.42). The integrals from 0 to ∞ are split into two integrals: from 0 to 1 and from 1 to ∞. A reasonable transformation of the integration variable in the first integral is to set $\xi = \sin u$. The singularity is removed, because $d\xi = \cos u\ du$ cancels the denominator having the singularity. In the second integral from 1 to ∞, we first notice that $\sqrt{1-\xi^2} = -j\sqrt{\xi^2-1}$ (the negative sign is chosen to get a decaying exponential) and then substitute $\sqrt{\xi^2-1} = u$. The singularity is again removed, and accurate integration is possible even with quite simple quadratures. The exact results presented below are calculated by implementing numerical integrations with the midpoint rule. The differentiated gaussian pulse of the form

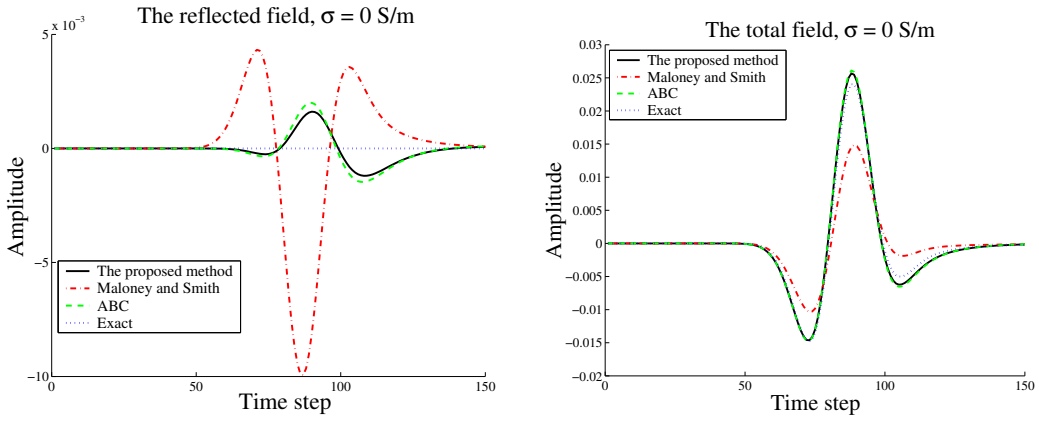

(a) (b)

Figure 2.2: (a) The reflected electric field at the observation point. The numerical reflection from the interface is small, if the proposed model is used. However, due to the fact that the higher-order terms were neglected in the model by Maloney and Smith, there is significant error in the reflected wave if that model is used. It is noticeable that the proposed model gives very similar results as a third-order analytical absorbing boundary condition. (b) The total electric field at the observation point. The total electric field simulated with the present model is close to the analytically calculated total electric field.

$$I(t) = \frac{t-\tau_0}{\tau} e^{-\left(\frac{t-\tau_0}{\tau}\right)^2} \tag{2.43}$$

with $\tau_0 = 40\Delta t, \quad \tau = 12\Delta t$ is used as a source throughout the simulations. The analytical Fourier transform $I(\omega)$ of this function can be easily calculated.

It is natural to start the numerical examples with the case $\sigma_2 = 0$, $\epsilon_{2,r} = 1$ to see how well the proposed method reduces to an absorbing boundary condition (ABC). The results are shown in Figure 2.2. A third order analytical ABC with Chebyshev on a subinterval approximation of the square root was used to calculate the numerical reference result in the figure. The analytical ABC is based on [25]. It is seen that the proposed method reduces to a quite good ABC. To see which ABC is better, further studies would be necessary. Liao's third order ABC's [26] are used at the other boundaries throughout the simulations.

The reflected and total waveforms for $\sigma_2 = 0.01$ S/m calculated with the proposed method, the method proposed by Maloney and Smith, and the exact waveforms at the observation point on the interface are shown in Figure 2.3. Liao's third order ABC's [26] are used at the other boundaries. To illustrate the performance of the proposed method at oblique incidence, the fields are observed at point $(x_0, 0)$, where $x_0 = 20\Delta x$. The distance from the interface to the source is $d = 10\Delta y$. Square grid cells are used with $\Delta x = \Delta y = 0.015$ m. The size of the time step was chosen to be $\Delta t = \Delta x/(2c_0)$ in all the simulations. Based on the numerical experiments, we found that the stability limit for our

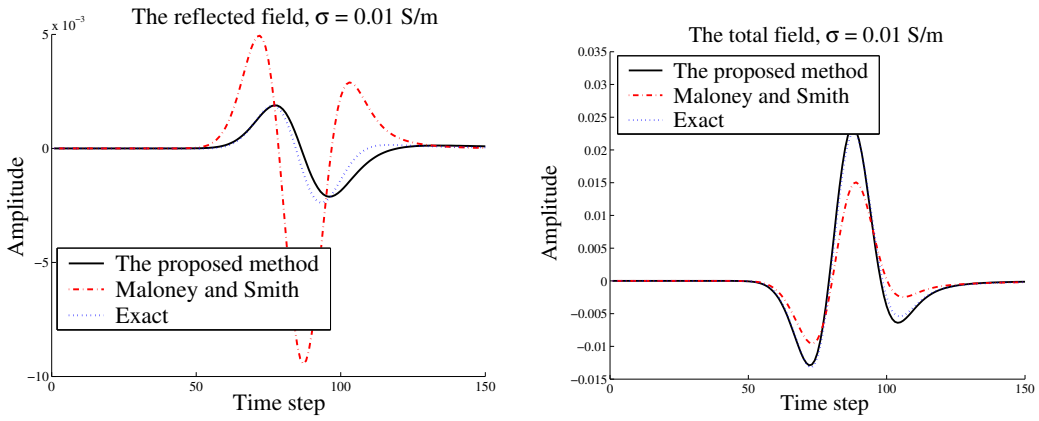

(a) (b)

Figure 2.3: (a) The reflected electric field at the observation point. (b) The total electric field at the observation point.

model is stricter than the usual Courant limit for the Yee algorithm. However, a suitable choice of the time step yields stable results, also at late times. Analytical derivation of the stability limit for the proposed technique may be quite difficult.

The proposed method gives rather accurate results for $\sigma_2 = 0.01$ S/m (Figure 2.3), while the SIBC implementation of Maloney and Smith yields clearly incorrect reflected waveform and too small amplitude for the total field. The conductivity is rather small in this case, and the possible errors are more clearly visible in the reflected wave, which is the smaller quantity. Actually, the analytical SIBC is almost an ABC in this case. The loss tangent $p = \sigma_2/\omega\epsilon_2$ at the peak frequency is $p \approx 0.24$. It is clear that the high conductivity approximation made in [7]–[8] is not valid in this case.

Snapshots of the total electric field distributions at time step $n = 110$ are shown in Figure 2.4. The source is in the grid position $(50, 10)$. Discrepancy near the boundary is evident. The largest difference occurs near the boundary where the angle of incidence is far enough from the normal. In Figure 2.5, the waves are calculated for a larger conductivity, namely for $\sigma_2 = 0.1$ S/m. In this case, the proposed method agrees very well with the exact result. The Maloney-Smith scheme produces slightly worse results. The reflected and the total electric field are of the same order of magnitude, the reflected field still being the smaller quantity. The third case which is considered is the case when $\sigma_2 = 1$ S/m. The results are presented in Figure 2.6. In this case, the total field is slightly smaller quantity. Both methods agree well with the exact waveforms. For still larger conductivities the SIBC is quite close to the PEC boundary condition. This situation is shown in Figure 2.7, where $\sigma_2 = 10$ S/m. The total field is clearly smaller than the reflected field. The agreement is seen to be quite good for both methods and for both the reflected and total

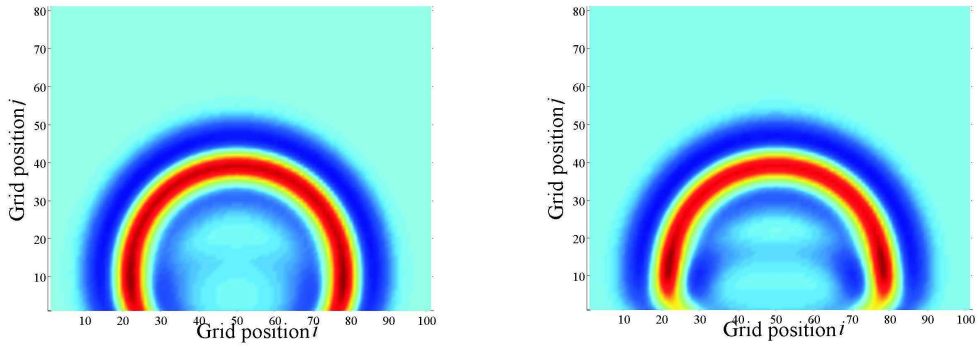

(a) (b)

Figure 2.4: (a) The total electric field distribution near the interface at $n = 110$ using the proposed method. A line current has radiated a pulse near the interface. Due to the small conductivity ($\sigma_2 = 0.01$ S/m) and the absence of dielectric contrast ($\epsilon_{2,r} = 1$), the boundary absorbs most of the energy, and the reflected wave is very small. (b) The total electric field distribution at $n = 110$ using the Maloney and Smith method.

electric fields. In this case, the loss tangent at the peak frequency is already quite large: $p \approx 240$. The high conductivity approximation made in [7]–[8] can be seen to be valid in this case. Indeed, the numerical and the exact solutions are almost indistinguishable.

2.5 Discussion

A new finite-difference time-domain model of conductors and dielectrics with nonzero conductivity using a higher order impedance boundary condition has been introduced. The advantage of the new approach compared to the previously published methods is that it takes the angle of incidence into account while not making assumptions about a large conductivity of the material. The differences and the similarities to the existing methods have been discussed and the method has been validated by comparing to the analytical results for a half space excited by a line current over a wide range of conductivities.

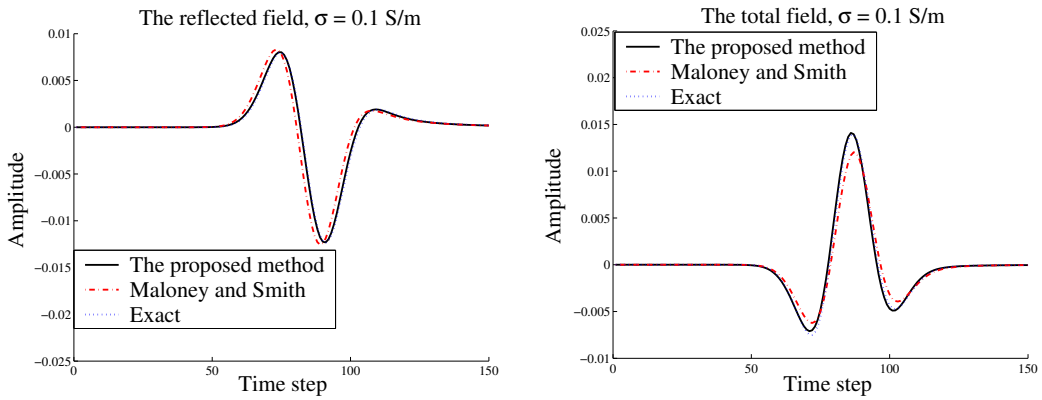

(a) (b)

Figure 2.5: (a) The reflected electric field at the observation point. (b) The total electric field at the observation point.

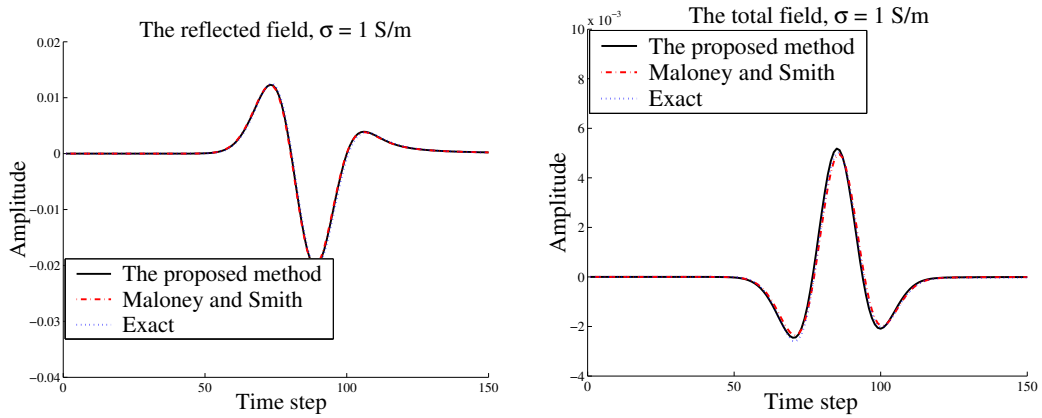

(a) (b)

Figure 2.6: (a) The reflected electric field at the observation point. (b) The total electric field at the observation point.

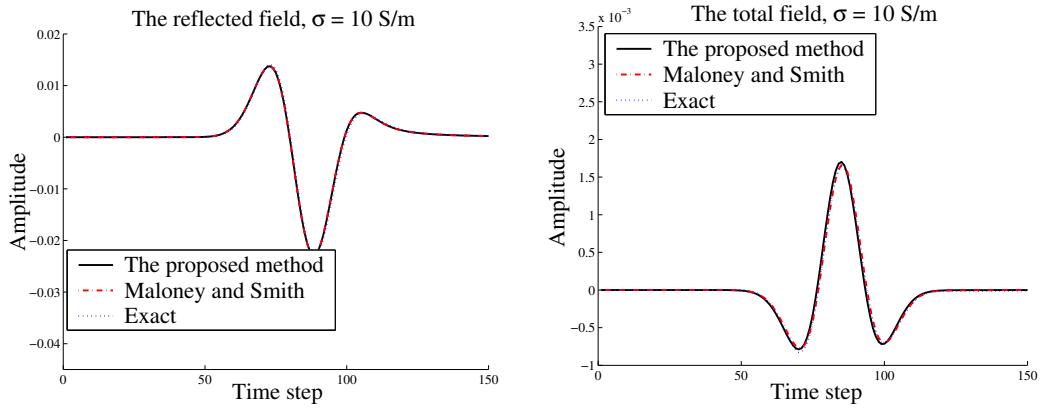

(a) (b)

Figure 2.7: (a) The reflected electric field at the observation point. It is seen that the proposed model yields similar results as the model by Maloney and Smith, if the conductivity of the half-space is very high. (b) The total electric field at the observation point.

Chapter 3

Analytical Absorbing Boundary Conditions

Absorbing boundary conditions (ABC) are widely used within the FDTD method. Ideally, an ABC should absorb all electromagnetic waves impinging to the lattice boundary regardless of the angle of incidence or the frequency of the incident wave. In this chapter, the history of ABC's is briefly discussed first. Then, a new class of analytical absorbing boundary conditions based on the exact surface impedance boundary condition simulating an empty half space will be derived. The ABC's are verified with a two-dimensional FDTD program with comparison to some analytical ABC's based on the Engquist-Majda one-way wave equation [25].

3.1 History of Absorbing Boundary Conditions

The use of absorbing boundary conditions to truncate the computational lattice is a very common feature in FDTD simulations. Several approaches have been taken during the recent decades to solve this problem.

An old class of analytical ABC's is based on the so called Bayliss-Turkel radiation operators. The idea is to construct a linear partial differential operator where spatial and time derivatives of the fields are present [30]–[31]. An appropriately constructed operator annihilates the outgoing waves and the numerical lattice can be truncated, an important feature in modeling antennas, for example. Bayliss-Turkel radiation operators are usually written in cylindrical or spherical coordinates. This fact makes the implementation into cartesian FDTD-programs quite cumbersome. A better idea is to consider the wave equation in cartesian coordinate system and to derive the ABC's locally.

The simplest analytical ABC's based on Engquist-Majda wave equation are the first and the second order Mur ABC's [44]. They are easy to implement, and

the computational burden does not become prohibitive even in large computational domains. This kind of ABC's are formulated for one field component only. As an example, the two-dimensional wave equation in cartesian coordinates reads

$$\frac{\partial^2 U}{\partial x^2} + \frac{\partial^2 U}{\partial y^2} - \frac{1}{c^2}\frac{\partial^2 U}{\partial t^2} = 0, \tag{3.1}$$

where U is a scalar function, for example an electric field component in the FDTD algorithm, and c is the wave phase velocity [27]. Defining a partial differential operator G as

$$G = \frac{\partial^2}{\partial x^2} + \frac{\partial^2}{\partial y^2} - \frac{1}{c^2}\frac{\partial^2}{\partial t^2}, \tag{3.2}$$

the wave equation can be compactly written as $GU = 0$. Engquist and Majda showed [25] that decomposition of the partial differential operator G into product of two operators as $G = G^+G^-$ where

$$\begin{aligned} G^+ &= \frac{\partial}{\partial x} + \frac{\partial}{c\partial t}\sqrt{1 - \frac{c^2\frac{\partial^2}{\partial y^2}}{\frac{\partial^2}{\partial t^2}}} \\ G^- &= \frac{\partial}{\partial x} - \frac{\partial}{c\partial t}\sqrt{1 - \frac{c^2\frac{\partial^2}{\partial y^2}}{\frac{\partial^2}{\partial t^2}}} \end{aligned} \tag{3.3}$$

leads to a possibility to exactly absorb the outgoing numerical waves of arbitrary incidence angles at the lattice boundary $x = x_{min}$ by applying the operator G^- to the wave function. The operator G^+ performs the same operation at the lattice boundary $x = x_{max}$ [27]. The operators G^- and G^+ are pseudo-differential operators. Thus, they cannot be directly applied to numerical analysis. The problem is how to approximate the function $\sqrt{1-x^2}$ as uniformly as possible on the interval $-1 \leq x \leq 1$. It has been found that quite good approximation properties can be achieved with a rational approximation of the form

$$\sqrt{1-x^2} = \frac{a + bx^2}{1 + dx^2}. \tag{3.4}$$

This approximation was already used in the previous chapter. After the rational approximation, a partial differential equation (PDE) representing the corresponding analytical ABC may be derived. It is worth noticing that the rational approximation above is valid only for propagating waves. To efficiently absorb also evanescent waves, the square root should be approximated outside the interval $-1 \leq x \leq 1$ as well. This possibility is not explored in this treatise.

Higdon introduced a series of linear partial differential operators for the absorbtion of outgoing waves [32]. This feature is similar to the method by Bayliss and Turkel. The exact absorption occurs at specific angles of incidence. As an example, consider plane waves traveling with the speed c towards the lattice

boundary $x = 0$ in a two-dimensional cartesian FDTD grid. Higdon proposed a differential annihilator as a product of the form

$$\left[\prod_{l=1}^{L}\left(\cos\alpha_l\frac{\partial}{\partial t} - c\frac{\partial}{\partial x}\right)\right] = 0 \tag{3.5}$$

for exact absorption of waves at incidence angles $\alpha_l, l = 1, \ldots, L$ (relative to the $-x$-axis). It may be shown that the Engquist-Majda analytical ABC's are a special case of the more general Higdon ABC, corresponding to some set of coefficients α_l. Higdon's ABC's have the convenient feature of not requiring space derivatives tangential to the grid outer boundary. Thus, the problem of evaluating the parallel space derivatives near lattice corners is removed.

Liao *et al.* presented a totally different ABC in [26] which is based on extrapolation in space and time. Numerical experiments indicate that Liao's ABC is much better than the second-order Mur ABC [27]. Unlike the ABC's discussed earlier, Liao's ABC are capable of realizing the theoretical level of reflection [27]. The underlying Newton's extrapolation process is robust and makes no assumptions about the angle of incidence of the waves.

The perfectly matching layer (PML) absorbing boundary condition, first introduced by Berenger in [33] should be used, when only a very small reflection from the lattice boundary is allowed. However, PML's require quite large computational efforts and are more tedious to efficiently implement into FDTD programs. PML's are based on constructing an artificial layer with a suitable conductivity profile to terminate the computational lattice. More sophisticated versions of PML ABC's have been recently developed. PML's will not be discussed here in detail, because a contribution to the analytical ABC's is the main topic is this chapter.

In the rest of this chapter, a new class of analytical ABC's which stems from the exact impedance boundary condition simulating empty half space is introduced. The key characteristic feature of this approach is the presence of both tangential electric and magnetic fields in the ABC, which, as we show, leads to a possibility to derive ABC with only second-order differentiations which is approximately as accurate as the conventional third-order schemes.

We start with a discussion of an interesting connection between the exact impedance boundary condition for isotropic half space and the Engquist-Majda equation [25] for the absorption of plane waves. The Engquist-Majda wave operator operates on one field component. Thus, all the resulting absorbing boundary conditions are always for one field component only. In section 3.2 we introduce the exact surface impedance boundary condition for modeling the behavior of an isotropic half-space with material parameters ϵ and μ. In the case when $\epsilon = \epsilon_0$ and $\mu = \mu_0$, the resulting surface impedance boundary condition should work as an ABC. The Engquist-Majda wave operator is also derived in this case.

In section 3.3, a class of ABC's connecting the tangential field components

is derived using a general form of rational approximation to approximate the involved pseudo-differential operator. The performance of the proposed ABC's is studied and comparisons with some previously introduced analytical ABC's are made with a test 2D FDTD program. These results are presented in section 3.4.

3.2 SIBC and Its Relation to the Engquist-Majda Equation

To set up the scene and introduce the necessary relations, we will now discuss the surface impedance boundary condition and the Engquist-Majda equation, since both can be used in derivations of analytical ABC's. To terminate the grid of calculation domain, we should somehow simulate a virtual boundary with free space. It is known that the Engquist-Majda equation applied to every tangential component of the electric field on the boundary can serve for this purpose. On the other hand, theoretically one can demand that the exact surface impedance boundary condition (SIBC) connecting tangential electric and magnetic fields on the same boundary be satisfied. This condition can be derived, for instance, using the equivalent circuit theory [23]. The SIBC reads

$$\mathbf{E}_t = \overline{\overline{Z}}_s \cdot \mathbf{n} \times \mathbf{H}_t, \tag{3.6}$$

where the impedance operator is of the form

$$\overline{\overline{Z}}_s = \eta \frac{k\left(\overline{\overline{I}}_t + \frac{\nabla_t \nabla_t}{k^2}\right)}{\sqrt{k^2 + \nabla_t^2}}. \tag{3.7}$$

Index t denotes the tangential field components, and $\mathbf{n}$ is the unit vector pointing outwards from the dielectric (or vacuum) half space. To simplify the notation, let the interface be located at $y = 0$ with $\mathbf{n} = \mathbf{u}_y$. Equations (3.6) and (3.7) for plane waves $e^{-j(k_x x + k_y y + k_z z)}$ take the form

$$E_x \mathbf{u}_x + E_z \mathbf{u}_z = \eta \frac{\overline{\overline{I}}_t - \mathbf{k}_t \mathbf{k}_t / k^2}{\sqrt{1 - \left(\frac{k_x^2 + k_z^2}{k^2}\right)}} \cdot \mathbf{u}_y \times \left(H_x \mathbf{u}_x + H_z \mathbf{u}_z\right). \tag{3.8}$$

where $\mathbf{k}_t = k_x \mathbf{u}_x + k_z \mathbf{u}_z$ is the tangential component of the wave vector. After simplifying equation (3.8), we obtain the SIBC's for the electric field components:

$$\begin{aligned} E_x &= \eta \frac{H_z - \frac{1}{k^2}\left(k_x^2 H_z - k_x k_z H_x\right)}{\sqrt{1 - \frac{k_x^2 + k_z^2}{k^2}}} \\ E_z &= \eta \frac{-H_x - \frac{1}{k^2}\left(k_x k_z H_z - k_z^2 H_x\right)}{\sqrt{1 - \frac{k_x^2 + k_z^2}{k^2}}}. \end{aligned} \tag{3.9}$$

Physically, these conditions simply demand that the electric and magnetic fields are related to each other as in plane waves traveling in an infinite isotropic space, so the surface impedance on the truncation boundary equals to the wave impedance of free space.

It is clear and it is known (see [45]) that the impedance formulation and the Engquist-Majda equation are related, as they express the same feature of the absence of reflection ("matching"). Let us show how the Engquist-Majda equation can be derived from the SIBC for the tangential electric field component E_z. Similar derivation may be done for E_x. We make use of the y-component of the Maxwell equation

$$\nabla \times \mathbf{H} = \epsilon_0 \frac{\partial \mathbf{E}}{\partial t} \tag{3.10}$$

in the form

$$-jk_x H_z + jk_z H_x = -\epsilon_0 j\omega E_y \tag{3.11}$$

and the equation

$$-jk_y E_z + jk_z E_y = -\mu_0 j\omega H_x \tag{3.12}$$

to obtain an equation for the E_z -component only:

$$\left(k\sqrt{1 - \frac{k_x^2 + k_z^2}{k^2}} + k_y \right) E_z = 0. \tag{3.13}$$

Finally, transforming the k's to partial differential operators ($\partial/\partial t \leftrightarrow D_t$ etc.) we obtain

$$\left(\frac{D_t}{c}\sqrt{1 - \frac{D_x^2 + D_z^2}{(D_t/c)^2}} - D_y \right) E_z = 0. \tag{3.14}$$

This is the Engquist-Majda pseudodifferential equation. With different approximations of the square root, a class of analytical absorbing boundary conditions can be derived, as is well known from the literature.

One can observe that in this derivation the Maxwell equations have been used once more, which involves differentiations of the fields. The same can be said about the ABC's derived from the one-way wave equation. The wave equation already contains second-order derivatives of the fields. On the other hand, the impedance boundary condition follows directly from the Maxwell equations. As we already pointed out, the SIBC is simply the relation between the electric and magnetic fields in plane waves. This suggests that one can expect to obtain a better accuracy from an ABC, if the same approximation for the square root is used in the surface impedance boundary condition as compared to ABC's based on the Engquist-Majda operator or on the one-way wave equation. This possibility will be explored next.

3.3 The Derivation of a Class of Analytical ABC's

In the following derivation, we consider the two-dimensional TM_z -case. Let us first introduce a rational approximation of the function $\sqrt{1-x^2}$ on the interval $-1 \leq x \leq 1$ in the form

$$\sqrt{1-x^2} \approx \frac{a+bx^2}{1+dx^2}. \tag{3.15}$$

Using this approximation, the second equation in (3.9) takes the form

$$(ak^2 + bk_x^2)E_z = -\eta(k^2 + dk_x^2)H_x \tag{3.16}$$

with $\eta = \sqrt{\mu_0/\epsilon_0}$. Using the free space dispersion relation $k^2 = \omega^2/c^2$ with the Fourier-transform pairs $j\omega \leftrightarrow \partial/\partial t$ and $-jk_x \leftrightarrow \partial/\partial x$ we obtain the partial differential equation

$$\frac{a}{c^2}\frac{\partial^2 E_z}{\partial t^2} + b\frac{\partial^2 E_z}{\partial x^2} = -\frac{\eta}{c^2}\frac{\partial^2 H_x}{\partial t^2} - \eta d\frac{\partial^2 H_x}{\partial x^2}. \tag{3.17}$$

It is worth noting that the second order time derivative of H_x can be expressed using the electric field E_z:

$$\frac{\partial^2 H_x}{\partial t^2} = -\frac{c}{\eta}\frac{\partial^2 E_z}{\partial y \partial t}. \tag{3.18}$$

The resulting equation is

$$\frac{a}{c^2}\frac{\partial^2 E_z}{\partial t^2} + b\frac{\partial^2 E_z}{\partial x^2} = \frac{1}{c}\frac{\partial^2 E_z}{\partial y \partial t} - \eta d\frac{\partial^2 H_x}{\partial x^2}. \tag{3.19}$$

We discretize this equation about an auxiliary lattice point, located half-cell away from the interface. Note that we do not have to neglect any spatial or temporal differences. The resulting update equation for the electric field is

$$\begin{aligned}
E_z|_{i,0}^{n+1} &= -E_z|_{i,1}^{n-1} + \frac{2a\Delta y}{c\Delta t + a\Delta y}\left(E_z|_{i,0}^{n} + E_z|_{i,1}^{n}\right) \\
&+ \frac{c\Delta t - a\Delta y}{c\Delta t + a\Delta y}\left(E_z|_{i,1}^{n+1} + E_z|_{i,0}^{n-1}\right) \\
&- \frac{b(c\Delta t)^2\Delta y}{\Delta x^2(c\Delta t + a\Delta y)}\left(\begin{array}{c} E_z|_{i+1,1}^{n} - 2E_z|_{i,1}^{n} + E_z|_{i-1,1}^{n} + \\ E_z|_{i+1,0}^{n} - 2E_z|_{i,0}^{n} + E_z|_{i-1,0}^{n} \end{array}\right) \\
&- \frac{\eta d(c\Delta t)^2\Delta y}{\Delta x^2(c\Delta t + a\Delta y)}\left(\begin{array}{c} H_x|_{i+1,1/2}^{n+1/2} - 2H_x|_{i,1/2}^{n+1/2} + H_x|_{i-1,1/2}^{n+1/2} + \\ H_x|_{i+1,1/2}^{n-1/2} - 2H_x|_{i,1/2}^{n-1/2} + H_x|_{i-1,1/2}^{n-1/2} \end{array}\right).
\end{aligned} \tag{3.20}$$

It may be noticed that in the cases $a = 1, b = d = 0$ and $a = 1, b = -1/2, d = 0$ this new ABC reduces to the first and the second order Mur ABC's, respectively. It is well known that these ABC's, however, are not quite good, which

is because they are based on rather coarse approximations of the square root in equation (3.15). By choosing the coefficients of the rational approximation appropriately, we obtain much better ABC's than the second order Mur ABC, while retaining essentially similar complexity of the update equation. A table of coefficients corresponding to different approximation methods designed to approximate (3.15) can be found in [24].

Usually, the third order ABC's resulting from the rational approximation of the square root in the form (3.15) are formulated as third order partial differential equations for one field component. We will show in numerical examples that we obtain similar performance with our second order PDE where both the electric and magnetic fields are present. Our analysis yields similar results as presented by Wang *et al.* in [34] and Ramadan *et al.* in [35] in the 2D-case, but the starting point is different, and our derivations establish the connection between SIBC's and ABC's. Next, we extend the proposed method to the general 3D-case.

3.4 Analytical ABC's in the 3D-case

In the three-dimensional situation, the derivatives in the numerator of (3.9) do not drop out. Hence, the analytical ABC cannot be directly formulated as a second order PDE. The reduction of order is, however, possible if we use Maxwell's equation and the following definitions:

$$\begin{aligned} A_x &= \frac{k_y}{\eta k} E_z, \\ A_z &= -\frac{k_y}{\eta k} E_x. \end{aligned} \tag{3.21}$$

With these definitions, we have the following equations relating the electric field and the just defined auxiliary field quantities:

$$\begin{aligned} (kk_y + ak^2 + b(k_x^2 + k_z^2))E_z &= -\eta d(k_x^2 + k_z^2)A_x, \\ (kk_y + ak^2 + b(k_x^2 + k_z^2))E_x &= \eta d(k_x^2 + k_z^2)A_z. \end{aligned} \tag{3.22}$$

Transforming these equations into the time domain, we obtain the following PDE's:

$$\begin{aligned} \frac{\partial^2 E_z}{\partial y \partial t} - \frac{a}{c}\frac{\partial^2 E_z}{\partial t^2} - bc\left(\frac{\partial^2 E_z}{\partial x^2} + \frac{\partial^2 E_z}{\partial z^2}\right) - d\eta c\left(\frac{\partial^2 A_x}{\partial x^2} + \frac{\partial^2 A_x}{\partial z^2}\right) &= 0, \\ \frac{\partial^2 E_x}{\partial y \partial t} - \frac{a}{c}\frac{\partial^2 E_x}{\partial t^2} - bc\left(\frac{\partial^2 E_x}{\partial x^2} + \frac{\partial^2 E_x}{\partial z^2}\right) + d\eta c\left(\frac{\partial^2 A_z}{\partial x^2} + \frac{\partial^2 A_z}{\partial z^2}\right) &= 0 \end{aligned} \tag{3.23}$$

These PDE's can be discretized in a similar way as in two dimensions. The definition of the auxiliary field quantities A_x and A_z does not induce extra complexity to the FDTD-algorithm, since they are actually already calculated in the normal Yee updating scheme as parts of the magnetic field components H_x and H_z, respectively.[1] So we just need to save those components for later

[1] The subindices of A refer to these two magnetic field components.

use in the discretized version of (3.23). As an example, consider the magnetic field H_x. In light of (3.21), we can update the auxiliary variables A_x and B_x according to

$$\begin{aligned} A_x|^{n+1/2}_{i,j+1/2,k+1/2} &= A_x|^{n-1/2}_{i,j+1/2,k+1/2} - \\ &\frac{\Delta t}{\mu_0 \Delta y}\left(E_z|^n_{i,j+1,k+1/2} - E_z|^n_{i,j,k+1/2}\right), \\ B_x|^{n+1/2}_{i,j+1/2,k+1/2} &= B_x|^{n-1/2}_{i,j+1/2,k+1/2} + \\ &\frac{\Delta t}{\mu_0 \Delta z}\left(E_y|^n_{i,j+1/2,k+1} - E_y|^n_{i,j+1/2,k}\right). \end{aligned} \tag{3.24}$$

These update equations are only needed on the boundary. After updating the $A's$ and $B's$ we add them together to get the magnetic fields on the boundary. We may think that we split the H_x located in the plane of discretization (half-cell from the actual boundary) as $H_x = A_x + B_x$, since the sum of the discrete equations in (3.24) yields the usual update equation of H_x in free space (after using $H_x = A_x + B_x$).

The ABC's in (3.23) are analogous to the 2D ABC's in the sense that the second order Mur ABC can be recovered by suitably choosing the parameters. However, in contrast to the Engquist-Majda conditions, third order accuracy is expected with these second order conditions when a suitable rational approximation is used.

3.5 Validation of the ABC's with Comparison Studies

To study the performance of the ABC in equation (3.20) we have constructed a two-dimensional test lattice with the size of 20×200 cells. The source is a hard source at the center of the lattice with the time-dependence

$$E_z|^n_{20,100} = \begin{cases} \frac{1}{32}\left[10 - 15\cos\left(2\pi f n \Delta t\right)\right. \\ \left. +6\cos\left(4\pi f n \Delta t\right) - \cos\left(6\pi f n \Delta t\right)\right], \ n \leq 30 \\ 0, \qquad n > 30 \end{cases} \tag{3.25}$$

where $f = 1$ GHz, $\Delta t = 0.9999\Delta x/(\sqrt{2}c)$, and $\Delta x = \Delta y = 0.015$ m. This pulse has a very smooth decay to zero. The reflection errors are studied on the left side of the lattice. The local error calculated at time step $n = 80$ is shown in Figure 3.1. It is clear that our ABC's corresponding to the Padé approximation ($a = 1, b = -0.75, d = -0.25$) and the Chebyshev on a subinterval ($a = 0.99973, b = -0.80864, d = -0.31657$) approximation of the square root in equation (3.15) are much better than the second order Mur ABC. To enable comparisons with a third order method, the Liao's third order ABC [26] was implemented. Actually, the performance of the proposed ABC with Chebyshev

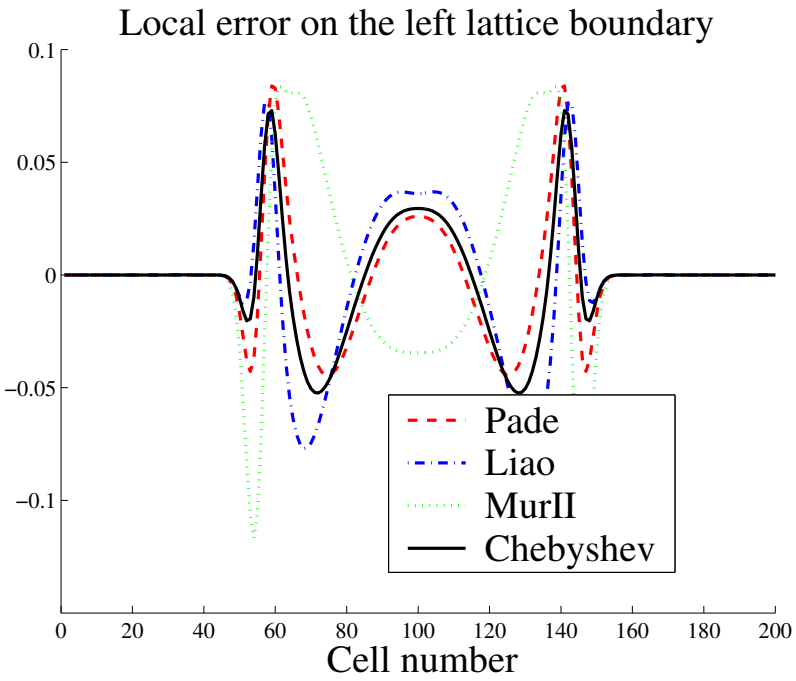

Figure 3.1: Local error on one side of the lattice at time-step n=80.

on a subinterval is seen to be about as good as that of the third order Liao's ABC. The standard discretization of the third order analytical PDE produces exactly the same results as the proposed analytical ABC's based on second order PDE, thus they have not been plotted in the figure.

Let us next study the global errors, which are probably a better measure for the performance of the ABC, since the squared errors are calculated and spatially summed over the whole two-dimensional FDTD-lattice. The global errors as functions of time steps are shown in Figure 3.2. It is evident from the figure that our second order ABC's perform much better than the second order Mur's ABC. In the case of Chebyshev on a subinterval, the global error is seen to be even smaller than for Liao's third order ABC. For time steps from 0 to 70 it is seen that the Padé approximation provides the smallest global error. This is natural, because the Padé approximation corresponds to having a triple zero of the wave reflection for normal incidence, and, at earlier times, the components propagating at grazing angles are small. The decay of the global error after about $n = 150$ just reflects the fact that the source has been switched off some time ago and the errors become smaller.

Comparison of second-order Mur and higher-order Lindman ABC's with PML ABC's can be found in [36]. It is evident that PMLs outperform those analytical ABC's. However, the use of analytical ABC's allows the efficient and accurate enough solving of many practical problems without the need to invoke PML ABC's.

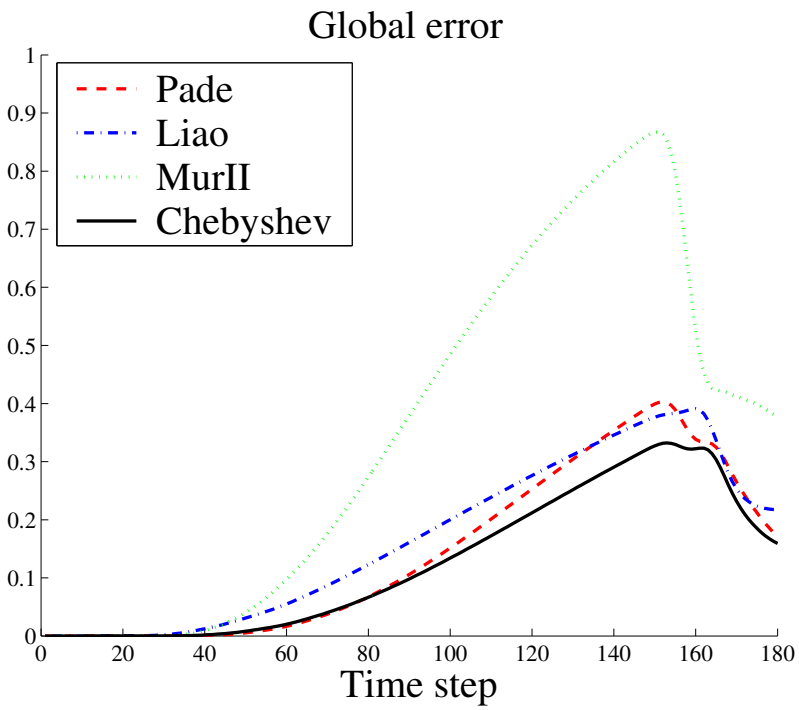

Figure 3.2: The global error power reflected back to the lattice as a function of time.

3.6 Conclusions

A new class of analytical absorbing boundary conditions has been derived and some comparisons have been made with other analytical ABC's. These new absorbing boundary conditions contain both electric and magnetic fields, and physically they are closely related to the exact surface impedance boundary condition. In the two-dimensional case, it was found that by keeping both the tangential electric and the magnetic field in the derivation, we may reduce the order of the PDE from 3 to 2 while keeping the performance of the third order ABC. In the 3D-case, we may reduce the order of the PDE by introducing two auxiliary variables that can be conveniently updated in the standard Yee algorithm. Also, the connection between the exact surface impedance boundary condition and the Engquist-Majda analytical absorbing boundary condition has been discussed, for better understanding of the background of the new method.

Chapter 4

Electrically Thick Coatings on Ideal Conductors

Modeling of material coatings is of interest in many electromagnetic problems. In this chapter, we introduce a new FDTD model of electrically thick layers on ideally conducting surfaces. The model is based on higher-order surface impedance boundary conditions. The model is numerically verified with some example problems, where analytical solutions are conveniently available.

4.1 Introduction

Numerical modeling of structures containing layers of materials with high electrical contrasts is a challenging task. A typical situation is a relatively electrically thick layer on a metal surface. Several models have been developed for the finite-difference time-domain method. The present problem, modeling of metal surfaces with a dispersive material coating, can be solved by the FDTD-method basically in three ways: 1) by a direct discretization of the fields inside the coating, 2) by using the surface impedance boundary condition (SIBC) or 3) by appropriately modifying the standard FDTD-update equations to include to effect of the material layer. The method based on the use of surface impedance boundary conditions is considered in this chapter. In contrast to the direct discretization, this approach is very effective if many small cells are needed to resolve the fields in the layer, and leads to significant computational savings.

The surface-impedance approach for solving the problem has already been considered in the literature. Probably the most well known is the formulation presented by Lee *et al.* in [13]. Their formulation is based on the use of the first order Leontovich SIBC relating the tangential electric field and its normal derivative to each other. Wang extended this method to be valid for any fixed *single* angle of incidence and reduced a two-dimensional problem to a

one-dimensional one. In his papers [37]–[38] he separately considers the parallel and perpendicular polarizations. Oh and Schutt-Aine discuss a simplistic SIBC-model in [10], where the tangent in the impedance function was simply approximated by its argument. That formulation is restricted to electrically thin layers.

The Leontovich SIBC was used by Penney *et al.* in [14], where radar cross section calculations for frequency-dispersive, coated targets were presented. They used frequency domain basis functions to expand the appropriate impedance function and applied z-transform techniques to derive the update equations for FDTD. Penney's approach requires a separate routine for finding the optimal coefficients for the basis functions, and the approximation may be coarse unless many basis functions are used.

The SIBC technique has also been successfully applied to model conductive bodies by Maloney and Smith in [7], by Beggs *et al.* in [8] and by Kellali *et al.* in [9]. Also, a higher-order SIBC model has been introduced by Farahat *et al.* in [12]. They use power series expansion with perturbation techniques and neglect some spatial errors in the discretization, which may lead to significant numerical errors and even deteriorate the expected increase in accuracy as compared with the Leontovich SIBC. No comparisons of the numerical results with analytical results were presented in [12], where scattering from conductive cylinders was considered. It appears that until now, no higher-order models for metal-backed coatings have been developed for FDTD. Overall, there exist only a few publications dealing with FDTD modeling of coated bodies using surface impedance boundary conditions.

So called subcell models have also been applied to model thin layers in FDTD. Some early papers were published by Tirkas and Demarest in [15] and by Maloney and Smith in [16]. Some other models have also been published by Luebbers and Kunz, Railton and McGeehan and by Wu and Han in [17, 18, 19], respectively. According to the comparison made by Maloney and Smith in [39], the models by Tirkas and Demarest and by Maloney and Smith appear to be more accurate than the other models. The subcell techniques can handle electrically thin layers only. The SIBC approach is more reasonable if electrically thick layers are modeled.

In this chapter, we start with the exact operational surface impedance and explicitly derive the higher-order SIBC in a 2D example problem. After presenting the methodology, numerical simulations with comparisons to the analytical results are shown in one- and two-dimensional example cases. The comparison studies are done in both time and frequency domains. In many numerical examples, comparison with Lee's model [13] is presented.

A rational approximation of the tangent appearing in the surface impedance function is very critical if accurate algorithms are desired. The proposed rational approximation is verified to lead to much more accurate results than reported in [13, 37, 38]. The tangential variation of the fields on the interface

is included by turning the tangential wave numbers into spatial derivatives, which leads to higher-order SIBCs. This was not done in [13, 37, 38]. Thus, the presented SIBC is a good approximation of the exact SIBC for a wide range of angles of incidence.

4.2 The Surface Impedance Model

Let us consider the problem where a metal plane is covered with a lossy dispersive material layer of thickness d. The complex permittivity of the layer is taken to be of the form

$$\epsilon(\omega) = \left(\epsilon_1 + \frac{\beta}{\omega_0^2 - \gamma\omega^2 + j\delta\omega}\right)\epsilon_0. \tag{4.1}$$

This is a rather general expression, and by suitably choosing the parameters $\epsilon_1, \beta, \gamma$ and δ we can model layers made of Lorentz, Debye or Drude medium. The usual conducting (with conductivity σ) dielectric (with dielectric constant ϵ_1) layer can also be obtained from (5.1) by choosing $\omega_0 = 0$, $\gamma = 0$, $\beta = \sigma$, $\delta = \epsilon_0$. The permeability of the layer is supposed be a constant $\mu = \mu_r\mu_0$. The exact surface impedance boundary condition for time-harmonic fields on the interface between the coating and free space reads

$$\mathbf{E}_t = \overline{\overline{Z}}_s \cdot \mathbf{n} \times \mathbf{H}_t, \tag{4.2}$$

where the surface impedance operator is of the form [23, 40]

$$\overline{\overline{Z}}_s = j\eta k \frac{\tan\left(\sqrt{k^2 + \nabla_t^2}d\right)}{\sqrt{k^2 + \nabla_t^2}} \left[\overline{\overline{I}}_t + \frac{\nabla_t \nabla_t}{k^2}\right]. \tag{4.3}$$

Index t denotes the tangential field components, k is the wave number within the layer and $\mathbf{n}$ is the unit vector pointing outwards from the interface. ∇_t is the restriction of the gradient operator to the plane of the interface, and $\overline{\overline{I}}_t$ is the unit dyadic in the plane of the interface. The wave impedance is defined in the usual way as

$$\eta = \sqrt{\frac{\mu}{\epsilon}}. \tag{4.4}$$

To be more explicit, let the air-dielectric interface be located at $y = 0$ with $\mathbf{n} = \mathbf{u}_y$, so that the appropriate tangential field components in our 2D case are E_z and H_x. The exact SIBC in (4.2)-(4.3) now takes the form :

$$E_z = -j\omega\mu \frac{\tan\left(\sqrt{k^2 - k_x^2}d\right)}{\sqrt{k^2 - k_x^2}} H_x. \tag{4.5}$$

The transformation of the tangential gradient operator to the spectral domain as $\nabla_t \leftrightarrow -jk_t$ has been used. In Lee's formulation, the operator ∇_t was dropped out, although he mentioned in [13] that the tangential variations of

the fields might be included. Wang's model is valid for a fixed *single* value of incidence angle only, clearly still a severe limitation. The inclusion of the angle of incidence in a general fashion is an important new feature of the proposed model.

In the following section, the required approximation techniques are discussed and the SIBC in equation (4.5) is transformed into the time-domain and discretized for the use in the FDTD method.

4.3 On the Required Approximations

Lee *et al.* approximated the tangent by writing it as a quotient of sine and cosine and using Taylor's polynomials to expand the sine and cosine functions. The problem in that approach is that quite many terms are required to obtain a wide enough range of accurate approximation required to model physically interesting phenomena. Regarding the accuracy of the model, this will turn out to be a severe limitation. The function $\tan(x)$ has the first singularity on the positive real axis at $x = \pi/2$ and the second singularity at $x = 3\pi/2$. If $x \ll \pi/2$, corresponding to an electrically thin layer, the problem reduces to a simple one. The more interesting and numerically challenging region is, however, around singularities, where the thickness resonances come into play.

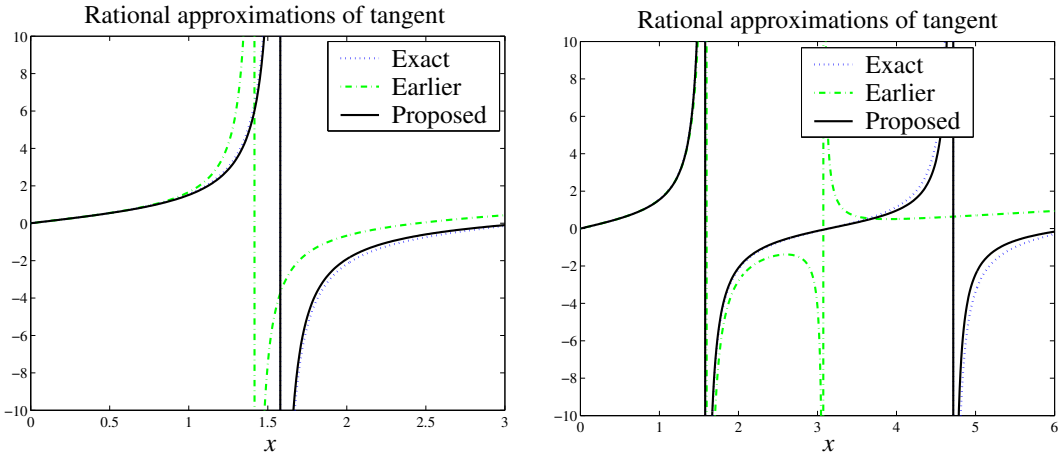

(a) (b)

Figure 4.1: (a) The (2,2) rational approximations. The singularity of the proposed rational approximation occurs in the correct position. (b) The (4,4) rational approximations. The proposed rational approximation has a much wider range of applicability.

For accurate numerical modeling, it is important that the singularities of the rational approximation coincide with the singularities of the tangent. This is

not the case in the scheme used in [13, 37, 38], where the following rational approximation was used:

$$\tan(x) = x\frac{1 + p_1x^2 + p_2x^4}{1 + q_1x^2 + q_2x^4} \tag{4.6}$$

with $p_1 = -1/6, p_2 = 0, q_1 = -1/2, q_2 = 0$ or $p_1 = -1/6, p_2 = 1/120, q_1 = -1/2, q_2 = 1/24$, if a more accurate approximation is desired. A considerably more uniform accuracy is obtained by requiring that the singularities of (4.6) coincide with the singularities of the tangent. Additionally, we may match the approximation with the exact expression in one or several points to get a linear system of equations for the coefficients. Based on this idea, the coefficients of the proposed rational approximation are $p_1 = -1/\pi^2, p_2 = 0, q_1 = -4/\pi^2, q_2 = 0$ if one pole-pair of the tangent is modeled, or $p_1 = -5/(4\pi^2), p_2 = 1/(4\pi^4), q_1 = -40/(9\pi^2), q_2 = 16/(9\pi^4)$ if two pole-pairs of the tangent are modeled. The tangent function and the different rational approximations are shown in Figure 4.1. The integers m and n in the notation (m, n) refer to the order of polynomials in the numerator and the denominator of the rational approximation, respectively. It is clearly seen that the proposed rational approximations are much more uniformly close to the tangent function than those used by Lee *et al.* and by Wang. This fact implies dramatically better accuracy in numerical simulations, as we will demonstrate in the following section.

At this point, we apply the proposed rational approximation to the SIBC in (4.5). We use the rational approximation with general coefficients and express the time derivative of the magnetic field H_x as a normal derivative of the electric field E_z according to $-\mu_0\partial H_x/\partial t = \partial E_z/\partial y$ to obtain the following SIBC in the frequency domain:

$$\left[1 + q_1(k^2 + \frac{\partial^2}{\partial x^2})d^2 + q_2(k^2 + \frac{\partial^2}{\partial x^2})^2d^4\right] E_z =$$
$$\mu_r d\left[1 + p_1(k^2 + \frac{\partial^2}{\partial x^2})d^2 + p_2(k^2 + \frac{\partial^2}{\partial x^2})^2d^4\right] \frac{\partial E_z}{\partial y}. \tag{4.7}$$

This may be transformed into the time domain using the substitutions $k^2 = \epsilon(\omega)\mu\omega^2$ and $j\omega \leftrightarrow \partial/\partial t$. It is seen that the tangential variations of the fields on the interface are accounted for in a general fashion by including the tangential derivatives of the fields to the SIBC. In the one-dimensional case, the spatial derivatives tangential to the interface just drop out.

In addition to the rational approximation, the evaluation of the normal derivative of the electric field ($\partial E_z/\partial y$ in this case) is a critical issue significantly influencing the accuracy. In earlier papers Lee *et al.* and Wang tried to include the effect of the dielectric coating into the evaluation of the normal derivative. Lagrange's interpolation polynomial was constructed from three points: one point on the metal surface, another on the dielectric-air interface where the SIBC is applied and the third point one cell away from the interface. However,

according to the very definition of the SIBC, the fields behind the dielectric-air boundary are not defined. Based on this fact, we construct a second-order accurate difference approximation of the normal derivative on the interface in the form

$$\left.\frac{\partial E_z}{\partial y}\right|_{i,0}^{n} \approx \frac{-3E_z\big|_{i,0}^{n} + 4E_z\big|_{i,1}^{n} - E_z\big|_{i,2}^{n}}{2\Delta y}. \tag{4.8}$$

The derivation of this expression can be easily done using the Taylor series and demanding second order accuracy. It may be noticed that this approximation does not depend on the dielectric parameters of the layer. Based on the numerical simulations, this approximation was found to be more accurate than that of [13, 37, 38].

Next, the SIBC in (4.7) will be transformed into time domain and discretized in the case of dielectric and conductive layers. Substituting $j\omega = s$ and $k^2 = -\epsilon\mu s^2 - \sigma\mu s$, the SIBC takes the form

$$\begin{aligned}
&\left[1 - q_1\epsilon_2\mu_2 d^2 s^2 - q_1\sigma\mu_2 d^2 s + q_1 d^2\frac{\partial^2}{\partial x^2} + \right.\\
&q_2 d^4(\epsilon_2^2\mu_2^2 s^4 + 2\epsilon_2\mu_2^2\sigma s^3 + \sigma^2\mu_2^2 s^2) + q_2 d^4\frac{\partial^4}{\partial x^4} - 2q_2\epsilon_2\mu_2 s^2\frac{\partial^2}{\partial x^2} - \\
&\left.2q_2\sigma\mu_2 s\frac{\partial^2}{\partial x^2}\right] E_z = \mu_r d\left[1 - p_1\epsilon_2\mu_2 d^2 s^2 - p_1\sigma\mu_2 d^2 s + p_1 d^2\frac{\partial^2}{\partial x^2} + \right.\\
&p_2 d^4(\epsilon_2^2\mu_2^2 s^4 + 2\epsilon_2\mu_2^2\sigma s^3 + \sigma^2\mu_2^2 s^2) + p_2 d^4\frac{\partial^4}{\partial x^4} - \\
&\left.2p_2\epsilon_2\mu_2 s^2\frac{\partial^2}{\partial x^2} - 2p_2\sigma\mu_2 s\frac{\partial^2}{\partial x^2}\right]\frac{\partial E_z}{\partial y},
\end{aligned} \tag{4.9}$$

where we have denoted $\epsilon_2 = \epsilon_1\epsilon_0$ and $\mu_2 = \mu_r\mu_0$. Transformation into time domain proceeds using the relation $s \leftrightarrow \partial/\partial t$. After minor simplification, the final form of the SIBC reads

$$\begin{aligned}
&\left[1 - (q_1\epsilon_2\mu_2 d^2 - q_2\sigma^2\mu_2^2 d^4)\frac{\partial^2}{\partial t^2} - q_1\sigma\mu_2 d^2\frac{\partial}{\partial t} + q_1 d^2\frac{\partial^2}{\partial x^2} + \right.\\
&q_2 d^4(\epsilon_2^2\mu_2^2\frac{\partial^4}{\partial t^4} + 2\epsilon_2\mu_2^2\sigma\frac{\partial^3}{\partial t^3}) - q_2 d^4\frac{\partial}{\partial x^4} + 2q_2\epsilon_2\mu_2\frac{\partial^4}{\partial t^2\partial x^2} - \\
&\left.2q_2\sigma\mu_2\frac{\partial^3}{\partial t\partial x^2}\right] E_z = \mu_r d\left[1 - (p_1\epsilon_2\mu_2 d^2 - p_2\sigma^2\mu_2^2 d^4)\frac{\partial^2}{\partial t^2} - \right.\\
&p_1\sigma\mu_2 d^2\frac{\partial}{\partial t} + p_1 d^2\frac{\partial^2}{\partial x^2} + p_2\epsilon_2^2\mu_2^2 d^4\frac{\partial^4}{\partial t^4} + 2p_2\epsilon_2\mu_2^2\sigma d^4\frac{\partial^3}{\partial t^3} + \\
&\left.p_2 d^4\frac{\partial^4}{\partial x^4} - 2p_2\epsilon_2\mu_2\frac{\partial^4}{\partial t^2\partial x^2} - 2p_2\sigma\mu_2\frac{\partial^3}{\partial t\partial x^2}\right]\frac{\partial E_z}{\partial y}.
\end{aligned} \tag{4.10}$$

The derived SIBC (4.10) is discretized at time step $t = n\cdot\Delta t$ if one pole-pair of the tangent is modeled, and at $t = (n-1)\cdot\Delta t$ if two pole-pairs are modeled. Spatially, the discretization is performed at grid location $(x, y) = (i\Delta x, 0)$ and the discrete equation is then solved for $E_z|_{i,0}^{n+1}$. Center differences are used, for

example

$$\left.\frac{\partial^4 E_z}{\partial t^4}\right|_{i,0}^{n-1} \approx \frac{E_z|_{i,0}^{n+1} - 4E_z|_{i,0}^{n} + 6E_z|_{i,0}^{n-1} - 4E_z|_{i,0}^{n-2} + E_z|_{i,0}^{n-3}}{\Delta t^2}. \tag{4.11}$$

for fourth order time derivatives and

$$\left.\frac{\partial^2 E_z}{\partial x^2}\right|_{i,0}^{n-1} \approx \frac{E_z|_{i+1,0}^{n-1} - 2E_z|_{i,0}^{n-1} + E_z|_{i-1,0}^{n-1}}{\Delta x^2} \tag{4.12}$$

for the second order spatial derivative along the interface. The difference scheme in equation (4.8) is applicable in evaluating the mixed derivatives. As an example, we discretize

$$\left.\frac{\partial^2 E_z}{\partial t \partial y}\right|_{i,0}^{n-1} \approx \frac{1}{2\Delta t}\left(\left.\frac{\partial E_z}{\partial y}\right|_{i,0}^{n+1} - \left.\frac{\partial E_z}{\partial y}\right|_{i,0}^{n-1}\right) = \frac{-3E_z|_{i,0}^{n+1} + 4E_z|_{i,1}^{n+1} - E_z|_{i,2}^{n+1} - (-3E_z|_{i,0}^{n-1} + 4E_z|_{i,1}^{n-1} - E_z|_{i,2}^{n-1})}{4\Delta t \Delta y}. \tag{4.13}$$

The difference approximations in (4.11)–(4.13) above are used in the case where two pole-pairs of the tangent are modeled. If one pole-pair is modeled, the discretization proceeds analogously at $t = n \cdot \Delta t$.

Let us first consider the discrete equations in the case where one pole-pair of the tangent is modeled. Using the discretization principles described above, we have the discretized SIBC in the form:

$$\begin{aligned} E_z|_{i,0}^{n} - \frac{q_1\mu_2 d^2}{\Delta t^2}\left(E_z|_{i,0}^{n+1} - 2E_z|_{i,0}^{n} + E_z|_{i,0}^{n-1}\right) - \\ \frac{q_1\sigma_2\mu_2 d^2}{2\Delta t}\left(E_z|_{i,0}^{n+1} - E_z|_{i,0}^{n-1}\right) + \frac{q_1 d^2}{\Delta x^2}\left(E_z|_{i+1,0}^{n} - 2E_z|_{i,0}^{n} + E_z|_{i-1,0}^{n}\right) = \\ \mu_r d\left\{\frac{-3E_z|_{i,0}^{n} + 4E_z|_{i,1}^{n} - E_z|_{i,2}^{n}}{2\Delta y} - \right. \\ \frac{p_1\epsilon_2\mu_2 d^2}{2\Delta y \Delta t^2}\begin{bmatrix} -3E_z|_{i,0}^{n+1} + 4E_z|_{i,1}^{n+1} - E_z|_{i,2}^{n+1} \\ -2(-3E_z|_{i,0}^{n} + 4E_z|_{i,1}^{n} - E_z|_{i,2}^{n}) \\ -3E_z|_{i,0}^{n-1} + 4E_z|_{i,1}^{n-1} - E_z|_{i,2}^{n-1} \end{bmatrix} - \\ \frac{p_1\sigma\mu_2 d^2}{4\Delta y \Delta t}\begin{bmatrix} -3E_z|_{i,0}^{n+1} + 4E_z|_{i,1}^{n+1} - E_z|_{i,2}^{n+1} \\ -(-3E_z|_{i,0}^{n-1} + 4E_z|_{i,1}^{n-1} - E_z|_{i,2}^{n-1}) \end{bmatrix} + \\ \left.\frac{p_1 d^2}{2\Delta x^2 \Delta y}\begin{bmatrix} -3E_z|_{i+1,0}^{n} + 4E_z|_{i+1,1}^{n} - E_z|_{i+1,2}^{n} \\ -2(-3E_z|_{i,0}^{n} + 4E_z|_{i,1}^{n} - E_z|_{i,2}^{n}) \\ -3E_z|_{i-1,0}^{n} + 4E_z|_{i-1,1}^{n} - E_z|_{i-1,2}^{n} \end{bmatrix}\right\} \end{aligned} \tag{4.14}$$

We find the terms containing $E_z|_{i,0}^{n+1}$ and solve for it to obtain the final SIBC

that can be implemented into FDTD programs:

$$E_z|_{i,0}^{n+1} = \frac{1}{A_1}\Big\{-12\Delta y\Delta t^2 E_z|_{i,0}^{n} + 12q_1\Delta y\epsilon_2\mu_2 d^2\left(-2E_z|_{i,0}^{n} + E_z|_{i,0}^{n-1}\right) - 6q_1\sigma\mu_2 d^2\Delta y\Delta t E_z|_{i,0}^{n-1} - 6p_1\mu_r\mu_2\epsilon_2 d^3\begin{bmatrix} 4E_z|_{i,1}^{n+1} - E_z|_{i,2}^{n+1} \\ -2(-3E_z|_{i,0}^{n} + 4E_z|_{i,1}^{n} - E_z|_{i,2}^{n}) \\ -3E_z|_{i,0}^{n-1} + 4E_z|_{i,1}^{n-1} - E_z|_{i,2}^{n-1}\end{bmatrix} - \frac{12q_1\Delta y\Delta t^2 d^2}{\Delta x^2}\left(E_z|_{i+1,0}^{n} - 2E_z|_{i,0}^{n} + E_z|_{i-1,0}^{n}\right) - 6\mu_r d\Delta t^2\left(-3E_z|_{i,0}^{n} + 4E_z|_{i,1}^{n} - E_z|_{i,2}^{n}\right) - 3p_1\mu_r\mu_2 d^3\sigma\Delta t\begin{bmatrix} 4E_z|_{i,1}^{n+1} - E_z|_{i,2}^{n+1} \\ -(-3E_z|_{i,0}^{n-1} + 4E_z|_{i,1}^{n-1} - E_z|_{i,2}^{n-1})\end{bmatrix} + \frac{6\mu_r p_1 d^3\Delta t^2}{\Delta x^2}\begin{bmatrix} 4E_z|_{i+1,1}^{n} - E_z|_{i+1,2}^{n} \\ -2(-3E_z|_{i,0}^{n} + 4E_z|_{i,1}^{n} - E_z|_{i,2}^{n}) \\ -3E_z|_{i-1,0}^{n} + 4E_z|_{i-1,1}^{n} - E_z|_{i-1,2}^{n}\end{bmatrix}\Big\}. \quad (4.15)$$

The constant A_1 in equation (4.15) is defined as

$$A_1 = -12q_1\Delta y\epsilon_2\mu_2 d^2 - 6q_1\sigma\mu_2 d^2\Delta y\Delta t - 18p_1\mu_r\mu_2\epsilon_2 d^3 - 9p_1\mu_r\mu_2\sigma d^3\Delta t. \quad (4.16)$$

This algorithm works well for electrically thick layers. However, it may be noticed that the constant A_1 tends to zero as the layer thickness d tends to zero. There is a simple trick to avoid the resulting instability for very thin layers, namely to write $E_z|_{i,0}^{n}$ in a more "implicit" manner as an average in the form $E_z|_{i,0}^{n} \approx (E_z|_{i,0}^{n+1} + E_z|_{i,0}^{n-1})/2$. The update equation will be slightly modified in that case, and the resulting scheme is stable for a wide range of layer thicknesses. However, the discretization scheme described above is more accurate for electrically thick coatings, which is the focus of our discussion.

Next, we derive the update equations in the case where two pole-pairs of the tangent are modeled. Some partial derivatives that do not contain $E_z|_{i,0}^{n+1}$ after discretization, have been written in the nondiscretized form for brevity.

Discretizing and solving for $E_z|_{i,0}^{n+1}$ yields

$$
\begin{aligned}
E_z|_{i,0}^{n+1} = \frac{1}{A_2}\Bigg\{ & -E_z|_{i,0}^{n-1} + q_1\sigma\mu_2 d^2 \frac{\partial E_z}{\partial t}\bigg|_{i,0}^{n-1} + \\
& \frac{q_1\epsilon_2\mu_2 d^2 - q_2\sigma^2\mu_2^2 d^4}{\Delta t^2}\left(E_z|_{i,0}^{n} - 2E_z|_{i,0}^{n-1} + E_z|_{i,0}^{n-2}\right) - \\
& \frac{q_2\epsilon_2\mu_2^2\sigma d^4}{\Delta t^3}\begin{bmatrix} -3E_z|_{i,0}^{n} + 3E_z|_{i,0}^{n-1} - E_z|_{i,0}^{n-2} \\ E_z|_{i,0}^{n} - 3E_z|_{i,0}^{n-1} + 3E_z|_{i,0}^{n-2} - E_z|_{i,0}^{n-3} \end{bmatrix} - \\
& \frac{q_2\epsilon_2^2\mu_2^2 d^4}{\Delta t^4}\left(-4E_z|_{i,0}^{n} + 6E_z|_{i,0}^{n-1} - 4E_z|_{i,0}^{n-2} + E_z|_{i,0}^{n-3}\right) - \\
& q_1 d^2 \frac{\partial^2 E_z}{\partial x^2}\bigg|_{i,0}^{n-1} - q_2 d^4 \frac{\partial^4 E_z}{\partial x^4}\bigg|_{i,0}^{n-1} = \\
& \mu_r d\Bigg[\frac{1}{2\Delta y}\left(-3E_z|_{i,0}^{n-1} + 4E_z|_{i,1}^{n-1} - E_z|_{i,2}^{n-1}\right) - \\
& \frac{p_1\sigma\mu_2 d^2}{2}\frac{\partial^2 E_z}{\partial y\partial t}\bigg|_{i,0}^{n-1} - (p_1\epsilon_2\mu_2 d^2 - p_2\sigma^2\mu_2^2 d^4)\frac{\partial^3 E_z}{\partial y\partial t^2}\bigg|_{i,0}^{n-1} + \\
& \frac{p_2\epsilon_2\mu_2^2\sigma d^4}{2\Delta y\Delta t}\begin{bmatrix} 4E_z|_{i,1}^{n+1} - E_z|_{i,2}^{n+1} - \\ 3\left(-3E_z|_{i,0}^{n} + 4E_z|_{i,1}^{n} - E_z|_{i,2}^{n}\right) - \\ 3\left(-3E_z|_{i,0}^{n-1} + 4E_z|_{i,1}^{n-1} - E_z|_{i,2}^{n-1}\right) + \\ 3\left(-3E_z|_{i,0}^{n-2} + 4E_z|_{i,1}^{n-2} - E_z|_{i,2}^{n-2}\right) - \\ 3E_z|_{i,0}^{n} + 4E_z|_{i,1}^{n} - E_z|_{i,2}^{n} - \\ 3E_z|_{i,0}^{n-1} + 4E_z|_{i,1}^{n-1} - E_z|_{i,2}^{n-1} + \\ 3\left(-3E_z|_{i,0}^{n-2} + 4E_z|_{i,1}^{n-2} - E_z|_{i,2}^{n-2}\right) - \\ 3E_z|_{i,0}^{n-3} + 4E_z|_{i,1}^{n-3} - E_z|_{i,2}^{n-3} \end{bmatrix} + \\
& \frac{p_2\epsilon_2^2\mu_2^2 d^4}{2\Delta y\Delta t^4}\begin{bmatrix} 4E_z|_{i,1}^{n+1} - E_z|_{i,2}^{n+1} - \\ 4\left(-3E_z|_{i,0}^{n} + 4E_z|_{i,1}^{n} - E_z|_{i,2}^{n}\right) + \\ 6\left(-3E_z|_{i,0}^{n-1} + 4E_z|_{i,1}^{n-1} - E_z|_{i,2}^{n-1}\right) - \\ 4\left(-3E_z|_{i,0}^{n-2} + 4E_z|_{i,1}^{n-2} - E_z|_{i,2}^{n-2}\right) \\ -3E_z|_{i,0}^{n+1} + 4E_z|_{i,1}^{n} - E_z|_{i,2}^{n} \end{bmatrix} + \\
& p_1 d^2 \frac{\partial^3 E_z}{\partial y\partial x^2}\bigg|_{i,0}^{n-1} + p_2 d^4 \frac{\partial^5 E_z}{\partial y\partial x^4}\bigg|_{i,0}^{n-1}\Bigg]\Bigg\}. \qquad (4.17)
\end{aligned}
$$

The constant A_2 in the update equation above is defined as

$$
A_2 = -\frac{q_2\epsilon_2\mu_2^2\sigma d^4}{\Delta t^3} - \frac{q_2\epsilon_2^2\mu_2^2 d^4}{\Delta t^4} - \frac{3p_2\epsilon_2\mu_2^2\sigma d^4}{2\Delta y\Delta t} - \frac{3p_2\epsilon_2^2\mu_2^2 d^4}{2\Delta y\Delta t^4}. \qquad (4.18)
$$

Similar remarks regarding the alternative discretization scheme as discussed above in the case of one pole-pair modeled apply here.

4.3.1 An Alternative Discretization Method

The impedance condition (4.7) can also be expressed as

$$\left[1 + q_1(k^2 + \frac{\partial^2}{\partial x^2})d^2 + q_2(k^2 + \frac{\partial^2}{\partial x^2})^2 d^4\right] E_z = \mu_2 d \left[1 + p_1(k^2 + \frac{\partial^2}{\partial x^2})d^2 + p_2(k^2 + \frac{\partial^2}{\partial x^2})^2 d^4\right] \frac{\partial H_x}{\partial t}. \tag{4.19}$$

This form of the boundary condition can be conveniently applied, if certain approximations are utilized. First, the magnetic field components are located half cell away from the interface. That difference can be neglected in the discretization without much loss in the accuracy. Further, if it is enough to model just one thickness resonance, we can set $p_2 = q_2 = 0$. Also, the spatial derivatives along the interface can be dropped out. The equation (4.19) now takes the form

$$\left[1 + q_1 k^2 d^2\right] E_z = -j\omega\mu_2 d \left[1 + p_1 k^2 d^2\right] H_x. \tag{4.20}$$

In the time domain, this is equivalent to

$$\left[1 - q_1\sigma\mu_2 d\frac{\partial}{\partial t} - q_1\epsilon_2\mu_2 d^2\frac{\partial^2}{\partial t^2}\right] E_z = -\mu_2 d \left[1 + p_1\sigma\mu_2 d^2\frac{\partial}{\partial t} + p_1\epsilon_2\mu_2 d^2\frac{\partial^2}{\partial t^2}\right] \frac{\partial H_x}{\partial t}. \tag{4.21}$$

Suppose we want to discretize at time step $t = n\Delta t$ using central differences. This would yield discrete electric field terms $E_z|^{n+1}$ to the left hand side, and magnetic field terms $H_x|^{n+3/2}$ to the right hand side of equation (4.21). At the time of imposing the value of $E_z|^{n+1}$ on the boundary, the magnetic fields at the time step $n + 1/2$ are known, but the fields at time step $n + 3/2$ are yet to be computed. Therefore, we have to neglect some terms or use other discretization techniques. A second and third order derivatives of the magnetic field can be approximated second-order accurately as

$$\left.\frac{\partial^2 H_x}{\partial t^2}\right|^n \approx \frac{3H_x|^{n+1/2} - 7H_x|^{n-1/2} + 5H_x|^{n-3/2} - H_x|^{n-5/2}}{2\Delta t^2} \tag{4.22}$$

and

$$\left.\frac{\partial^3 H_x}{\partial t^3}\right|^n \approx \frac{2H_x|^{n+1/2} - 7H_x|^{n-1/2} + 9H_x|^{n-3/2} - 5H_x|^{n-5/2} + H_x|^{n-7/2}}{\Delta t^3}. \tag{4.23}$$

These expressions were derived using Taylor series and requiring second-order accuracy. Notice that one extra term is required in both expressions as compared with central differences to obtain second-order accuracy. Numerical experiments were made with and without the second and third order time derivatives of the magnetic field, and no improvement in accuracy was observed if those terms are included. Stability problems were not observed when

the unconventional difference approximations (4.22–4.23) were tested. However, rather good results are obtained by simply setting $p_1 = 0$ so that just a single derivative of the magnetic field H_x remains in the right hand side. The discrete boundary condition reads

$$E_z|_{i,0}^{n+1} = \frac{1}{A_3}\left\{ -\left(\frac{1}{2} + \frac{q_1\sigma\mu_2 d}{2\Delta t}\right) E_z|_{i,0}^{n-1} \right.$$
$$\left. + \frac{q_1\epsilon_2\mu_2 d^2}{\Delta t^2}\left(-2E_z|_{i,0}^{n} + E_z|_{i,0}^{n-1}\right) - \frac{\mu_2 d}{\Delta t}\left(H_x|_{i,1/2}^{n+1/2} - H_x|_{i,1/2}^{n-1/2}\right)\right\}, \quad (4.24)$$

where

$$A_3 = -\frac{1}{2} - \frac{q_1\epsilon_2\mu_2 d^2}{\Delta t^2} - \frac{q_1\sigma\mu_2 d}{2\Delta t}. \quad (4.25)$$

This boundary condition was implemented: the results and comparisons with the original method published in [2] will be discussed in section 4.4.

4.3.2 Discretization Techniques for Dispersive Coatings

For more general coatings having frequency-dispersion, it is convenient to define a couple of auxiliary variables to avoid higher-order derivatives. The following auxiliary variables, defined on the interface only, are introduced:

$$A = \frac{\epsilon(\omega)}{\epsilon_0} E_z, \quad B = \mu_r d \frac{\epsilon(\omega)}{\epsilon_0}\frac{\partial E_z}{\partial y}. \quad (4.26)$$

Equation (4.7) with the simpler ($p_2 = q_2 = 0$) rational approximation now takes the form

$$\left[1 + q_1 d^2 \frac{\partial^2}{\partial x^2}\right] E_z + q_1\mu_2\epsilon_0 d^2\omega^2 A = \mu_r d \left[1 + p_1 d^2 \frac{\partial^2}{\partial x^2}\right] \frac{\partial E_z}{\partial y} + p_1\mu_0\epsilon_0 d^2\omega^2 B. \quad (4.27)$$

or in the time domain:

$$\left[1 + q_1 d^2 \frac{\partial^2}{\partial x^2}\right] E_z - q_1\mu_2\epsilon_0 d^2 \frac{\partial^2 A}{\partial t^2} = \mu_r d \left[1 + p_1 d^2 \frac{\partial^2}{\partial x^2}\right] \frac{\partial E_z}{\partial y} - p_1\mu_0\epsilon_0 d^2 \frac{\partial^2 B}{\partial t^2}. \quad (4.28)$$

The discretization of (4.28) is performed with central-differences in the usual manner, and the result is:

$$E_z|_{i,0}^{n} + \frac{q_1 d^2}{\Delta x^2}\left(E_z|_{i+1,0}^{n} - 2E_z|_{i,0}^{n} + E_z|_{i-1,0}^{n}\right) +$$
$$\frac{q_1\mu_2\epsilon_0 d^2}{\Delta t^2}\left(A|^{n+1} - 2A|^{n} + A|^{n-1}\right) =$$
$$\frac{\mu_r d}{2\Delta y}\left(-3E_z|_{i,0}^{n} + 4E_z|_{i,1}^{n} + E_z|_{i,2}^{n}\right) +$$
$$\frac{\mu_r p_1 d^3}{2\Delta x^2\Delta y}\begin{bmatrix} -3E_z|_{i+1,0}^{n} + 4E_z|_{i+1,1}^{n} - E_z|_{i+1,2}^{n} \\ -2(-3E_z|_{i,0}^{n} + 4E_z|_{i,1}^{n} - E_z|_{i,2}^{n}) \\ -3E_z|_{i-1,0}^{n} + 4E_z|_{i-1,1}^{n} - E_z|_{i-1,2}^{n} \end{bmatrix} +$$
$$\frac{p_1\mu_0\epsilon_0 d^2}{\Delta t^2}\left(B|^{n+1} - 2B|^{n} + B|^{n-1}\right). \quad (4.29)$$

The auxiliary equations (4.26) are now transformed into the time-domain and integrated once before discretization with central differences. The resulting discrete integrals are evaluated second-order-accurately using the trapezoidal rule. The auxiliary variables at time step $t = (n+1) \cdot \Delta t$ are then solved and substituted into (4.29). Consider the discretization of the auxiliary equation relating A and E_z on the interface. Substituting the expression for $\epsilon(\omega)$ and multiplying with the denominator, we obtain

$$(\omega_0^2 - \gamma\omega^2 + j\delta\omega)A = \left[(\epsilon_1\omega_0^2 + \beta) - \epsilon_1\gamma\omega^2 + j\epsilon_1\delta\omega\right] E_z. \tag{4.30}$$

This is transformed into the time domain using $j\omega \leftrightarrow \partial/\partial t$ and integrated once from 0 to $t = n \cdot \Delta t$. Then we have

$$\gamma\frac{\partial A}{\partial t} + \delta A + \omega_0^2 \int_0^t A \, d\tau = \epsilon_1\gamma\frac{\partial E_z}{\partial t} + \epsilon_1\delta E_z + (\epsilon_1\omega_0^2 + \beta)\int_0^t E_z \, d\tau. \tag{4.31}$$

The integrals are evaluated second-order-accurately with the trapezoidal rule. This approach leads to summations that can be performed recursively quite efficiently. We obtain the discrete equation

$$\begin{aligned}(4\gamma + \omega_0^2\Delta t^2 + 2\delta\Delta t)A|^{n+1} = (4\gamma - \omega_0^2\Delta t^2 - 2\delta t)A|^n + \\ \left[4\epsilon_1\gamma + (\epsilon_1\omega_0^2 + \beta)\Delta t^2 + 2\epsilon_1\delta\Delta t\right] E_z|_{i,0}^{n+1} - \\ \left[4\epsilon_1\gamma - (\epsilon_1\omega_0^2 + \beta)\Delta t^2 - 2\epsilon_1\delta\Delta t\right] E_z|_{i,0}^{n} - \\ 4\omega_0^2\Delta t^2 \sum_{m=1}^{n} \frac{1}{2}(A|^{n-m+1} + A|^{n-m}) + \\ 4(\epsilon_1\omega_0^2 + \beta)\Delta t^2 \sum_{m=1}^{n} \frac{1}{2}(E_z|^{n-m+1} + E_z|^{n-m}).\end{aligned} \tag{4.32}$$

The equation for $B|^{n+1}$ is derived completely analogously. The result is

$$\begin{aligned}(4\gamma + \omega_0^2\Delta t^2 + 2\delta\Delta t)B|^{n+1} = (4\gamma - \omega_0^2\Delta t^2 - 2\delta t)B|^n + \\ \left[4\epsilon_1\gamma + (\epsilon_1\omega_0^2 + \beta)\Delta t^2 + 2\epsilon_1\delta\Delta t\right] \frac{\mu_r d}{2\Delta y} \cdot \\ \left(-3E_z|_{i,0}^{n+1} + 4E_z|_{i,1}^{n+1} - E_z|_{i,2}^{n+1}\right) - \\ \left[4\epsilon_1\gamma - (\epsilon_1\omega_0^2 + \beta)\Delta t^2 - 2\epsilon_1\delta\Delta t\right] \frac{\mu_r d}{2}\left(-3E_z|_{i,0}^{n} + 4E_z|_{i,1}^{n} - E_z|_{i,2}^{n}\right) - \\ 4\omega_0^2\Delta t^2 \sum_{m=1}^{n} \frac{1}{2}(B|^{n-m+1} + B|^{n-m}) + \\ 4\mu_r d(\epsilon_1\omega_0^2 + \beta)\Delta t^2 \sum_{m=1}^{n} \frac{1}{2}\left(\left.\frac{\partial E_z}{\partial y}\right|^{n-m+1} + \left.\frac{\partial E_z}{\partial y}\right|^{n-m}\right).\end{aligned} \tag{4.33}$$

The final update equation for dispersive coating is obtained after substituting $A|^{n+1}$ and $B|^{n+1}$ from equations (4.32) and (4.33) into equation (4.29).

Defining variables R_1 and R_2 as

$$\begin{aligned} R_1 = (4\gamma - \omega_0^2\Delta t^2 - 2\delta t)A|^n - \\ \left[4\epsilon_1\gamma - (\epsilon_1\omega_0^2 + \beta)\Delta t^2 - 2\epsilon_1\delta\Delta t\right] E_z|_{i,0}^n - \\ 4\omega_0^2\Delta t^2 \sum_{m=1}^{n} \frac{1}{2}(A|^{n-m+1} + A|^{n-m}) + \\ 4(\epsilon_1\omega_0^2 + \beta)\Delta t^2 \sum_{m=1}^{n} \frac{1}{2}(E_z|^{n-m+1} + E_z|^{n-m}) \end{aligned} \tag{4.34}$$

and

$$\begin{aligned} R_2 = (4\gamma - \omega_0^2\Delta t^2 - 2\delta t)B|^n - \\ \left[4\epsilon_1\gamma - (\epsilon_1\omega_0^2 + \beta)\Delta t^2 - 2\epsilon_1\delta\Delta t\right] \frac{\mu_r d}{2\Delta y} \cdot \\ \left(-3E_z|_{i,0}^n + 4E_z|_{i,1}^n - E_z|_{i,2}^n\right) - \\ 4\omega_0^2\Delta t^2 \sum_{m=1}^{n} \frac{1}{2}(B|^{n-m+1} + B|^{n-m}) + \\ 4\mu_r d(\epsilon_1\omega_0^2 + \beta)\Delta t^2 \sum_{m=1}^{n} \frac{1}{2}\left(\left.\frac{\partial E_z}{\partial y}\right|^{n-m+1} + \left.\frac{\partial E_z}{\partial y}\right|^{n-m}\right), \end{aligned} \tag{4.35}$$

we may write the final update equation in the form

$$\begin{aligned} E_z|_{i,0}^{n+1} = \frac{C_1}{C_2}\Bigg\{-\Delta t^2 E_z|_{i,0}^n + q_1\mu_2\epsilon_0 d^2\left(\frac{R_1}{C_1} - 2A|^n + A|^{n-1}\right) + \\ q_1 d^2\Delta t^2 \left.\frac{\partial^2 E_z}{\partial x^2}\right|_{i,0}^n + \frac{\mu_r d\Delta t^2}{2\Delta y}\left(-3E_z|_{i,0}^n + 4E_z|_{i,1}^n - E_z|_{i,2}^n\right) - \\ p_1 d^2\Delta t^2 \left.\frac{\partial^3 E_z}{\partial y\partial x^2}\right|_{i,0}^n + p_1\mu_2\epsilon_0 d^2\left(\frac{R_2}{C_1} - 2B|^n + B|^{n-1}\right)\Bigg\}, \end{aligned} \tag{4.36}$$

with the constants C_1 and C_2 defined as $C_1 = 4\gamma + (\omega_0\Delta t)^2 + 2\delta\Delta t$ and

$$\begin{aligned} C_2 &= -q_1\mu_2\epsilon_0 d^2\left[4\epsilon_1\gamma + (\epsilon_1\omega_0^2 + \beta)\Delta t^2 + 2\epsilon_1\delta\Delta t\right] \\ &- \frac{3p_1\mu_2\epsilon_0 d^3}{2\Delta x}\left[4\epsilon_1\gamma + (\epsilon_1\omega_0^2 + \beta)\Delta t^2 + 2\epsilon_1\delta\Delta t\right]. \end{aligned} \tag{4.37}$$

Observe that the auxiliary variables at time steps $n-1$ and n have been calculated previously in the algorithm, according to equations (4.32) and (4.33). Next, we will numerically study the performance of the developed FDTD models.

4.4 Numerical Verification of the Proposed Models

4.4.1 Pulse Reflection in One Dimension

Let us now numerically verify the proposed model. In the first example, a differentiated Gaussian pulse is reflected from a coated ideal conductor. This problem can be formulated as a 1D problem in FDTD. The magnitude and the phase of the reflection coefficient on the boundary are calculated with the proposed method and with Lee's method. In this situation, the suggested more uniform approximation of the tangent function in the SIBC can be tested. Comparison is made with exact reflection coefficient at normal incidence.

Dielectric Conductive Layers

The exact reflection coefficient in the case of normal incidence to be considered first is of the form

$$R = \frac{j\eta \tan(kd) - \eta_0}{j\eta \tan(kd) + \eta_0}. \tag{4.38}$$

The wave impedance in free space is denoted by η_0. In numerical examples, we have $\mu = \mu_0$. Thus, the wave number k inside the layer is equal to $k = \omega\sqrt{\epsilon}/c$.

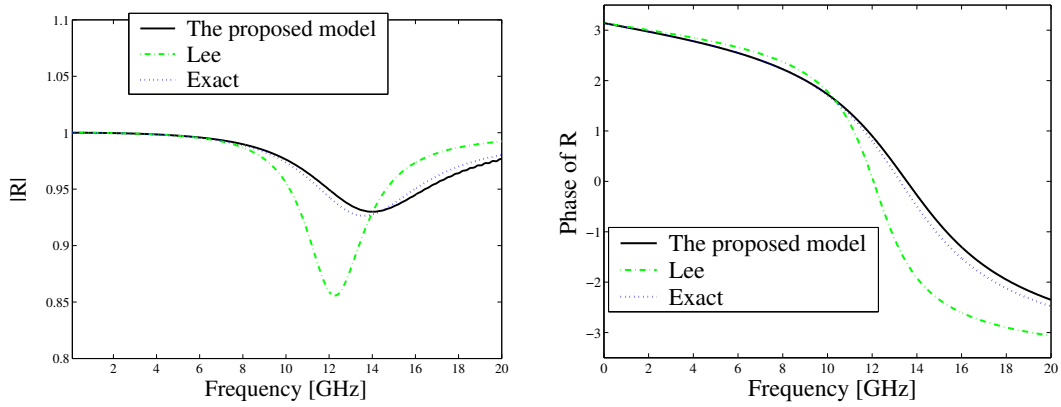

(a) (b)

Figure 4.2: (a) Magnitude of the reflection coefficient for $\epsilon_r = 8, \quad \sigma = 0.1$ S/m. (b) Phase of the reflection coefficient for $\epsilon_r = 8$, $\sigma = 0.1$ S/m.

Let us first study the models based on a coarser rational approximation where $p_2 = q_2 = 0$. The first simulation is done for the case, where $\epsilon_r = 8, \quad \sigma = 0.1$ S/m and $d = \Delta x = 2$ mm. The results are shown in Figure 4.2. The fields involved are E_z and H_y, and the SIBC is applied at the boundary $x = 0$. The

time step is equal to the Courant stability limit. At 4 GHz, the argument of the tangent is approximately equal to 1.34. Hence, on the frequency range from 0 to 4 GHz, good agreement should be expected. This is indeed the case for both the proposed method and Lee's method. At 8 GHz, the argument of the tangent is about 2.68. Hence, satisfactory agreement for the proposed method should be anticipated up to 8 GHz. The incorrect position of the singularity in Lee's method induces some deviation from the exact result. For larger frequencies, the accuracy is slightly worse for both methods.

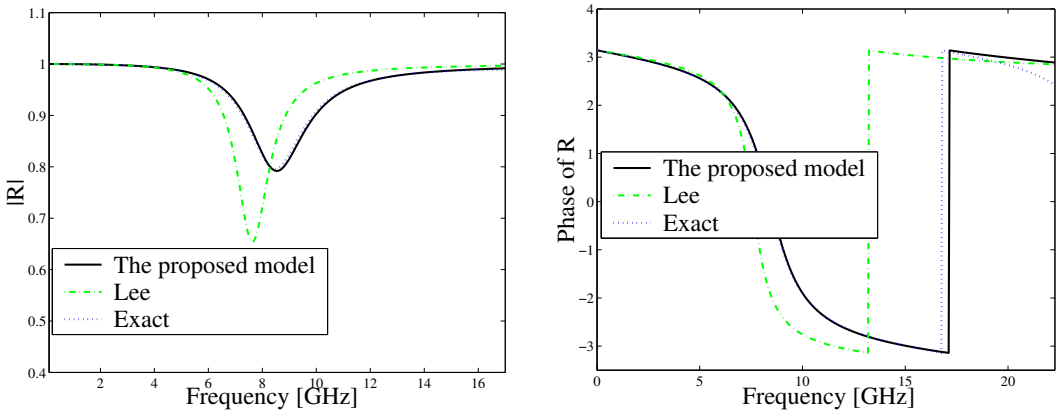

(a) (b)

Figure 4.3: (a) Magnitude of the reflection coefficient for $\epsilon_r = 20$, $\sigma = 0.3$ S/m. (b) Phase of the reflection coefficient for $\epsilon_r = 20$, $\sigma = 0.3$ S/m.

Next we increase the dielectric constant and the conductivity of the layer to $\epsilon_r = 20$ and $\sigma = 0.3$ S/m, respectively. The thickness of the layer is the same as in the first example, $d = 2$ mm. There is a jump discontinuity in the phase of the reflection coefficient, as is seen in Figure 4.3. The proposed method yields quite accurate results for both the magnitude and the phase of the reflection coefficient, whereas the local minimum of the magnitude and the position of the jump discontinuity of the phase of the reflection coefficient are incorrectly given by Lee's method. The discrepancy is most likely mainly due to the erroneously positioned pole of the rational approximation.

Before proceeding to numerical examples where two pole-pairs of the tangent are modeled, one example where $\epsilon_r = 50$, $\sigma = 0.5$ S/m is considered. The results are shown in Figure 4.4. The proposed method agrees well with the exact results up to about 12 GHz. For larger frequencies, the results are totally wrong. The reason for this is evidently the limited validity range of the rational approximation. Again, Lee's method is much less accurate than the proposed method. It will be seen later that the proposed higher-order formulation correctly models also the frequency range from 12 GHz to 20 GHz if two pole-pairs of the tangent are modeled.

Next, we include nonzero coefficients p_2 and q_2 with the appropriate extra terms

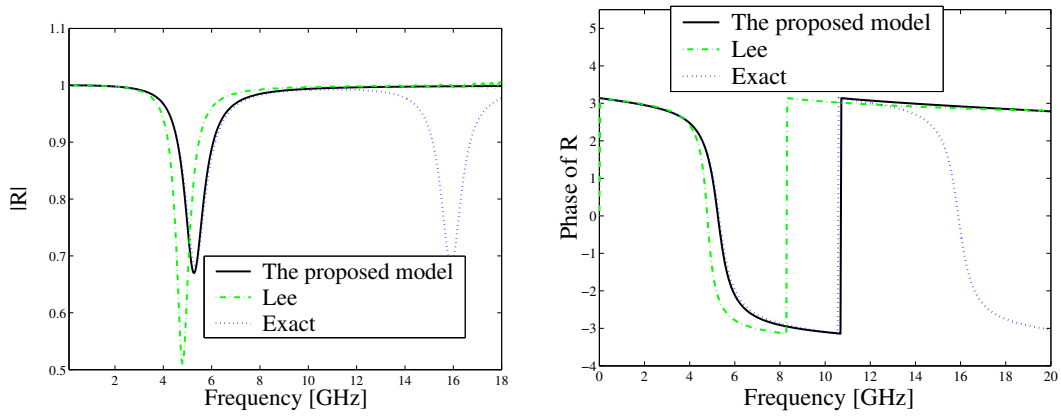

(a) (b)

Figure 4.4: (a) Magnitude of the reflection coefficient for $\epsilon_r = 50$, $\sigma = 0.5$ S/m. It is stressed that the simpler rational approximation is not valid after $f = 12$ GHz. (b) Phase of the reflection coefficient for $\epsilon_r = 50$, $\sigma = 0.5$ S/m.

into the model. In Figure 4.5, results for $\epsilon_r = 5$, $\sigma = 0.5$ S/m are shown. In this case, we have changed the thickness of the layer to be $d = 4$ mm. It is interesting to see that even with one pole-pair modeled ($p_2 = q_2 = 0$), the proposed higher-order model yields approximately as accurate results as the lower-order Lee's formulation with $p_2 \neq 0, q_2 \neq 0$. Now, the local minimum of the magnitude of the reflection coefficient calculated with Lee's method occurs in the correct frequency region, as expected, since the singularity of the rational approximation used by Lee *et al.* is now properly positioned, as can be seen in Figure 4.1 b).

The disadvantage of the rational approximation with $p_2 \neq 0, q_2 \neq 0$ used by Lee *et al.* is that there is a singularity at about $x = 3$ (see Figure 4.1 b)). This is the most probable reason for the qualitatively incorrect results of Lee's method for $f > 14$ GHz. Another possible reason is the inaccurate evaluation of the normal derivative in the Lee's model. The version of the proposed model where two pole-pairs are modeled agrees very well with the analytical results.

Another example of the proposed higher-order model with $p_2 \neq 0, q_2 \neq 0$ is shown in Figure 4.6. There was a stability problem in Lee's method for these parameters, hence those results are missing from the figure. The results should be compared with Figure 4.4, where the same parameters of the coating were used but the results were calculated with simpler rational approximations. The range of applicability is seen to be much wider when two pole-pairs of the tangent are modeled. The agreement is seen to be excellent for f=0 . . . 12 GHz and quite satisfactory for f=12 . . . 20 GHz for both the magnitude and the phase of the reflection coefficient. The thickness of the coating is about $d = (0.57 \ldots 0.94)\lambda$ at these frequencies. Here, λ denotes the wavelength inside the layer. The convergence of the algorithm with decreasing cell size is also

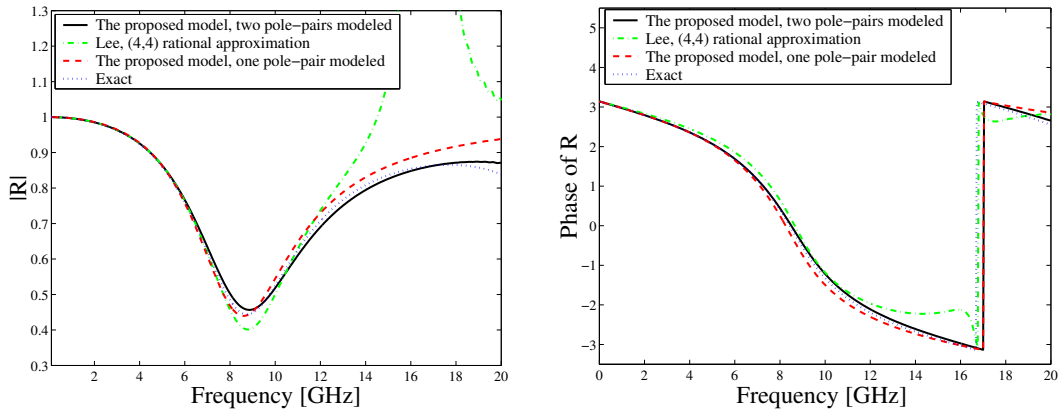

(a) (b)

Figure 4.5: (a) Magnitude of the reflection coefficient for $\epsilon_r = 5$, $\sigma = 0.5$ S/m. (b) Phase of the reflection coefficient for $\epsilon_r = 5$, $\sigma = 0.5$ S/m.

demonstrated in Figure 4.6. It is noticed that the thickness resonance is shifted to correct position when smaller cells are used. However, small discrepancy in the magnitude of the reflection coefficient remains. This is due to limited accuracy of the rational approximation.

A further numerical study of the choice of the coefficients of the rational approximation reveals that the coefficients may be optimized to yield still better accuracy. We observe some discrepancy in the position and the depth of the magnitude of the reflection coefficient in Figure 4.6 when the cell size is $\Delta x = 2$ mm. It turns out that slightly increasing parameter q_2 shifts the position of the second thickness resonance closer to the exact value ($\Delta x = 2$ mm). In Figure 4.7 we see how the results change if we increase the parameter q_2 by 4 percent. The resonance occurs at the correct frequency, but the depth of the dip is overestimated. The depth can be adjusted by reducing parameter p_2 by 6 percent. After the modification of q_2 and p_2, the accuracy is seen to be excellent. Increase in the accuracy for these empirically modified parameters occurs for other parameters of electrically thick coatings, too. A good analytical basis to determine the optical parameters p_1, p_2 and q_1, q_2 could be the minimization of the error of the input impedance over certain frequency range in a certain norm. This issue is not addressed here.

The proposed model can correctly handle layers with thickness up to about one wavelength. This is considered to be a significant improvement to the earlier models, which are only applicable to relatively thin layers.

Layers of Lorentz, Debye, and Drude Media

Next we show that the model also correctly handles more complicated layers made of Lorentz, Debye or Drude materials. The problem setting is the same

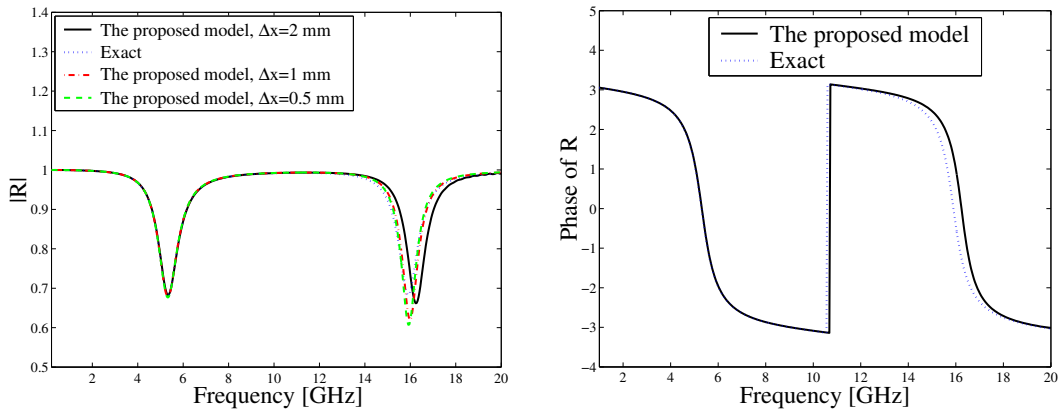

(a) (b)

Figure 4.6: (a) Magnitude of the reflection coefficient for $\epsilon_r = 50$, $\sigma = 0.5$ S/m. (b) Phase of the reflection coefficient for $\epsilon_r = 50$, $\sigma = 0.5$ S/m.

as described above. The magnitudes of the reflection coefficients are calculated for each of the different layers. The permittivity of the Lorentz coating is assumed to have a single pole-pair. The following parameters are used for the Lorentz coating: $\epsilon_1 = 5, \beta = 7.0 \cdot 10^{21}$ rad^2/s^2, $\omega_0 = 5.0 \cdot 10^{10}$ rad/s, $\gamma = 1, \delta = 5.0 \cdot 10^9$ s. Here, β is the change in the relative permittivity due to the Lorentz pole pair, ω_0 is the undamped frequency of the pole pair and δ is the damping factor. The corresponding relative permittivity is shown in Figure 4.8 a). Although not shown here, the reflected wave is highly oscillatory. Figure 4.8 b) shows that despite the complexity of the coating the magnitude of the reflection coefficient agrees rather well with the exact result. The thickness of the coating is $d = 2$ mm. In the rational approximation of the tangent, we have $p_2 = q_2 = 0$ with nonzero p_1 and q_1.

For Debye coating, we choose $\epsilon_1 = 15, \beta = 5$, $\omega_0 = 1$ rad/s,$\gamma = 0, \delta = 1.0 \cdot 10^{11}$ s. Here, β is the change in relative permittivity due to the pole and δ is the pole relaxation time. The magnitude of the reflection coefficient agrees well with the exact result in Figure 4.9 b). The thickness of the coating is 2 mm.

Finally, Drude coating of thickness $d = 3$ mm is considered. The parameters are $\epsilon_1 = 1$, $\omega_0 = 0$, $\beta = 5.0 \cdot 10^{20}$ rad^2/s^2, $\gamma = 1$ and $\delta = 8.33 \cdot 10^7$ s. In the simulated frequency range, the agreement of the reflection coefficient in Figure 4.10 b) with the exact result is seen to be good. The real part of the relative permittivity is close to unity, while the imaginary part has a singularity at $\omega = 0$, tending to 0 as $\omega \to \infty$.

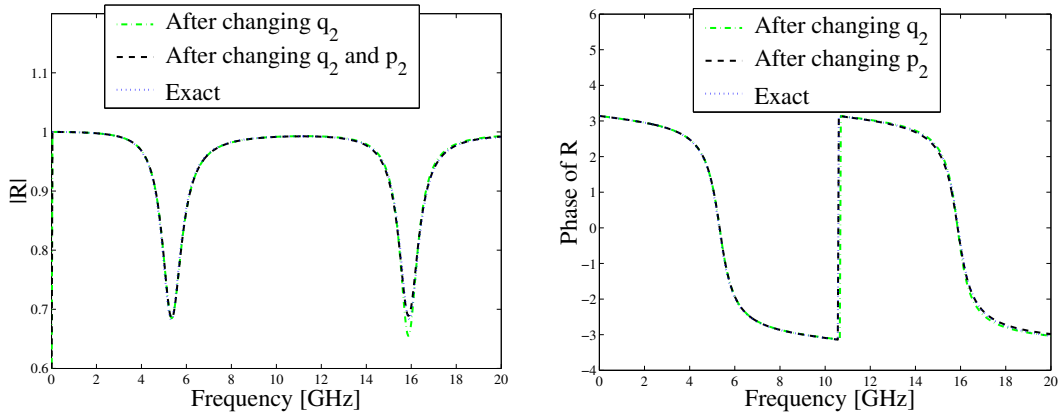

(a) (b)

Figure 4.7: (a) Magnitude of the reflection coefficient for $d = 2$ mm, $\epsilon_r = 50$, $\sigma = 0.5$ S/m. Better accuracy is obtained by empirically adjusting the parameters of the rational approximation. (b) Phase of the reflection coefficient for $\epsilon_r = 50$, $\sigma = 0.5$ S/m.

4.4.2 Cylindrical Wave in Two Dimensions

In this example, we consider a two-dimensional TM_z case (electric field component E_z is excited), where a cylindrical line source is placed above the dielectric conductive coating. Comparison will be made in the time domain, where the reflected and the total waveforms on the interface are calculated in a position, where the angle of incidence is oblique. One pole-pair of the tangent is modeled in this example. Comparison is made with the analytical results obtained by evaluating the integrals (2.40) and (2.42) with the appropriate exact reflection coefficient at oblique incidence.

Dielectric and Conductive Coatings

Arbitrarily choosing $\epsilon_r = 5$, $\sigma = 0.5$ S/m, the reflected and the total waveforms on the interface were calculated by numerically computing the inverse Fourier transform of the exact frequency-domain solution. The line source (a differentiated Gaussian pulse) is located 10 cells above the air-dielectric interface and 15 cells along the interface away from under the line source in the example results shown in Figures 4.11–4.15. The methodology to calculate the exact solution is based on the plane wave spectrum [28], similarly as in chapter 2.

In Figure 4.11 a) both methods are seen to agree quite well with the exact reflected waveform, the proposed method being slightly more accurate. In Figure 4.11 b), however, the proposed method is seen to be much more accurate. By increasing the dielectric constant of the layer, we obtain more complicated waveforms. The results for $\epsilon_r = 20$, $\sigma = 0.2$ S/m are shown in Figure 4.12.

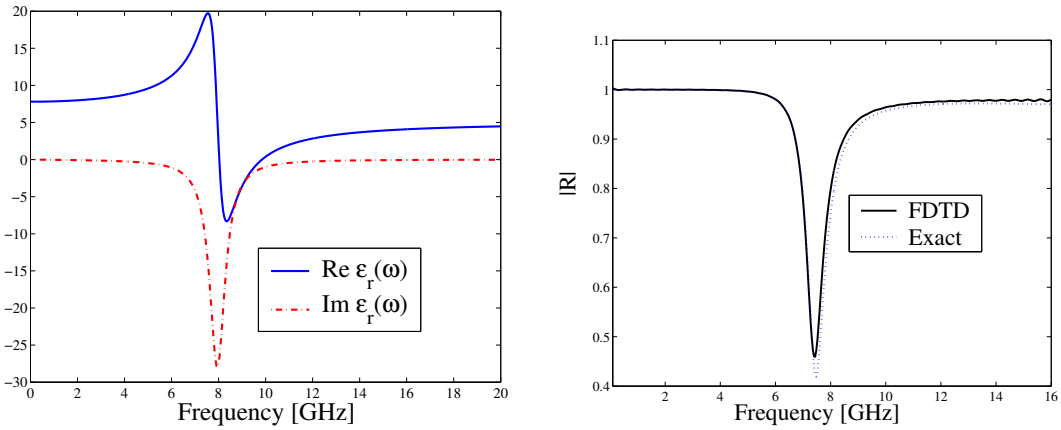

(a) (b)

Figure 4.8: (a) The frequency dependence of the relative permittivity function of the Lorentz coating. (b) The magnitude of the reflection coefficient.

The source is now 20 cells above the interface. It it seen that the proposed method still follows the exact solution quite accurately. The results are again compared with the results calculated with Lee's model. The proposed method seems to be more accurate in this case. Many other simulations that are not shown here support the superiority of the proposed model with respect to Lee's model. In this latter example, the layer thickness is $d = 1.5$ cm, corresponding to 1.06λ at the peak frequency of the spectrum of the incident wave.

The surface impedance is quite sensitive to the change of the permeability of the coating. Let us examine this case by letting the relative permeability of the coating to be $\mu_r = 2$. The corresponding reflected electric field is shown in Figure 4.13 a). We further change the relative permeability to $\mu_r = 3$, and the agreement of the simulated and the analytical results in Figure 4.13 b) is seen to be good. The reflected wave has become highly oscillatory, and the model has some difficulties to produce the correct amplitude of the electric field. Simulation with the simpler discretization technique was also run, and the simpler model was found to be less accurate with these parameters. Notice that the present model can only handle coatings whose permeability is constant, more complicated layers with frequency-dispersive permeability function can be modeled with the subcell technique, as will be shown in chapter 6.

Let us further compare the different discretization techniques. Let the coating have the parameters $\epsilon_r = 80$, $\sigma = 0.2$ S/m, $d = 1.5$ cm and the source be located 20 cells above the interface, and 15 cells along the interface away from under the source. From the results in Figure 4.14, it is obvious that the simpler model is very useful, although slightly less accurate than the original model. The difference between the results calculated with the models is more evident in Figure 4.14 b), where the total electric field at the observation point as a function of time is shown.

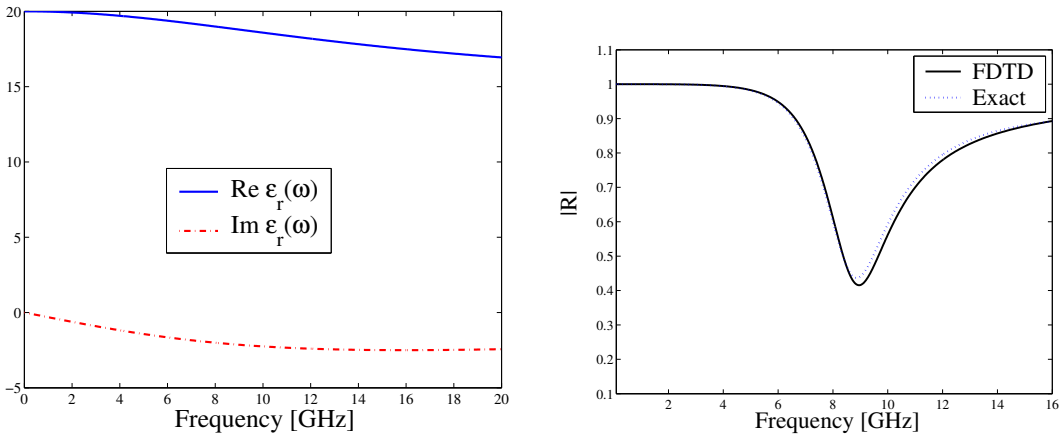

(a) (b)

Figure 4.9: (a) The frequency dependence of the relative permittivity function of the Debye coating. (b) The magnitude of the reflection coefficient.

Dispersive Coatings

In the following, we test the developed model for dispersive coatings. The source is located 20 cells above the interface and 15 cells away along the interface. Thus, the angle of incidence is 36.9 degrees. The rather complicated updating scheme works very accurately, as can be seen in Figure 4.15 a), where the reflected electric field on the air-dielectric interface is numerically simulated with FDTD and compared with analytical results. Similar level of agreement was observed in the total field, too. The relative permittivity function versus angular frequency is shown in Figure 4.15 b). The position of the resonance is chosen so that the incident wave has significant amount of energy near that frequency.

To obtain a coating of Drude type, we set $\omega_0 = 0$. Some other parameters of the coating are also modified. A totally different frequency-dependence of the permittivity function is realized [see Figure 4.16 b)]. The reflected electric field in Figure 4.16 a) agrees very well with the analytical solution.

Finally, we check the model performance for a coating of Debye type. Sea water is a common example of a material obeying Debye-type permittivity relation. A numerical example is given in Figure 4.17 a), and the permittivity expression is presented in Figure 4.17 b).

These coatings are electrically rather thick, and neglecting the spatial derivatives along the interface will not noticeably change the results. Our rigorous analytical approach is seen to yield very accurate results for many different coatings, and the derived scheme is the same for different types of frequency dispersion, as long as we assume a single pole-pair. In fact, dielectric and conductive coatings can be obtained as special cases from the general formu-

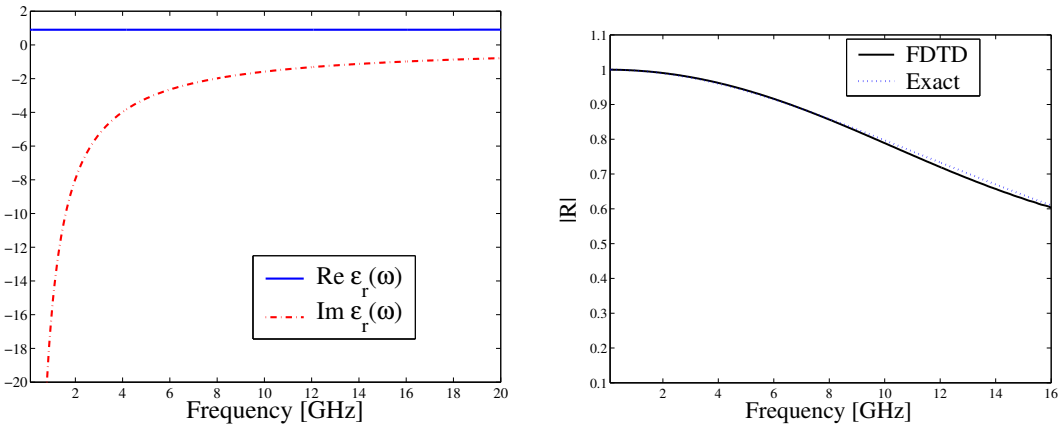

(a) (b)

Figure 4.10: (a) The frequency dependence of the relative permittivity function of the Drude coating. (b) The magnitude of the reflection coefficient.

lation for frequency-dispersive coatings. However, it is possible to avoid the cumbersome auxiliary variables if frequency-dispersion is negligible, enabling simpler updating techniques.

4.5 Scattering width calculations

It is well known that the scattering cross section of an object can be manipulated with a dielectric coating. This issue is demonstrated with FDTD simulations in this section. An FDTD code based on pure scattered-field formulation was written for this purpose. Another possibility would be to use the total-field/scattered-field formulation, which is, however, less attractive since there are dispersion errors in the incident fields. Contrary to the total-field/scattered-field technique, the pure scattered-field technique has the obvious advantage that the incident fields are calculated from exact analytical expressions. The scattered fields are updated according to the conventional FDTD algorithm outside the scattering body. When the simulation proceeds, the scattered field is effectively generated on the surface of the object. The impedance boundary conditions on the surface of the object are formulated in terms of the incident and scattered fields as follows:

$$\mathbf{E}_t^{scat} = -\mathbf{E}_t^{inc} + \overline{\overline{Z}}_s(\omega) \cdot \left[\mathbf{n} \times \left(\mathbf{H}_t^{inc} + \mathbf{H}_t^{scat}\right)\right]. \tag{4.39}$$

The simulations are made in 2D situation, hence the object is infinitely long in one spatial dimension and the scattering cross section reduces to the scattering width of the object. Scattering from a square cylinder is studied here. The square shape is easy to accommodate in our rectangular Yee lattice, hence this simple geometry has been chosen. The problem geometry is shown in Figure 4.18. A near-field to far-field transformation is implemented [41] to calculate

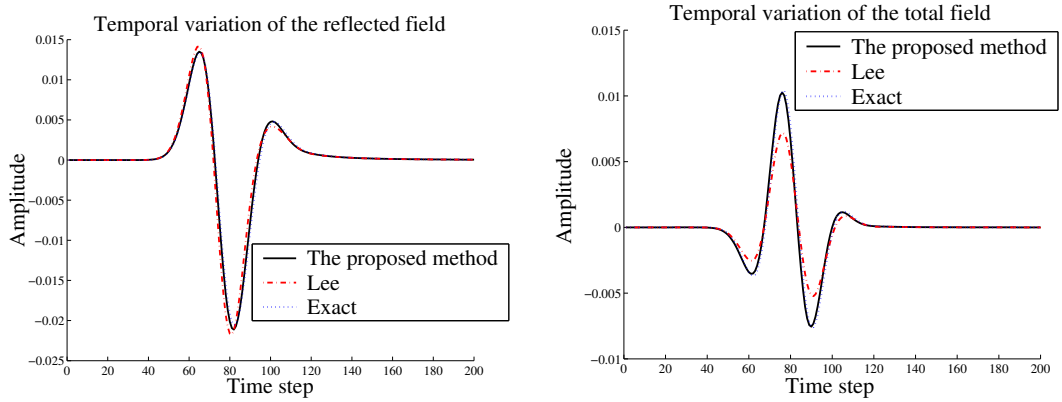

(a) (b)

Figure 4.11: (a) Reflected waveform at the observation point on the interface. (b) Total waveform at the observation point.

the scattered far-fields. It was observed that the low-frequency behavior of scattering width is correctly modeled only if the transformation boundary is relatively close to the object. For larger frequencies, the exact position of the transformation boundary has negligible effect on the scattered far-fields. On the transformation boundary, equivalent electric and magnetic currents ($\mathbf{J}_{eq}$ and $\mathbf{M}_{eq}$, respectively) are calculated according to

$$\mathbf{J}_{eq} = \mathbf{n} \times \mathbf{H}, \qquad \mathbf{M}_{eq} = -\mathbf{n} \times \mathbf{E}. \tag{4.40}$$

Here, $\mathbf{n}$ denotes the unit normal vector pointing outwards from the transformation boundary. Using the equivalent surface currents $\mathbf{J}_{eq}$ and $\mathbf{M}_{eq}$, a complex-valued pattern function $F(\theta)$, independent of the radial distance r, is computed as

$$F(\theta) = \frac{e^{j\frac{\pi}{4}}}{\sqrt{8\pi k}} \oint_C \left[\omega\mu_0 \mathbf{u}_z' \cdot \mathbf{J}_{eq}(\mathbf{r}') - k\mathbf{u}_z' \times \mathbf{M}_{eq}(\mathbf{r}') \cdot \mathbf{u}_r\right] e^{jk\mathbf{u}_r \cdot \mathbf{r}'} dC', \tag{4.41}$$

where primes denote the coordinates on the transformation contour C, and $\mathbf{u}_r$ is the radial unit vector.

The two-dimensional bistatic radar cross section is defined as the ratio of the power scattered per unit angle in certain direction divided by the incident power per unit length. Mathematically, the radar cross section is given by [27]

$$\mathrm{RCS}(\theta) = 2\pi \frac{|F(\theta)|^2}{|E^{inc}|^2}, \tag{4.42}$$

and it has the dimensions of meters.

A wide band differentiated Gaussian pulse is used as the incident pulse. The incident electric field is of the form

$$E_z^{inc} = f(ct - x\cos(\theta_{inc}) - y\sin(\theta_{inc})), \tag{4.43}$$

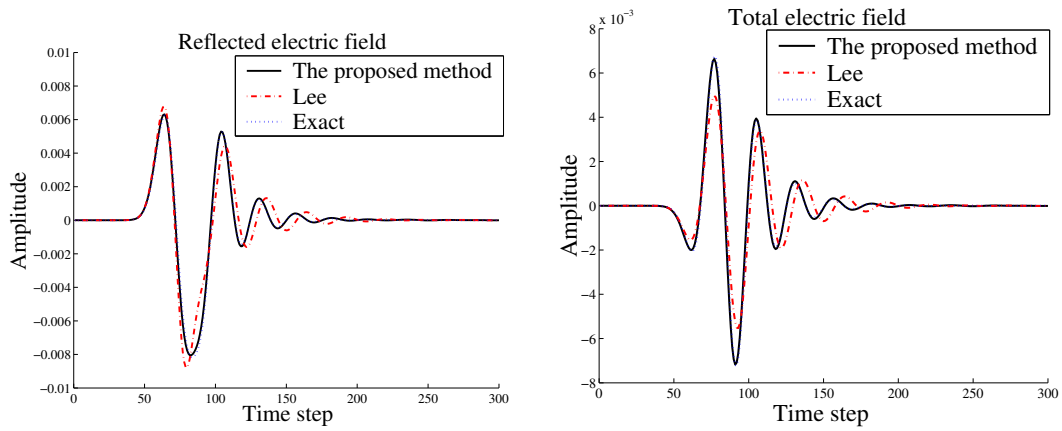

(a) (b)

Figure 4.12: (a) The reflected electric fields at the observation point. Comparison with Lee's method reveals that the proposed method is much more accurate. (b) The total electric field at the observation point.

where f is the differentiated Gaussian pulse and θ_{inc} is the angle of incidence. The coordinate origin is located in the geometrical center point of the scatterer. The incident magnetic field components are readily calculated from Maxwell's equations:

$$H_x^{inc} = -\frac{\sin(\theta_{inc})}{\eta_0} E_z^{inc}, \quad H_y^{inc} = \frac{\cos(\theta_{inc})}{\eta_0} E_z^{inc}. \tag{4.44}$$

The scattering width is calculated to a direction specified by the angle θ_{scat} (see Figure 4.18). Let the cylinder have a square cross section with side length $L = 10$ cm (corresponding to 50 cells in FDTD). In Figure 4.19 a), results for $\theta_{inc} = \theta_{scat} = 0$ are shown. For a reference see [8], where the scattering width magnitude for a well-conducting ($\sigma = 20$ S/m) cylinder with the same dimensions is shown.

It is seen in Figure 4.19 a) that coatings can dramatically reduce scattering in a certain frequency range. The scattering width magnitude for small frequencies behaves similarly regardless of the coating. For very small frequencies, the scattering width magnitude becomes negligible. This is natural since the incident waves do not "see" the scatterer if the wavelength is very large compared with the size of the object. It is also seen that a change in the conductivity of the coating controls the depth of the peak of the scattering width magnitude in this particular case. For a thicker coating, the resonance occurs at lower frequencies, as expected. For electrically thinner coatings (the physical thickness is kept constant), the resonance is shifted to higher frequencies. Scattering width magnitudes at scattering angle $\theta_{scat} = 60$ degrees are presented in Figure 4.19 b). Results for the PEC cylinder are similar to those presented in [8] for a well-conducting cylinder.

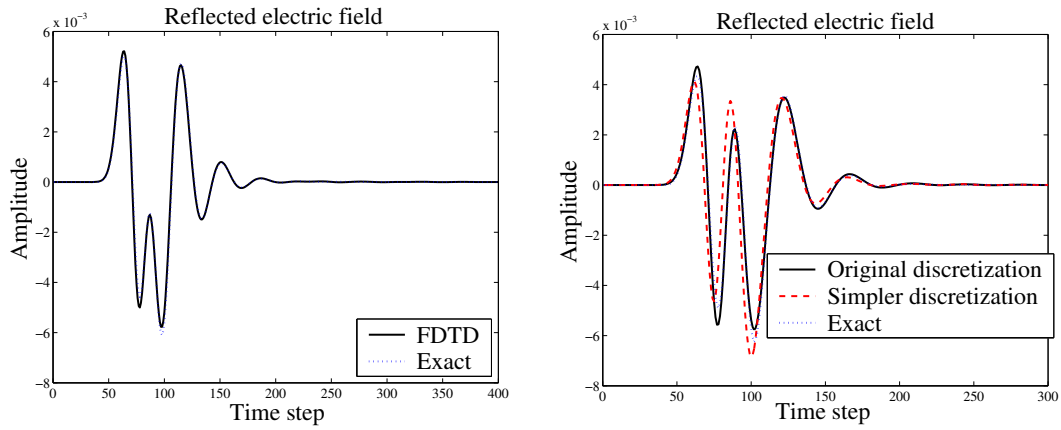

(a) (b)

Figure 4.13: (a) The reflected electric fields at the observation point. The relative permeability of the coating is $\mu_r = 2$, other parameters as in Figure 4.12. (b) The reflected electric fields at the observation point. The relative permeability of the coating is $\mu_r = 3$, other parameters as in Figure 4.12. Apparently, the reflected electric field is quite sensitive to the change of permeability of the coating. The simpler discrete model is less accurate.

4.6 Conclusions

A new accurate SIBC-based FDTD model of dispersive and conductive material layers on metal surfaces has been presented and verified by comparison with analytical results. Three significant improvements to the existing models were introduced. As the first important new feature, tangential variations of the fields on the interface were accounted for in a general fashion using spatial derivatives. Secondly, an accurate approximation of the surface impedance function was presented. As a third improvement, the proposed model can handle more complicated dispersive coatings, where the permittivity function is of Lorentz, Debye or Drude type. Many numerical examples clearly indicate the advantages of the proposed model as compared with the earlier models.

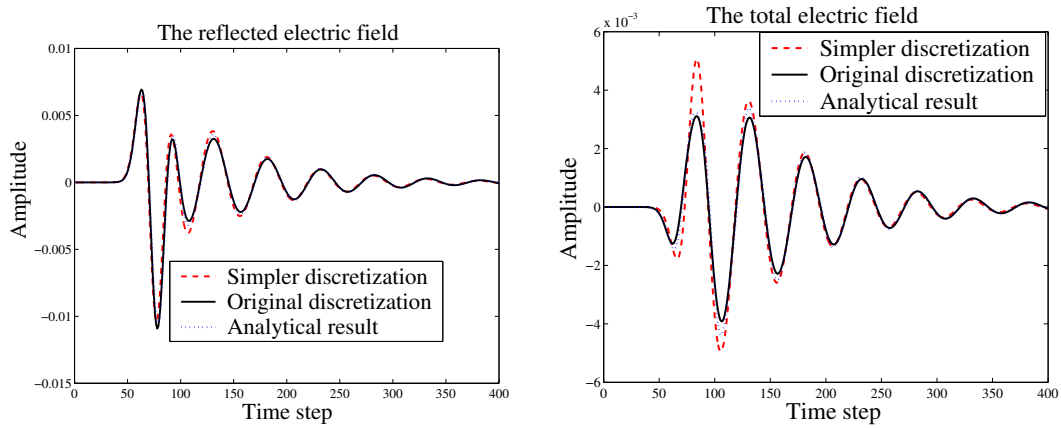

(a) (b)

Figure 4.14: (a) Reflected waveform at the observation point on the interface. The simpler model appears to yield almost as accurate reflected waveform as the original more complicated model. The approximation $E_z|^n \approx (E_z|^{n+1} + E_z|^{n-1})/2$ has been used in the discretization. Results without this unnecessary approximation are so close to these results that they have not been plotted in the figure for the sake of clarity. (b) Total waveform at the observation point. Here, a more significant deviation from the analytical result can be observed. In particular, the simpler model overestimates the amplitude of the first three peaks. At later times, both models yield essentially similar results, which agree well with the analytical result.

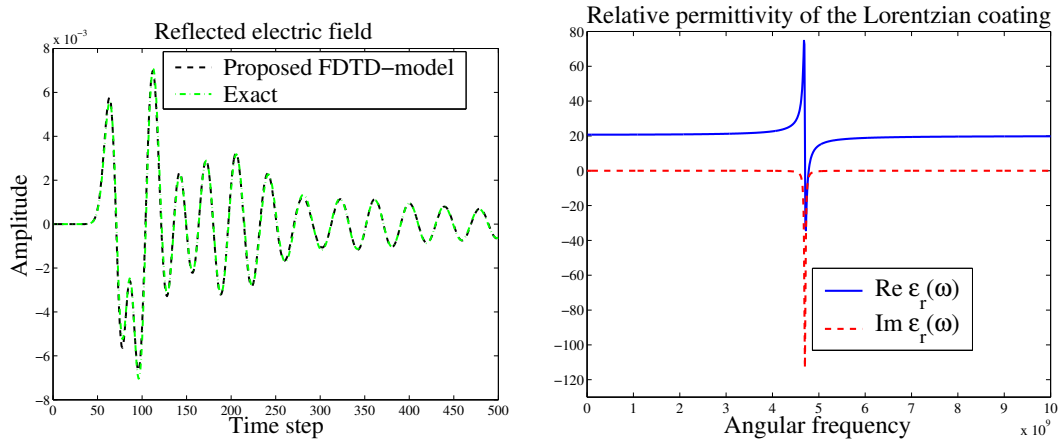

(a) (b)

Figure 4.15: (a) The reflected electric field at the observation point on the interface. Ideally conducting planar metal interface is coated with a Lorentzian layer with one pole-pair. The parameters of the coating are: $d = 2.0$ cm, $\epsilon_1 = 20$, $\beta = 1.6 \cdot 10^{19}$ 1/s^2, $\omega_0 = 4.7 \cdot 10^9$ 1/s, $\gamma = 1$, $\delta = 3.0 \cdot 10^7$ s. (b) The relative permittivity of the Lorentzian coating as a function of angular frequency.

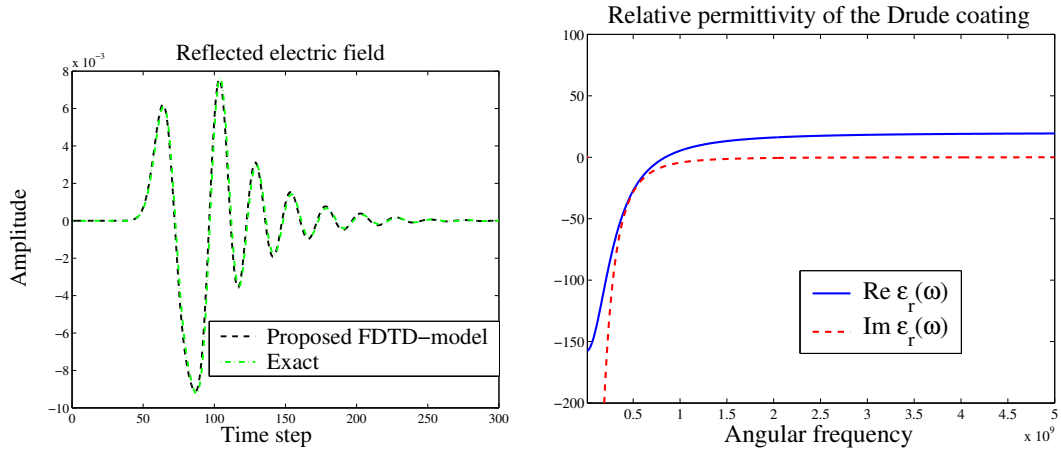

(a) (b)

Figure 4.16: (a) The reflected electric field at the observation point on the interface. The parameters of the Drude coating are: $d = 1.5$ cm, $\epsilon_1 = 20$, $\beta = 1.6 \cdot 10^{19}$ 1/s^2, $\omega_0 = 0$, $\gamma = 1$, $\delta = 3.0 \cdot 10^8$ s. (b) The relative permittivity of the Drude coating as a function of angular frequency.

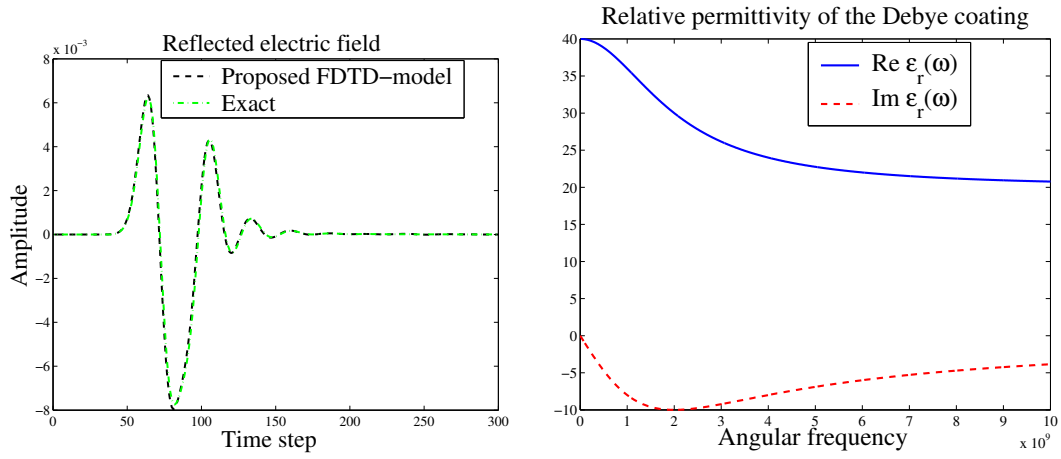

(a) (b)

Figure 4.17: (a) The reflected electric field at the observation point on the interface. The parameters of the Debye coating are: $d = 1.5$ cm, $\epsilon_1 = 20$, $\beta = 20$, $\omega_0 = 1$, $\gamma = 0$, $\delta = 5.0 \cdot 10^{-10}$ s. (b) The relative permittivity of the Debye coating as a function of angular frequency.

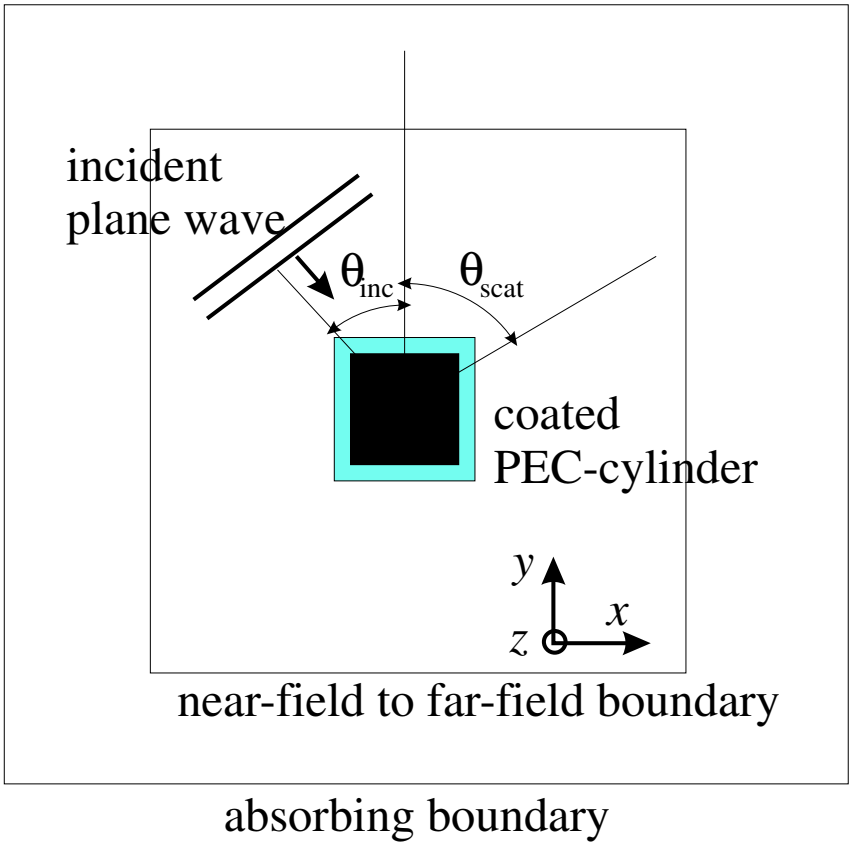

Figure 4.18: The problem geometry. Scattering widths of cylinders are computed with FDTD using impedance boundary conditions.

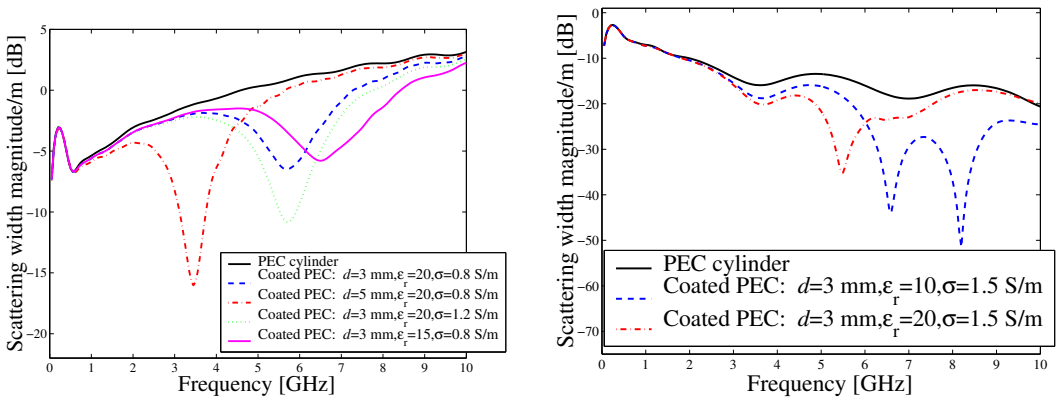

(a) (b)

Figure 4.19: (a) The scattering width magnitude of square cylinders at scattering angle $\theta_{scat} = 0$ degrees versus frequency. (b) The scattering width magnitude of square cylinders at scattering angle $\theta_{scat} = 60$ degrees versus frequency.

Chapter 5

Coatings on More General Conductors

FDTD-modeling of various coatings on conductors is continued in this chapter. Instead of an ideally conducting backing, a more general conductor backing is now considered. Modeling of general conductors requires the recursive convolution technique, which was described in chapter 2. In this rather general situation, the higher-order SIBC would become too complicated to implement in a stable manner, and we deal with first-order boundary conditions.

5.1 Introduction

If the field diffusion into the conductor backing is not negligible, we must work with more general impedance boundary conditions accounting for the field diffusion. This extension is implemented here in a novel and consistent way.

We start with an analytical impedance boundary condition simulating coated dielectric and conductive materials. Utilizing some approximations in the analytical frequency-domain SIBC, we derive the appropriate impedance boundary conditions in the time domain in section 5.2 and develop the associated discrete FDTD model in section 5.3. The model is then carefully verified by comparison with exact results in 1D and 2D example problems. In the one-dimensional case, we simulate reflection of a pulse from the interface between air and a coated conductor. In the 2D case, we simulate the reflection of a cylindrical, obliquely incident pulse from the interface. Both time and frequency domain comparisons are made, and normal and oblique incidence angles are tested. As special cases, the proposed model is equivalent to modeling a coating on perfect electric conductor or a dielectric and conductive material body without the coating, or even empty space. Hence, the proposed method is a considerably more general tool for FDTD modeling than the earlier methods. Numerical examples are given to demonstrate that the model properly reduces to the

earlier models in the aforementioned special cases.

5.2 The Analytical Surface Impedance Model

Let us consider a problem where a dielectric and conductive body is covered with a dielectric and conductive coating of thickness d. The complex permittivity of the coating is of the form

$$\epsilon_c = \epsilon_c' - j\frac{\sigma_c}{\omega} \tag{5.1}$$

and the permittivity of the material body under the coating is

$$\epsilon_m = \epsilon_m' - j\frac{\sigma_m}{\omega}. \tag{5.2}$$

The relative dielectric constants are denoted by $\epsilon_{c,r}'$ and $\epsilon_{m,r}'$. The permeabilities are supposed to be constants: μ_c and μ_m for the coating and the conductive backing, respectively. The problem geometry and the equivalent surface impedance model are shown in Figure 5.1.

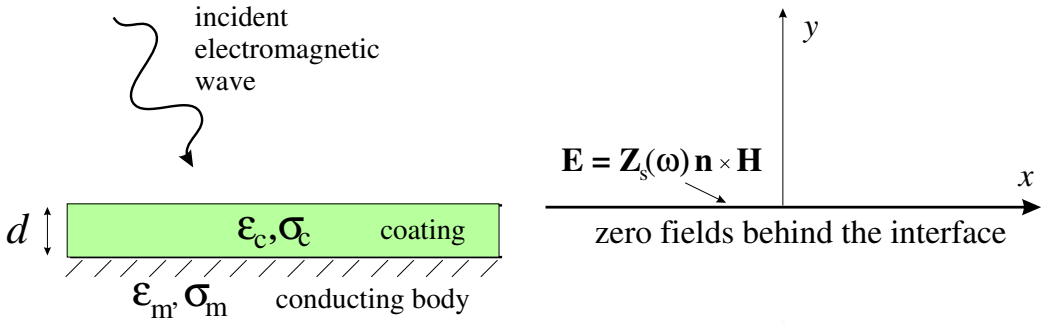

Figure 5.1: (a) The problem geometry. The reflection of an electromagnetic wave from a coated conducting target is modeled. (b) The equivalent surface impedance model and the chosen coordinate system. This coordinate system is used in the analytical considerations (z-axis upwards).

The classical surface impedance boundary condition on the interface between free space and a coating is of the form

$$\mathbf{E}_t = Z_s(\omega)\mathbf{n} \times \mathbf{H}_t, \tag{5.3}$$

where the subscript t refers to the tangential components of the fields and $\mathbf{n}$ is the unit surface normal pointing outwards from the interface.

The analytical surface impedance may be obtained from a simple transmission-line model [42]. Let the thickness of the coating with the characteristic impedance η_c be equal to d, and the material under the coating have the characteristic impedance equal to η_m. Considering the coating as a section of a

transmission line of length d with the characteristic impedance equal to η_c, terminated with the impedance η_m, the input impedance (corresponds to the surface impedance in this model) seen by a normally incident wave at distance d from the termination reads

$$Z_s(\omega) = \eta_c \frac{\eta_m + j\eta_c \tan(k_c d)}{\eta_c + j\eta_m \tan(k_c d)}, \tag{5.4}$$

where k_c is the wave number inside the coating. Similar expression as (5.4) is frequently encountered in microwave engineering, where the term (input) impedance is usually used [42]. The surface impedance boundary condition based on (5.4) is the basis of the proposed model. The earlier SIBC models for conductors by Maloney and Smith and by the author (see chapter 2) assume $\eta_c = 0$ (no coating), and the models for coated *ideal* conductors by Lee *et al.* and by the author suppose that $\eta_m = 0$ (see chapter 4). In the following section, the generalization of the earlier FDTD models is investigated.

5.3 Derivation of the SIBC in the Time domain

Let the unit surface normal vector of the planar interface be $\mathbf{n} = \mathbf{u}_y$, so that the interface is parallel to the xz-plane. The impedance boundary condition (5.3)–(5.4) now takes the form

$$E_x = Z_s(\omega) H_z, \qquad E_z = -Z_s(\omega) H_x. \tag{5.5}$$

In the following, we will derive the SIBC relating E_z and H_x as an example. The derivation for E_x and H_z proceeds similarly. For numerical purposes, a rational approximation of the tangent function appearing in the surface impedance function (5.4) must be introduced. Some authors (see, e.g. [10]) have simply utilized the approximation $\tan(x) \approx x$, which is valid for quite small arguments of the tangent function. Obviously, any algorithm (like that presented in [10]) based on the approximation $\tan(x) \approx x$ is restricted to electrically thin coatings without thickness resonances. In fact, if the coating is PEC-backed, the entire impedance function *does not depend* on the permittivity and conductivity of the coating at all. A more accurate yet simple approximation that is used here reads:

$$\tan(x) \approx \frac{x}{1 - q_1 x^2}, \tag{5.6}$$

where the parameter $q_1 = 4/\pi^2$ is chosen to correctly capture the singular behavior at $x = \pi/2$, a pole of the tangent. Evidently, it is reasonable to use approximation (5.6) rather than $\tan(x) \approx x$ if it does not cause troubles in the discrete model. These two approximations will be compared in section 5.5. Although it is easy to construct arbitrarily accurate approximations of the impedance function, they are increasingly complicated to implement in discrete form. A more accurate rational approximation was used by the author

in chapter 4 where the backing was an ideal conductor, but we will show that the very simple approximation in (5.6) is enough to yield very accurate results in many cases. The reason for choosing a simpler rational approximation here is that we want to avoid very high-order derivatives in the model that would lead to unconventional discretization techniques or even stability problems.

We write $k = \omega\sqrt{\epsilon_c\mu_c}$ and substitute the approximation of the tangent into the analytical SIBC obtaining

$$\left[1 + j\sqrt{\frac{\mu_m}{\epsilon_m}}\sqrt{\frac{\epsilon_c}{\mu_c}}\frac{\omega\sqrt{\epsilon_c\mu_c}d}{1 - q_1\omega^2\epsilon_c\mu_c d^2}\right] E_z = - \left[\sqrt{\frac{\mu_m}{\epsilon_m}} + j\sqrt{\frac{\mu_c}{\epsilon_c}}\frac{\omega\sqrt{\epsilon_c\mu_c}d}{1 - q_1\omega^2\epsilon_c\mu_c d^2}\right] H_x. \tag{5.7}$$

5.3.1 Dielectric and Conductive Coatings

Let us first discuss dielectric and conductive coatings without frequency dispersion. The model will be later generalized to dispersive coatings as well. We multiply with the term $1 - q_1\omega^2\epsilon_c\mu_c d^2$ and substitute expressions (5.1)–(5.2) into (5.7). After minor simplification we get

$$\left[1 - q_1\epsilon_c'\mu_c d^2\omega^2 + jq_1\mu_c\sigma_c d^2\omega + \sqrt{\frac{j\omega\mu_m}{j\omega\epsilon_m' + \sigma_m}}(j\omega\epsilon_c' + \sigma_c)d\right] E_z = -\sqrt{\frac{j\omega\mu_m}{j\omega\epsilon_m' + \sigma_m}}\left(1 - q_1\epsilon_c'\mu_c d^2\omega^2 + jq_1\mu_c\sigma_c d^2\omega\right) H_x - j\omega\mu_c d H_x. \tag{5.8}$$

We use the Laplace transform as in chapter 2 obtaining the time-domain boundary condition:

$$\begin{aligned} E_z + q_1\epsilon_c'\mu_c d^2\frac{\partial^2 E_z}{\partial t^2} + (q_1\mu_c\sigma_c d^2 + \hat{\eta}_m\epsilon_c' d)\frac{\partial E_z}{\partial t} + \hat{\eta}_m\sigma_c d E_z + \\ \hat{\eta}_m\int_0^t \alpha e^{\alpha\tau}\left[I_0(\alpha\tau) + I_1(\alpha\tau)\right]\epsilon_c' d\frac{\partial E_z}{\partial(t-\tau)}\,d\tau = \\ -\mu_c d\frac{\partial H_x}{\partial t} - \hat{\eta}_m\left(H_x + q_1\epsilon_c'\mu_c d^2\frac{\partial^2 H_x}{\partial t^2} + q_1\mu_c\sigma_c d^2\frac{\partial H_x}{\partial t}\right) - \\ \hat{\eta}_m\int_0^t \alpha e^{\alpha\tau}\left[I_0(\alpha\tau) + I_1(\alpha\tau)\right]\cdot \\ \left(\sigma_c d E_z(t-\tau) + H_x(t-\tau) + q_1\epsilon_c'\mu_c d^2\frac{\partial^2 H_x}{\partial(t-\tau)^2} + q_1\mu_c\sigma_c d^2\frac{\partial H_x}{\partial(t-\tau)}\right)\,d\tau, \end{aligned} \tag{5.9}$$

where we have denoted

$$\hat{\eta}_m = \sqrt{\frac{\mu_m}{\epsilon_m'}}. \tag{5.10}$$

The term $\sigma_c d E_z(t-\tau)$ was moved under the second integral because the recursive relations used to evaluate the two integrals are different.

5.3.2 Frequency-Dispersive Coatings

The model will now be extended to coatings with frequency dispersion. However, we will assume a constant permeability as before. We define auxiliary variables in the same manner as earlier to simplify the algorithm:

$$A = \frac{\epsilon_c(\omega)}{\epsilon_0} E_z, \quad B = \frac{\epsilon_c(\omega)}{\epsilon_0} H_x. \tag{5.11}$$

Similar definitions are made for E_x and H_z. Here we will derive the update equation for E_z only, as above. Regarding constants C_1, C_2 and variable R_1, the notation is the same as in chapter 4, where dispersive coatings on ideally conducting surfaces were dealt with.

After straightforward derivation, we obtain the time-domain boundary condition:

$$\begin{aligned} E_z + q_1\epsilon_0\mu_c d^2\frac{\partial^2 A}{\partial t^2} + \hat{\eta}_m\epsilon_0 d\frac{\partial A}{\partial t} + \\ \hat{\eta}_m \int_0^t \alpha e^{\alpha\tau}\left[I_0(\alpha\tau) + I_1(\alpha\tau)\right]\left(\epsilon_0 d\frac{\partial A}{\partial(t-\tau)}\right) d\tau = \\ -\mu_c d\frac{\partial H_x}{\partial t} - \hat{\eta}_m\left(H_x + q_1\epsilon_0\mu_c d^2\frac{\partial^2 B}{\partial t^2}\right) - \\ \hat{\eta}_m \int_0^t \alpha e^{\alpha\tau}\left[I_0(\alpha\tau) + I_1(\alpha\tau)\right]\cdot \\ \left(H_x(t-\tau) + q_1\epsilon_0\mu_c d^2\frac{\partial^2 B}{\partial(t-\tau)^2}\right) d\tau, \end{aligned} \tag{5.12}$$

The discrete models will be developed next.

5.4 The Discrete FDTD Model

The convolution integrals are approximated as sums of the form

$$\sum_{m=0}^{n} F(m) f(E_z|^{n-m}, H_x|^{n-m}), \tag{5.13}$$

where the function f refers to the part of the integrand that depends on the fields E_z and/or H_x at time steps $1 \ldots n$. Assuming a piecewise linear behavior of f, the coefficients $F(m)$ may be calculated as in chapter 2. The coefficients β_l and γ_l are obtained as solutions of linear systems of equations and polynomial equations as in chapter 2, described in detail in [7, 28]. Now, the first integral of $\epsilon_c' d\partial E_z/\partial(t-\tau)$ in (5.9) at the grid position $(x, y, z) = (i\Delta x, 0, (k+1/2)\Delta z)$

can be expressed as a discrete sum in the form

$$\sum_{m=0}^{n} F(m)\left(\epsilon_c' d\frac{E_z|_{i,0,k+1/2}^{n-m+1} - E_z|_{i,0,k+1/2}^{n-m-1}}{2\Delta t}\right) =$$
$$F(0)\left(\epsilon_c' d\frac{E_z|_{i,0,k+1/2}^{n+1} - E_z|_{i,0,k+1/2}^{n-1}}{\Delta t}\right)$$
$$+\sum_{l=1}^{p}\sum_{m=1}^{n}\beta_l\gamma_l^m\left(\epsilon_c' d\frac{E_z|_{i,0,k+1/2}^{n-m+1} - E_z|_{i,0,k+1/2}^{n-m-1}}{2\Delta t}\right)$$
$$= F(0)\left(\epsilon_c' d\frac{E_z|_{i,0,k+1/2}^{n+1} - E_z|_{i,0,k+1/2}^{n-1}}{2\Delta t}\right) + \sum_{l=1}^{p}\Phi_l|_{i,0,k+1/2}^{n}, \tag{5.14}$$

where the variable Φ_l satisfies the recursive relation of the form

$$\begin{aligned}
\Phi_l|_{i,0,k+1/2}^{1} &= 0 \ , l = 1,\ldots,p \\
\Phi_l|_{i,0,k+1/2}^{n} &= \gamma_l\Phi_l|_{i,0,k+1/2}^{n-1} \\
&+ \beta_l\gamma_l\frac{\epsilon_c' d}{2\Delta t}(E_z|_{i,0,k+1/2}^{n} - E_z|_{i,0,k+1/2}^{n-2}) \ , l = 1,\ldots,p.
\end{aligned} \tag{5.15}$$

Notice that the term with $F(0) = \sum_{l=1}^{p}\beta_l$ as a multiplier is extracted from the recursion formula. This is due to the fact that the term $E_z|_{i,0,k+1/2}^{n+1}$ occurs within the convolution integral, disabling the direct recursion. The second convolution integral involving the term $\sigma_c d E_z(t-\tau)$ and the magnetic fields can be computed recursively according to

$$\begin{aligned}
\Psi_l|_{i,0,k+1/2}^{1} &= 0 \ , l = 1,\ldots,p \\
\Psi_l|_{i,0,k+1/2}^{n} &= \gamma_l\Psi_l|_{i,0,k+1/2}^{n-1} + \beta_l\Big[\sigma_c d E_z|_{i,0,k+1/2}^{n} + H_x|_{i,1/2,k+1/2}^{n-1/2} \\
&+ \frac{q_1\epsilon_c'\mu_c d^2}{\Delta t^2}\left(H_x|_{i,1/2,k+1/2}^{n+1/2} - 2H_x|_{i,1/2,k+1/2}^{n-1/2} + H_x|_{i,1/2,k+1/2}^{n-3/2}\right) \\
&+ \frac{q_1\mu_c\sigma_c d^2}{2\Delta t}(H_x|_{i,1/2,k+1/2}^{n+1/2} - H_x|_{i,1/2,k+1/2}^{n-3/2})\Big] \ , l = 1,\ldots,p
\end{aligned} \tag{5.16}$$

The tangential electric and magnetic fields in the Yee lattice are not collocated. This is not a severe problem, as will be shown with numerical examples in the following section. Suppose we want to discretize the analytical SIBC at time moment $t = n\cdot\Delta t$, where Δt is the time step in the FDTD algorithm. The electric field component, for instance E_z at time step $t = n\cdot\Delta t$ at the grid position $(x,0,z) = (i\Delta x, 0, (k+\frac{1}{2})\Delta z)$, denoted shortly $E_z|_{i,0,k+1/2}^{n}$, is related to the magnetic field component at the same position, which may be approximated with the magnetic field component H_x located at half-cell distance away from the interface and half time step earlier in time. That is,

$$H_x|_{i,0,k+1/2}^{n} \approx H_x|_{i,1/2,k+1/2}^{n-1/2}. \tag{5.17}$$

This approach has been successfully used by some authors [7, 8]. Another simple approach is to just neglect the spatial error. This approach has been

used in [14] without significant loss of accuracy. Extrapolation techniques may also be developed, but they easily lead to stricter stability limits or even stability problems. In some problems, the magnetic field may be eliminated using Maxwell's equations, leading to a boundary condition involving only the electric field. This approach has been utilized in [50]. Let us now discuss how the time-domain SIBC (5.9) derived above can be discretized.

5.4.1 Discrete Model for Dielectric and Conductive Coatings

The derivatives in the left hand size of (5.9) are discretized with the usual central differences at time step $t = n \cdot \Delta t$. The update equation will be derived for $E_z|^{n+1}_{i,0,k+1/2}$, necessitating the approximation

$$E_z|^{n}_{i,0,k+1/2} \approx \frac{E_z|^{n+1}_{i,0,k+1/2} + E_z|^{n-1}_{i,0,k+1/2}}{2} \tag{5.18}$$

to obtain a stable algorithm when the coating thickness tends to zero[1]. A good discussion of Prony's method to calculate the coefficients β_l and γ_l in the context of impedance boundary conditions can be found in [7]. Here, the discrete time derivative under the convolution integral has the term $E_z|^{n+1}_{i,0,k+1/2}$. Hence, we have to extract that one term separately from the sum approximating the integral. The first term in the right-hand side of (5.9) is discretized at $t = n \cdot \Delta t$ and $(i, 1/2, k + 1/2)$. The second term in parentheses is evaluated at the same position at $t = (n - 1/2) \cdot \Delta t$, because of the presence of the second-order time derivative, which could not be directly evaluated at $t = n \cdot \Delta t$ (since $H_x|^{n+3/2}$ is not known at time step $t = (n+1) \cdot \Delta t$). Using these discretization principles and solving for $E_z|^{n+1}_{i,0,k+1/2}$, we obtain the update equation

$$\begin{aligned} E_z|^{n+1}_{i,0,k+1/2} = \frac{1}{A}\Bigg\{ & -\frac{1}{2}E_z|^{n-1}_{i,0,k+1/2} - \frac{q_1\epsilon_c'\mu_c d^2}{\Delta t^2}\left(-2E_z|^{n}_{i,0,k+1/2} + E_z|^{n-1}_{i,0,k+1/2}\right) \\ & + \frac{\hat{\eta}_m\epsilon_c' d(1+F(0)) + q_1\mu_c\sigma_c d^2}{2\Delta t}E_z|^{n-1}_{i,0,k+1/2} \\ & - \hat{\eta}_m\left(\sigma_c d E_z|^{n}_{i,0,k+1/2} + \sum_{l=1}^{p}\Psi_l|^{n}_{i,0,k+1/2}\right) \\ & - \hat{\eta}_m H_x|^{n-1/2}_{i,1/2,k+1/2} - \frac{\hat{\eta}_m q_1\epsilon_c'\mu_c d^2}{\Delta t^2}\Big(H_x|^{n+1/2}_{i,1/2,k+1/2} - 2H_x|^{n-1/2}_{i,1/2,k+1/2} \\ & + H_x|^{n-3/2}_{i,1/2,k+1/2}\Big) - \frac{\mu_c d}{\Delta t}(H_x|^{n+1/2}_{i,1/2,k+1/2} - H_x|^{n-1/2}_{i,1/2,k+1/2}) \\ & - \frac{\hat{\eta}_m q_1\mu_c\sigma_c d^2}{2\Delta t}(H_x|^{n+1/2}_{i,1/2,k+1/2} - H_x|^{n-3/2}_{i,1/2,k+1/2}) - \hat{\eta}_m\sum_{l=1}^{p}\Phi_l|^{n}_{i,0,k+1/2}\Bigg\} \end{aligned} \tag{5.19}$$

[1] In the previous chapter this approximation was not necessary for relatively thick coatings. However, for very thin coatings, this approximation must be used also in the model of the previous chapter to ensure stability.

where the constant A is defined as

$$A = \frac{1}{2} + \frac{q_1 \epsilon_c' \mu_c d^2}{\Delta t^2} + \frac{\hat{\eta}_m \epsilon_c' d(1 + F(0)) + q_1 \mu_c \sigma_c d^2}{2\Delta t}. \tag{5.20}$$

The variables Ψ and Φ, defined on the interface only, satisfy the recursive relations (5.15) and (5.16) as discussed above. A simpler algorithm corresponding to the approximation $\tan(x) \approx x$ is obtained by letting $q_1 = 0$ in (5.20). To obtain the update equation for E_x, we need to replace E_z with E_x and H_x with $-H_z$ in the above derivations and to define the corresponding auxiliary variables.

5.4.2 Discrete Model for Dispersive Coatings

Using the auxiliary variables, we obtain the discrete equation (the same as (4.32), repeated here for convenience)

$$\begin{aligned}(4\gamma + \omega_0^2 \Delta t^2 + 2\delta\Delta t)A|^{n+1} = (4\gamma - \omega_0^2 \Delta t^2 - 2\delta t)A|^n + \\ \left[4\epsilon_1\gamma + (\epsilon_1\omega_0^2 + \beta)\Delta t^2 + 2\epsilon_1\delta\Delta t\right] E_z|_{i,0}^{n+1} - \\ \left[4\epsilon_1\gamma - (\epsilon_1\omega_0^2 + \beta)\Delta t^2 - 2\epsilon_1\delta\Delta t\right] E_z|_{i,0}^{n} - \\ 4\omega_0^2\Delta t^2 \sum_{m=1}^{n} \frac{1}{2}(A|^{n-m+1} + A|^{n-m}) + \\ 4(\epsilon_1\omega_0^2 + \beta)\Delta t^2 \sum_{m=1}^{n} \frac{1}{2}(E_z|^{n-m+1} + E_z|^{n-m}).\end{aligned} \tag{5.21}$$

Similarly, the auxiliary equation relating H_x and B is discretized, and we obtain

$$\begin{aligned}(4\gamma + \omega_0^2 \Delta t^2 + 2\delta\Delta t)B|^{n+1/2} = (4\gamma - \omega_0^2 \Delta t^2 - 2\delta t)B|^{n-1/2} + \\ \left[4\epsilon_1\gamma + (\epsilon_1\omega_0^2 + \beta)\Delta t^2 + 2\epsilon_1\delta\Delta t\right] H_x|_{i,0}^{n+1/2} - \\ \left[4\epsilon_1\gamma - (\epsilon_1\omega_0^2 + \beta)\Delta t^2 - 2\epsilon_1\delta\Delta t\right] H_x|_{i,0}^{n-1/2} - \\ 4\omega_0^2\Delta t^2 \sum_{m=1}^{n} \frac{1}{2}(B|^{n-m+1/2} + B|^{n-m-1/2}) + \\ 4(\epsilon_1\omega_0^2 + \beta)\Delta t^2 \sum_{m=1}^{n} \frac{1}{2}(H_x|^{n-m+1/2} + H_x|^{n-m-1/2}).\end{aligned} \tag{5.22}$$

We define constant C_1 as $C_1 = 4\gamma + \omega_0^2\Delta t^2 + 2\delta\Delta t$. Variable R_1 is defined as

$$\begin{aligned}R_1 = (4\gamma - \omega_0^2 \Delta t^2 - 2\delta t)A|^n - \\ \left[4\epsilon_1\gamma - (\epsilon_1\omega_0^2 + \beta)\Delta t^2 - 2\epsilon_1\delta\Delta t\right] E_z|_{i,0}^{n} - \\ 4\omega_0^2\Delta t^2 \sum_{m=1}^{n} \frac{1}{2}(A|^{n-m+1} + A|^{n-m}) + \\ 4(\epsilon_1\omega_0^2 + \beta)\Delta t^2 \sum_{m=1}^{n} \frac{1}{2}(E_z|^{n-m+1} + E_z|^{n-m}).\end{aligned} \tag{5.23}$$

The discrete boundary condition becomes

$$E_z|^{n+1}_{i,0,k+1/2} = \frac{1}{A}\left\{-\frac{1}{2}E_z|^{n-1}_{i,0,k+1/2} - \frac{q_1\epsilon_0\mu_c d^2}{\Delta t^2}\left(\frac{R_1}{C_1} - 2A|^n + A|^{n-1}\right)\right.$$
$$-\frac{\hat{\eta}_m\epsilon_0 d(1+F(0))}{2\Delta t}\left(\frac{R_1}{C_1} - A|^{n-1}\right) - \frac{\mu_c d}{\Delta t}\left(H_x|^{n+1/2}_{i,1/2,k+1/2} - H_x|^{n-1/2}_{i,1/2,k+1/2}\right)$$
$$-\hat{\eta}_m H_x|^{n-1/2}_{i,1/2,k+1/2} - \frac{\hat{\eta}_m q_1\epsilon_0\mu_c d^2}{\Delta t^2}\left(B|^{n+1/2}_{i,1/2,k+1/2} - 2B|^{n-1/2}_{i,1/2,k+1/2} + B|^{n-3/2}_{i,0,k+1/2}\right)$$
$$\left.-\hat{\eta}_m\sum_{l=1}^{p}\Psi_l|^n_{i,0,k+1/2} - \hat{\eta}_m\sum_{l=1}^{p}\Phi_l|^{n+1/2}_{i,1/2,k+1/2}\right\} \quad (5.24)$$

The discrete convolutions are evaluated according to following recursive relations:

$$\begin{aligned}
\Psi_l|^1_{i,0,k+1/2} &= 0 \ , l = 1,\ldots,p \\
\Psi_l|^n_{i,0,k+1/2} &= \gamma_l\Psi_l|^{n-1}_{i,0,k+1/2} \\
&+ \beta_l\gamma_l\frac{\epsilon_0 d}{2\Delta t}(A|^n_{i,0,k+1/2} - A|^{n-2}_{i,0,k+1/2}) \ , l = 1,\ldots,p. \quad (5.25)
\end{aligned}$$

and

$$\begin{aligned}
\Phi_l|^1_{i,0,k+1/2} &= 0 \ , l = 1,\ldots,p \\
\Phi_l|^{n+1/2}_{i,0,k+1/2} &= \gamma_l\Phi_l|^{n-1/2}_{i,0,k+1/2} + \beta_l\left[H_x|^{n-1/2}_{i,1/2,k+1/2} + \frac{q_1\epsilon_0\mu_c d^2}{\Delta t^2}\right. \\
&\cdot \quad \left.\left(B|^{n+1/2}_{i,1/2,k+1/2} - 2B|^{n-1/2}_{i,1/2,k+1/2} + B|^{n-3/2}_{i,1/2,k+1/2}\right)\right] , \\
&\quad l = 1,\ldots,p. \quad (5.26)
\end{aligned}$$

Again, the general model for dispersive coatings can be used to model dielectric and conductive coatings without frequency dispersion. However, the algorithm is unnecessarily complicated due to the auxiliary variables.

The present discrete scheme should be straightforward to apply in other coordinate systems as well, since we only need the tangential electric field on the interface and the tangential magnetic field defined at half-cell distance from the interface. In rectangular coordinates, one might utilize the contour-path algorithm [43] to account for the curvature of the impedance surface. An attempt towards this direction was made by Farahat *et al.* in [12].

The absence of spatial derivatives along the interface is a convenient feature near corner points, since the same discrete scheme can be applied. Although the surface impedance is not defined at corner points, because the tangential vectors cannot be defined, we can use the same scheme with acceptable errors. In [8], scattering of infinitely long conducting cylinders with rectangular cross-section was studied using first-order accurate impedance boundary conditions. It has been demonstrated in [8] that the use SIBCs and the direct discretization approach give similar results for the scattering width magnitude.

5.5 Numerical Verification of the Model

Let us study the accuracy of the proposed model with numerical examples. One and two-dimensional example problems are considered. In both example problems, the electric field is excited with a differentiated Gaussian pulse of the form

$$I(t) = (t - \tau_1)e^{-\left(\frac{t-\tau_1}{\tau_2}\right)^2}. \tag{5.27}$$

The smoothness and the wide spectrum of this pulse enable a convenient study of reflected waves in both time and frequency domains. Some of the problems are solved by directly discretizing the fields within the coating and the conductor backing. Comparison of the memory requirements and the CPU times of the two approaches reveal that huge computational savings can be realized.

5.5.1 Reflection from a Coated Conductor at Normal Incidence

For normally incident waves, we can easily calculate the exact reflection coefficient versus frequency as

$$R(\omega) = \frac{Z_s(\omega) - \eta_0}{Z_s(\omega) + \eta_0}. \tag{5.28}$$

The numerical reflection coefficient is calculated as the ratio of the reflected and the incident spectrums, which are computed in the FDTD simulation as running sums, according to the discrete Fourier transform.

The problem is solved with the FDTD method as a one-dimensional problem. The spatial cell size is $\Delta x = 2$ mm, and the time step size is equal to the Courant stability limit: $\Delta t = \Delta x/c_0$, where c_0 is the speed of light in vacuum. The parameters of the pulse in (5.27) are $\tau_1 = 24\Delta t$, $\tau_2 = 7.2\Delta t$.

Let us first consider the case when the thickness of the coating is $d = 2$ mm, the relative dielectric constant of the coating is $\epsilon'_{c,r} = 2$, and the conductivity of the coating is $\sigma_c = 0.01$ S/m. The material body behind the coating is assumed to have the parameters $\epsilon'_{m,r} = 1$, $\sigma_m = 0.05$ S/m. Unless otherwise mentioned, the relative permeabilities of the materials are equal to unity. Notice that the conductivities and the relative dielectric constants of the materials are quite small. Therefore, rather weak reflection should be expected. The simulated and the exact reflection coefficients are shown in Figure 5.2. The agreement in the magnitude of the reflection coefficient in Figure 5.2 a) is very good in the frequency range from 0 GHz to about 8 GHz, and satisfactory for higher frequencies from 8 GHz to 20 GHz. This is expected, since the rational approximation of the tangent has a limited range of good accuracy. For frequencies near 6 GHz, the waves are mostly absorbed. Indeed, an *absorbing boundary condition* may be obtained by setting $\epsilon'_{c,r} = 1$, $\sigma_c = 0$ S/m, $\epsilon'_{m,r} = 1$ and $\sigma_m = 0$ S/m. The simulated phase of the reflection coefficient

agrees quite well with the analytical result in the entire frequency range under consideration. Notice that also the simpler model based on the approximation $\tan(x) \approx x$ yields quite reasonable results for this electrically thin coating. However, the limitations of the simpler approach become evident in the case of an electrically thicker coating to be considered next.

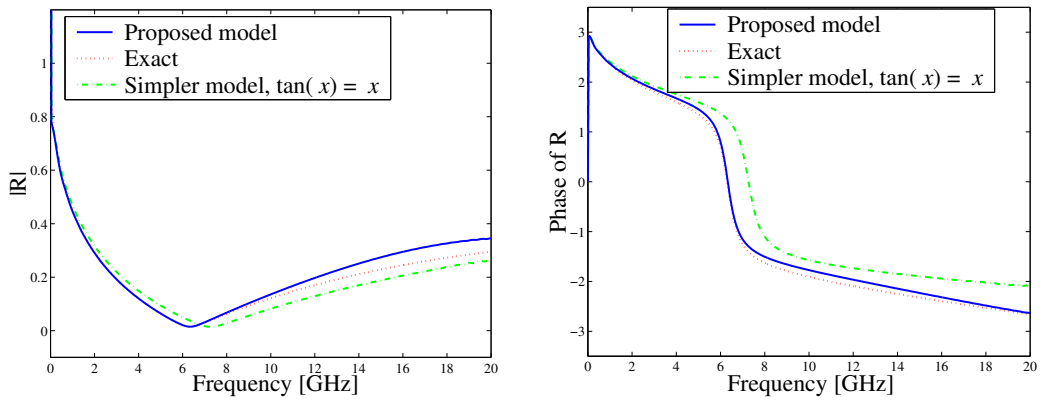

(a) (b)

Figure 5.2: (a) Magnitude of the reflection coefficient. Parameters of the coating: $d = 2$ mm, $\epsilon'_{c,r} = 2$, $\sigma_c = 0.01$ S/m. Parameters of the conductive material: $\epsilon'_{m,r} = 1$, $\sigma_m = 0.2$ S/m. (b) Phase of the reflection coefficient.

Indeed, let us consider the case when the thickness of the coating is $d = 1$ mm, the relative dielectric constant of the coating is $\epsilon'_{c,r} = 30$, and the conductivity of the coating is $\sigma_c = 0.4$ S/m. Now, larger differences between the methods based on the two approximations of the tangent should occur, because the coating is electrically thicker. The conductor behind the coating is assumed to have the parameters $\epsilon'_{m,r} = 5$, $\sigma_m = 80$ S/m. The simulated and the exact reflection coefficients are presented in Figure 5.3. The accuracy is quite good in the frequency range from 0 GHz to 20 GHz. It is seen that the simple rational approximation in (5.6) is enough to model the first thickness resonance quite accurately. On the contrary, the simpler model based on the approximation $\tan(x) \approx x$ is much less accurate.

This problem was also solved with straightforward discretization of the fields inside the coating and the conducting backing. Based on numerical experiments, six times denser mesh ($\Delta x = 0.333$ mm) is required for this particular problem to obtain similar accuracy as with the SIBC approach if the fields are directly discretized with a uniform mesh. Thus, the equivalent problem space in terms of cells increases by a factor of six to 1200 cells, plus the space required for the coating and the conductor backing. Here, six cells are enough to resolve the fields inside the coating. Since the fields decay exponentially in the lossy conductor, the infinite conductor backing can be modeled as a finite structure spanning 60 cells in FDTD. Obviously, although the analytical SIBC is for infinite half-spaces, it can be applied to modeling of finite structures.

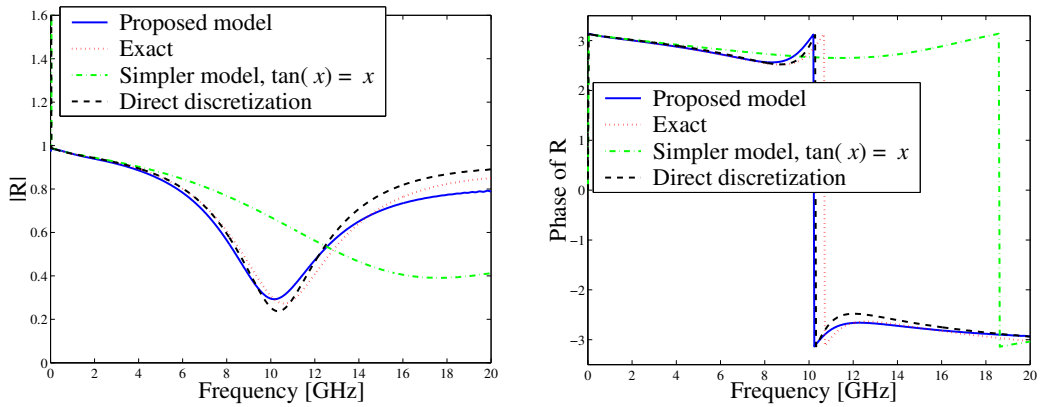

(a) (b)

Figure 5.3: (a) Magnitude of the reflection coefficient. Parameters of the coating: $d = 1$ mm, $\epsilon'_{c,r} = 30$, $\sigma_c = 0.4$ S/m. Parameters of the conductive material: $\epsilon'_{m,r} = 5$, $\sigma_m = 80$ S/m. The small ripples at higher frequencies do not indicate instability of the method. They appear because the FDTD mesh is very coarse (7.5 cells per free space wavelength at 20 GHz). The precise shape of the excitation pulse also affects the results. (b) Phase of the reflection coefficient.

In such situations, one must be assured that the fields decay enough within the structure. For highly conducting backings, the SIBC technique is applicable for relatively small structures with negligible difference as compared with structures having infinite backings.

The CPU times of these two approaches were compared. The simulation using the proposed SIBC technique took 3.0 seconds, 1.9 seconds of which were consumed to Prony's method and just 1.1 seconds were enough for the definition of variables and time-marching. The simulation with the direct discretization method took 15.0 seconds. We will see that the differences are more prominent in 2D problems.

As the last example in the frequency domain, we consider the case when $d = 2$ mm, $\epsilon'_{c,r} = 10$, $\sigma_c = 0.1$ S/m, $\epsilon'_{m,r} = 1$, $\sigma_m = 0.5$ S/m. The magnitude and the phase of the reflection coefficient are presented in Figures 5.4 a) and 5.4 b). Again, the agreement is very good for smaller frequencies and slightly worse for higher frequencies.

Here, the direct calculation using the direct discretization is performed with four times denser mesh ($\Delta x = 0.5$ mm) than the computation based on the proposed SIBC model. The conducting backing can be modeled as a finite structure with a thickness $120\Delta x = 6$ cm.

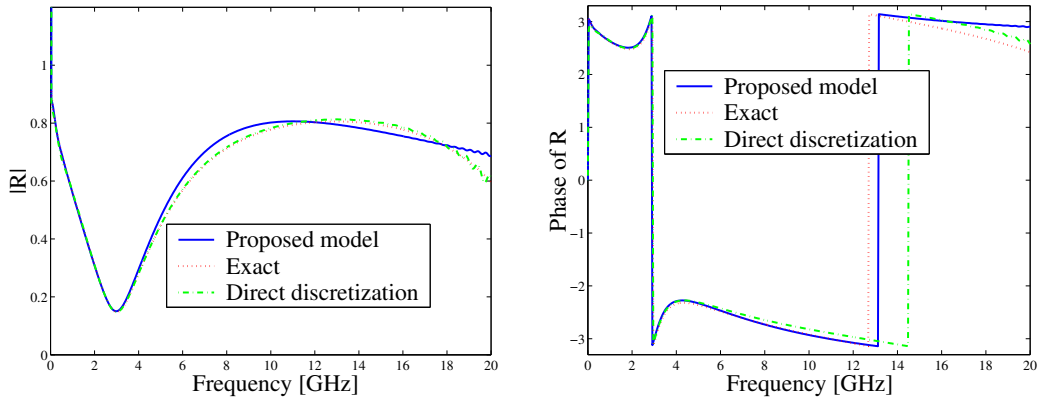

(a) (b)

Figure 5.4: (a) Magnitude of the reflection coefficient. Parameters of the coating: $d = 2$ mm, $\epsilon'_{c,r} = 10$, $\sigma_c = 0.1$ S/m. Parameters of the conductive material: $\epsilon'_{m,r} = 1$, $\sigma_m = 0.5$ S/m. (b) Phase of the reflection coefficient. Four times sparser mesh can be used with the proposed technique than with the direct discretization approach to obtain roughly similar level of accuracy.

5.5.2 Line Current in Two Dimensions, Oblique Incidence

Next we consider the problem of a line current radiating a cylindrical wave over a coated material body. We compare our simulation results with the exact results directly in the time domain. The analytical time domain waveforms at a given point on the interface can be calculated by representing the incident cylindrical wave as a sum of plane waves in the frequency domain, integrating over the interface, and taking the inverse Fourier transform. The plane wave expansion technique can be found in [28]. The FDTD model was implemented into a 2D FDTD program, with field components H_x,H_y, and E_z, and a z-polarized excitation (TE-polarization). The spatial cell size is $\Delta x = \Delta y = 1.5$ cm, and the time step is equal to the Courant stability limit: $\Delta t = \Delta x/(\sqrt{2}c_0)$. The time dependence of the point excitation is the same as in the first example, with $\tau_1 = 40\Delta t$, $\tau_2 = 12\Delta t$. The fields are calculated at points, where the incidence angle is oblique. Different angles of incidence will be studied.

Coatings on Semiconducting Surfaces

Here, the model in its most general form is examined. Let the line current be located at the distance $20\Delta y = 30$ cm from the interface. In the first example, the fields are calculated on the interface, $15\Delta x = 22.5$ cm away from the point just below the source. Thus, the angle of incidence for the results in Figure 5.5 a) is 36.9 degrees, while the results in Figure 5.5 b) are for the angle of incidence equal to 53.1 degrees (the source is located at the distance

$15\Delta y = 22.5$ cm from the interface and the fields are calculated at the distance $20\Delta x = 30$ cm to the x-direction from the source).

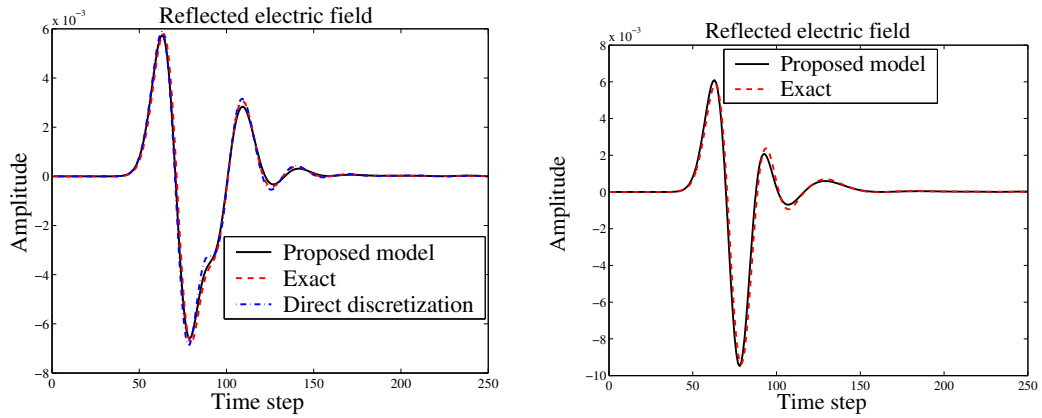

(a) (b)

Figure 5.5: (a) Reflected waveform at the observation point. Parameters of the coating: $d = 1.5$ cm, $\epsilon'_{c,r} = 20$, $\sigma_c = 0.1$ S/m. Parameters of the conductive backing: $\epsilon'_m = 1$, $\sigma_m = 10$ S/m. (b) Parameters of the coating: $d = 3.0$ cm, $\epsilon'_{c,r} = 15$, $\sigma_c = 0.2$ S/m. Parameters of the conductive backing: $\epsilon'_{m,r} = 2$, $\sigma_m = 3$ S/m. Despite the oblique angle of incidence, the agreement with the exact results is very good.

The reflected waves in the time domain are displayed in Figure 5.5 a). The parameters of the coating are: $d = 1.5$ cm, $\epsilon'_{c,r} = 10$, $\sigma = 0.1$ S/m, and the parameters of the conducting backing are $\epsilon'_{m,r} = 1$, $\sigma_m = 10$ S/m. The agreement with the exact results is excellent. The results in Figure 5.5 b) have been calculated with the following parameters: $d = 3.0$ cm, $\epsilon'_{c,r} = 15$, $\sigma_c = 0.2$ S/m, $\epsilon'_{m,r} = 2$, $\sigma_m = 3$ S/m. Again, the proposed model yields very accurate results for incidence angle equal to 53.1 degrees.

Let us discretize the fields within the coating and the conductor in the usual fashion using five times denser mesh: $\Delta x = \Delta y = 0.3$ cm. The reflected field using this technique is plotted in Figure 5.5 a). The required CPU time to run the total field FDTD code using the present impedance boundary condition is 3.1 s, while the CPU time with the direct approach is much longer: 458.3 s or 7.64 min. The computation lattice has the size 100×80 square cells when the SIBC is used, and 500×400 square cells when direct the discretization approach is used. Every fifth electric field value from the time domain data from the larger simulation is recorded, enabling the data to be plotted in Figure 5.5 a). Also, the amplitude of the waves has to be corrected by a factor of five due to the finer grid. Evidently, huge reduction in the computation time is achievable already in this relatively small 2D problem. Even more significant computational benefits would be obtained in large 3D problems.

Obviously, the direct approach requires roughly $5 \times 5 = 25$ times more memory in this 2D example than the SIBC approach. The exact factor can be slightly

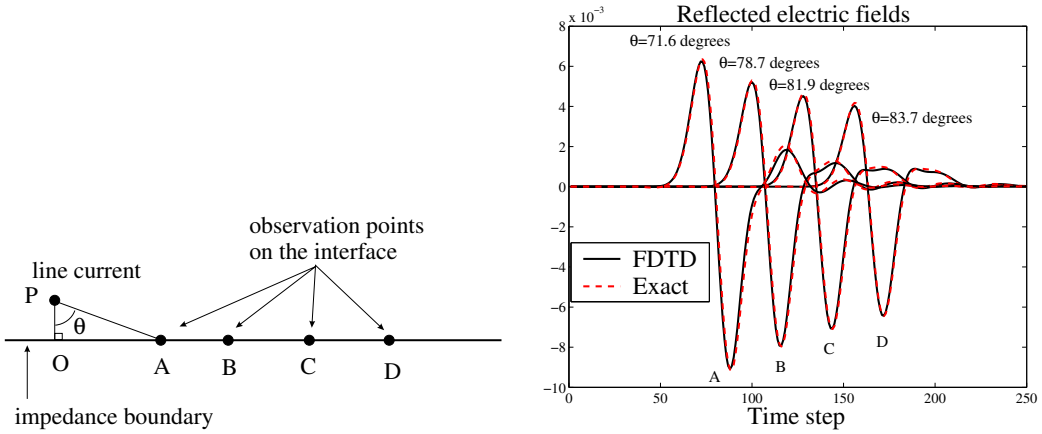

(a) (b)

Figure 5.6: (a) The problem geometry to study the performance of the model near grazing incidence. P denotes the position of the source and O is the point on the interface under the source. The reflected electric fields are observed at points A,B,C and D. OP= $10\Delta y$, OA= $30\Delta x$, OB= $50\Delta x$, OC= $70\Delta x$, OD= $90\Delta x$. (b) The reflected electric fields at different observation points on the interface. The proposed model is seen to be accurate also near grazing incidence.

smaller, because extra variables have to be defined on the impedance boundary. Typically, the number of boundary cells is a relatively small fraction of the total number of cells in the discrete space. Therefore, the additional cost of defining extra variables on the impedance boundary is indeed very small, especially in 3D problems.

We will now study how the model performs near grazing incidence. Towards this objective, we observe the reflected electric fields at different points on the air-coating interface, corresponding to different angles of incidence [see Figure 5.6 a)]. The distance of the source from the interface is now decreased to $10\Delta y = 15$ cm to keep the computational domain smaller for faster calculation. The simulated and the analytical waveforms at the observation point A,B,C, and D are plotted in Figure 5.6 b). We see in Figure 5.6 b) that the proposed model is very accurate also near grazing incidence. The time delays and the decaying amplitudes of the pulses corresponding to the increasing distance from the source are evident in Figure 5.6 b).

The validity of the Prony's method in this particular problem is seen in Figure 5.7 a), where the analytical impulse response and the series representation of it are presented as functions of the discrete time step. The impulse responses for the 1D problem, the results of which were displayed in Figure 5.2, are shown in Figure 5.7 b). The agreement is very good indeed.

The surface impedance is quite sensitive to the change of the permeability of the coating. Let us examine this case by letting the relative permeability of the coating to be $\mu_r = 1.2$, other parameters are as in Figure 5.5 a). The

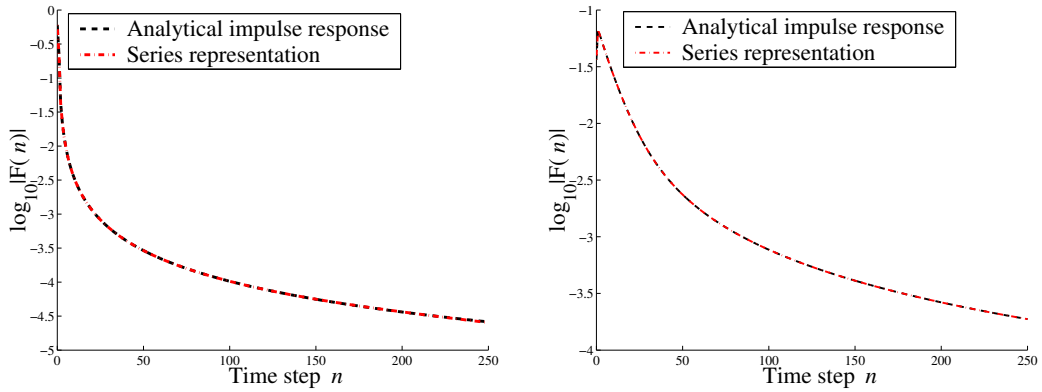

(a) (b)

Figure 5.7: (a) The discrete impulse response ($\sigma_m = 10$ S/m, $\epsilon_{m,r} = 1$), calculated directly with numerical integration, and as a series of exponential functions according to Prony's method. Obviously, the analytical impulse response can be very accurately represented as a series of exponential functions. The number of terms in the series is $p = 20$. The matrix systems that needs to solved to obtain the coefficients β_l and γ_l can be close to singular, especially larger systems. Therefore, it is reasonable to keep the parameter p quite moderate to avoid unstable solutions. (b) The impulse responses for the 1D problem in 5.2 ($\sigma_m = 0.2$ S/m, $\epsilon_{m,r} = 1$). The number of terms is $p = 14$.

corresponding reflected electric field is shown in Figure 5.8 a). An extra hump appears in the reflected field near time step $n = 80$. We further change the relative permeability to $\mu_r = 1.5$, and the agreement of the simulated and the analytical results in Figure 5.8 b) is seen to be slightly worse than in Figure 5.8 a). This is not surprising: the coating is already electrically so thick that the approximation of the impedance function matches worse with the exact impedance function.

The analytical SIBC was derived considering the normal incidence. However, it is expected to produce accurate results if the material coating and the metal backing are electrically dense enough, as in the previous example. Let us now study numerically how the model performs if the coating is electrically thin or both the coating and the metal backing are just air. Let the coating be 1.0 cm thick and have the parameters $\epsilon'_{c,r} = 2$ and $\sigma_c = 0.1$ S/m. The peak of the spectrum of the incident wave occurs at $f_p = 0.53$ GHz so that the imaginary part of the relative permittivity at the peak frequency f_p is equal to -3.4. Obviously, the coating is electrically rather thin: at the peak frequency we have $\sqrt{|\epsilon'_{c,r}|}k_p d \approx 0.22$ (the wavenumber in free space at f_p is denoted by k_p). The parameters of the backing are $\epsilon'_{m,r} = 2$, $\sigma_m = 1$ S/m. Figure 5.9 a) shows that the simulated reflected electric field agrees well with the analytical result. The positions of the source and the observation point are the same as in the previous example.

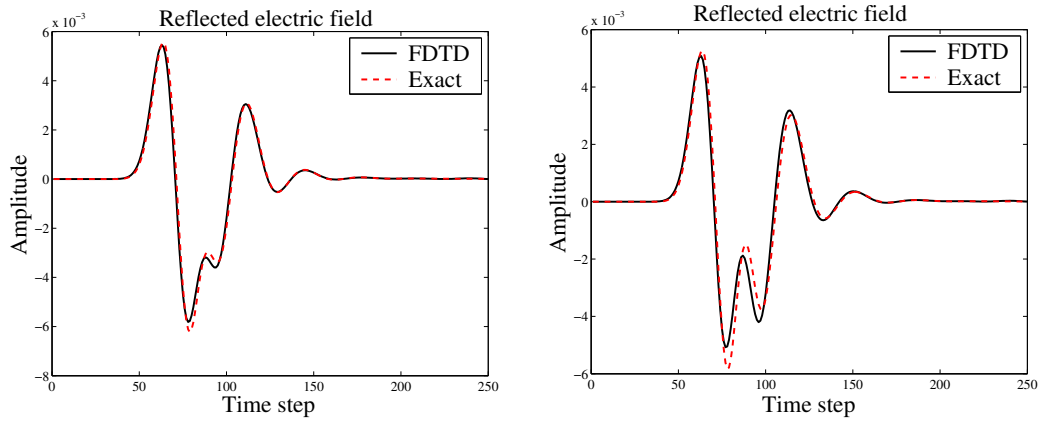

(a) (b)

Figure 5.8: (a) Reflected waveform at the observation point. Parameters are as in Figure 5.5 a), except that the relative permeability of the coating is $\mu_r = 1.2$. (b) Reflected waveform at the observation point. Parameters as in Figure 5.5 a), except that the relative permeability of the coating is $\mu_r = 1.5$. The reflected wave becomes more oscillatory, and the accuracy is slightly worse.

Reduction to an Absorbing Boundary Condition

Here we demonstrate that the model properly reduces to an *absorbing boundary condition*. Suppose now that the coating is removed and the backing consists of free space. For this purpose, we choose $\epsilon'_{c,r} = 1$, $\sigma_c = 0$ S/m and $\epsilon'_{m,r} = 1$, $\sigma_m = 0$ S/m. An absorbing boundary condition, valid for normal incidence, should be obtained in this case. We compare the results of the proposed model with the Mur first order analytical ABC [44] in Figure 5.9 b). It is seen that the proposed model reduces to an ABC that is quite similar to the first-order Mur ABC in terms of performance, although the discretization details are different. In this case, when we actually simulate just empty space, it is expected that higher-order models would be more accurate. Any higher-order version of the present model should obviously be constructed so that the resulting ABC in the case of free space material parameters is considerably better than the first order Mur ABC.

Further confidence about the performance of the ABC is obtained with a 2D example problem, schematically shown in Figure 5.10. The point source is implemented exactly as in [4]. The spatial cell size and the time step are also the same as in [4]: $\Delta x = \Delta y = 1.5$ cm, $\Delta t = 0.9999\Delta t_c$, where Δt_c is the Courant stability limit. The local reflection error is calculated on the lower boundary of the lattice at time step $n = 80$ and it is plotted in Figure 5.11 a) as a function of the grid position along the lattice boundary. It is seen that the maximum local error with the present ABC is smaller than with the first order Mur ABC and larger than with the second order Mur ABC. A good measure of the overall quality of any ABC is obtained by integrating the reflected fields

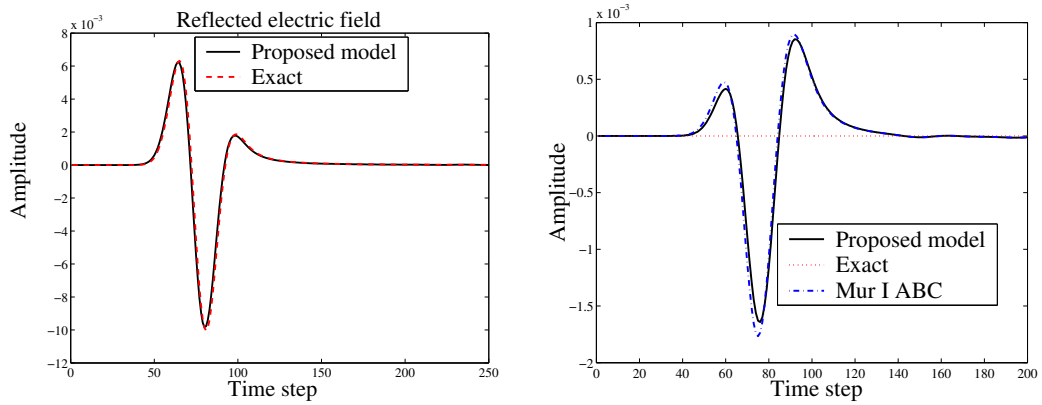

(a) (b)

Figure 5.9: (a) Reflected waveform at the observation point. Parameters of the coating: $d = 1.0$ cm, $\epsilon'_{c,r} = 2$, $\sigma_c = 0.1$ S/m. Parameters of the conductive backing: $\epsilon'_{m,r} = 2$, $\sigma_m = 1$ S/m. Very good correspondence with the exact result is obtained also for this electrically thin coating at oblique incidence. (b) The coating is removed and the backing is free space. The reflected electric field magnitude decreases and an absorbing boundary condition is obtained.

over the whole spatial lattice. The results of this procedure are shown in Figure 5.11 b). It appears that the proposed SIBC model reduces to an ABC, which is better than the first order Mur ABC but worse than the second order Mur ABC. At early times in the simulation, the present ABC reflects more than the first-order Mur ABC. However, the reflected error power with the present method becomes smaller than with Mur I after time step $n \approx 60$.

Reduction of the Model to Conducting Bodies Without Coatings

An interesting special case occurs if the coating is removed, that is $\epsilon'_{c,r} = 1$, $\sigma_c = 0$ S/m, and only the conducting backing is left. An FDTD model for this case has been introduced by Maloney and Smith in [7]. The results in Figure 5.12, calculated for two different sets of parameters for the metal body, verify that the proposed model gives similar results as the model by Maloney and Smith in the special case when the coating is removed. The agreement with the exact results is good. The computational savings in modeling conducting structures using impedance boundary conditions are discussed in [7, 8].

Coatings on Ideally Conducting Surfaces

Finally, we study the case when the coating is present and the backing is a perfect electric conductor (PEC). We compare with the exact results and with the model in chapter 4 by letting $\sigma_m \longrightarrow \infty$ in the present model. The re-

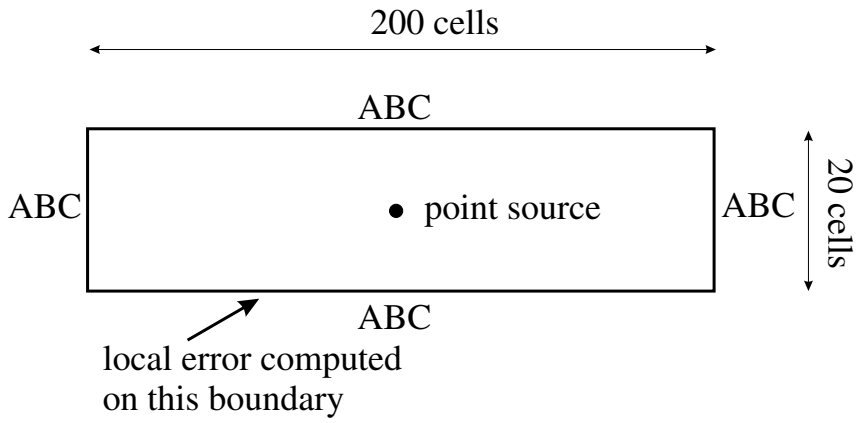

Figure 5.10: A 2D test problem to test the performance of the ABC, which can be obtained from the proposed impedance boundary condition. The excitation is a short pulse, implemented as a hard source in FDTD (i.e. the time dependence of the electric field E_z is fixed in a single grid point).

sults in Figure 5.13 are for the angle of incidence equal to 36.9 degrees. It is interesting to see that the proposed first-order model yields almost as accurate results as the higher-order model in [50]. The coatings here are already electrically rather thick, but if still thicker coatings need to be modeled, the higher-order model in [50] should be employed with a more accurate rational approximation.

Comparison of results in Figures 5.5 a) and 5.13 a) reveals that the oscillations after the first two peaks are smaller in Figure 5.5 a) than in 5.13 a). The difference could have been anticipated; the lossy backing present in the simulation of Figure 5.5 a) suppresses the waves. For the coating ($\epsilon'_{c,r} = 100$, $\sigma_c = 0.01$ S/m) on PEC-backing [results of the FDTD model in Figure 5.13 b)], the differences in the computational efficiency between the SIBC model and the direct discretization technique are even more prominent than in the earlier example. This is because the coating here is electrically thick *and* physically three times thinner than in the earlier example [Figure 5.5 a)]. The present SIBC method requires only 1.31 seconds of computation. The higher-order model of [50] takes just 0.86 seconds of computation, since the discrete scheme is slightly simpler in the case of PEC-backings and fewer auxiliary variables are required than in the more general model considered in this paper. The use of 18 times finer mesh requires 85.8 minutes of computation with the direct approach. The computation lattice is 40×50 square cells with the SIBC method and 900×720 square cells with the direct approach. Hence, approximately 324 times more memory is required to store the fields with the direct approach than with the SIBC approach. A smaller lattice for the SIBC code was chosen than in the previous example to keep the calculation time of the direct approach reasonable. In fact, the direct approach would require even finer mesh to obtain similar accuracy as the SIBC model in Figure 5.13 b). The results of the direct technique are not shown in the figure to maintain clarity.

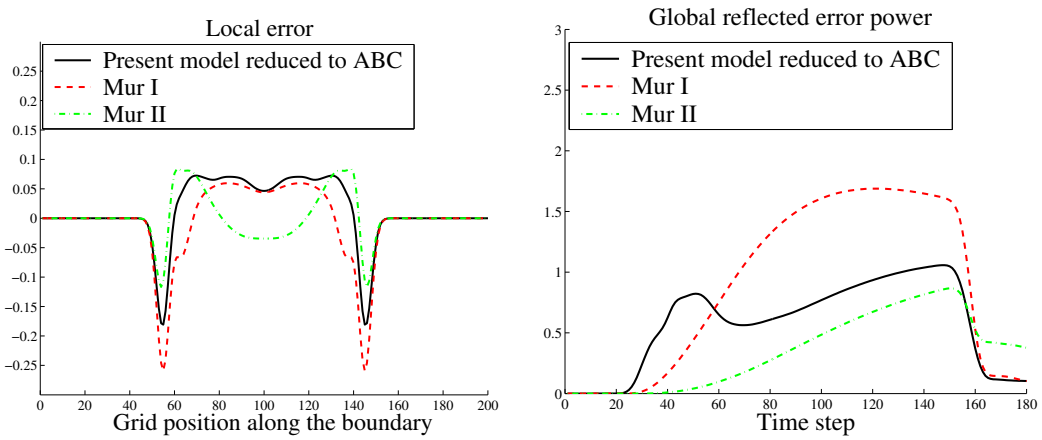

(a) (b)

Figure 5.11: (a) The local reflection error along the lattice boundary. (b) The global reflected error power as a function of time.

To be assured that the model works well also in the case of electrically thin coatings, we show one more example with the parameters $d = 1.0$ cm, $\epsilon'_{c,r} = 3$, and $\sigma_c = 0.01$ S/m. The reflected and the total field at the observation point on the interface (the angle of incidence is 36.9 degrees) as functions of time are shown in Figure 5.13. The simulated results using the proposed model agree very well with the analytical results and the results of the higher-order model [50].

As in the previous chapter, we also verify that the model developed for dispersive coatings is valid. Consider first a coating with Lorentzian parameters. The source is 20 cells above the interface (OP= $20\Delta y$), and OA= $15\Delta x$. Reflected electric fields as functions of time for coatings of Lorentz and Drude type are shown in Figure 5.15. The agreement was found to be good also near grazing incidence.

Based on the numerical experiments with the proposed model, we conclude that the proposed model is suitable for accurate modeling of electrically thin and relatively thick coatings on dielectric and conductive materials, that can be electrically dense or sparse. It is stressed that the model presented in this chapter can be directly applied in a general 3D situation if an orthogonal mesh is used.

5.6 Conclusions

A new accurate SIBC-based FDTD model for dielectric and conductive material layers with dielectric and conductive backings has been presented and verified by comparison with analytical results. The numerical results show

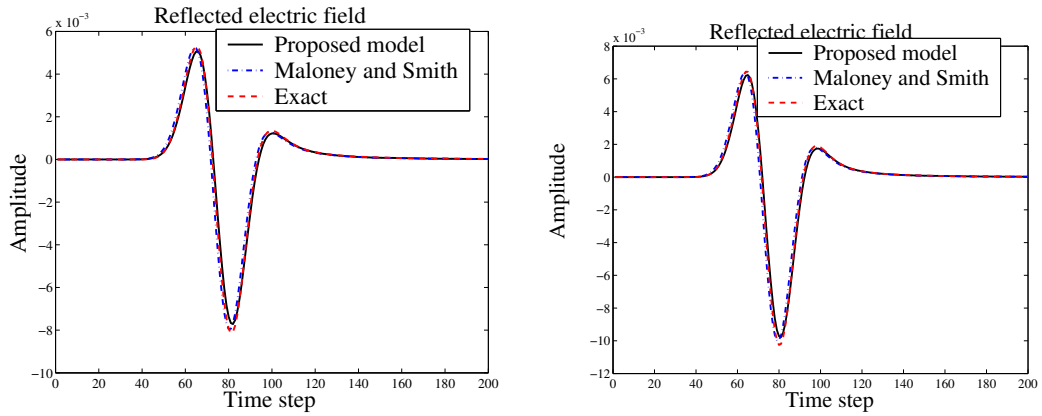

(a) (b)

Figure 5.12: (a) Reflected waveform at the observation point. Parameters of the conductive material: $\epsilon'_m = 1$, $\sigma_m = 0.3$ S/m. (b) Reflected waveform at the observation point. Parameters of the conductive material: $\epsilon'_m = 5$, $\sigma_m = 1.0$ S/m. Evidently, the proposed model yields similar results as the method by Maloney and Smith in the special case when the coating is removed.

that despite the first-order SIBC was used, which is exact only for the normal incidence, the model is very accurate also near grazing incidence provided that the materials to be simulated do not have negligible electrical density. Also in the extreme case when the simulated materials are just free space, the proposed model properly reduces to an absorbing boundary condition, although the resulting ABC is a simple first-order ABC. The proposed model accounts for the first thickness resonance of the coating, enabling accurate numerical modeling of many practical coatings. The suggested FDTD model was shown to properly reduce to some existing models in the important special cases where we simulate an empty space, or the coating is absent or the conductor backing consists of a perfect electric conductor. The computational savings obtained using the proposed model as compared to the use of direct discretization techniques were discussed and found to be significant.

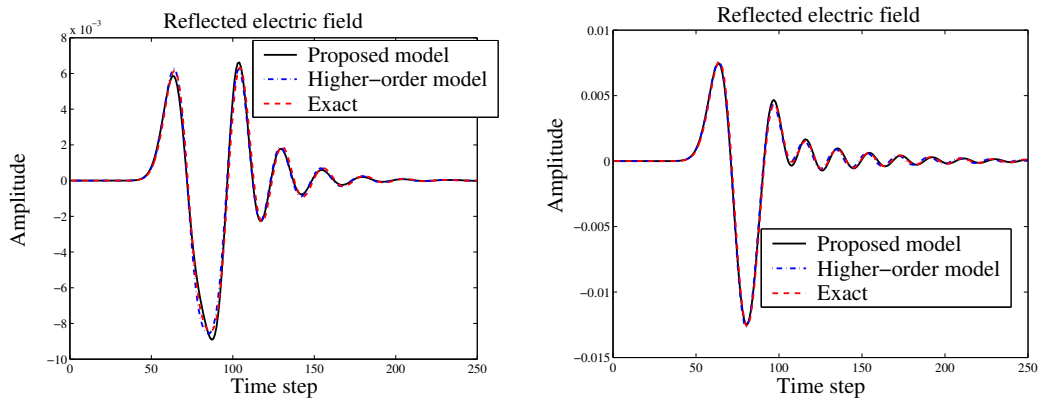

(a) (b)

Figure 5.13: (a) Reflected waveform at the observation point. Parameters of the coating: $d = 1.5$ cm, $\epsilon'_{c,r} = 20$, $\sigma_c = 0.1$ S/m. Perfectly conducting backing. (b) Parameters of the coating: $d = 0.5$ cm, $\epsilon'_{c,r} = 100$, $\sigma_c = 0.01$ S/m. Perfectly conducting backing. The proposed model correctly reduces to an existing model for coatings on perfect conductors (the discretization details are slightly different). The proposed first-order model is almost as accurate as the higher-order model introduced in [50], even though a simpler rational approximation is used here than in [50].

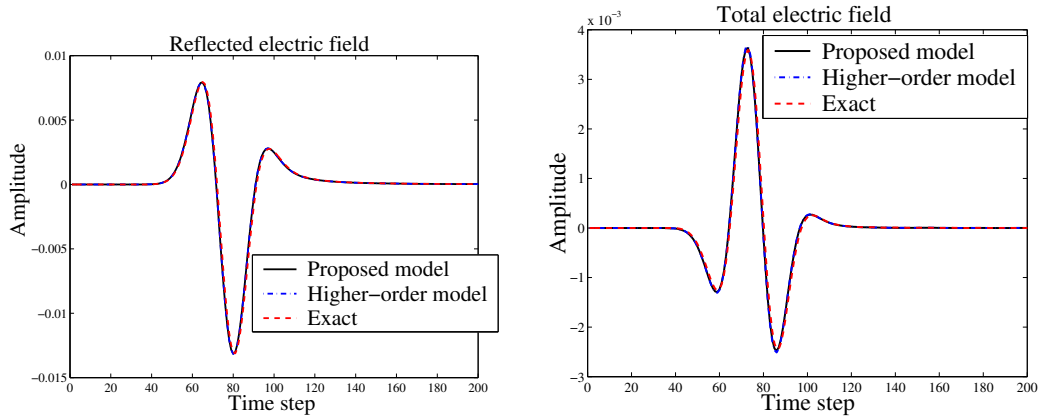

(a) (b)

Figure 5.14: (a) Reflected waveform at the observation point. Parameters of the coating: $d = 1.0$ cm, $\epsilon'_{c,r} = 3$, $\sigma_c = 0.01$ S/m. Perfectly conducting backing. (b) Total electric field at the observation point. The results of the proposed model, the higher-order model and the analytical calculation are almost indistinguishable.

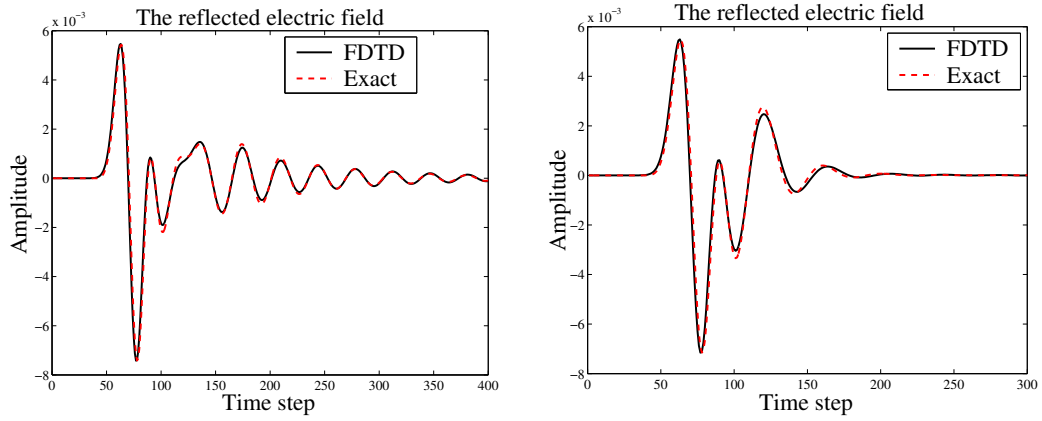

(a) (b)

Figure 5.15: (a) Reflected waveform at the observation point. Parameters of the Lorentzian coating: $d = 2.0$ cm, $\epsilon_1 = 20$, $\beta = 2.5 \cdot 10^{19}$ 1/s^2, $\omega_0 = 5.0 \cdot 10^9$ 1/s, $\gamma = 1$, $\delta = 2.0 \cdot 10^8$ s. Parameters of the conductor backing: $\epsilon_{m,r} = 1$, $\sigma_m = 4$ S/m. Similar level of agreement was observed also for the total electric field. (b) Reflected waveform at the observation point. Parameters of the Drude coating: $d = 2.0$ cm, $\epsilon_1 = 20$, $\beta = 2.5 \cdot 10^{19}$ 1/s^2, $\omega_0 = 0$ 1/s, $\gamma = 1$, $\delta = 2.0 \cdot 10^8$ s. Parameters of the conductor backing: $\epsilon_{m,r} = 1$, $\sigma_m = 4$ S/m. Similar level of agreement was observed also for the total electric field. The Drude coating is obtained from the Lorentzian coating simply by setting $\omega_0 = 0$ 1/s.

Chapter 6

Subcell Model for Dispersive Layers

An alternative technique to model electrically thin material layers is introduced in this chapter. The model is more useful than the SIBC model in cases, where there is no metal backing. The model is also better than the SIBC model if the material parameters of the layer have multiple pole pairs. Again, the model is verified with several numerical examples by comparison with analytical results.

6.1 Introduction

There is one main reason to use subcell techniques rather than SIBC methods for frequency-dispersive layers: the application of the SIBC approach for more general dispersive layers, where there is no metal backing, leads to transition conditions, which are very complicated to accurately implement into FDTD method.

The subcell technique is clearly an efficient approach, since coarse mesh may be used, and the memory requirements remain almost unchanged after the insertion of a layer provided that the layer fills only a small amount of the computation space. Some models for dielectric and conductive layers based on subcell techniques can be found in the literature. Tirkas and Demarest proposed a model for thin dielectric layers in [15]. Maloney and Smith took a slightly different approach in [16] when modeling dielectric and conductive layers. Some other models have also been suggested [17, 18, 19], but they have been verified by Maloney and Smith in [39] to be less accurate than the models by Maloney and Smith and by Tirkas and Demarest. A disadvantage of the subcell method is its inability to model electrically thick layers. In such situations, one should resort to SIBC's or to direct discretization methods. A review of direct discretization algorithms has been presented by Young in [51]. Notice that the previous subcell techniques [15, 16, 17, 18, 19] are not

applicable to dispersive layers.

In this chapter, we formulate a new subcell technique, which allows modeling quite general dispersive layers, possibly having multiple pole pairs. The proposed model reduces to the model by Maloney and Smith in the case of dielectric and conductive layers. The new model is formulated in the general 3D case in section 6.2, and validation studies are conducted with 1D and 2D FDTD programs in section 6.2 both in time and frequency domains. Quite good agreement with the analytical results is observed.

6.2 The Subcell Technique for Dispersive Layers

The basic idea of the model is quite simple: we will average the electric and magnetic flux densities so that they will simulate the presence of a thin dispersive layer. The layer is assumed to be located in free space, although this need not necessarily be the case. Both tangential and normal to the layer field components will be affected by the model. Consider deriving update equations for the tangential magnetic field components in the vicinity of a dispersive layer of thickness d and with the frequency-dependent isotropic permeability

$$\mu(\omega) = \mu_0 \left(\mu_\infty + \sum_{k=1}^{P} \frac{\beta_{m,k}}{\omega_{0m,k}^2 - \gamma_{m,k}\omega^2 + j\delta_{m,k}\omega} \right), \tag{6.1}$$

where P is the number of pole pairs and the subscript k refers to the k'th pole pair. The subscript m refers to magnetic layer. An appropriate choice of the parameters in the above expression allows us to obtain a layer of Lorentz, Debye or Drude type as special cases. Similarly, the expression for the permittivity is taken to be of the form

$$\epsilon(\omega) = \epsilon_0 \left(\epsilon_\infty + \sum_{k=1}^{P} \frac{\beta_{e,k}}{\omega_{0e,k}^2 - \gamma_{e,k}\omega^2 + j\delta_{e,k}\omega} \right) \tag{6.2}$$

with analogous definitions of the parameters as above. Let the layer partially fill a single plane of FDTD cells in the 3D FDTD lattice. A slice of the FDTD lattice in xy-plane in shown in Figure 6.1 a). The geometry of a one-dimensional interface problem, which is considered later, is shown in Figure 6.1 b). If the volume fraction occupied by the layer is α, then we may calculate the averaged magnetic flux density inside the cells containing the dispersive layer according to $\mathbf{B} = \alpha\mu(\omega)\mathbf{H}_{\text{layer}} + (1-\alpha)\mu_0\mathbf{H}_{\text{free space}}$ with $0 \leq \alpha \leq 1$. Using the magnetic susceptibility $\chi_{m,k}(\omega)$ associated with the k'th pole pair, defined as

$$\chi_{m,k}(\omega) = \frac{\beta_{m,k}}{\omega_{0m,k}^2 - \gamma_{m,k}\omega^2 + j\delta_{m,k}\omega}, \tag{6.3}$$

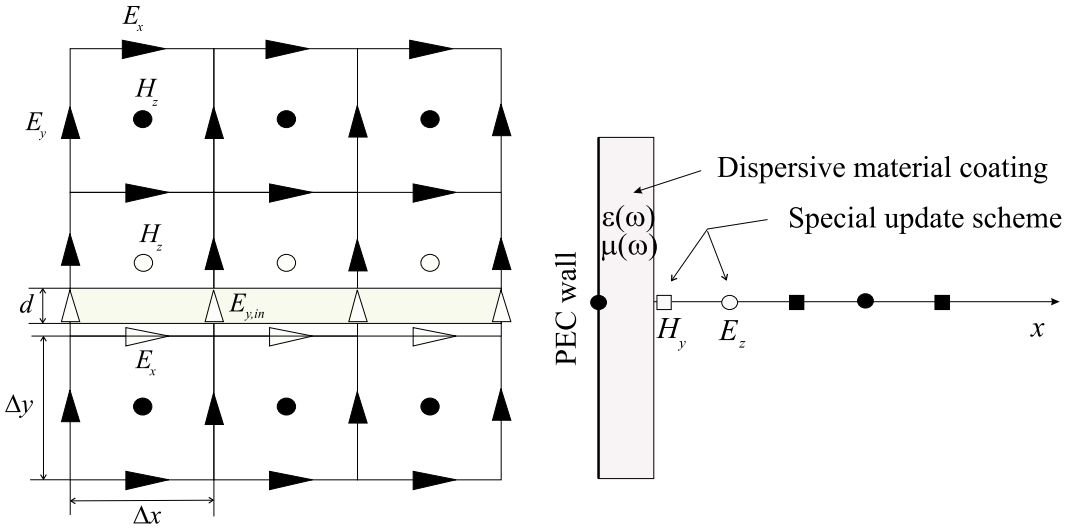

(a) (b)

Figure 6.1: (a) A slice of the FDTD lattice in the xy-plane. A special update scheme is developed for the field components denoted with non-filled objects. Extra variables are introduced for the field components normal to and inside the layer. (b) The problem geometry in a 1D problem. The reflection of a z-polarized pulse from a coated ideal conductor is studied.

we obtain the equation

$$\mathbf{B} = \alpha\mu_0 \left[\mu_\infty + \sum_{k=1}^{P} \chi_{m,k}(\omega) \right] \mathbf{H} + (1-\alpha)\mu_0 \mathbf{H}. \tag{6.4}$$

As an example, let us derive the update equation for the z-component of the tangential magnetic field [see Figure 6.1 a)]. The magnetization $M_{z,k}$ and the magnetic field H_z are related through the magnetic susceptibility according to

$$M_{z,k} = \mu_0 \chi_{m,k}(\omega) H_z \tag{6.5}$$

and the magnetic current $K_{z,k}$ may be expressed with the magnetization $M_{z,k}$ as

$$K_{z,k} = j\omega M_{z,k}. \tag{6.6}$$

From the z-component of the Faraday law, we obtain the equation

$$[1 + \alpha(\mu_\infty - 1)]\mu_0 \frac{\partial H_z}{\partial t} = -\mathbf{u}_z \cdot (\nabla \times \mathbf{E}) - \alpha \sum_{k=1}^{P} K_{z,k}. \tag{6.7}$$

The dot product of the curl and the unit vector $\mathbf{u}_z$ picks the z-component from the curl. The discrete form of equation (6.7) in integral form reads

$$\begin{aligned} H_z|^{n+1/2}_{i+1/2,j+1/2,k+1/2} &= H_z|^{n-1/2}_{i+1/2,j+1/2,k+1/2} - \frac{\Delta t}{[1+\alpha(\mu_\infty-1)]\mu_0}\{ \\ &\cdot \quad \alpha\Delta y\left(E_{y,in}|^n_{i+1,j_*,k+1/2} - E_{y,in}|^n_{i,j_*,k+1/2}\right) \\ &+ \quad (1-\alpha)\Delta y\left(E_y|^n_{i+1,j+1/2,k+1/2} - E_y|^n_{i,j+1/2,k+1/2}\right) \\ &- \quad \Delta x\left(E_x|^n_{i+1/2,j+1,k+1/2} - E_x|^n_{i+1/2,j,k+1/2}\right) \\ &- \quad \frac{\alpha\Delta t}{[1+\alpha(\mu_\infty-1)]\mu_0}\sum_{k=1}^{P} K_{z,k}|^n_{i+1/2,j+1/2,k+1/2}\Bigg\}. \end{aligned} \tag{6.8}$$

By j_* we emphasize that $E_{y,in}$ lies within the layer, between the grid locations j and $j+1/2$. Using the definitions for the magnetization $M_{z,k}$ in (6.5) and for the magnetic current $K_{z,k}$ in (6.6) we obtain the auxiliary equation

$$\omega^2_{0m,k}M_{z,k} + j\omega\gamma_{m,k}K_{z,k} + \delta_{m,k}K_{z,k} = \mu_0\beta_{m,k}H_z. \tag{6.9}$$

The update equations for the auxiliary variables $K_{z,k}$ and $M_{z,k}$ for any k can now be obtained by discretizing equations (6.9) and (6.6):

$$\begin{aligned} K_{z,k}|^{n+1}_{i+1/2,j+1/2,k+1/2} &= \frac{2\gamma_{m,k}-\delta_{m,k}\Delta t}{2\gamma_{m,k}+\delta_{m,k}\Delta t}K_{z,k}|^n_{i+1/2,j+1/2,k+1/2} \\ &+ \frac{2\mu_0\beta_{m,k}\Delta t}{2\gamma_{m,k}+\delta_{m,k}\Delta t}H_z|^{n+1/2}_{i+1/2,j+1/2,k+1/2} \\ &- \frac{2\omega^2_{0m,k}\Delta t}{2\gamma_{m,k}+\delta_{m,k}\Delta t}M_{z,k}|^{n+1/2}_{i+1/2,j+1/2,k+1/2}, \\ M_{z,k}|^{n+3/2}_{i+1/2,j+1/2,k+1/2} &= M_{z,k}|^{n+1/2}_{i+1/2,j+1/2,k+1/2} \\ &+ \Delta t K_{z,k}|^{n+1}_{i+1/2,j+1/2,k+1/2}. \end{aligned} \tag{6.10}$$

Notice that in the limit $\alpha \longrightarrow 0$ with $\mu_\infty = 1$ the coupling between H_z and the auxiliary variables $K_{z,k}$ and $M_{z,k}$ disappears, and we obtain the usual update equation for the magnetic field H_z in free space, as required for consistency of the model. Also, if $\beta_{m,k} = 0$ for all k and $\mu_\infty = 1$ implying that the auxiliary variables are zero, leads to the usual update equations in free space.

The quantity $1+\alpha(\mu_\infty-1)$ can be regarded as the averaged relative permeability in the limit $\omega \longrightarrow \infty$. To get the update equation for the normal component of the magnetic field H_y, which is inside the layer, we need to replace $1+\alpha(\mu_\infty-1)$ with μ_∞ and set $\alpha = 1$ in the equations (6.8) and (6.10) above with appropriate changes in the subscripts. Then, $H_{y,in}$ (or $E_{y,in}$ in the subsequent verifications) inside the coating is involved in the calculation through the integral form of Maxwell's equations or the curl in equation (6.8) should be interpreted as to be evaluated with averaged quantities along each edge of the FDTD-cell.

The derivation of the update equations for the electric field components in the case of a layer in free space is quite analogous and is not shown here. However,

in the case when metal is coated with a layer, we must account for the fact that the tangential electric field decays to zero in the vicinity of the ideal conductor. This situation is most conveniently described in the 1D case. Suppose that there is an ideally conducting wall at $x = 0$ [see Figure 6.1 b)] and let the coating on the wall have thickness d. Let the electric field be polarized along the z-axis. The PEC wall implies that we have $E_z|_0 = 0$ all the time. The tangential magnetic field half-cell away from the PEC wall can be updated as described above. However, the simple averaging of the electric flux density D_z in the vicinity of the PEC wall is not a good approach.

To demonstrate how the PEC wall is accounted for, consider deriving the update equation for the field component $E_z|_1$ in the immediate vicinity of the coating. Usually, the fields are assumed to be piecewise linear across each FDTD cell. Hence, we make a very natural assumption that the electric field behaves linearly in the range $\Delta x/2 < x < 3\Delta x/2$ with the slope chosen so that a linear extrapolation to $x = 0$ would yield zero electric field. Thus, we assume that

$$E_z(x) = \frac{x}{\Delta x} E_z|_1. \tag{6.11}$$

Next, we calculate the spatially averaged electric flux density near the wall and use it to deduce the effective permittivity of the coating in the limit $\omega \longrightarrow \infty$. Integrating from $x = \Delta x/2$ to $x = 3\Delta x/2$ we obtain

$$\begin{aligned} D_z|_1 &= \frac{1}{\Delta x} \int_{\frac{\Delta x}{2}}^{\frac{3\Delta x}{2}} \epsilon_{\omega\to\infty}(x) \frac{x}{\Delta x} E_z|_1 \, dx \\ &= \epsilon_0 \left[\frac{9 - \epsilon_\infty}{8} + \frac{d^2}{2\Delta x^2}(\epsilon_\infty - 1) \right] E_z|_1 \\ &= \epsilon_0 \epsilon_{r,\infty,ave}(d, \epsilon_\infty) E_z|_1. \end{aligned} \tag{6.12}$$

This relation is utilized when updating the electric field near the boundary. The consistency requirements are easy to check: if $\epsilon_\infty = 1$, we have $\epsilon_{r,\infty,ave} = 1$ regardless of the layer thickness d and if $d = 0$, we obtain $\epsilon_{r,\infty,ave} = 1$ for $\epsilon_\infty = 1$. Notice that the above derivation is only necessary if the layer thickness $d > \Delta x/2$. For smaller thicknesses, magnetic properties of the layer are known to dominate the shape of the reflected waveform. This fact can be easily seen from the Leontovich SIBC, which takes the form

$$E_z = j\omega\mu(\omega) d H_y, \tag{6.13}$$

if the tangent function in the impedance $Z_s(\omega) = j\eta \tan(kd)$ is approximated with its argument: $\tan(kd) \approx kd$. Hence, we may use $\epsilon_{r,\infty,ave} = 1$ if $d < \Delta x/2$ and the wavelength inside the layer is not very small. In the next section, we will demonstrate a pulse reflection from a wall coated with a layer having a rather complicated frequency-dependence of the material parameters.

It was observed from numerical experiments that the conductivity of the layer may be approximated by simple averaging according to $\sigma_{ave} = \alpha\sigma$, where α is the volume fraction of the layer occupying the adjacent cells to $E_z|_1$. Thus,

for a coating of thickness d and conductivity σ, we obtain

$$\sigma_{ave} = \frac{d}{2\Delta x}\sigma \tag{6.14}$$

Introducing the electric polarization current $\mathbf{J}$ and polarization $\mathbf{P}$ we obtain the update equation for the electric field $E_z|_1$ next to the metal wall in 1D-case:

$$E_z|_1^{n+1} = \frac{2\epsilon_{r,\infty,ave}\epsilon_0 - \sigma_{ave}\Delta t}{2\epsilon_{r,\infty,ave}\epsilon_0 + \sigma_{ave}\Delta t} E_z|_1^n + \frac{2\Delta t}{\Delta x\left(2\epsilon_{r,\infty,ave}\epsilon_0 + \sigma_{ave}\Delta t\right)}\left(H_y|_{3/2}^{n+1/2} - H_y|_{1/2}^{n+1/2}\right) - \frac{2\alpha\Delta t}{2\epsilon_{r,\infty,ave}\epsilon_0 + \sigma_{ave}\Delta t}\sum_{k=1}^{P} J_{z,k}|_1^n, \tag{6.15}$$

where the magnetic field $H_y|_{1/2}$ in updated as described above. In equation (6.15) we use expressions (6.12) and (6.14) for the averaged permittivity and conductivity. The variables $J_{z,k}$ and $P_{z,k}$ are updated completely analogously to $K_{z,k}$ and $M_{z,k}$ in (6.10).

6.3 Verification of the Proposed Model

6.3.1 Pulse Reflection from a Coated Ideal Conductor

We start with a problem of a TE-polarized pulse reflecting from a metal wall coated with a dispersive layer. We consider a fixed set of material parameters of the coating, and calculate the numerical reflection coefficients and time-domain waveforms varying the thickness of the coating. The numerical results are then compared to the exact results.

Frequency-Domain Validation

Consider as an example a layer of a material whose relative permittivity and permeability are shown in Figure 6.2. The parameters are of the Lorentz type. The permittivity has one resonance, while the permeability has two resonances. The parameters for the permeability are $\mu_\infty = 1$, $\beta_{m,1} = 4 \cdot 10^{20}$ (rad/s)^2, $\beta_{m,2} = 1.25 \cdot 10^{21}$ (rad/s)^2, $\omega_{pm,1} = 2 \cdot 10^{10}$ (rad/s), $\omega_{pm,2} = 5 \cdot 10^{10}$ (rad/s), $\gamma_{m,1} = \gamma_{m,2} = 1$, $\delta_{m,1} = 5 \cdot 10^9$ rad/s, $\delta_{m,2} = 4 \cdot 10^9$ rad/s. The permittivity has parameters $\epsilon_\infty = 2$, $\beta_{e,1} = 9 \cdot 10^{20}$ (rad/s)^2, $\omega_{pe,1} = 3 \cdot 10^{10}$ rad/s, $\gamma_{e,1} = 1$, $\delta_{e,1} = 5 \cdot 10^8$ rad/s. The electrical conductivity is taken to be zero. The goal here is to demonstrate how the thickness of the coating affects the results. Hence, the above parameters are kept fixed and the thickness of the layer is varied in the numerical examples below.

The fields are recorded one cell away from the PEC boundary. Notice that a confident comparison of the phase of the reflection coefficient is only possible provided that the thickness of the layer is close to Δx, since the electric field on the air-coating interface is not available unless $d = \Delta x$. For the magnitude of the reflection coefficient, this is not critical in this 1D case. Only the magnitude of the reflection coefficient is shown for thinner coatings.

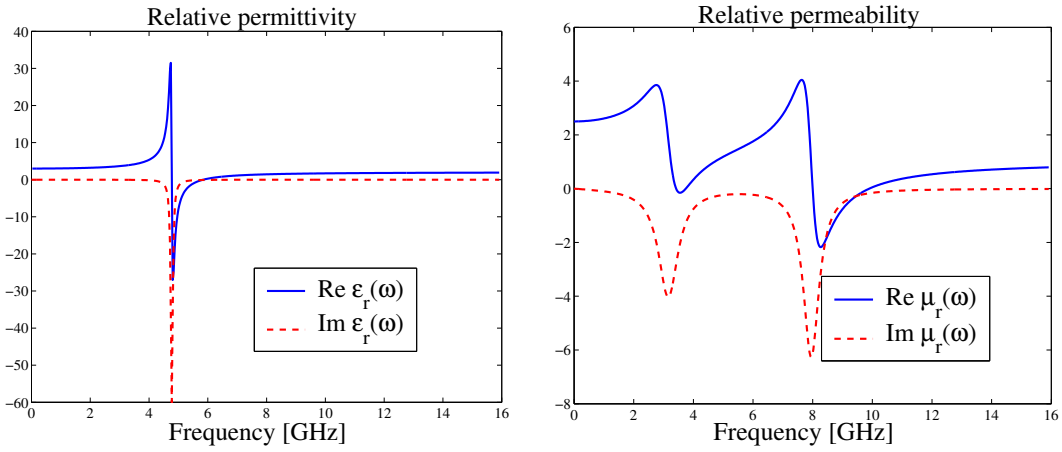

(a) (b)

Figure 6.2: (a) Relative permittivity of the coating. (b) Relative permeability of the coating.

The magnitude and the phase of the reflection coefficient in the case when $d = 0.9\Delta x = 1.8$ mm are shown in Figure 6.3. Rather good agreement with the exact results is obtained. In Figure 6.3 a), the largest discrepancy occurs near the second resonance, corresponding to the pole of the permittivity. The jump discontinuity of the phase of the reflection coefficient in Figure 6.3 b) occurs at slightly smaller frequency than it should. Anyway, every resonance of the layer is qualitatively very well and quantitatively rather accurately modeled.

Next we decrease the thickness of the coating, choosing $d = 0.5\Delta x = 1$ mm. The numerically calculated and the exact magnitude of the reflection coefficient as a function of frequency are shown in Figure 6.4 a). It is observed that the resonance associated with the permittivity is not so strong as in Figure 6.3 a). In Figure 6.4 a), there is almost zero reflection at about 8 GHz, the position of the second resonance of the permeability. Further decreasing the thickness of the coating, we set $d = 0.1\Delta x = 0.2$ mm. The result is presented in Figure 6.4 b). The resonance associated to the permittivity near 4.8 GHz has almost been smeared out, and the dips are not so deep as in the case of a thicker coating. These results show that the model works properly when the thickness of the coating is varied and also verifies that the magnetic properties of the coating dominate when the coating is electrically very thin. Simulations for smaller damping factors for permeability were made, and very good agreement was observed even in that case. However, a more realistic case, where the

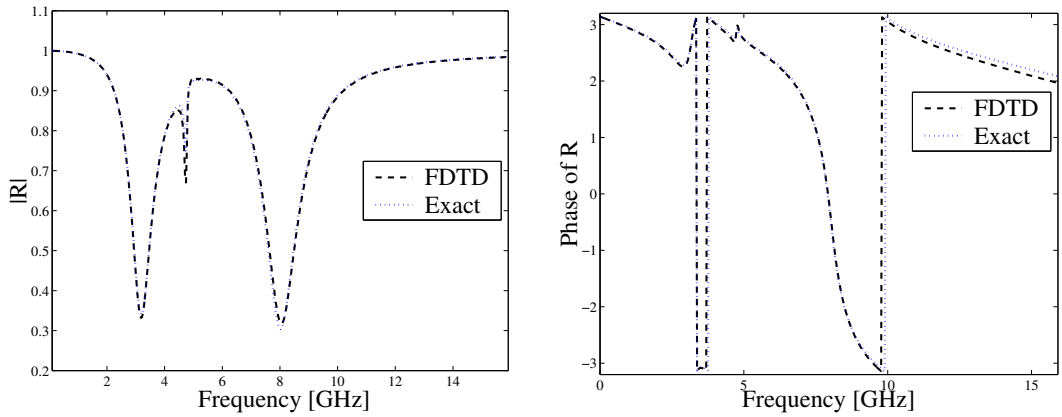

(a) (b)

Figure 6.3: (a) The magnitude of the reflection coefficient. (b) The phase of the reflection coefficient. The material parameters as a function of frequency are shown in Figure 6.2.

maximum real part of the permeability in the considered frequency range is about 4 was chosen as a numerical example.

Time-Domain Validation

We show some time domain waveforms for the cases considered above. The incident electric field is a differentiated gaussian pulse throughout the simulations. The exact reflected electric field on the interface as a function of time may be calculated via inverse Fourier transform. Thus, the integral

$$E_z^{ref}(t) = \frac{1}{\sqrt{2\pi}} \int_{-\infty}^{\infty} R(\omega) E_z^{inc}(\omega) e^{j\omega t}\, d\omega \tag{6.16}$$

must be evaluated. The total field is obtained by replacing $R(\omega)$ with $1 + R(\omega)$ in the expression above. The surface impedance model may be used to calculate the exact reflection coefficient. In this problem, the PEC-backed coating can be modeled with a surface impedance of the form

$$Z_s(\omega) = j\sqrt{\frac{\mu(\omega)}{\epsilon(\omega)}} \tan\left(\sqrt{\epsilon(\omega)\mu(\omega)}\omega d\right). \tag{6.17}$$

The exact reflection coefficient as a function of frequency is then obtained from

$$R = \frac{Z_s(\omega) - \eta_0}{Z_s(\omega) + \eta_0}, \tag{6.18}$$

where η_0 is the free space wave impedance. The material parameters in Figure 6.2 were used to calculate the results in Figures 6.5–6.6. The agreement with the exact results is seen to be good also in the time domain. It is seen that

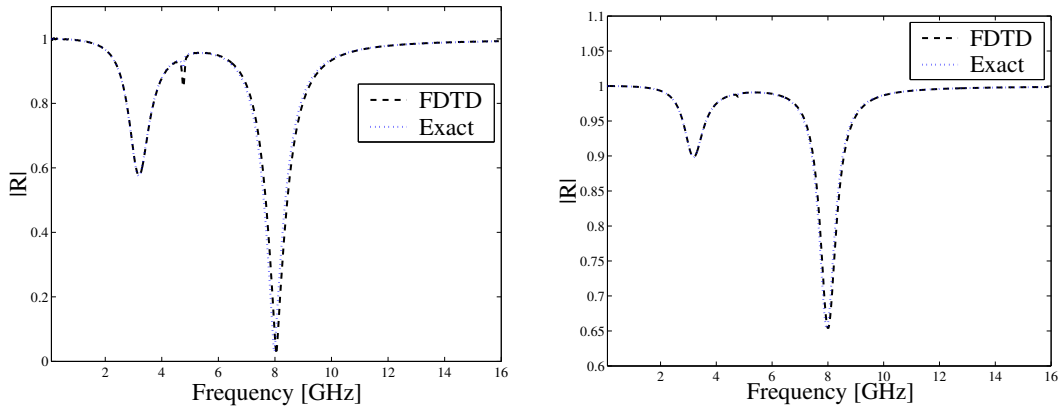

(a) (b)

Figure 6.4: (a) The magnitude of the reflection coefficient. Layer thickness $d = 1$ mm. (b) The magnitude of the reflection coefficient. Layer thickness $d = 0.2$ mm.

the oscillations of the reflected wave become smaller when the thickness of the coating is decreased. This is natural, since a PEC wall is obtained in the limit $d = 0$.

6.3.2 Cut-off Frequency of a Loaded Waveguide

First, consider a rectangular waveguide with the widths of the walls equal to $a = 30$ mm and $b = 15$ mm. Suppose there is a thin magnetic layer of thickness d along the broader wall in the middle of the waveguide. The permeability of the layer is taken to be of the Lorentz type with a single pole pair. In the lossless case, we may calculate the exact cut-off frequencies of this waveguide. Contrary to the previous example, we keep the thickness of the layer fixed and present a more detailed validation of the model by varying the material parameters and by comparing with the exact results. For a single pole-pair lossless Lorentz layer, there are three parameters to vary: μ_∞, $\beta_m = \omega_{pm}^2$ and ω_{0m}.

The problem geometries are shown in Figure 6.7. Before numerical examples, we present an analytical expression for the cut-off frequencies of the waveguide loaded with a dispersive layer. For the fundamental TE_{10}-mode to be considered here, the field distributions over the small height of the waveguide remain almost uniform for the components tangential to the layer. Hence, the approximate expression for the propagation constant (the cross section of the waveguide is uniform in the x-direction) is applicable [63]:

$$k_x = \sqrt{\omega^2 \frac{d\mu(\omega) + (b-d)\mu_0}{\frac{d}{\epsilon(\omega)} + \frac{b-d}{\epsilon_0}} - \left(\frac{\pi}{a}\right)^2}. \tag{6.19}$$

The cut-off frequency of the TE_{10}-mode is obtained by requiring that $k_x = 0$

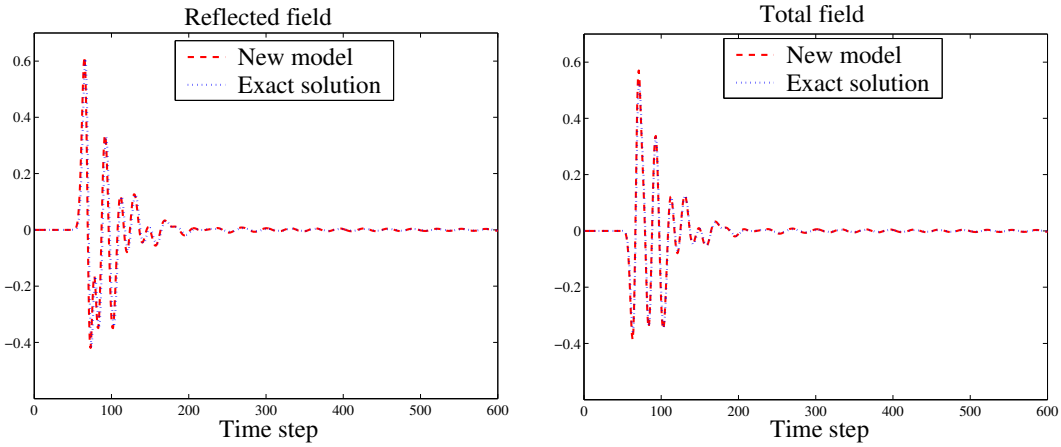

(a) (b)

Figure 6.5: (a) Reflected waveform on the boundary. $d = 1.8$ mm. (b) Total waveform on the boundary. $d = 1.8$ mm.

and solving for ω. Notice that the approximate analytical result does not see the position of the layer. However, the expression (6.19) is very accurate for the TE_{10}-mode, and reduces to the exact result for an empty waveguide if $\epsilon(\omega) = \epsilon_0$ and $\mu(\omega) = \mu_0$. Rigorous derivation of the exact cut-off frequency is omitted here, because it would lead to extremely long and tedious transcendental equations without significant increase of accuracy for the TE_{10}-mode. The cut-off frequency may be calculated in a 2D-FDTD program using, for instance, a differentiated gaussian pulse point excitation inside the waveguide, and recording the time domain waveforms at an observation point. The observed fields are transformed into the frequency domain and the peaks in the spectrum correspond to the cut-off frequencies of the different modes propagating in the waveguide.

The thickness of the layer is equal to $d = 0.25\Delta x = 0.25\Delta y = 0.375$ mm. Hence, we have discretized the cross section of the waveguide with a grid of 20×10 FDTD cells. We first take the permeability to be independent of the frequency and vary the relative permeability. The cut-off frequency of the TE_{10}-mode is seen to decrease with increasing permeability, as expected. The agreement with the analytical results is rather good: the maximum relative error in Figure 6.8 a) is about one percent.

The results for varying $\beta_m = \omega_{pm}^2$ are shown in Figure 6.8 b). Here, we fix $\mu_\infty = 1$ and the resonant frequency of the layer is chosen to be less than the cut-off frequency of the TE_{10}-mode of an empty waveguide. We have chosen $\omega_{0m} = 2 \cdot 10^{10}$ rad/s. The maximum relative error is less than one percent. In Figure 6.9 a), $\omega_{0m} = 4 \cdot 10^{10}$ rad/s, being larger than the cut-off of an empty waveguide ($\omega_{c,TE_{10}} = \pi \cdot 10^{10}$ rad/s). The result is seen to be clearly different from that in Figure 6.8 b).

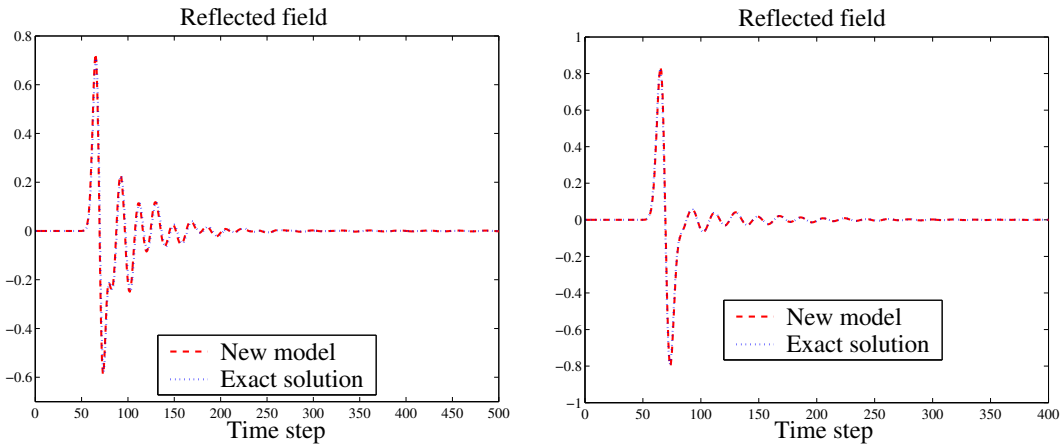

(a) (b)

Figure 6.6: (a) Reflected waveform on the boundary. $d = 1$ mm. (b) Reflected waveform on the boundary. $d = 0.2$ mm.

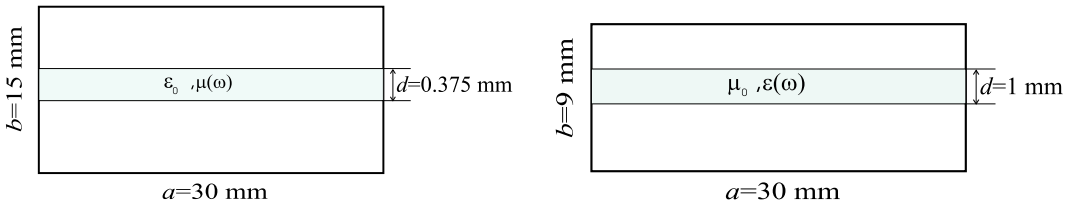

(a) (b)

Figure 6.7: (a) A cross-section of a rectangular waveguide with perfectly conducting walls loaded with a dispersive magnetic layer of the Lorentz type. (b) A cross-section of a rectangular waveguide loaded with a dispersive dielectric layer of the Lorentz type. The thickness of the layer is exaggerated in the figures.

In Figure 6.9 b), we vary the resonant frequency of the layer around the cut-off frequency of the unloaded waveguide. We set $\mu_\infty = 1$ and $\omega_{pm} = \pi \cdot 10^{10}$ rad/s. The cut-off frequency of the loaded waveguide is seen to converge towards the cut-off frequency of the empty waveguide when we move away from the resonant frequency of the layer. More precisely, the cut-off frequency $f_{c,l}$ of the loaded waveguide tends to the cut-off frequency $f_{c,u}$ of the unloaded waveguide with increasing resonant frequency of the layer. On the other hand, $f_{c,l}$ remains slightly above $f_{c,u}$ even if the resonant frequency of the layer is arbitrarily small.

As regards the tangential components of the fields, the results presented so far confirm that the proposed new model works correctly. We present one more example, where the normal components are also affected. We place a layer with the Lorentzian permittivity (with a single pole pair) in the middle of the waveguide and calculate the cut-off frequencies versus the parameters

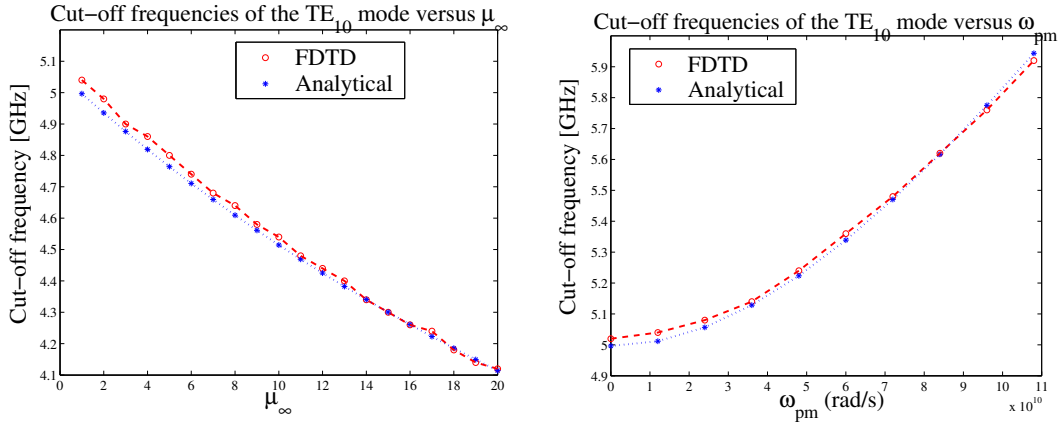

(a) (b)

Figure 6.8: (a) The numerical and the analytical cut-off frequencies of the TE_{10}-mode in the loaded waveguide versus μ_∞. (b) The numerical and the analytical cut-off frequencies of the TE_{10}-mode in the loaded waveguide versus ω_{pm}. The resonant frequency of the layer is smaller than the cut-off frequency of the TE_{10}-mode of an empty waveguide.

of the layer. The shorter wall of the waveguide is now supposed to be 9 mm, and the thickness of the layer is equal to 1 mm. The layer thickness is increased from the previous example to observe a significant change in the cut-off frequency. It is seen from the analytical expression that the cut-off frequency is more sensitive to magnetic layers than to dielectric layers. The FDTD results and the analytical results are shown in Figures 6.10–6.11. In Figure 6.10 a), $\omega_{pe} = 0$, and the ϵ_∞ is varied. In Figure 6.10 b), $\epsilon_\infty = 1$, $\omega_{0e} = 2 \cdot 10^{10}$ rad/s and ω_{pe} is changed. This is also the case with the results in Figure 6.11 a), except that $\omega_{0e} = 4 \cdot 10^{10}$ rad/s. Finally, in Figure 6.11 b), $\epsilon_\infty = 1$, $\omega_{pe} = \pi \cdot 10^{10}$ rad/s and the resonant frequency ω_{0e} of the layer is varied. The maximum relative error of the cut-off frequency is at most one percent in all the cases considered in this paper.

6.4 Introduction to FDTD Modeling of Ferrite Layers

Some FDTD algorithms for the treatment of magnetized ferrites have been formulated. Usually, the algorithms utilize a direct discretization of the electric and magnetic fields inside ferrites. An FDTD model for thin ferrite layers is introduced in this chapter. The model is based on the Leontovich SIBC. Also, techniques to handle thin layers without SIBC-formulation are discussed.

Some good papers dealing with FDTD-modeling of magnetic materials have been published. Okoniewski and Okoniewska have modeled ferrite-loaded

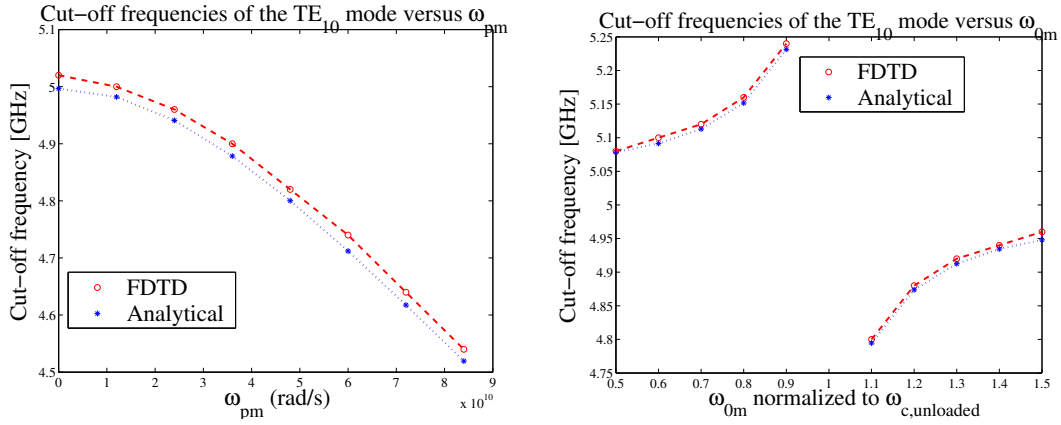

(a) (b)

Figure 6.9: (a) The numerical and the analytical cut-off frequencies of the TE_{10}-mode in the loaded waveguide versus ω_{pm}. The resonant frequency of the layer is larger than the cut-off frequency of the TE_{10}-mode of an empty waveguide. (b) The numerical and the analytical cut-off frequencies of the TE_{10}-mode in the loaded waveguide versus ω_{0m}.

waveguides in [52]. They supplemented Maxwell's equations with an equation of motion describing the physics of ferrites and then implemented their numerical algorithm.

Partially magnetized ferrites were modeled by Pereda *et al.* in [53]. Their model is based on the constitutive relation, where an empirical expression for the permeability tensor is used. Due to the complicated frequency dependence of the permeability, they made a severe approximation and removed some frequency dependence by averaging over the frequency range of interest. However, the results for the phase constant of the fundamental mode of a ferrite-loaded waveguide presented in [53] show that the accuracy is relatively good: errors are typically a couple of percent. Pereda *et al.* also introduce a method to reduce the errors introduced by their approximation.

Like ferrites, also plasmas exhibit anisotropic constitutive parameters. FDTD modeling of magnetized plasmas has been discussed by Hunsberger *et al.* in [54]. Hunsberger *et al.* modeled electronic plasmas with recursive convolution techniques. Their formulation takes both the frequency dispersion and the anisotropy into account at the same time. Very good results were reported in [54] for the reflection and transmission coefficients in a one-dimensional example case. Also, Faraday's rotation was demonstrated.

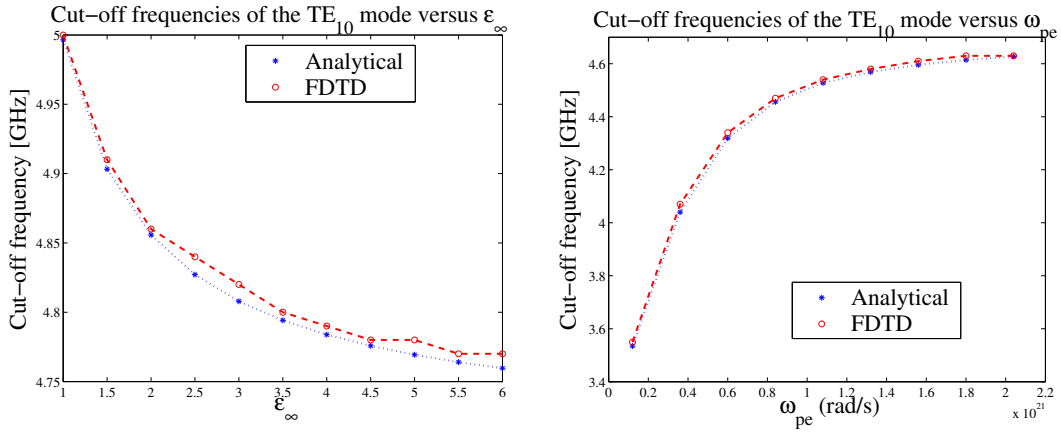

(a) (b)

Figure 6.10: (a) The numerical and the analytical cut-off frequencies of the TE_{10}-mode in the loaded waveguide versus ϵ_∞. (b) The numerical and the analytical cut-off frequencies of the TE_{10}-mode in the loaded waveguide versus ω_{pe}. The resonant frequency of the layer is smaller than the cut-off frequency of the TE_{10}-mode in an empty waveguide.

6.5 Constitutive Relation and SIBC for Ferrites

For a saturated ferrite medium the permeability is a dyadic of the form

$$\overline{\overline{\mu}} = \mu_0 \left[\mu \overline{\overline{I}} - (\mu - 1)\mathbf{h}_0\mathbf{h}_0 - j\mu_a \times \overline{\overline{I}} \right] \tag{6.20}$$

where $\overline{\overline{I}}$ is the unit dyadic and the unit vector $\mathbf{h}_0$ is parallel to the constant bias magnetic field. The parameters μ and μ_a for lossless ferrites are defined as

$$\mu = \frac{\omega_H(\omega_H + \omega_M) - \omega^2}{\omega_H^2 - \omega^2}, \quad \mu_a = \frac{\omega_M \omega}{\omega_H^2 - \omega^2}. \tag{6.21}$$

The constants ω_H and ω_M are related to the constant magnetic field amplitude H_0 and the saturation magnetization M_0 through the gyromagnetic ratio γ according to $\omega_H = \gamma H_0, \quad \omega_M = \gamma M_0$. In the subsequent derivations, the vector $\mathbf{h}_0$ is assumed to be directed along one of the cartesian coordinate axis.

In the following, modeling of a ferrite slab positioned on an ideally conducting surface magnetized in the direction normal to the surface is mainly discussed. In the locally quasistatic approximation, a surface impedance boundary condition may be derived that is valid for relatively thin slabs. The appropriate SIBC on the air-ferrite interface reads [55]

$$\mathbf{E}_t = j\omega\mu_0 d \left(\mu \overline{\overline{I}}_t - j\mu_a \mathbf{n} \times \overline{\overline{I}}_t + \frac{1}{\omega^2 \epsilon \mu_0} \nabla_t \nabla_t \right) \cdot \mathbf{n} \times \mathbf{H}_t. \tag{6.22}$$

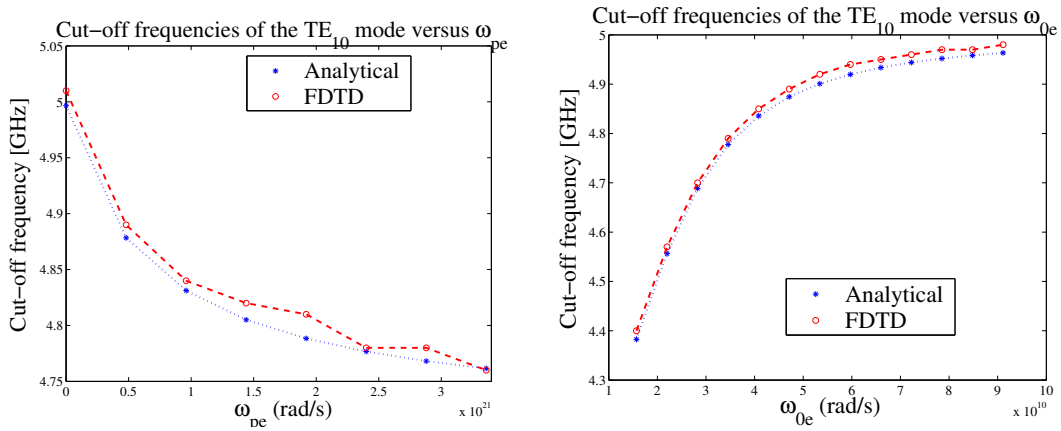

(a) (b)

Figure 6.11: (a) The numerical and the analytical cut-off frequencies of the TE_{10}-mode in the loaded waveguide versus ω_{pe}. The resonant frequency of the layer is larger than the cut-off frequency of the TE_{10}-mode of an empty waveguide. (b) The numerical and the analytical cut-off frequencies of the TE_{10}-mode the loaded waveguide versus ω_{0e}.

As before, $\mathbf{n}$ is the unit normal vector pointing outwards from the interface and ∇_t is the restriction of the gradient operator to the plane of the interface. The thickness of the slab is denoted by d.

6.6 FDTD Model for Ferrite Layers

Despite of approximations, the SIBC in (6.22) is rather complicated. In one-dimensional case, it becomes simpler, because the spatial derivatives drop out. The algorithm is most conveniently described in the one-dimensional case, although similar ideas may be used in two and three dimensions. In what follows, it is seen that the algorithm is rather complicated already in the one dimensional case. Therefore, let us start with the 1D-case of a pulsed wave reflection from a ferrite layer on a metal surface. Assuming that the interface is located at $x = 0$, we have the following SIBC's for the tangential fields:

$$\begin{aligned} E_y &= -j\omega d\,(\mu_0\mu H_z - j\mu_0\mu_a H_y) = -j\omega dA, \\ E_z &= j\omega d\,(\mu_0\mu H_y + j\mu_0\mu_a H_z) = j\omega dB, \end{aligned} \tag{6.23}$$

where auxiliary variables A and B have been introduced. If the term containing ∇_t can be neglected in (6.22), then equations (6.23) result in the general 3D-case, and the subsequent derivations can be modified appropriately. Some problems may, however, arise with the spatially (in the tangential direction) non-collocated nature of the field components. Simply neglecting the tangential spatial errors may lead to a bad algorithm.

Assuming z-polarized incident field, the incident field has only E_z– and H_y– components, but the slab causes the plane of polarization to rotate. Therefore, it is necessary to introduce the field components E_y and H_z. For good stability properties of the FDTD model, it is desired to obtain update equations for the magnetic field components located half cell away from the interface. The electric field components are calculated from the SIBC's above and substituted into the update equations for the magnetic fields. It is noticed that due to the anisotropy of the layer, a linear pair of equations must be solved to obtain the final update equations.

It was found that attempts to straightforwardly discretice the SIBC's in (6.23) lead to poor stability properties. For some parameter choices, the resulting algorithm may work, but the fields blow up for some other choices. The goal here is to develop an algorithm that is stable for any reasonable set of parameters ω_H, ω_M, d. However, the condition $kd \ll 1$ must be satisfied, since the SIBC is based on the approximation $\tan(kd) \approx kd$, which is only valid under the aforementioned condition. For larger values of kd, usual discretization of the fields inside the slab is a feasible approach although a fine mesh may be then necessary.

Consider the discretization of the relation between the auxiliary variable A and H_y and H_z. After multiplication, we obtain from (6.23) the equation

$$(\omega_H^2 - \omega^2)A = \mu_0 \left[\omega_H(\omega_H + \omega_M) - \omega^2\right] H_z - j\mu_0\omega_M\omega H_y. \tag{6.24}$$

An important issue at this point is the discretization of this equation. It could be easily discretized at $t = (n-1/2)\Delta t$, using center differences for derivatives. Then, the coefficients of the component at time step $t = (n+1/2)\Delta t$ would not include both ω_H and ω_M. This is a severe problem if a robust algorithm is desired. To avoid this problem, we turn the equation (6.24) into the time domain and integrate it once to obtain

$$\omega_H^2 \int_0^t A \, \mathrm{d}t + \frac{\partial A}{\partial t} = \mu_0\omega_H(\omega_H + \omega_M) \int_0^t H_z \, \mathrm{d}t + \mu_0 \frac{\partial H_z}{\partial t} - \mu_0\omega_M H_y. \tag{6.25}$$

The spatial indices are not shown; it is understood that the fields are evaluated near the interface. Equation (6.25) is discretized at time step $t = n\Delta t$. The integration is performed second-order-accurately with the trapezoidal rule using the linear interpolation of the fields. In the discrete form, we obtain, after some algebraic manipulation,

$$\begin{aligned}
(4 + \omega_H^2\Delta t^2)A|^{n+1/2} = (4 - \omega^2\Delta t^2)A|^{n-1/2} + \\
\mu_0(4 + \omega_H(\omega_H + \omega_M)\Delta t^2)H_z|^{n+1/2} - \\
\mu_0(4 - \omega_H(\omega_H + \omega_M)\Delta t^2)H_z|^{n-1/2} - \\
2\mu_0\omega_M\Delta t(H_y|^{n+1/2} + H_y|^{n-1/2}) - \\
2\omega_H^2\Delta t^2 \sum_{m=1}^{n}(A|^{n-m+1/2} + A|^{n-m-1/2}) + \\
2\mu_0\omega_H(\omega_H + \omega_M)\Delta t^2 \sum_{m=1}^{n}(H_z|^{n-m+1/2} + H_z|^{n-m-1/2}).
\end{aligned} \tag{6.26}$$

It is seen that once the magnetic fields are known at time step $t = (n-1/2)\Delta t$, the auxiliary variable A at the same time step can be calculated according to (6.26). To solve for E_y at time step $t = n\Delta t$, we remember that A and E_y are related according to $E_y = -j\omega dA$, or in discrete form at $t = n\Delta t$:

$$A|^{n+1/2} = A|^{n-1/2} - \frac{\Delta t}{d} E_y|^n. \tag{6.27}$$

This expression for $A|^{n+1/2}$ is now substituted into (6.26) and solved for $E_y|^n$. The result is

$$\begin{aligned}(4+\omega_H^2\Delta t^2)\Delta t E_y|^n = d\,\big[2\omega_H^2\Delta t^2 A|^{n-1/2} - \\ \mu_0(4+\omega_H(\omega_H+\omega_M)\Delta t^2)H_z|^{n+1/2} + \mu_0(4-\omega_H(\omega_H+\omega_M)\Delta t^2)H_z|^{n-1/2} + \\ 2\mu_0\omega_M\Delta t(H_y|^{n+1/2} + H_y|^{n-1/2}) + \\ +2\omega_H^2\Delta t^2\sum_{m=1}^{n}(A|^{n-m+1/2} + A|^{n-m-1/2}) - \\ 2\mu_0\omega_H(\omega_H+\omega_M)\Delta t^2\sum_{m=1}^{n}(H_z|^{n-m+1/2} + H_z|^{n-m-1/2})\Big].\end{aligned}$$

Finally, the $E_y|^n$ is substituted into usual Maxwell's equation in discrete form:

$$H_z|_{1/2}^{n+1/2} = H_z|_{1/2}^{n-1/2} - \frac{\Delta t}{\mu_0\Delta x}\left(E_y|_1^n - E_y|_0^n\right). \tag{6.28}$$

After simplification, the following equations relating $H_z|^{n+1/2}$ and $H_y|^{n+1/2}$ are obtained:

$$\begin{aligned}C_1 H_z|_{1/2}^{n+1/2} - C_2 H_y|_{1/2}^{n+1/2} = C_3 H_z|_{1/2}^{n-1/2} - \Delta t(4+\omega_H^2\Delta t^2)E_y|_1^n - \\ d\Bigg[-2\omega_H^2\Delta t^2\sum_{m=1}^{n}(A|^{n-m+1/2} + A|^{n-m-1/2}) + \\ 4\mu_0\omega_H(\omega_H+\omega_M)\Delta t^2\sum_{m=1}^{n}\frac{1}{2}(H_z|_{1/2}^{n-m+1/2} + H_z|_{1/2}^{n-m-1/2}) - \\ 2\omega_H^2\Delta t^2 A|^{n-1/2} - 2\mu_0\omega_M\Delta t H_y|_{1/2}^{n-1/2}\Bigg]\end{aligned} \tag{6.29}$$

and

$$\begin{aligned}C_1 H_y|_{1/2}^{n+1/2} + C_2 H_z|_{1/2}^{n+1/2} = C_3 H_y|_{1/2}^{n-1/2} + \Delta t(4+\omega_H^2\Delta t^2)E_z|_1^n - \\ d\Bigg[-2\omega_H^2\Delta t^2\sum_{m=1}^{n}(B|^{n-m+1/2} + B|^{n-m-1/2}) + \\ 2\mu_0\omega_H(\omega_H+\omega_M)\Delta t^2\sum_{m=1}^{n}(H_y|_{1/2}^{n-m+1/2} + H_y|_{1/2}^{n-m-1/2}) - \\ 2\omega_H^2\Delta t^2 B|^{n-1/2} + 2\mu_0\omega_M\Delta t H_z|_{1/2}^{n-1/2}\Bigg].\end{aligned} \tag{6.30}$$

In the equations above, the constants C_1, C_2, C_3 are defined as

$$\begin{aligned} C_1 &= \mu_0 \left[\Delta x(4+\omega_H^2\Delta t^2) + d(4+\omega_H(\omega_H+\omega_M)\Delta t^2)\right], \\ C_2 &= 2d\mu_0\omega_M\Delta t, \\ C_3 &= \mu_0 \left[\Delta x(4+\omega_H^2\Delta t^2) + d(4-\omega_H(\omega_H+\omega_M)\Delta t^2)\right]. \end{aligned} \tag{6.31}$$

Denoting the right-hand sides of equations (6.29–6.30) by RHS_2 and RHS_1, respectively, we obtain the final update equations for the tangential magnetic field components:

$$\begin{aligned} H_y|_{1/2}^{n+1/2} &= \frac{1}{C_1^2+C_2^2}\left[C_1\cdot RHS_1 - C_2\cdot RHS_2\right], \\ H_z|_{1/2}^{n+1/2} &= \frac{1}{C_1^2+C_2^2}\left[C_2\cdot RHS_1 + C_1\cdot RHS_2\right]. \end{aligned} \tag{6.32}$$

It is seen that as $d = 0$, then $C_2 = 0$ and H_y and H_z become actually decoupled. If only H_y is nonzero in the incident wave, H_z remains zero all the time. This is correct, since in the case $d = 0$ we have just an ideally conducting wall. Examining the update equation for H_y in the case of $d = 0$ reveals that it corresponds to the case where the electric field component on the interface is equal to zero. Thus, the model correctly reduces to the PEC boundary condition if $d = 0$. If $\omega_M \gg \omega_H$, then the surface impedance is very large, and the discrete model should reduce to a PMC boundary condition. Now, $|C_1|$ and $|C_2|$ are large, and we correctly have just zero magnetic fields on the boundary.

The discrete sums can be implemented recursively adding one term to the sum. Comparing to the usual FDTD algorithm, three additional variables are needed per magnetic field component on the boundary: the auxiliary variable, its integral and the integral of the related magnetic field component. The model can be modified to include a loss term. For example, it is possible to incorporate parameters μ and μ_a of the form

$$\mu = \frac{\omega_H(\omega_H+\omega_M)-\omega^2}{\omega_H^2-\omega^2+j\Gamma\omega}, \quad \mu_a = \frac{\omega_M\omega}{\omega_H^2-\omega^2+j\Gamma\omega} \tag{6.33}$$

into the model. If these parameters were used, all the described steps would proceed in an analogous fashion.

6.7 A Subcell Technique for Thin Ferrite Layers

Before numerical examples, an alternative approach for modeling electrically thin ferrite layers is introduced. It is not evident from the literature if anyone has adopted this approach when modeling ferrites. FDTD-models for dielectric and conducting layers using subcell techniques have been presented by Tirkas

and Demarest in [15] and by Maloney and Smith in [16]. Both of these models are based on modifying Maxwell equations within or in the vicinity of the layer.

Consider the same one-dimensional test problem. If the thickness d of the layer is very small, so that $d < \Delta x$, then a subcell technique may be used. Denoting $0 \leq \alpha = d/\Delta x \leq 1$, we may average the operational and the scalar constitutive relations just in front of the metal boundary to obtain the averaged constitutive relation in the form:

$$\mathbf{B} = \alpha\overline{\overline{\mu}} \cdot \mathbf{H} + (1-\alpha)\mu_0\mathbf{H}. \tag{6.34}$$

This rather simple equation is the basis of the proposed subcell technique. It is immediately seen that if $d = 0$, then $\alpha = 0$ and the usual constitutive relation in free space is used. The same discretization techniques as above may be utilized in discretizing (6.34). In the general 3D-case, a special update scheme for the normal components have to be developed. Similar ideas were used as in the beginning of this chapter (see also [5]).

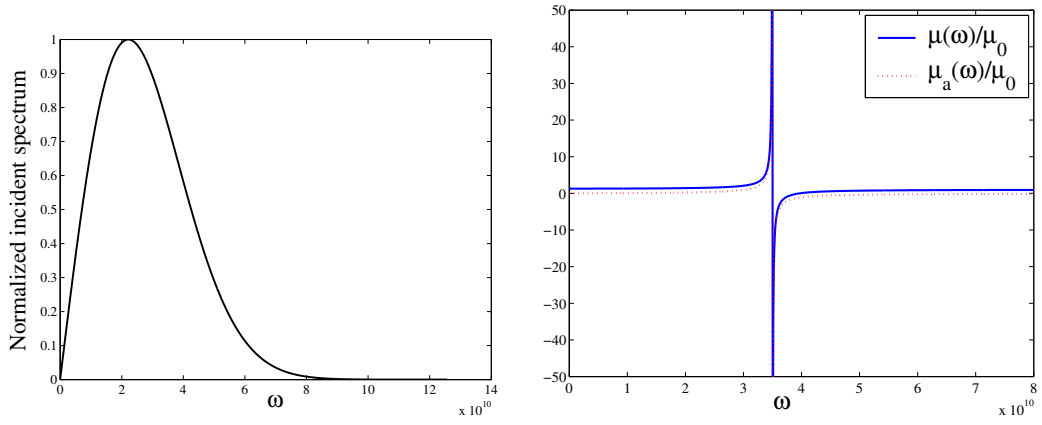

(a) (b)

Figure 6.12: (a) The spectrum of the incident electric field E_z. The peak occurs at $\omega_{peak} = 2.2 \cdot 10^{10}$ 1/s. (b) The parameters μ and μ_a versus ω for $\omega_H = 3.5 \cdot 10^{10}$ 1/s and $\omega_M = 1.0 \cdot 10^{10}$ 1/s.

It is observed that the Yee algorithm can be easily extended for the treatment of magnetized ferrites using the discretization scheme presented above. Setting $\alpha = 1$, we merely supplement the usual Maxwell equations with the constitutive relation relating $\mathbf{B}$ and $\mathbf{H}$ in regions, where ferrites are located. This can be done regardless of the dimension of the computational space.

6.7.1 Numerical Examples in 1D-Case

The two models are demonstrated with a one-dimensional FDTD-code calculating pulse reflection from a ferrite layer located on an ideally conducting

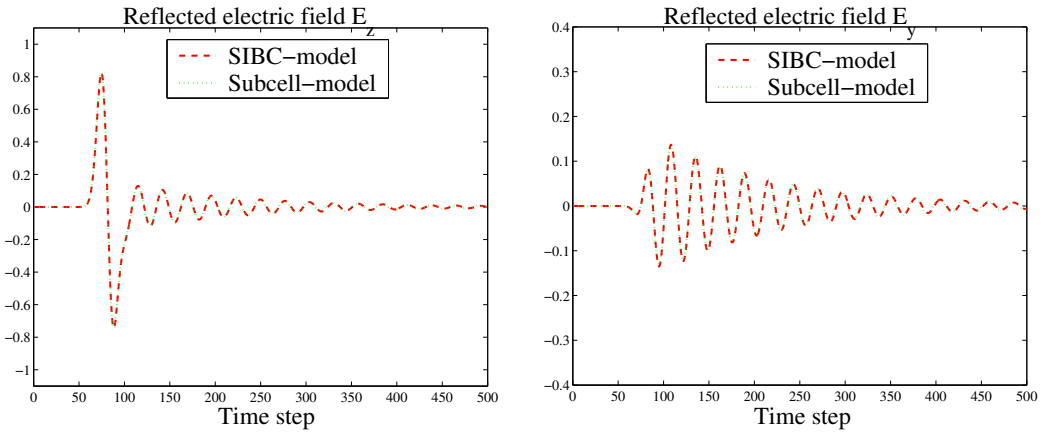

(a) (b)

Figure 6.13: (a) Reflected time-domain electric field E_z on the air-ferrite interface. $\omega_M = 1.0 \cdot 10^{10}$ 1/s. (b) Reflected time-domain electric field E_y on the air-ferrite interface. There is only a small reflected E_y-component due to the Faraday rotation within the ferrite layer.

surface. The incident pulse is a differentiated gaussian pulse with electric field oscillating in the xz-plane, with the peak of the spectrum occurring at about $\omega_{\text{peak}} = 2.2 \cdot 10^{10}$ 1/s. For angular frequencies larger than $\omega = 9 \cdot 10^{10}$ 1/s, there is negligible amount of spectral content. The spectrum of the incident electric field E_z is shown in Figure 6.12 a). The parameters μ and μ_a versus angular frequency are shown in Figure 6.12 b).

We arbitrarily choose $\omega_H = 3.5 \cdot 10^{10}$ 1/s and $d = 1$ mm. The thickness of the layer is equal to $d = \Delta x/2$. Setting $\omega_M = 1.0 \cdot 10^{10}$ 1/s we calculate the reflected electric fields on the air-ferrite interface with both models. The results are seen in Figure 6.13.

Next, we take $\omega_M = \omega_H = 3.5 \cdot 10^{10}$ 1/s. The corresponding reflected fields are presented in Figure 6.14. Increasing ω_M to $\omega_M = 8 \cdot 10^{10}$ 1/s we obtain the results in Figure 6.15.

It is interesting to check the special case when $\omega_H = 0$, (without considering whether this is physical or not) since then we have $\mu = 1$ and $E_z = j\omega\mu_0 dH_z + \mu_0\omega_M dH_y$. We choose $\omega_M = 3.0 \cdot 10^{11}$ 1/s obtaining $E_z = 377\Omega \cdot H_y + j28\Omega \cdot H_z$ at $\omega = \omega_{\text{peak}} = 2.2 \cdot 10^{10}$ 1/s. This almost corresponds to matching the E_z to the free space: $E_z = 377\Omega \cdot H_y$. Indeed, it is seen from Figure 6.16 that the plane of the polarization has rotated almost exactly 90 degrees and the reflected E_z-component is rather small, while the shape of the reflected E_y-component is like the incident field. Some discrepancy between the subcell and the SIBC-based methods in Figure 6.16 a) is also observed.

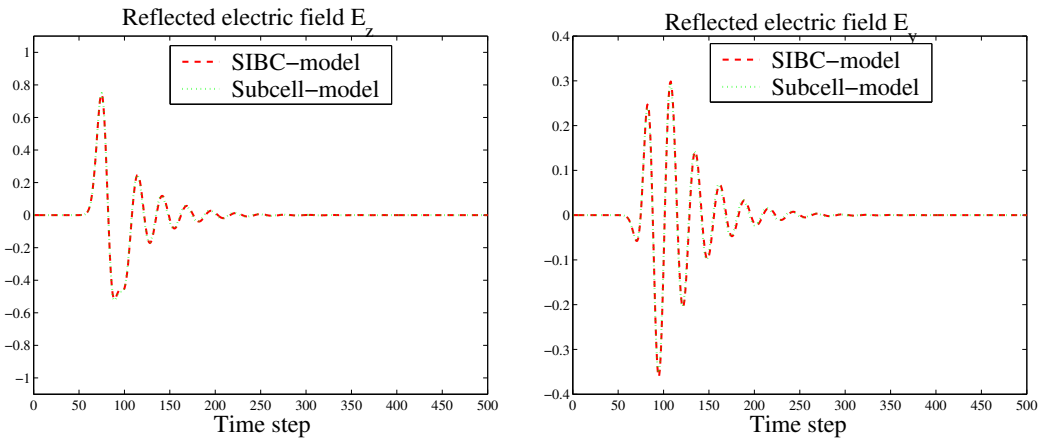

(a) (b)

Figure 6.14: (a) Reflected time-domain electric field E_z on the air-ferrite interface. $\omega_M = 3.5 \cdot 10^{10}$ 1/s. (b) Reflected time-domain electric field E_y on the air-ferrite interface. There is a larger reflected E_y-component than in Figure 6.13.

6.8 Conclusions

A new model for treating electrically thin dispersive layers and coatings in FDTD simulations was introduced. The model is based on an appropriate averaging of the electric and magnetic flux densities and on the use of auxiliary quantities like polarization current and magnetization. The most important feature of the model is its ability to accurately model dispersive layers having multiple resonances of material parameters. The model is applicable for electrically thin layers. A great advantage of the model is that we do not have to consider the angle of incidence of the incident waves, because the local nature of the model accounts for oblique incidence as well. With the proposed model, the use of cumbersome surface impedance boundary conditions for dispersive layers having multiple pole pairs is avoided. The proposed model was numerically verified with a couple of test problems by comparison with the analytical results. The results given both in time and frequency domains indicate rather good accuracy of the model. The model was found to be suitable for the analysis of waveguides loaded with a dispersive layer.

Also, FDTD modeling of saturated ferrites has been dealt with. A novel SIBC-based technique was introduced for modeling relatively thin ferrite layers on ideally conducting surfaces. Some numerical examples were given in the one-dimensional case. The developed model could be applied to the analysis of ferrite-loaded waveguides, where the thickness of the ferrite layer is so small that a direct quantization of the fields is not a feasible approach. An alternative subcell technique was briefly discussed, and it was found to produce similar results as the SIBC-model.

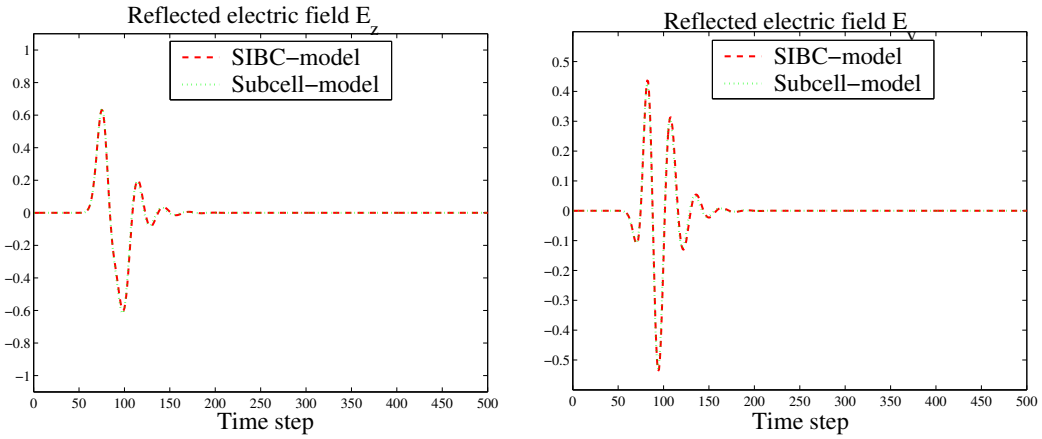

(a) (b)

Figure 6.15: (a) Reflected time-domain electric field E_z on the air-ferrite interface. $\omega_M = 8 \cdot 10^{10}$ 1/s. (b) Reflected time-domain electric field E_y on the air-ferrite interface.

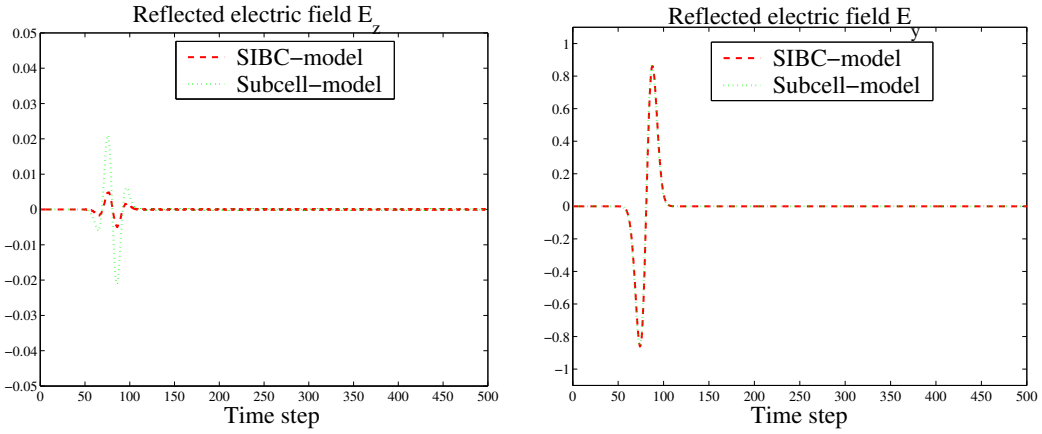

(a) (b)

Figure 6.16: (a) Reflected time-domain electric field E_z on the air-ferrite interface. The rotation of the plane of polarization from xz-plane close to xy-plane is evident. This is natural, since the fields E_z and E_y on the interface are coupled through μ_a. Notice the scaling in the figure is refined. (b) Reflected time-domain electric field E_y on the air-ferrite interface. The incident z-polarized electric field has been transformed into y-polarized electric field.

Chapter 7

Metamaterials

Wave propagation and refraction phenomena in metamaterials are considered in this chapter. Metamaterials are materials that cannot be found or are not readily available in nature. Metamaterials are artificially engineered materials. In this chapter, FDTD algorithms for dispersive media are briefly discussed first. The FDTD method is then applied in the numerical simulations of a slab having unusual electromagnetic properties implied by the negative values of the material parameters in a certain frequency range. Wave propagation phenomena are mainly observed as predicted by the theory, but our simulations do not support a possibility of making a "perfect" lens from a slab of isotropic double negative material. The behavior of evanescent waves in metamaterials is numerically studied using a special type of source function in FDTD.

7.1 Introduction

Metamaterials have received much attention during the last years, because they possess unusual electromagnetic properties, like, for example, the opposite directions of phase and group velocities. Double negative (DNG) materials have negative permittivity and permeability, and they belong to the class of metamaterials. These media that are capable of supporting backward waves, have been also called backward wave (BW) media in the literature [56]. In BW media, the refraction phenomenon is anomalous in the sense that the power flow is refracted negatively, i.e. to the same side of the normal of the interface. As discussed in [56], it is not necessary for the medium to be a DNG medium to be able to support backward waves, because anomalous refraction can also be realized with anisotropic media with only one negative material parameter.

The pioneering work on BW materials by Veselago [57], where slab lenses were mentioned, has gained much attention during recent years, despite some differing opinions on the subject [58]. Isotropic BW materials are often called Veselago materials. The possibility to realize a perfect lens with isotropic BW

slabs was discussed by Pendry in [59]. Numerical and theoretical considerations of wave propagation in isotropic BW slabs excited with a line current above the slab were presented by Ziolkowski and Heyman in [62]. Guidance of waves in a slab of uniaxially anisotropic metamaterial has been theoretically discussed by Lindell and Ilvonen in [72].

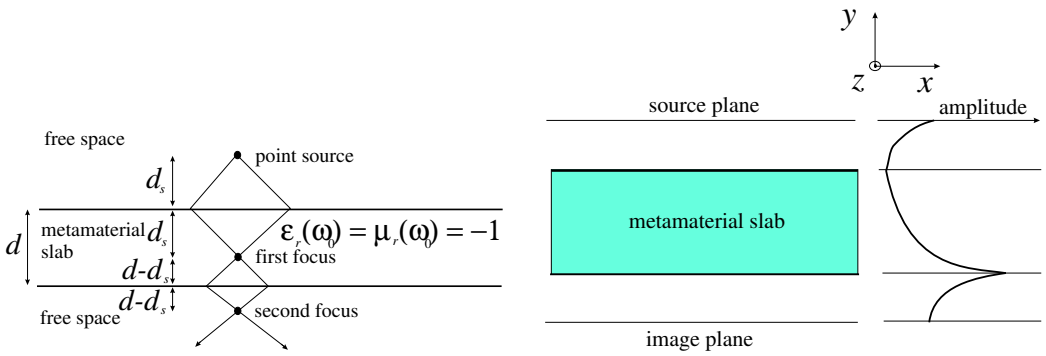

(a) (b)

Figure 7.1: (a) The ray picture of perfect lens. The near fields created by the point source are focused inside the slab, and the source field is reproduced in the second focus behind the slab. (b) The profile of the magnitude of evanescent fields within a DNG slab. The amplitude of evanescent fields grow exponentially inside a lossless slab having the relative material parameters equal to $\epsilon_r = \mu_r = -1$ at the excitation frequency.

Controversial opinions regarding negative refraction effect and the perfect lens call for more detailed studies of the wave phenomena in backward-wave media. In this thesis, wave propagation through uniaxially anisotropic BW slabs is numerically studied, and comparison is made with the theory presented in [56]. The theory predicts that there are regions in certain BW media, where the wave vector becomes complex, thus resulting in exponentially decaying waves. These regions are bounded by the asymptotes of the wave vector surfaces, which can be shown to be hyperbola. We study these phenomena numerically using the finite-difference time-domain (FDTD) method in a 2D-problem of a line current radiating in the vicinity of a BW slab. Also, the existence of surface waves on the interface between free space and BW medium is demonstrated with an example case. The BW medium is realized with Lorentzian constitutive parameters having a single pole pair.

Negative material parameters within certain frequency band have been realized using an array of split ring resonators and wire segments [64]. The wires provide negative effective permittivity, and the split rings the negative effective permeability of the medium.

An important topic in this chapter is the numerical study of propagation of electromagnetic fields created by a line source in a planar DNG slab. Uniaxially anisotropic slabs are first studied, and the isotropic DNG slab is considered as

a special case. A ray picture of the fields produced by a point source above an isotropic DNG slab is shown in Figure 7.1 a). In Figure 7.1 b), the behavior of evanescent fields within a planar DNG slab is presented.

An example problem with some theoretical discussion are presented in section 7.3. Results from the numerical simulations are shown and discussed in section 7.4. Our numerical simulations show that the wave propagation and refraction phenomena heavily depend on the parameter choices of the BW medium and are qualitatively in agreement with the theory.

7.2 Numerical Model of Dispersive Medium

The constitutive relations for a frequency dispersive isotropic medium read

$$\mathbf{D} = \epsilon(\omega)\mathbf{E}, \quad \mathbf{B} = \mu(\omega)\mathbf{H}. \tag{7.1}$$

Negative permittivity and permeability are realized with the Lorentz medium model. The expressions for the permittivity and permeability are of the form

$$\begin{aligned} \epsilon(\omega) &= \epsilon_0 \left(1 + \frac{\omega_{pe}^2}{\omega_{0e}^2 - \omega^2 + j\Gamma_e\omega}\right), \\ \mu(\omega) &= \mu_0 \left(1 + \frac{\omega_{pm}^2}{\omega_{0m}^2 - \omega^2 + j\Gamma_m\omega}\right). \end{aligned} \tag{7.2}$$

This model corresponds to a realization of BW materials as mixtures of conductive spirals or omega particles, as discussed in [73]. In this artificial material both electric and magnetic polarizations are due to currents induced on particles of only one shape, which provides a possibility to realize the same dispersion rule for both material parameters, as in (7.2). Note that the medium realized by Smith *et al.* is built using different principles [64]. For the uniaxial materials that we consider in this thesis we assume that the negative components of the material parameters are realized by small uniaxial spiral inclusions (racemic arrays with equal number of right- and left-handed particles) and possess frequency dispersion defined by (7.2). The positive components of the material parameters are equal to the free-space permittivity and permeability values, assuming that there are no particles oriented along these axes.

In numerical simulations, it is important to use frequency-dependent material parameters, since there is no possibility to use constant negative material parameters in FDTD and have it run stably. Also, any physical realization of metamaterials is dispersive, since constant and negative material parameters would imply negative stored energy density in the medium. Hence, a good FDTD model for frequency-dispersive media should be employed even when working with essentially point frequency, as in the subsequent simulations.

Equations (7.1) and (7.2) form the basis of the used FDTD model for BW materials. The two most important known FDTD methods for modeling dispersive materials like Lorentz materials are the recursive convolution method

and the auxiliary differential equation method, where the constitutive parameters are expressed with the help of susceptibility. In the first method, **D** and **E** and **B** and **H** are related through a convolution integral. This approach is rather tedious. Another possibility is to use the auxiliary differential equation technique, which is slightly easier to implement. In this latter method, the polarization current associated to each Lorentz pole pair is introduced. These two models are discussed in detail in [27].

A third method to discretize fields in Lorentz medium, classified as direct integration method in [51], is based on the direct discretization of the PDE representing the time-domain equivalent of the simplified frequency-domain constitutive relation. The proposed discretization scheme is a modification of this method. The idea is to transform (7.1) into the time domain using the relation $j\omega \leftrightarrow \partial/\partial t$ with one integration before discretization using center differences. Usually, FDTD models based on the constitutive relation are directly (after multiplication with the denominator) discretized, as discussed in a summary of FDTD algorithms for dispersive media in [51]. We found in [65] that one integration prior to discretization yields naturally a stable scheme without heuristic tricks, such as the (in principle) unnecessary approximation $E_z|^n \approx (E_z|^{n+1} - E_z|^{n-1})/2$, which has to be utilized to preserve stability for wider variety of material parameters.

As an example, an update equation for the electric field component E_z inside BW material is next derived. Multiplying with the denominator of the permittivity in (7.2) we obtain the equation

$$(\omega_{0e}^2 - \omega^2 + j\Gamma_e\omega)D_z = \epsilon_0(\omega_{0e}^2 + \omega_{pe}^2 - \omega^2 + j\Gamma_e\omega)E_z. \tag{7.3}$$

Transforming into the time domain and integrating once yields

$$\epsilon_0(\omega_{0e}^2+\omega_{pe}^2)\int_0^t E_z\, d\tau + \epsilon_0\Gamma_e E_z + \epsilon_0\frac{\partial E_z}{\partial t} = \omega_{0e}^2\int_0^t D_z\, d\tau + \Gamma_e D_z + \frac{\partial D_z}{\partial t}. \tag{7.4}$$

The integral is evaluated with the trapezoidal rule, corresponding to the discrete approximation

$$\int_0^t E_z(x,y,\tau)\, d\tau \approx \frac{1}{4}\left(E_z|_{i,j}^{n+1} + E_z|_{i,j}^{n}\right) + \sum_{m=1}^{n}\frac{1}{2}\left(E_z|_{i,j}^{n-m+1} + E_z|_{i,j}^{n-m}\right), \tag{7.5}$$

where $t = n\Delta t$ and $(x,y) = (i\Delta x, j\Delta y)$, according to the common notation. Discretizing equation (7.4) at the time step $t = n\Delta t$ using center differences and the trapezoidal rule, and solving for $E_z|_{i,j}^{n+1}$ gives the following update equation:

$$\begin{aligned} E_z|_{i,j}^{n+1} &= \frac{1}{4 + (\omega_{pe}^2+\omega_{0e}^2)\Delta t^2 + 2\Gamma_e\Delta t}\left[(4 - (\omega_{pe}^2+\omega_{0e}^2)\Delta t^2 - 2\Gamma_e\Delta t)E_z|_{i,j}^{n}\right. \\ &+ \frac{1}{\epsilon_0}(4 + \omega_{pe}^2\Delta t^2 + 2\Gamma_e\Delta t)D_z|_{i,j}^{n+1} - \frac{1}{\epsilon_0}(4 - \omega_{pe}^2\Delta t^2 - 2\Gamma_e\Delta t)D_z|_{i,j}^{n} \\ &- \left. 4(\omega_{pe}^2+\omega_{0e}^2)\Delta t^2\Psi|_1^n + \frac{4}{\epsilon_0}\omega_{pe}^2\Delta t^2\Psi|_2^n\right], \end{aligned} \tag{7.6}$$

where

$$\Psi|_1^n = \Psi|_1^{n-1} + \frac{1}{2}\left(E_z|_{i,j}^n + E_z|_{i,j}^{n-1}\right), \quad \Psi|_2^n = \Psi|_2^{n-1} + \frac{1}{2}\left(D_z|_{i,j}^n + D_z|_{i,j}^{n-1}\right). \quad (7.7)$$

Thus, the discrete sums of the time histories of E_z and D_z are stored in variables Ψ_1 and Ψ_2. The memory requirements for the suggested discretization technique are the same as in the case of the direct discretization without integration. This model has been published in [65] and it is used in the following simulations. This scheme produces similar results as other known models. However, even the largest time step dictated by the stability limit for the Yee algorithm in free space can be used in all the results presented in this chapter. This feature is common to the direct-integration method in [51]. The auxiliary differential equation technique becomes unstable unless the time step is somewhat reduced from the Yee limit.

7.3 An Example Problem and Theoretical Discussion

Consider a z-directed line current in free space located at distance d_s from a BW slab of thickness d. Let the interface between free space and the BW slab be located at $y = 0$. The problem space is two-dimensional, with the field components H_x, H_y, and E_z. The peak of the incident spectrum is at $\omega_p = 5.0 \cdot 10^9$ rad/s, and the parameters in (7.2) are the following: $\omega_{0e} = \omega_{0m} = 1.0 \cdot 10^9$ rad/s, $\omega_{pe}^2 = \omega_{pm}^2 = 4.8 \cdot 10^{19}$ (rad/s)^2, $\Gamma_e = \Gamma_m = 0$. With these choices, we obtain $\epsilon(\omega) = \mu(\omega)$ for all ω and $\epsilon(\omega)/\epsilon_0 = \mu(\omega)/\mu_0 = -1$ at $\omega = \omega_p$. The spatial resolution $\Delta x = \Delta y = 1.5$ cm is used throughout the simulations. To be able to demonstrate the properties of BW materials, the incident spectrum is quite narrow, so that the relative constitutive parameters are close to minus one for the frequencies having significant spectral content. Absorbing boundary conditions are used to terminate the computational domain at the outer boundaries of the lattice. For simplicity, we have used Liao's third order ABC, although more sophisticated ABC's are available. The use of usual ABC's requires a small gap between the outer boundary of the computational space and the BW material slab. The chosen coordinate axes and the problem geometry are shown in Figure 7.2. Next, we briefly present some theoretical

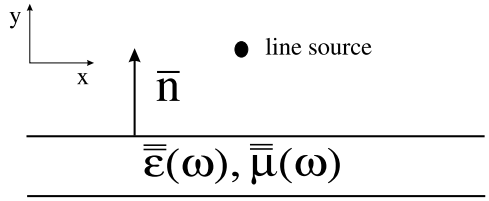

Figure 7.2: The slab problem under consideration and the chosen coordinate system.

results from [56] (see also [6]) that are important here for comparison purposes with our numerical results. Wave propagation in BW slabs is studied with different value combinations of the medium parameters μ_x, μ_y and ϵ_z. For our TE-polarized case, the Poynting vector $\mathbf{S}_{TE}$ can be shown to read [56]

$$\mathbf{S}_{TE} = \frac{\overline{\overline{\mu}} \cdot \mathbf{k}_{TE}}{2k_0\eta_0\mu_0\mu_x\mu_y}|E_0|^2, \tag{7.8}$$

where $|E_0|$ is the amplitude of the TE-polarized electric field of the plane wave, $\mathbf{k}_{TE}$ is the wave vector with two cartesian components k_x and k_y, $k_0 = \omega\sqrt{\epsilon_0\mu_0}$ is the free space wave number, and $\eta_0 = \sqrt{\mu_0/\epsilon_0}$ is the free space wave impedance. Denoting the angle between the outwards-pointing unit normal vector $\mathbf{u}_y$ and the wave vector $\mathbf{k}_{TE}$ by θ, one can derive the dispersion equation and solve it for the wave number as in [56]. The result is

$$k_{TE}(\theta) = k_0\sqrt{\frac{\mu_x\epsilon_z}{\cos^2\theta + \frac{\mu_x}{\mu_y}\sin^2\theta}}. \tag{7.9}$$

For any given set of parameters, we may plot the projection curves of the wave vector surfaces in the plane. For certain choices of the medium parameters, the wave number becomes complex, resulting in exponentially decaying waves inside the BW material. In our simulations, $|k_{\mathrm{TE}}| = k_0$ at the operation frequency, and after substituting $k_x = k_0\sin(\theta), k_y = k_0\cos(\theta)$, we readily obtain an alternative representation of (7.9):

$$k_x^2\frac{\mu_x}{\mu_y} + k_y^2 = k_0^2\mu_x\epsilon_z. \tag{7.10}$$

For infinite slabs, any physical power flow must be directed downwards away from the source. This requires that

$$\mathbf{u}_y \cdot \mathbf{S}_{TE} < 0. \tag{7.11}$$

The necessary condition for any transmission is

$$\frac{\mathbf{u}_y \cdot \mathbf{k}_{TE}}{\mu_x} < 0 \Longleftrightarrow \frac{k_y}{\mu_x} < 0. \tag{7.12}$$

Clearly, the phase velocity is directed oppositely to the power flow provided that $\mu_x < 0$. Negative refraction of the Poynting vector requires that

$$k_x\mathbf{u}_x \cdot \mathbf{S}_{TE} < 0 \Longleftrightarrow \mu_y < 0. \tag{7.13}$$

For the interface problem, we will also need to know conditions for the existence of surface waves. The input impedance on the surface filled by a uniaxial material is, for TE-polarized fields,

$$Z_{\mathrm{inp}} = \frac{\omega\mu_x}{\beta_{\mathrm{TE}}}, \tag{7.14}$$

where the normal component of the propagation factor reads

$$\beta_{\mathrm{TE}} = \sqrt{\frac{\mu_x}{\mu_y}\left(\omega^2 \epsilon_z \mu_y - k_x^2\right)} \tag{7.15}$$

with the square root branch defined by $\mathrm{Im}(\beta_{\mathrm{TE}}) < 0$. k_x is the propagation factor along the surface. Thus, the eigensolutions for an interface between this medium and free space satisfy the following equation:

$$\frac{\mu_x}{\beta_{\mathrm{TE}}} + \frac{\mu_0}{\beta_0} = 0, \tag{7.16}$$

where

$$\beta_0 = \sqrt{\omega^2 \epsilon_0 \mu_0 - k_x^2}, \tag{7.17}$$

with $\mathrm{Im}(\beta_0) < 0$.

Surface waves along the interface exist provided that both betas are imaginary, of course with negative imaginary parts: $\beta_{\mathrm{TE}} = -j\alpha_{\mathrm{TE}}$ and $\beta_0 = -j\alpha_0$, where $\alpha_{\mathrm{TE}} > 0$ and $\alpha_0 > 0$. The eigenvalue equation becomes

$$\frac{\mu_x}{\alpha_{\mathrm{TE}}} + \frac{\mu_0}{\alpha_0} = 0. \tag{7.18}$$

Obviously, if all the material parameters are positive, this equation has no solutions, but if $\mu_x < 0$, surface wave solutions are possible. This is well known for interfaces with free-electron plasma.

Five different cases will be considered in the following. In the first case, we choose $\mu_x > 0$, $\mu_y < 0$, and $\epsilon_z < 0$. The wave vector surface is a two-sheeted hyperboloid with the axis parallel to the x-axis. The asymptotes of the hyperbola in the xy-plane divide the plane into regions of complex and real wave vectors. Waves that are propagating parallel to the y-axis are supposed to decay exponentially inside the slab. Indeed, for $\mu_x = 1, \mu_y = -1, \epsilon_z = -1$ the dispersion equation (7.10) takes the form

$$-k_x^2 + k_y^2 = -k_0^2, \tag{7.19}$$

which represents, for a given k_0, the two-sheeted hyperboloid in $k_x k_y$ -plane with the axis parallel to k_x. It is easily seen from (7.19) that for waves with $k_x = 0$, k_y becomes complex and the fields inside the slab decay exponentially with the distance from the interface.

In the second case, $\mu_x > 0$, $\mu_y < 0$, $\epsilon_z > 0$. The wave vector surface is a two-sheeted hyperboloid with the axis parallel to the surface normal. In our 2D-case, real wave vectors exist inside the region bounded by the asymptotes of the hyperbola associated to the wave vector surfaces. In this case, the dispersion equation (7.10) for $\mu_x = 1, \mu_y = -1, \epsilon_z = 1$ takes the form

$$-k_x^2 + k_y^2 = k_0^2. \tag{7.20}$$

As a third case, we consider the situation complementary to the second case in the sense that the signs of all the parameters are changed. Notice that this

does not affect the shape of the wave vector curves, so that the dispersion equation is of the form (7.20). We have $\mu_x < 0$, $\mu_y > 0$, and $\epsilon_z < 0$. In fact, the Poynting vector is refracted positively in this case [see (7.13)], but this is an interesting case anyway because of the aforementioned contrast with respect to the second case.

The fourth case consists of the usual isotropic BW slab ($\mu_x = \mu_y < 0$, and $\epsilon_z < 0$) where focusing and negative refraction phenomena are present. The wave vector curves are ellipses (in our case of two equal parameters they are circles), and real wave vectors exist everywhere inside the slab.

The fifth case is specially chosen to show the existence of surface waves in the case when $\mu_x < 0$, $\mu_y < 0$, and $\epsilon_z > 0$. We can easily see from (7.10) that there are neither real wave vectors nor backward waves, since $k_x^2 + k_y^2 = -k_0^2 < 0$ for $\mu_x = \mu_y = -1, \epsilon_z = 1$. However, it was found that surface waves on the interface are easily excited in this case. Let us now present the numerical results.

7.4 Numerical Results and Comparison with the Theory

In the first four cases, we show the electric field distribution at three suitable chosen increasing time steps to illustrate the wave propagation and refraction phenomena. In the fifth case, we illuminate a rectangular cylinder to see the surface waves. Whenever a constitutive parameter is said to be positive, it is supposed to be a constant and equal to the free space permittivity or permeability. Negative material parameters obey the Lorentzian dispersion rule and equal $-\epsilon_0$ or $-\mu_0$ at the center frequency.

7.4.1 Case I: $\mu_x > 0$, $\mu_y < 0$, $\epsilon_z < 0$

In this case, the theory shows that the wave vectors are complex inside the slab within a region bounded by the asymptotes of a hyperbola. Inspection of Figure 7.3 c) reveals that there is indeed a region in the slab, where the electric field in negligible all the time. There are some fields within the slab just under the source. The hyperbola-shaped wavefronts propagate obliquely downwards inside the slab and the power flow is refracted negatively. The distance of the source from the first interface is discretized with 5 cells, and the thickness of the slab corresponds to 80 cells.

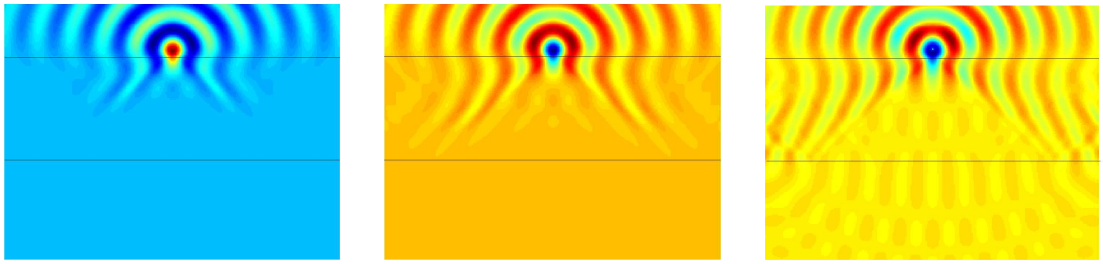

(a) (b) (c)

Figure 7.3: (a) The electric field E_z penetrating into the slab. Slab boundaries are indicated by black lines. The snapshot is taken at time step $n = 400$. (b) The electric field within the slab. Notice the region in the center of the slab, where the field amplitudes are very small. The snapshot is taken at time step $n = 560$. (c) It appears that the wavefronts inside the slab are hyperbolas, in agreement with the theory. The snapshot is taken at time step $n = 1060$.

7.4.2 Case II: $\mu_x > 0$, $\mu_y < 0$, $\epsilon_z > 0$

In Figure 7.4 a), a cylindrical wave is penetrating into the BW slab. In Figure 7.4 b), some numerical dispersion is visible. There are significant fields inside the region where the theory yields real wave vectors, while the fields are rather small elsewhere. Despite some dispersive effects, the wavefronts of constant field value are reminiscent of hyperbolas. The phase velocity is directed downwards. Some weak focusing of the power flow is seen in Figure 7.4 b). The phase velocity inside the slab is directed downwards, as can be seen from the theory.

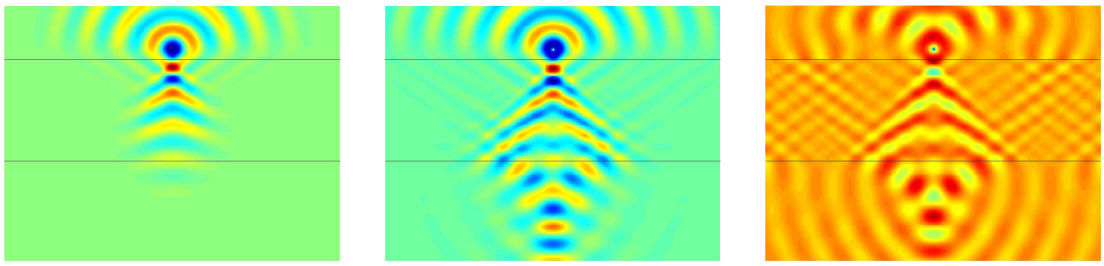

(a) (b) (c)

Figure 7.4: (a) The electric field E_z penetrating into the slab. The snapshot is taken at time step $n = 240$. (b) The electric field within the slab. Some waves have already passed through the slab. It is seen that there are small fields in the region, where the wave vector is complex, as predicted by the theory. The snapshot is taken at time step $n = 400$. (c) Dispersive effects are more clearly seen inside the slab. The electric field is concentrated to the lower side of the slab. The wavefronts behind the slab outside the region of large amplitudes are prolate ellipses. $d_s = 5\Delta y, d = 80\Delta y$. The snapshot is taken at time step $n = 980$.

7.4.3 Case III: $\mu_x < 0$, $\mu_y > 0$, $\epsilon_z < 0$

To complete the analysis, we change the signs of the parameters of the second case. Clearly, the wave vector surfaces as defined by (7.9) are not changed. In fact, the Poynting vector is refracted positively in this case. However, the phase velocity is directed upwards [see (7.12) and (7.13)]. This phenomenon is clearly seen during the simulation. From Figure 7.5 we see that the electric field distributions inside the slab are quite similar to those of Figure 7.4 except that the wavefronts are less distorted in Figure 7.5. In Figure 7.5 c), the wavefronts behind the slab are seen to be oblate ellipses with the center on the lower interface of the slab.

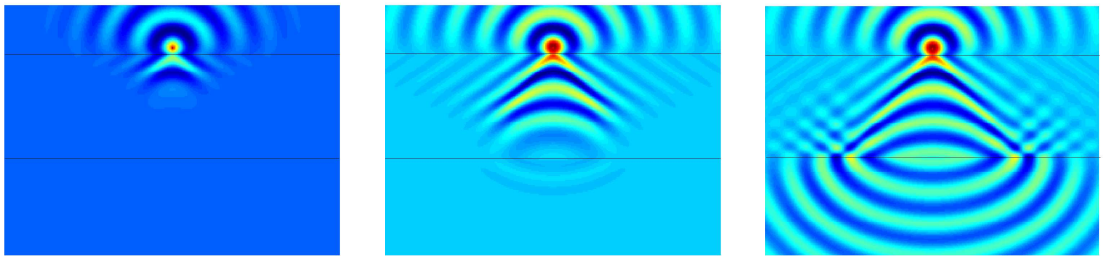

(a) (b) (c)

Figure 7.5: (a) The electric field E_z penetrating into the slab. Wavefronts are dramatically bent. The electric field distribution is recorded at time step $n = 220$. (b) The electric field within the slab. Some waves have already passed through the slab. The wavefronts are seen to be hyperbolas. The electric field distribution is recorded at time step $n = 400$. (c) Interestingly, the wavefronts behind the slab appear to be ellipses with the center on the lower interface of the slab. $d_s = 5\Delta y, d = 80\Delta y$. The electric field distribution is recorded at time step $n = 720$.

7.4.4 Case IV: an Isotropic Slab with $\mu_x < 0$, $\mu_y < 0$, $\epsilon_z < 0$

Here we consider the usual isotropic BW (or double negative) slab with all the relative material parameters close to minus one. This case has been studied, for example, by Ziolkowski and Heyman in [62] in the case of Drude slabs. We obtained quite similar results with our alternative discretization technique in the case of isotropic Lorentz medium. The electric field distributions are shown in Figure 7.6. We can calculate the positions of the foci from the slab thickness d and the distance d_s of the source from the interface. Notice that we must have $d_s < d$ to have a focus inside the slab. The foci should appear at $y = -d_s$ inside the slab and at $y = -(2d - d_s)$ behind the slab. The appropriate derivations can be found in [62].

From Figure 7.6 a) we see that the electric field is concentrated in the expected position of the first focus. In Figure 7.6 c), the second focus behind the slab is

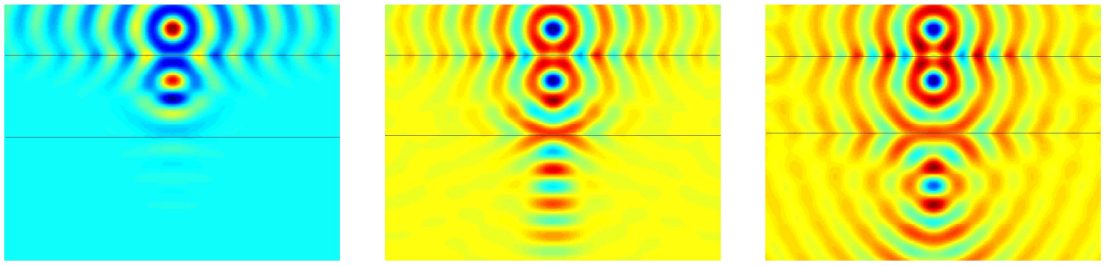

(a) (b) (c)

Figure 7.6: (a) The electric field E_z penetrating into an isotropic BW slab. The electric field E_z is shown at time step $n = 400$. (b) The electric field within the isotropic BW slab. Some waves have already passed through the slab. The first focus inside the slab is seen in the figure. The electric field E_z is shown at time step $n = 560$. (c) The second focus behind the BW slab has become visible. $d_s = 20\Delta y, d = 60\Delta y$. The electric field E_z is shown at time step $n = 900$.

also visible. It takes some time for the foci to develop, as is seen from Figure 7.6 b), where the second focus is not yet seen. The incident spectrum has some small components for which the relative material parameters are not exactly minus unity. Hence the wavefronts are not perfect circles as predicted by the theory. Anyway, these results are in agreement with the theory concerning negative refraction of the Poynting vector. However, no "perfect" focusing has been observed, meaning that the focus area is always not smaller that about half wavelength. Steady state solutions for the foci were not obtained. This same observation was also made by Ziolkowski and Heyman in [62]. Numerical experiments to study focusing have been also reported by Loscialpo in [68] and by Cummer in [69].

7.4.5 Case V: $\mu_x < 0$, $\mu_y < 0$, $\epsilon_z > 0$

For this set of material parameters, the theory predicts that the waves decay exponentially everywhere inside the slab. However, we have found that surface waves, i.e. waves that decay exponentially with the distance from the interface, are easily excited in this case, in accordance with the theoretical prediction, see 7.18. To see this phenomenon, we illuminate a rectangular cylinder with a pulse having a slightly broader spectrum. The electric field distribution induced on the surface of the cylinder is shown in Figure 7.7. Figure 7.7 a) shows how the surface waves begin to develop. The source has just been switched off in Figure 7.7 a). In Figure 7.7 b), surface waves have propagated along the surface to the opposite side of the cylinder as well. In agreement with the theory, there are no fields inside the cylinder except for the immediate vicinity of the surface of the cylinder.

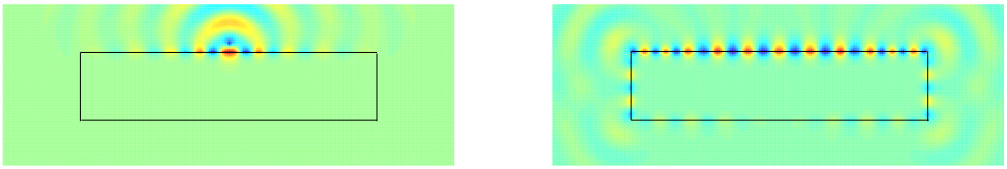

(a) (b)

Figure 7.7: (a) The surface waves begin to develop. The source has just been switched off at time step $n = 360$. (b) At a later moment of time ($n = 1020$), surface waves exist around the cylinder. As is known from the theory, there are negligible fields inside the cylinder.

7.5 Evanescent Fields in Backward-Wave Slabs

The resolution wave limit of any optical device is well known: it is impossible to resolve details smaller than half wavelength. The physical reason of this limitation comes from the fact that evanescent waves in the Fourier spectrum of an object exponentially decay in the direction from the object plane. The decay factor reads $\alpha = \sqrt{k_t^2 - k_0^2}$, where k_0 is the wavenumber in free space, and k_t is the wavenumber of Fourier components in the object plane. The faster the field varies in the object plane, the faster it decays in the direction normal to the object plane. However, it was recently found that a very special kind of lens made of a material with negative relative parameters $\epsilon_r = -1, \mu_r = -1$ (at a certain frequency) can "amplify" the evanescent part of the spectrum, thus opening a way to realize a "superlens" with sub-wavelength resolution [59, 60, 61].

The reason for this counterintuitive behavior is the fact that for a fixed frequency, an interface between free space and a backward-wave medium with $\epsilon_r = -1, \mu_r = -1$ supports surface waves with arbitrary propagation constants along the interface [63]. Indeed, the eigenvalue equation for surface modes (surface polaritons) on an interface between two isotropic media with parameters $\epsilon_{1,2}$ and $\mu_{1,2}$ reads

$$\frac{\sqrt{k_1^2 - k_t^2}}{\epsilon_1} + \frac{\sqrt{k_2^2 - k_t^2}}{\epsilon_2} = 0, \qquad \text{TM modes} \tag{7.21}$$

$$\frac{\mu_1}{\sqrt{k_1^2 - k_t^2}} + \frac{\mu_2}{\sqrt{k_2^2 - k_t^2}} = 0, \qquad \text{TE modes} \tag{7.22}$$

where indices $1, 2$ correspond to the two media. If $\epsilon_2 = -\epsilon_1$ and $\mu_2 = -\mu_1$, both (7.21) and (7.22) are identically satisfied for all propagation constants k_t along the interface. This means that any evanescent incident plane wave is exactly in phase with one of the eigenmodes of the surface wave spectrum. If

the interface is infinite in space, the amplitude of the excited surface wave becomes infinite. The amplification of evanescent fields in backward-wave slabs utilizes this resonant excitation of waveguide modes with large propagation constants. The incident field excites an eigenmode of the slab that is formed by two exponentially decaying field components inside the slab. The spectrum of eigenmodes traveling along a slab can be found from the expression for the reflection or transmission coefficients: they have singularities at the spectral points. For material parameters satisfying $\mu_r = -1$ and $\epsilon_r = -1$ the transmission coefficient equals simply $\exp(\alpha d)$, where α is the decay factor of an evanescent mode from the source and d is the slab thickness [59]. Thus, there is only one eigenmode, and that solution corresponds to infinitely large k_t and α. For larger values of α the excitation is closer to the resonance with this eigenmode, and the field amplitude excited in the slab waveguide is larger.

In paper [66], however, it has been concluded that if the width of the slab is limited, the restoration of fields is physically meaningless as it involves infinite energy. To clarify the behavior of the evanescent fields in a BW slab or a finite width, we study the fields from a source that creates *only* evanescent spectrum in the time domain with the finite-difference time-domain (FDTD) method. Time domain waveforms at suitably chosen observation points and snapshot field distributions are calculated. Our simulations show that the amplification indeed occurs, and it is due to the surface modes excited on the slab boundaries.

7.5.1 The Problem Formulation

In any backward-wave medium the negative permittivity and permeability must be dispersive, and here we adopt the Lorentz model to account for the frequency dispersion. The expressions for the permittivity and permeability are of the form (7.2). Numerical techniques appropriate to simulations of a material with the above parameters with FDTD can be found in [65, 27, 51]. The discretization scheme used in this thesis is described in detail in [65].

Let the interface between free space and a BW slab lie along the x-axis. The excitation plane (a line in our 2D cut) is located at distance d_s from the BW slab of thickness d. In order to be able to study the behavior of the evanescent field, we excite a BW slab by a source which produces no traveling waves in the direction orthogonal to the source plane. We choose the incident electric field that depends on the x-coordinate along the interface and on the time t in the following manner:

$$E(x,t) = e^{-\left(\frac{x-x_0}{x_d}\right)^2} r(t)\cos\left(k_x x - \omega_0 t\right). \tag{7.23}$$

The ramp function $r(t)$ increases smoothly from 0 to 1 over about 50 periods of the cosine function. It is very important that the amplitude grows slowly enough; a rapid increase in the amplitude does not yield a constant amplitude

on the second slab interface or in the image plane, because of a wide frequency spectrum of the source. x_0 is taken to be the x-coordinate in the middle of the slab and x_d determines the rate of decay of the incident electric field amplitude as measured from x_0. ω_0 is the center angular frequency of the excitation. Due to the finite simulation space, we have given a spatial profile to the incident field to obtain a decaying amplitude near the boundaries of the simulation space. The shape of the profile is the normal distribution. The incident fields propagate to $+x$-direction along the interface but decay exponentially in the y-direction normal to the slab boundaries. From the dispersion relation in free space, $k_x^2 + k_y^2 = \omega^2/c^2$ we see that by choosing $k_x > \omega_0/c$ ($k_y = 0$) in (7.23) we obtain exponentially decaying fields away from the source in the y-direction. In our numerical simulations, we use $k_x = 13.62$ m^{-1} ($k_0 = 9.17$ m^{-1}).

The problem space is two-dimensional, with the field components H_x, H_y, and E_z. The peak of the incident spectrum is at $\omega_0 = 2.75 \cdot 10^9$ rad/s, and the parameters in (7.2) are the following: $\omega_{0e} = \omega_{0m} = 0.55 \cdot 10^9$ rad/s, $\omega_{pe}^2 = \omega_{pm}^2 = 1.482 \cdot 10^{19}$ (rad/s)^2, $\Gamma_e = \Gamma_m = 0$. With these choices, we obtain $\epsilon(\omega) = \mu(\omega)$ for all ω and $\epsilon(\omega)/\epsilon_0 = \mu(\omega)/\mu_0 = -1$ at $\omega = \omega_0$.

When losses are included, we keep ω_{0e} and ω_{0m} as above and modify ω_{pe} and ω_{pm} appropriately to obtain $\Re\epsilon_r(\omega) = \Re\mu_r(\omega) = -1$. Liao's third-order absorbing boundary conditions (ABC) [26] are used to terminate the computational domain at the outer boundaries of the lattice. The slab has finite width, which is large compared with the thickness of the slab.

We excite a slab of thickness $7\Delta y = 9$ cm, carrying out the simulations in a 500×60 lattice. The source plane is located at a distance $d_s = 3\Delta y = 4.5$ cm from the boundary of the slab (tangential magnetic field components are defined on the interfaces). Determining the precise spatial profile of the source, we take $x_0 = 250\Delta x$ and $x_d = x_0/3.5$ in (7.23).

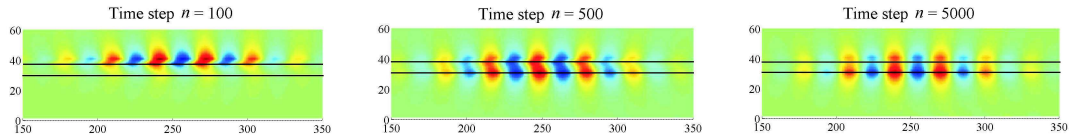

(a) (b) (c)

Figure 7.8: (a) The source fields are visible above the slab. (b) The evanescent fields above the slab create surface waves on the boundaries of the slab. (c) The evanescent mode has been amplified by the slab: strong field amplitudes are visible on the second interface. The fields are stronger on the second interface than on the first interface and the source region.

The problem formulation described above enables us to study how the evanescent fields behave in a BW slab and how the surface modes are excited. The numerical results are presented and discussed next. Majority of these results have been published in [67].

7.5.2 Numerical Results

FDTD simulations have been run to see how the electric fields behave on the slab boundaries and inside the slab. The electric fields created by the source at an early stage of the simulation are seen in Figure 7.8 a). The snapshot electric field distribution in Figure 7.8 b) shows that the fields have passed through the slab and the field amplitudes on the slab boundaries are high. The electric field distribution in Figure 7.8 c) is recorded at a later moment of time. Figure 7.8 c) reveals that the electric fields are much stronger on the second interface than on the first interface. Evidently, the excited evanescent mode is amplified by the slab. Notice that the source is just reaching its maximum amplitude at $n = 3000$, although the fields created by the source are not visible in Figure 7.8 c) due to the scaling.

Next we record the electric fields as a function of time at some observation points. Both lossless and lossy slabs will be considered. All the observation points are on the line $x = 250\Delta x$: one in the middle of the slab, another on the lower interface and the third in air in the image plane, which is located at the distance $d - d_s$ from the second interface. The electric fields at these points as functions of time are shown in Figures 7.9 and 7.10. Figure 7.9 a) shows that the electric field amplitude is larger on the lower boundary of the slab than inside the slab. The incident electric field amplitude in the source plane is equal to unity. The source and the observation point inside the slab are located at equal distances from the upper slab boundary. Therefore, it is expected that the electric field amplitude in the middle of the slab is equal to 1. We have observed slightly larger amplitude in the middle of the slab. The incident electric fields and the fields in the image plane are compared in Figure 7.10. From the theory, is it expected that the electric field amplitude in the image plane equals the incident electric field amplitude. The fields in the source plane and in the image plane are quite close to each other, see Figure 7.10.

Let us now compare the results in Figure 7.9 with analytical results. The evanescent mode decays away from the source plane as a function of distance y by a factor of

$$T_1 = e^{-\sqrt{k_x^2 - k_0^2}y} \tag{7.24}$$

until it hits the upper boundary of the slab. In the slab of thickness d, the fields are amplified by a factor of

$$T_2 = e^{\sqrt{k_x^2 - k_0^2}d}. \tag{7.25}$$

Combining these factors, we obtain the transmission coefficient from the source plane to the second interface as

$$T = e^{\sqrt{k_x^2 - k_0^2}(d - d_s)}, \tag{7.26}$$

where d_s is the distance of the source from the upper boundary of the slab. Substituting the parameters we obtain $T \approx 1.57$. In the numerical simulations,

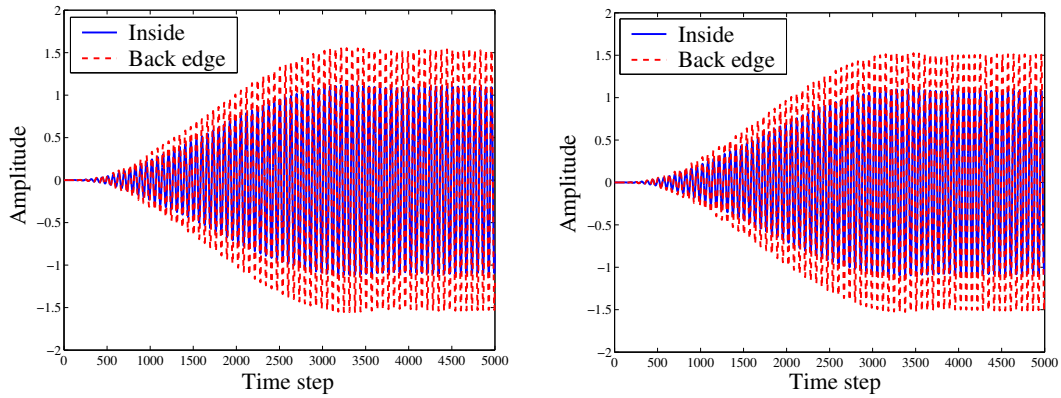

(a) (b)

Figure 7.9: (a) The electric field amplitude on the second boundary of the slab is larger than that of the source field, and also larger than the amplitude in the middle of the slab. This result verifies that the evanescent fields are amplified by the slab. (b) Small losses slightly reduce the amplification effect. The relative permittivity equals $\epsilon_r(\omega) = \mu_r(\omega) = -1 - j0.019$ at the operation frequency.

the maximum ratio of the field amplitudes on the lower interface and on the source plane equals 1.55, being quite close to the analytical result. The fact that the calculated value is smaller should have been expected, because in the numerical model the incident field amplitude decays from the slab center, while the estimation is for the plane-wave excitation. It is observed that some amplitude variation occurs in the image plane. This phenomenon has also been reported by Rao and Ong in [71]. The amplitude modulation takes longer time for smaller losses. In our simulation, we see smaller variations in the amplitude than Rao and Ong observed in [71]. This may be explained with a longer turn-on-time of the source or with different problem parameters k_x or d.

Let us check how a further increase of losses affect the results. In Figures 7.11, results for $\Gamma_e = \Gamma_m = 1.0 \cdot 10^8$ 1/s and $\Gamma_e = \Gamma_m = 2.0 \cdot 10^8$ 1/s are shown, respectively. The results are quite expected: the field amplitudes and their variations in the image plane are smaller.

7.6 Conclusions

Wave propagation and refraction phenomena in uniaxially anisotropic BW slabs have been studied with the FDTD method. Special attention was paid to the shape of the wavefronts and to the regions inside the slabs, where the wave vector becomes complex, thus resulting in exponentially decaying waves. The numerical results for anisotropic BW slabs were seen to qualitatively agree with the theoretical results. The effects of negative refraction, (imperfect) focusing, and surface wave excitation have been demonstrated. Potentially useful

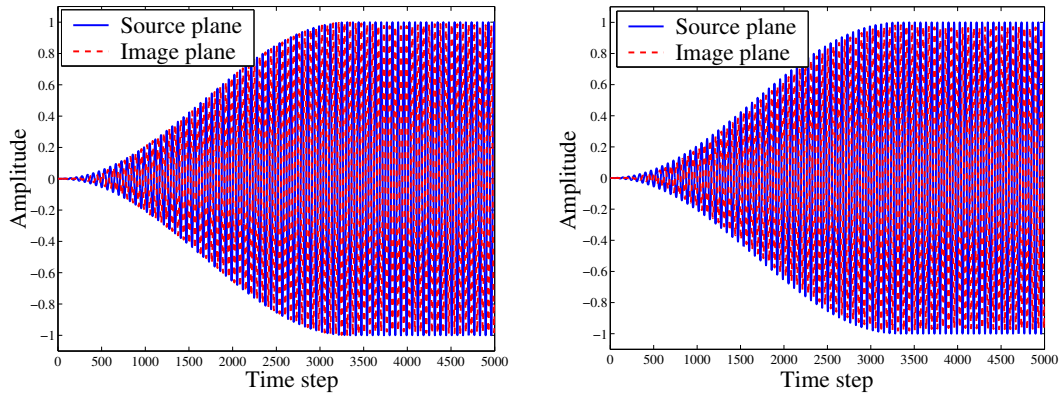

(a) (b)

Figure 7.10: (a) The evanescent electric fields in the image plane are close to the fields in the source plane. This is also in agreement with the theory. (b) Small losses decrease the image quality, but evanescent waves are obviously still amplified and they contribute to the fields in the image plane. The relative material parameters equal $\epsilon_r(\omega) = \mu_r(\omega) = -1 - j0.019$ at the operation frequency.

transformations of wave fronts between spherical, elliptical, and hyperbolical can be realized in homogeneous uniaxial backward wave slabs.

We have also numerically demonstrated that the evanescent modes are amplified in a lossless frequency dispersive backward-wave slab. The field amplitude at the other side of the slab is larger than the source amplitude, and the "amplification ratio" agrees well with the analytical estimation. The numerically observed electric fields in the image plane approximately reconstruct the source fields above the slab. Thus, our numerical results support the conclusion of paper [59] based on the theoretical analysis of an infinite lossless backward-wave slab. Our results do not contradict the conclusion of [66] about infinite field energy required for the restoration of evanescent fields. This is because due to the finite cell size all the wavenumbers in the spectrum are finite and the field amplitudes are finite everywhere.

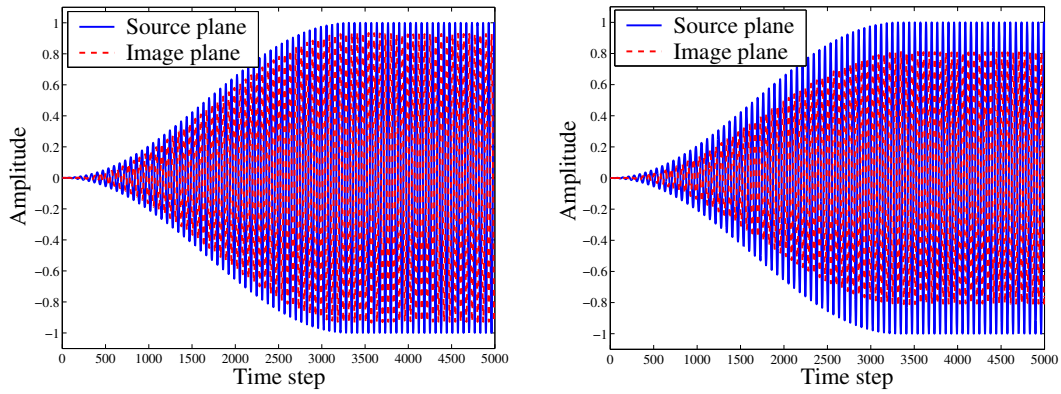

(a) (b)

Figure 7.11: (a) As expected, the field amplitude in the image plane decreases with increasing losses. The relative material parameters equal $\epsilon_r(\omega) = \mu_r(\omega) = -1 - j0.038$ at the operation frequency. (b) The relative permittivity equals $\epsilon_r(\omega) = \mu_r(\omega) = -1 - j0.076$ at the operation frequency.

Chapter 8

Application of the SIBC-FDTD Technique to Modeling of Antennas

FDTD modeling of certain antennas are dealt with in this chapter. In particular, novel antennas with artificial impedance surfaces is studied. A simple analytical model was used in [75] to study the radiation properties of antennas with impedance surfaces. Although some understanding about the radiation characteristics of antennas with impedance screens can be obtained with that model, it was limited to the case of infinite screen width. An FDTD model for finite-size antenna structures with impedance surfaces is developed in this chapter. Monopole and dipole antennas near impedance surfaces are numerically analyzed using FDTD codes developed by the author. The impedance boundary conditions are again applied in the conventional rectangular Yee lattice.

Some simulation results are also compared to measurement results obtained in the Radio Laboratory. The required FDTD theory is first developed and verified against analytical results with simple examples. The example problems used in the verification of the model are not realistic problems, since realistic problems rarely possess analytical solutions. After being convinced that the numerical model works properly, we study numerically some realistic antennas. The results indicate that some rather simple devices can have interesting properties and might be useful in mobile terminals.

8.1 Motivation

Novel artificial impedance surfaces have been introduced in some applications: in antenna reflectors to double the field of a wire antenna [74], in mobile antennas [75], and in microwave filters [76], to name but a few.

The artificially engineered, so called mushroom structure, considered in this thesis, belongs to a wider class of electromagnetic band gap (EBG) structures. Within the surface wave bandgap, EBG materials suppress surface waves. Surface wave suppression is desirable since they distort the radiation pattern of an antenna and degrade the efficiency. The promise of EBG structures stems from the fact that they can mimic perfect magnetic conductors near the resonant frequency. Hence, the reflected field of an antenna placed in proximity of such a reactive lossless impedance surface will be in phase with the incident field, thus contributing to the radiation of the antenna. This is contrary to the situation, where an antenna radiates near an ideal electric conductor. In that case, the reflected waves are out of phase and the radiation of the antenna is decreased. Artificial impedance surfaces are often called artificial magnetic conductors (AMC) or high impedance surfaces (HIS), since they behave like ideal magnetic conductors in the resonance, where the equivalent surface impedance of the structure tends to infinity.

We will study the effect of certain impedance screens to the properties of different antennas. A simple prototype consists of a half of a folded dipole or a straight dipole antenna near an impedance surface. The impedance screen will change the directivity properties of such an antenna and enables better input matching when the radiating element is fed with a 50 Ω transmission line.

8.2 Surface Impedance Model

The classical Leontovich surface impedance relation on the impedance surface reads

$$\mathbf{E}_t = Z_s \mathbf{n} \times \mathbf{H}_t, \tag{8.1}$$

where index t marks the tangential field components, and $\mathbf{n}$ is the unit vector normal to the surface.

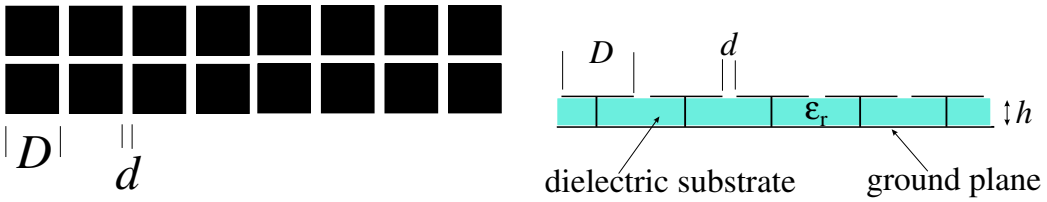

(a) (b)

Figure 8.1: (a) The artificial impedance surface with closely spaced metal patches, top view. (b) Side view.

The artificial impedance surface considered in this thesis is an array of conducting patches located at a distance h from the ground plane. The space between the array of patches and the ground is filled with a dielectric with a

relative permittivity ϵ_r. A waveguide structure is formed between the ground and the array. To prevent electromagnetic waves from traveling there, vias arrays may be positioned between the array and the ground [74]. The square patches have the side length D and spacing $d \ll D$. The patches are also supposed to be small compared to the wavelength: $D \ll \lambda$. The structure described above will be referred to as a mushroom structure. See Figure 8.1, where the structure is illustrated and the dimensions are defined. For the mushroom structure, the surface impedance is of the form [77]

$$Z_s(\omega) = \eta \frac{\frac{j}{\sqrt{\epsilon_r}} \tan(k\sqrt{\epsilon_r}h)}{1 - \frac{(\epsilon_r+1)kD}{\pi\sqrt{\epsilon_r}} \log\left(\frac{2D}{\pi d}\right) \tan(k\sqrt{\epsilon_r}h)}, \tag{8.2}$$

where η is the wave impedance in the substrate. For small arguments of tangent, a reasonable approximation is $\tan(x) \approx x$ and the surface impedance

$$Z_s(\omega) = \frac{j\omega L}{1 - \omega^2 LC} \tag{8.3}$$

may be used with

$$L = \mu_0 h, \quad C = \frac{D\epsilon_0(\epsilon_r + 1)}{\pi} \log\left(\frac{2D}{\pi d}\right), \tag{8.4}$$

as introduced in [74]. The FDTD-model will be derived from these equations. The parameters L (surface inductance) and C (surface capacitance) describe the properties of the structure introduced in [74]. A dynamic model for artificial reactive impedance surfaces has been later introduced by Tretyakov and Simovski in [77], where the expressions for the surface inductance and capacitance with different models are presented.

Let us see how the surface impedance expression (8.2) reduces to the expression (8.3) if we use a rational approximation of the tangent as in chapter 5. Approximating

$$\tan(x) \approx \frac{x}{1 - q_1 x^2}, \tag{8.5}$$

where the constant $q_1 = 4/\pi^2$, we obtain from (8.2) that

$$Z_s(\omega) = \frac{\frac{j\sqrt{\frac{\mu_0}{\epsilon_r\epsilon_0}} k_0\sqrt{\epsilon_r}h}{1 - q_1 k_0^2 \epsilon_r h^2}}{1 - \frac{(\epsilon_r+1)k_0 D \log\left(\frac{2D}{\pi d}\right) k_0\sqrt{\epsilon_r}h}{\pi\sqrt{\epsilon_r}(1 - q_1 k_0^2 \epsilon_r h^2)}}. \tag{8.6}$$

Multiplying both the numerator and the denominator by $1 - q_1 k_0^2 \epsilon_r h^2$ and simplifying, we obtain

$$Z_s(\omega) = \frac{j\omega\mu_0 h}{1 - q_1\omega^2\mu_0\epsilon_0\epsilon_r h^2 - \frac{(\epsilon_r+1)\omega^2 D\mu_0 h}{\pi} \log\left(\frac{2D}{\pi d}\right)}. \tag{8.7}$$

It is seen that this expression is of the form (8.3) with the same inductance but with a modified capacitance

$$C' = C + q_1\epsilon_r\epsilon_0 h. \tag{8.8}$$

If $q_1 = 0$, corresponding to $\tan(x) \approx x$, we consistently obtain $C' = C$.

We will first develop an FDTD model for the impedance boundary condition (8.1) and show some simulation results calculated with 1D and 2D FDTD programs. After being convinced that the FDTD model works properly, we will perform the simulations in the 3D situation, where the dimensions in (8.2) are meaningful.

8.3 FDTD Implementation of the Surface Impedance

Let the interface between free space and the impedance surface lie on the xz-plane. Let us derive the update equation for the electric field component E_z on that interface. As before, the algorithm is designed for the conventional Yee lattice [20](we consider the 2D TM_z situation first). From equations (8.3) and (8.1) we get, in the frequency domain:

$$-j\omega L H_x = E_z + (j\omega)^2 LC E_z. \tag{8.9}$$

This can be easily transformed into the time domain using the inverse Fourier transform:

$$-L\frac{\partial H_x}{\partial t}(x,y,t) = E_z(x,y,t) + LC\frac{\partial^2 E_z}{\partial t^2}(x,y,t). \tag{8.10}$$

This could be easily discretized to obtain an update equation for one field component. However, the resulting scheme would be unstable for relatively large impedances. The goal here is to develop a robust algorithm, which produces reasonable results for surface impedance ranging from zero to $j\infty$. Thus, a naive discretization of (8.10) with possibly extrapolating one of the field components on the surface to reduce the error originating from the spatial interleaving of the field components is not a clever approach. Instead, we integrate equation (8.10) from $t = 0$ to $t = n\Delta t$ using the trapezoidal rule. In discrete form, on the impedance surface, we have:

$$\begin{aligned} H_x|_{i,0}^{n+1/2} &= -\frac{\Delta t}{2L}\sum_{l=1}^{n}\left(E_z|_{i,0}^{n-l+1} + E_z|_{i,0}^{n-l}\right) - \frac{\Delta t}{4L}\left(E_z|_{i,0}^{n+1} + E_z|_{i,0}^{n}\right) \\ &- \frac{C}{\Delta t}\left(E_z|_{i,0}^{n+1} - E_z|_{i,0}^{n}\right). \end{aligned} \tag{8.11}$$

Good stability properties of the algorithm are very much appreciated. Therefore, a half-cell spatial error between H_x and E_z was neglected in the discretization in (8.11) and compatibility with Yee's algorithm is maintained combining the equation with the normal Yee update equations. It will be demonstrated that excellent agreement with exact results can be obtained. Equation (8.11) requires the whole time history of E_z. To avoid storing all the past values of E_z we calculate the sum recursively in the following manner. Let

$$\Psi|_{i,0}^{n} = \sum_{l=1}^{n}\frac{1}{2}\left(E_z|_{i,0}^{n-l+1} + E_z|_{i,0}^{n-l}\right). \tag{8.12}$$

The auxiliary variable Ψ can be updated as follows:

$$\begin{aligned} \Psi|_{i,0}^{0} &= 0, \\ \Psi|_{i,0}^{1} &= \frac{1}{2} E_z|_{i,0}^{1}, \\ \Psi|_{i,0}^{n} &= \Psi|_{i,0}^{n-1} + \frac{1}{2}\left(E_z|_{i,0}^{n} + E_z|_{i,0}^{n-1}\right). \end{aligned} \tag{8.13}$$

Now, we can use the Maxwell-Ampère law in integral form to obtain a time-stepping relation for electric field E_z on the impedance surface. We have

$$\begin{aligned} E_z|_{i,0}^{n+1} - E_z|_{i,0}^{n} &= \left(H_x|_{i,-1/2}^{n+1/2} - H_x|_{i,1/2}^{n+1/2}\right) \frac{\Delta t}{\epsilon_0 \Delta y} \\ &+ \left(H_y|_{i+1/2,0}^{n+1/2} - H_y|_{i-1/2,0}^{n+1/2}\right) \frac{\Delta t}{\epsilon_0 \Delta x}. \end{aligned} \tag{8.14}$$

Finally, we combine equations (8.11)–(8.14) and get the update equation for the E_z-component:

$$\begin{aligned} E_z|_{i,0}^{n+1} = \frac{1}{A}\left\{\left(4\epsilon_0 \Delta y L + 4LC - \Delta t^2\right) E_z|_{i,0}^{n} + \right. \\ \left. 4L\Delta t\left[\left(H_y|_{i+1/2,1}^{n+1/2} - H_y|_{i-1/2,1}^{n+1/2}\right)\frac{\Delta y}{\Delta x} - H_x|_{i,1/2}^{n+1/2}\right] - 4\Delta t^2 \Psi|_{i,0}^{n}, \end{aligned} \tag{8.15}$$

where the constant A is defined as

$$A = 4\epsilon_0 \Delta y L + 4LC + \Delta t^2 \tag{8.16}$$

If the surface impedance approaches zero, then the electric field components are zero all the time, corresponding to the PEC boundary condition. If the surface impedance tends to infinity, then the update equation reduces to the normal update equation for electric field in free space except that the tangential magnetic field is zero at the boundary. Hence, assuming continuity of the performance of the FDTD algorithm using equation (8.15), the algorithm remains stable for all values of the surface inductance L and for any surface capacitance C. Numerical experiments support this hypothesis.

8.4 Verification of the Model

A convenient way to validate the proposed FDTD model is to calculate the reflection coefficient from a one-dimensional interface. This is performed in the following subsection. Another validation study is conducted in a two-dimensional TM$_z$-case, where the near-field radiation patterns are calculated and comparison is made to the exact results. Validation of the model in [29] was done quite briefly and in 2D-case only. A more careful verification is presented here.

8.4.1 Pulse Reflection from a One-Dimensional Interface

The exact reflection coefficient based on the surface impedance model is

$$R = \frac{Z_s(\omega) - \eta_0}{Z_s(\omega) + \eta_0} = \frac{j\omega L - \eta_0(1 - \omega^2 LC)}{j\omega L + \eta_0(1 - \omega^2 LC)}. \tag{8.17}$$

The magnitude of R is equal to unity for all frequencies. The numerically calculated real and imaginary parts of R are compared to the exact results. The incident and the reflected waveforms are recorded on the boundary of a one-dimensional FDTD grid, and the numerical reflection coefficient is evaluated as

$$R(\omega) = \frac{E_{ref}(\omega)}{E_{inc}(\omega)}, \tag{8.18}$$

where the $E_{ref}(\omega)$ and the $E_{inc}(\omega)$ are the Fourier-transformed incident and reflected electric fields, respectively. The Fourier-transform can be calculated "on the fly" so that the appropriate discrete sum

$$E(\omega) = \Delta t \sum_{n=1}^{N} E(n\Delta t) e^{-j\omega n \Delta t} \tag{8.19}$$

is evaluated recursively within the time-loop of the FDTD program. Arbitrarily

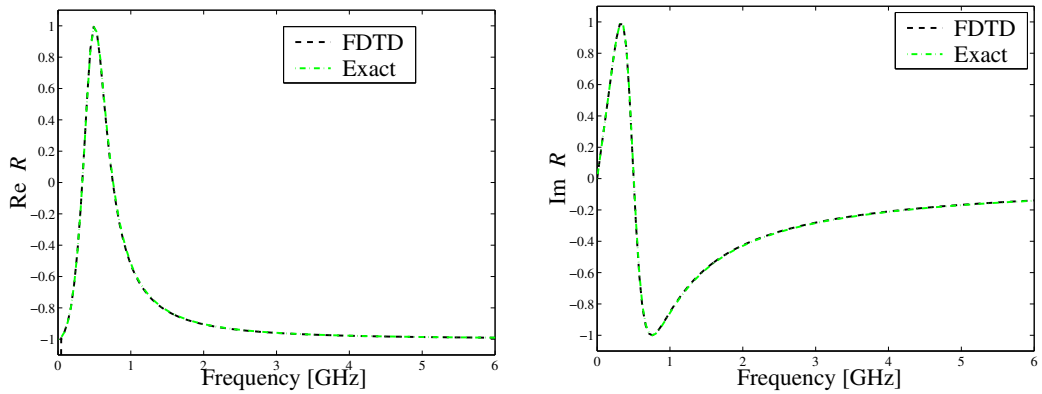

(a) (b)

Figure 8.2: (a) Real part of the reflection coefficient. (b) Imaginary part of the reflection coefficient.

setting $L = 100$ nH and $C = 1$ pF, the first results are calculated. The numerically calculated and the exact reflection coefficients are shown in Figure 8.2. The agreement is just excellent, even though a half-cell error was made in the discretization. It is seen that for very small frequencies, the boundary is like an electric wall. Looking at the expression for the surface impedance, this is expected. For about 0.5 GHz, the real part of the reflection coefficient is equal to one. The peak in Figure 8.2 a) is seen to occur approximately at

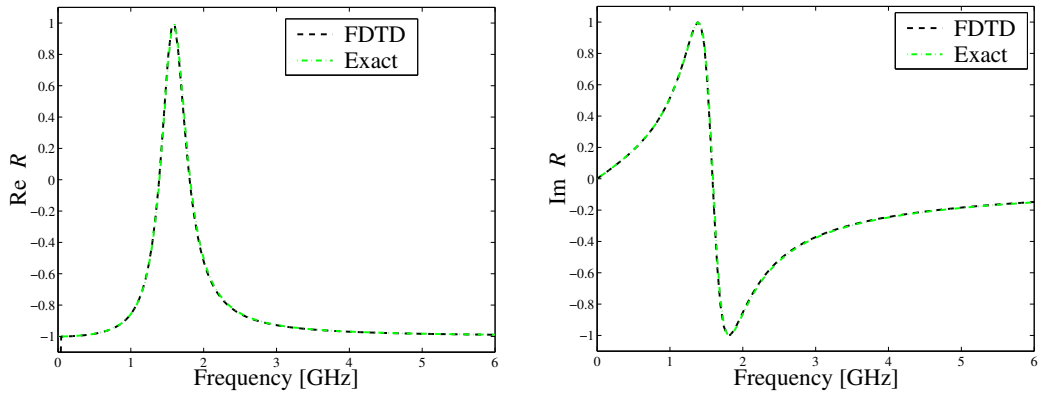

(a) (b)

Figure 8.3: (a) Real part of the reflection coefficient. (b) Imaginary part of the reflection coefficient.

this frequency. From the expression for the surface impedance (8.3), we may calculate the resonant frequency. For the parameters used above, it is

$$f_{res} = \frac{1}{2\pi\sqrt{LC}} \approx 0.5 \text{ GHz}. \tag{8.20}$$

Notice that for larger frequencies the denominator of (8.3) becomes negative

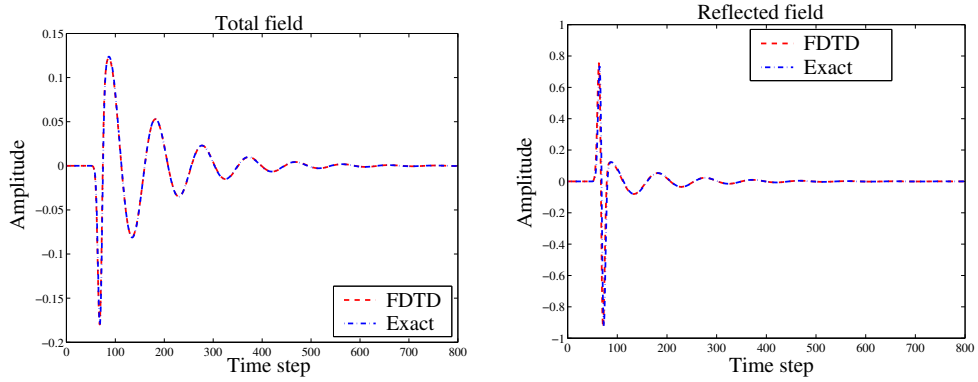

(a) (b)

Figure 8.4: (a) The total electric field on the boundary. (b) The reflected electric field on the boundary.

and the surface impedance tends to zero. Therefore, the reflection coefficient $R \longrightarrow -1$ as $\omega \longrightarrow \infty$. Now, let us choose $L = 10$ nH while keeping C the same. From Figure 8.3 it is seen that the peak is shifted to higher frequencies. It is also interesting to look at the time-domain variation of the fields. The exact reflected electric field on the interface as a function of time may be

calculated via inverse Fourier transform. Thus, the integral

$$E_z^{ref}(t) = \frac{1}{\sqrt{2\pi}} \int_{-\infty}^{\infty} R(\omega) E_z^{inc}(\omega) e^{j\omega t}\, d\omega \tag{8.21}$$

must be evaluated. With a simple transformation of variable, this may be transformed to an integral from 0 to ∞. The integration is then performed with a second-order accurate mid-point rule by terminating the integration interval in the point, where the spectrum of the incident pulse has decayed to a negligible value. The total electric field and the reflected electric field in the time-domain are shown in Figure 8.4.

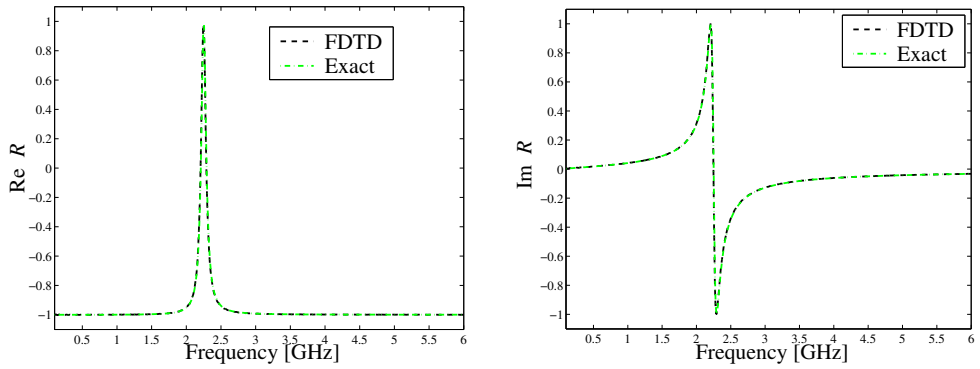

(a) (b)

Figure 8.5: (a) Real part of the reflection coefficient. (b) Imaginary part of the reflection coefficient.

As the final example, we set $L = 1$ nH and change the capacitance to $C = 5$ pF. The peak is now considerably narrower, as can be seen in Figure 8.5. This is due to a smaller value of L, which tends to keep the surface impedance close to zero unless the frequency is very close to the resonant frequency. Again, the agreement with the exact results is very good. The FDTD-simulated resonant frequency is about 0.4 percent smaller than the exact resonant frequency. This is a characteristic feature of the FDTD method, because the actual numerical wave velocity in the discrete lattice is less than the speed of light in vacuum. Hence, FDTD-calculated resonant frequencies are typically slightly smaller than the exact values.

8.4.2 Near-Field Patterns in Two-Dimensional Case

Another validation consists of making comparisons to the results calculated with the exact image theory [56] in [73]. In [73], the wire antenna was located above an infinite impedance surface. In our model, we take the impedance surface to be wide ($w = 47.7$ cm) enough to enable comparison.

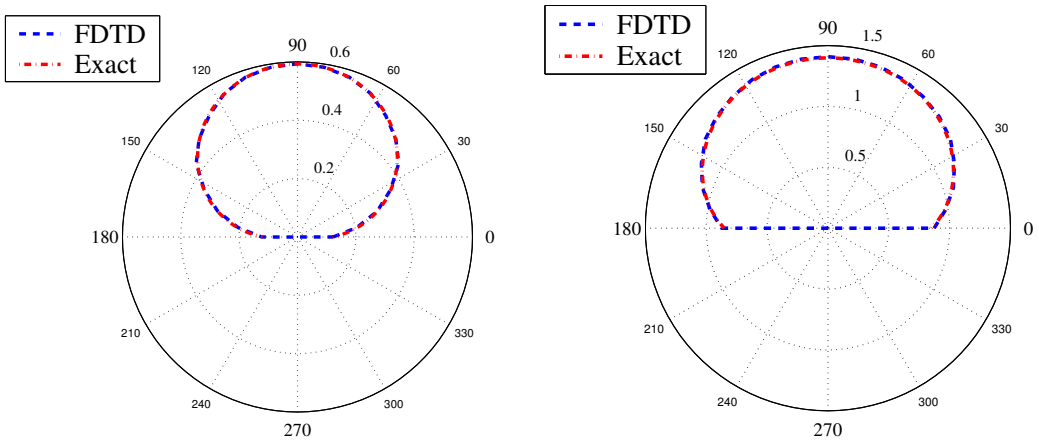

(a) (b)

Figure 8.6: (a) The normalized near-field pattern for wide screen with $Z_s = j0.2 \cdot \eta$. (b) The normalized near-field pattern for wide screen with $Z_s = j \cdot \eta$.

The results of our numerical simulations together with the exact results are presented in Figure 8.6. In our simulations, we take for simplicity $C = 0$ and change the value of L to get the desired surface impedance ($\eta = \sqrt{\mu_0/\epsilon_0}$ is the free space wave impedance). The excitation frequency is 1 GHz and the fields are observed at $r = 4.77$ cm distance ($kr = 1, k = 2\pi/\lambda$) from the origin, which is taken to be on the surface just below the antenna. The antenna is located at 4.77 mm distance from the origin. The patterns are calculated dividing the observed electric field magnitude by the corresponding quantity in free space. The numerically calculated patterns in Figures 8.6 a) and b) agree very well with the exact patterns [73]. Note that the patterns shown in [29] were calculated with a coarser mesh, with only 10 cells corresponding to the distance r. The agreement with exact results is better here than in [29], since the patterns in Figure 8.6 have been calculated with two times denser grid: $r = 20\Delta x = 20\Delta y$. The distance of the line source from the surface is only 2 cells. It is remarkable that the results are still so accurate. PML absorbing boundary conditions with quadratic polynomial grading are used to truncate the computational zone with negligible reflection from the outer boundaries of the lattice.

The reference result may be calculated employing the exact image theory [48]. The image of a time-harmonic current I ($j\omega$ suppressed) reads

$$I_i = \delta_+(\zeta)I - \frac{2jk\eta}{Z_s(\omega)} e^{-\frac{jk\eta}{Z_s(\omega)}} u(\zeta)I. \tag{8.22}$$

The image current consists of the geometrical image (delta function) and the distributed image along the semi-infinite line $\zeta \geq 0$ ($\zeta = 0$ at the position of the image current). Line current I creates an electric field

$$E = -\frac{\eta k}{4} H_0^{(2)}(kR)I, \tag{8.23}$$

where R is the distance from the antenna to the observation point and $H_0^{(2)}$ is the Hankel function. Using the polar coordinates in Figure 8.7, we have the distance from the antenna as

$$R_0 = \sqrt{r^2 \sin^2\theta + (r\cos\theta - h)^2} \tag{8.24}$$

and the distance from an arbitrary point on the line $\zeta \geq 0$ reads

$$R(\zeta) = \sqrt{r^2 \sin^2\theta + (r\cos\theta + h + \zeta)^2}. \tag{8.25}$$

The reflected electric field is calculated as an integral

$$\begin{aligned} E^{\mathbf{ref}}(r,\theta) = -\frac{\eta k}{4}\int_0^\infty H_0^{(2)}\left(kR(\zeta)\right) I_i(\zeta) = \\ -\frac{\eta k}{4} H_0^{(2)}\left(kR(0)\right) I - \frac{2j\eta k G}{Z_s(\omega)} I, \end{aligned} \tag{8.26}$$

where

$$G = \int_0^\infty e^{-\frac{jk\eta\zeta}{Z_s(\omega)}} H_0^{(2)}\left(kR(\zeta)\right)\, d\zeta. \tag{8.27}$$

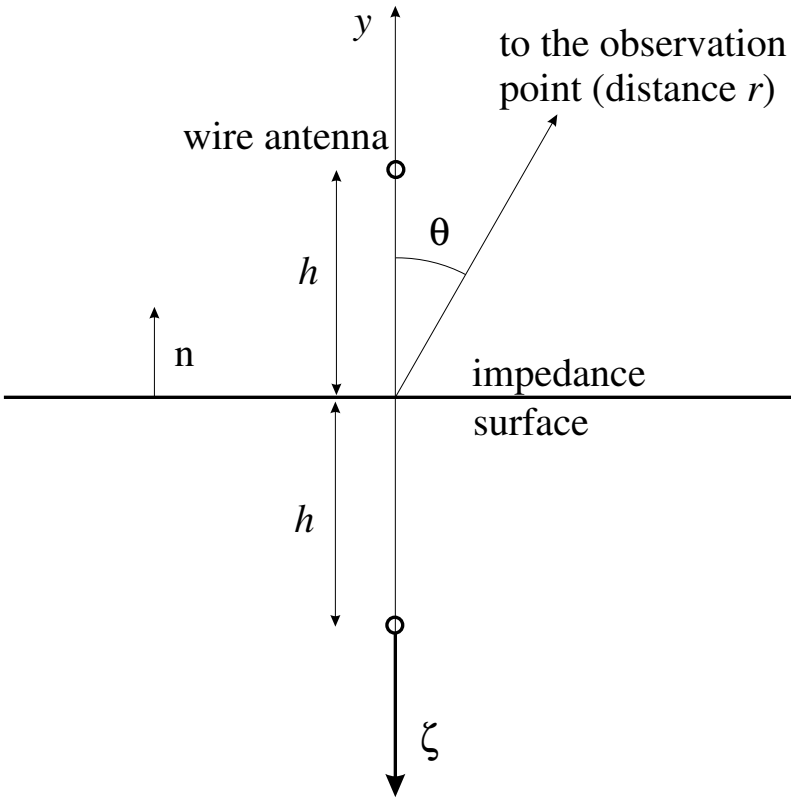

Figure 8.7: The problem geometry: wire antenna radiating over an impedance surface. Exact image theory is applied to calculate the analytical near-field pattern.

A transformation of the integration variable according to $k\zeta \to \xi$ allows us to eliminate k from the integrand. This may be useful if the exponent is large, and

the numerical integration would require very fine sampling of the integration variable. The total electric field pattern, normalized to a field pattern produced by a single line current takes the form

$$F(r,\theta) = 1 + \frac{H_0^{(2)}\left(kR(0)\right) - \frac{2jk\eta G}{Z_s(\omega)}}{H_0^{(2)}\left(kR_0\right)} \tag{8.28}$$

The reference results in Figure 8.6 have been calculated by numerically evaluating $F(r,\theta)$, using the simple mid-point rule in the numerical integration, and truncating the integration at sufficiently large value of ζ.

8.5 FDTD Modeling of a Finite-Size Antenna

The goal of this study is to calculate the near-field pattern of a device with finite rectangular cross-section. As an example, we consider a rectangular PEC-cylinder that is covered with an artificial impedance layer, modeled by a certain reactive impedance. This simplistic example helps to understand how the directivity and radiation properties of more realistic antennas might be manipulated using impedance surfaces. In our example, only the surface of the PEC-cylinder closest to the wire antenna is covered by an impedance layer. The other three sides are ideally conducting. When calculating in two dimensions, the wire antenna is modeled as a single soft-sourced E_z-component near the metal cylinder. The fields are observed at a distance of 5 cm. The size of the cross-section of the cylinder is 2×4 cm and the excitation frequency is 1.0 GHz.

The normalized near-field patterns in this case for two different surface impedances are presented in Figure 8.8. As in the case of a very wide impedance surface, we see that the radiation is increased when the surface impedance is increased. The fields are concentrated on the upper side of the device, as was predicted in paper [73].

We may also study the currents induced on the surface of the same cylinder (size of the cross-section is 2 cm $\times$ 4 cm). The surface currents $\mathbf{J}_s$ are easily calculated from the magnetic fields on the surface according to

$$\mathbf{J}_s = \mathbf{n} \times \mathbf{H}. \tag{8.29}$$

Here, $\mathbf{n}$ is the unit normal vector pointing outward from the surface. The surface current (normalized absolute values of the currents) distributions for the same surface impedance values are presented in Figure 8.9. The goal here is to qualitatively see how the surface currents behave around the box. This gives further confidence about the validity of the FDTD model. The plotting index runs clockwise around the box, starting from the lower left corner.

The peaks in Figure 8.9 a) have a clear explanation: the surface currents close to the antenna are large for the case of small impedances, and there

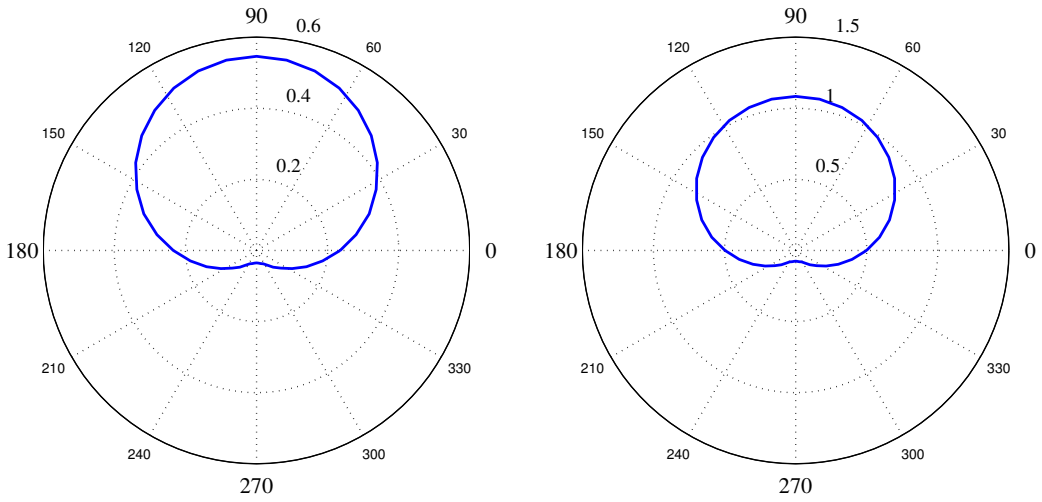

(a) (b)

Figure 8.8: (a) Near-field pattern for a finite-size (cross section) antenna with $Z_s = j0.2 \cdot \eta$. (b) Near-field pattern for a finite-size (cross-section) antenna with $Z_s = j \cdot \eta$.

are current singularities at the box corners. We observe that also the current density induced on the box are mainly concentrated on one side of the device. In Figure 8.9 b), the peak in the middle is clearly smaller, but the singularities in the current distribution in the corners of the structure (indices near 20 and 60) become more clearly visible. This again corresponds to the conclusions made from the simple analytical model: in this case when the properties of the surface are closer to magnetic screen, the near fields and induced currents are less localized near the source.

8.6 Modeling of Antenna Prototypes

Some antenna prototypes were built to study the radiation properties of antennas with impedance surfaces. In the near field, good screening is desired on the user side of a mobile phone. On the other hand, the radiation field should be large enough in the far zone. This treatise focuses on the calculation of the input return loss parameter, voltage standing wave ratio and the relative bandwidth. Also, near-field patterns are presented. Far-field radiation patterns are not studied here, they could be examined by implementing the near-field to far-zone transformation into FDTD codes. Numerical results suggest that the directivity in the near-field changes very dramatically with the dimensions of the antenna. It was also found that the impedance bandwidth can be quite large, if impedance surfaces are appropriately utilized.

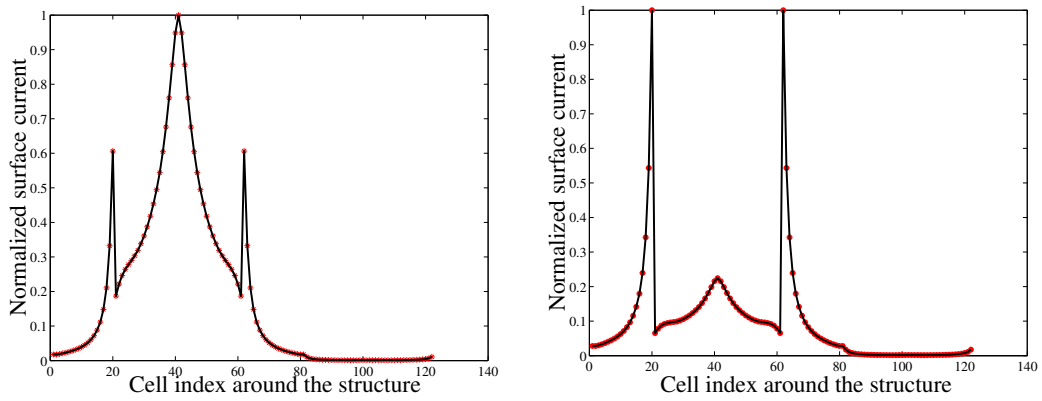

(a) (b)

Figure 8.9: (a) The surface current distribution with $Z_s = j0.2\eta$. Since the surface impedance on the top side of the structure is quite low, most currents are induced there, near the source. (b) The surface current distribution with $Z_s = j\eta$. Strong singularities in the current distribution appear near the corners of the structure, where the surface impedance abruptly changes. The induced currents are relatively low on the top surface, since the impedance of that surface is relatively high.

8.6.1 Antenna Prototypes

Measurements have been conducted in the Radio Laboratory within the AMEST project. Some parameters for several antenna prototypes have been measured. Input impedance of an antenna is an important quantity to know for matching purposes, and it has been measured for some simplistic prototypes. The surface currents induced on the impedance surface were also measured for a couple of antenna prototypes. These quantities can be numerically calculated with the FDTD method.

In Figure 8.10 a), a simple prototype is shown, were one half of a folded dipole is located near a metal screen. The antenna is fed with a 50 Ω coaxial cable through a small hole in the metal plate. The metal plate is large enough to practically completely confine the fields above the plate. The support of the antenna strip is made of a dielectric material with a dielectric constant approximately equal to $\epsilon_r \approx 4.5$.

Another series of measurements was performed for a prototype shown in Figure 8.10 b), where the metal screen is replaced with an impedance surface with metal patches on a dielectric layer with metal backing. The surface impedance of the screen depends on the size of the patches, the width of the narrow slots between them and on the thickness of the dielectric material, as discussed in [77]. If these parameters are properly adjusted, the radiation properties of an antenna with the screen are supposed to be much better than with metal screen. This was already numerically seen in the previous section: the radiation increases with increasing surface impedance.

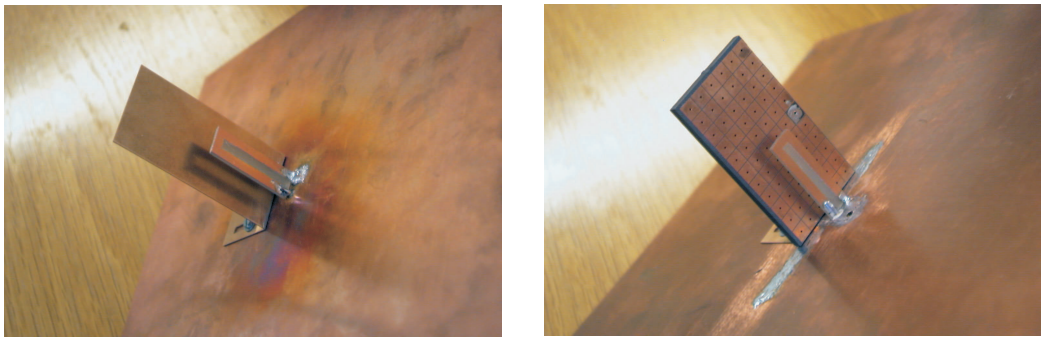

(a) (b)

Figure 8.10: (a) One half of a folded dipole near metal screen. (b) One half of a folded dipole near an impedance screen with an array of metal patches. The antenna is fed with a 50 Ω coaxial cable through the metal plane. The center conductor of the coaxial cable is connected to the metal strip of the radiator. The other end of the radiator is connected to the large metal ground plane. Due to the metal ground plane, the mirror image of one half of the antenna simulates the other half of the antenna, so that the whole system radiates as the complete antenna in the upper half space where the radiator is located.

8.6.2 FDTD Model in the 3D Case

The presented two-dimensional FDTD model is easily extended to the three-dimensional case. Taking the surface lie parallel to the xz-plane, we merely introduce another SIBC for the other tangential electric field component, E_x in the form

$$(1 - \omega^2 LC)E_x = j\omega L H_z. \tag{8.30}$$

This is discretized completely analogously as in two dimensions. The largest modifications to the $2D$-model come from the antenna feed models. Some good models have been published. In this work, a simple coaxial feed model is implemented into FDTD program. The outer conductor of the coaxial cable is attached to the metal plate, and the inner conductor is connected to the strip. This is modeled by setting the electric field components inside the conductors equal to zero. A virtual one-dimensional transmission line serves as the feeding transmission line. It is understood that there is no need to model the transmission line structure because it is located behind the metal plate. The only important issue here is that the fields at the feed point are realistically modeled. The currents and voltages inside the coaxial cable are time-stepped with Yee's algorithm. The voltage between the inner and the outer conductor in the plane of the plate is related to the electric field in the following form

$$E_x = \pm \frac{V}{\Delta x}, \tag{8.31}$$

where the sign depends on the orientation of the electric field component in the FDTD lattice. The E_y -component is related to the feeding voltage in a

similar fashion.

It is pointed out that the approximation (8.5) of the exact surface (8.2) is a good approximation for $k\sqrt{\epsilon_r}h < \pi/2$, where h is the thickness of the dielectric layer (dielectric constant is ϵ_r) in the mushroom structure in Figure 8.10 b). In our simulations, we work around 2 GHz, and the thickness is at most 10 mm. For the used prototypes, $\epsilon_r = 2.3$ and the condition $k\sqrt{\epsilon_r}h < \pi/2$ is clearly valid.

8.6.3 Basic Definitions

The relative bandwidth is defined as

$$\mathrm{BW} = \frac{\Delta f}{f_r}, \tag{8.32}$$

where f_r is the resonant frequency and Δf is the width of the frequency range where usually VSWR < 2 (-9.5 dB input return loss allowed) or VSWR < 3 (-6 dB input return loss allowed). The voltage standing wave ratio is defined as

$$\mathrm{VSWR} = \frac{1 + |S_{11}|}{1 - |S_{11}|}. \tag{8.33}$$

8.6.4 Half of a Folded Dipole Near Impedance Surface

Let us first consider the prototype in Figure 8.10 a). The sizes of the structures in the FDTD program are chosen so that they correspond to the actual sizes. In this first case, the surface impedance model is not needed, and we can just add a metal layer into the problem space. The S_{11} parameter is calculated by extracting the input and reflected voltages and taking a Fourier-transform of these quantities. A good discussion of the calculation of different antenna parameters can be found in [46]. Denoting the input and the reflected Fourier-transformed voltages by $V_{inp}(\omega)$ and $V_{ref}(\omega)$ we have

$$S_{11}(\omega) = \frac{V_{ref}(\omega)}{V_{inp}(\omega)}. \tag{8.34}$$

The input impedance of the antenna may be calculated utilizing the S_{11} parameter or directly taking the ratio of the input voltage $V_{inp}(\omega)$ and the input current $I_{inp}(\omega)$:

$$Z_{in}(\omega) = \frac{V_{inp}(\omega)}{I_{inp}(\omega)}. \tag{8.35}$$

The input current in (8.35) can be obtained using Faraday's law at the feed point. Hence, in the FDTD lattice, the input current is obtained from the magnetic field components surrounding the feed point. The input voltage is

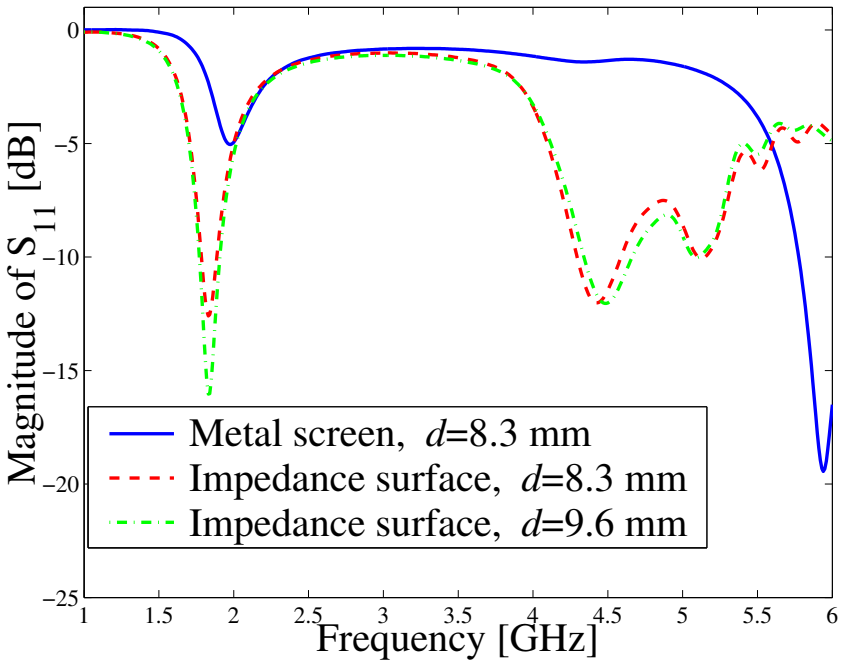

Figure 8.11: Magnitudes of S_{11}-parameters as functions of frequency for antennas near metal screen and near impedance screen. The distance of the metal loop from the surface is denoted by d. Better matching is obtained for larger distances.

obtained from the transmission-line feed model. The S_{11} parameters for the antennas in Figure 8.10 are shown in Figure 8.11. The minimum magnitude of the reflected voltage at the feeding point occurs at about $f \approx 1.98$ GHz for the metal screen.

Experimentally, the real part of the input impedance was measured at the frequency point at which the imaginary part of the input impedance vanishes. Hewlett-Packard network analyzer was used, and the Smith chart was traced to find the frequency corresponding to zero input reactance: the frequency was 1.946 GHz for antenna near metal screen. The corresponding input resistance was then found to be $R \approx 10.9\ \Omega$. To enable comparison, we find the frequency from the numerical results corresponding to the zero of the input reactance. It is found at about $f \approx 1.893$ GHz. For $f \approx 1.893$ GHz, it is seen from Figure 8.12 b) that the real part of the input impedance is $R \approx 10.8\ \Omega$, being very close to the experimentally obtained value.

Input return loss parameters for the antenna with impedance surface have also been plotted in Figure 8.11. The effect of increasing the distance of the antenna from the impedance surface is clearly seen in Figure 8.11: better matching is obtained for larger distances from the impedance screen. If the distance of the antenna from the impedance screen is 8.3 mm, the input resistance at $f = 1.793$ GHz, where $X = 0$, increases to $R \approx 27.5\ \Omega$. The measured values are relatively close to the simulated ones: $X = 0$ at $f = 1.832$ GHz and $R = 25.7\ \Omega$. For larger distance from the impedance screen, the simulated input resistance at $X = 0$ is $R = 33.4\ \Omega$ ($f = 1.806$ GHz), whereas the

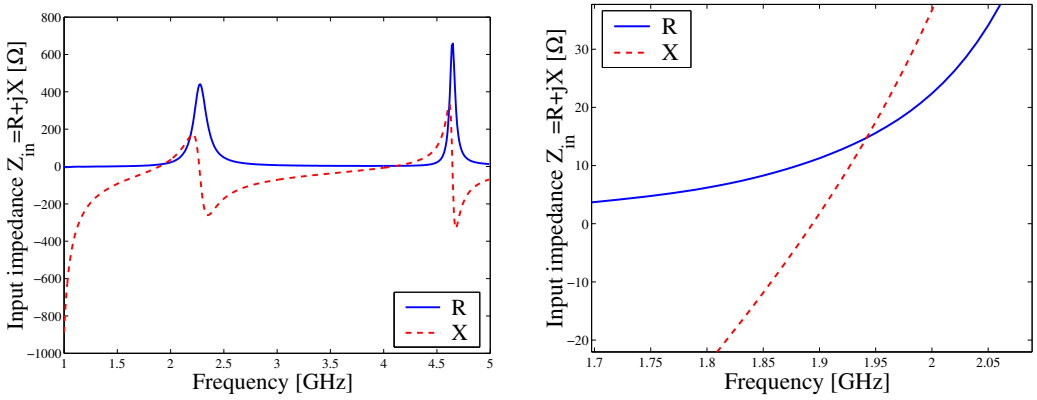

(a) (b)

Figure 8.12: (a) Input impedance of the simple antenna prototype with a metal screen. (b) A magnification.

measured values are $R = 34.4\ \Omega$ and $f = 1.868$ GHz, respectively. The agreement between the measured and the simulated results can be regarded as relatively good. The resonances near 5 GHz can be explained with the resonance of the impedance surface: the surface impedance near 5 GHz is rather large, and the surface behaves nearly as a magnetic conductor.

The reflection phase characterizations of the EBG ground plane for low profile wire antenna applications have been discussed by Yang *et al.* in [79]. They found that the frequency band for which the phase of the reflection coefficient from the impedance surface is about 90 ± 45 degrees yields good input matching. Obviously, this is not the frequency region where the EBG surface behaves like a PMC or a PEC surface. The the resonance band of an artificial impedance surface can be defined, for instance, as the frequency band where the reflection coefficient has the phase within -90 degrees and $+90$ degrees. The operational bandwidth of a wire antenna over an impedance surface should preferably lie in both the input match frequency band and the resonance band of the high impedance surface. The simulated results in Figure 8.11 support the above referenced claim regarding input matching, although the structure here is not optimized and higher surface impedance (thicker structure) than realized here would lead to better input matching.

Input resistances were calculated and measured as a function of the distance of the antenna from the screen. The results are shown in Figure 8.13 a). The voltage standing wave ratios and the relative bandwidth at -6 dB matching level for two specific distances are given in Figure 8.13 b). The input impedance for a fixed distance of the antenna from the screen is shown in Figure 8.14.

The dielectric antenna support is modeled by properly adjusting the relative permittivities of the involved cells in the discrete space. The cross-section of the support is taken to be 2×1 cells. Averaging is employed at the edges

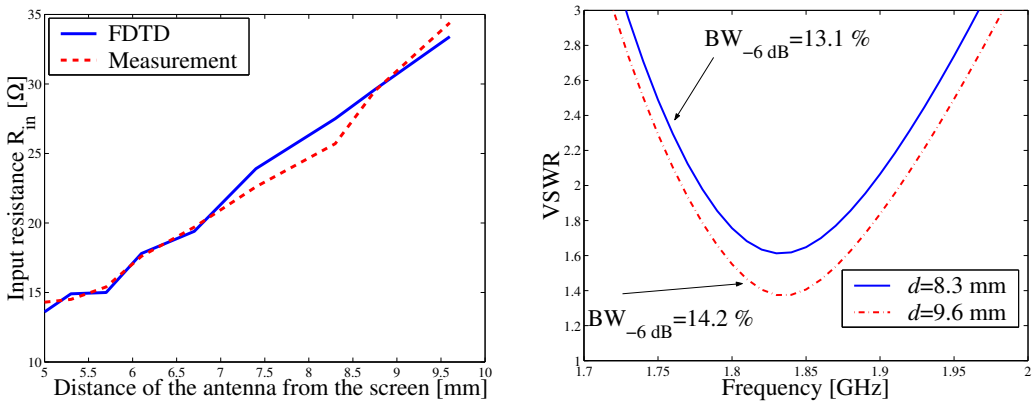

(a) (b)

Figure 8.13: (a) The input resistance of the antenna near the impedance surface as a function of the distance of the antenna from the screen. The simulated and measured values correspond relatively well with each other. (b) The voltage standing wave ratios of antennas near impedance surface, corresponding to distances $d = 8.3$ mm and $d = 9.6$ mm.

and corners in accordance with Maxwell's equations in integral form. The dielectrics has the relative permittivity $\epsilon_r = 4.5$. The dielectric support is electrically rather thin. Hence, few cells are enough to model the dielectric support. The very small thickness of the strip is neglected. If the thickness of the strip were directly modeled, the increased computational requirements would severely slow down the calculation. The size of the metal screen is 30 mm $\times$ 62 mm (20 $\times$ 42 cells in discrete space). Liao's third-order ABC's [26] are used at the outer boundaries of the lattice to terminate the computational domain. They are simple (much simpler than PML) to implement and provide rather good absorbtion of the waves at the boundaries.

The following parameters have been used in the simulations of the mushroom structure in Figures 8.13 a)–b): $h = 3.4$ mm, $D = 5.0$ mm, $d = 0.3$ mm. The size of the impedance screen is 33 mm $\times$ 58 mm, and the distance of the antenna from the screen is varied. The height of the antenna is 30.9 mm and the width is 9.0 mm. The impedance surface is discretized with a 22×40 mesh. The surface impedance of this structure is readily calculated from (8.3) to be $Z_s \approx j53\ \Omega$ at the resonant frequency. This is quite moderate value, and is not supposed to dramatically increase the radiation of the antenna as compared to the case where the metal screen is used. The maxima of R and X in the investigated frequency range are increased as compared to the case of metal screen. The correspondence between the dimensions of the actual structure and the *effective* dimensions of the FDTD-modeled structure is not perfect. For instance, the *effective* sizes of the antenna and the impedance screen are larger than the actual sizes. This is well known to be a characteristic feature of the FDTD method. For PEC objects, the dimensions are effectively about one quarter of a cell larger than the actual sizes. With this in mind, one can try to

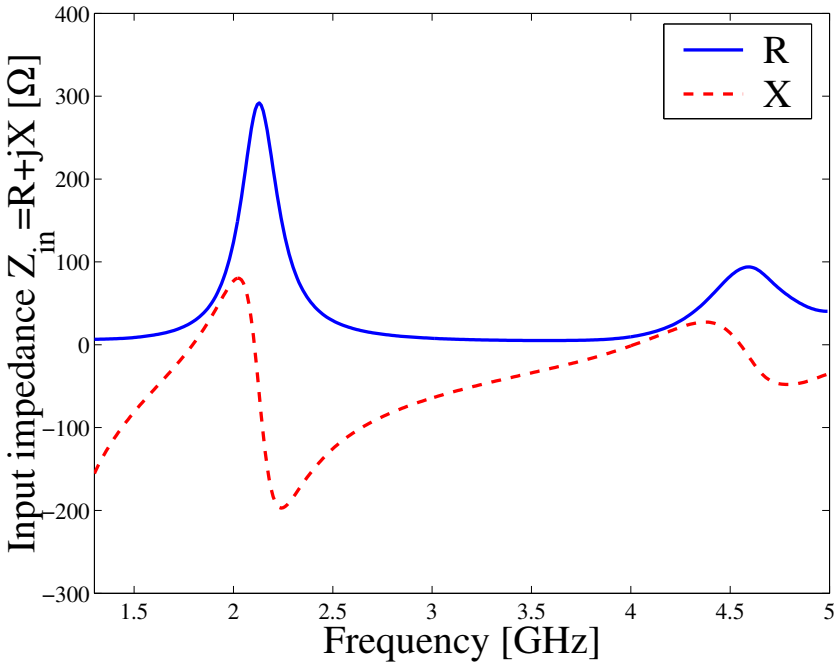

Figure 8.14: Input impedance of the simple antenna prototype with the impedance surface. $X \approx 0$ at 1.79 GHz and $R \approx 27.5\ \Omega$ at 1.79 GHz. The resonant frequency is smaller as compared with that of the antenna with a metal screen. The distance of the antenna from the impedance screen is 8.3 mm.

compensate for the resulting simulation errors by setting slightly smaller than actual sizes to FDTD codes. It is worth noticing that the effective gap sizes may be *smaller* than the actual size. In our antenna problem, the distance of the antenna from the screen could be effectively smaller than what is wanted to simulate. Considerably finer cell size would remove these problems, but the increased computational requirements would be unacceptable.

Normalized near-field patterns of the antenna with the mushroom structure are presented in Figure 8.15. The patterns are slightly broader in the case of impedance screen. The patterns have been calculated with respect to an origin, which is located in the plane of the screen, below the top point of the loop. The angle in the patterns is with respect to the plane of the screen in the horizontal counterclockwise direction.

If the impedance of the screen is further increased, the resonant frequency continues to decrease. However, it is not obvious whether such an impedance surface could be realized using the mushroom structure. To obtain high-impedance surfaces, we should work closer to the resonance. Hence, we should increase the surface inductance L or the surface capacitance C or both. If we considerably increased the substrate thickness h to increase L, the structure could not be considered as a surface and the surface impedance model would not apply. On the other hand, trying to significantly increase the capacitance would require unrealistically high permittivity of the substrate or very small

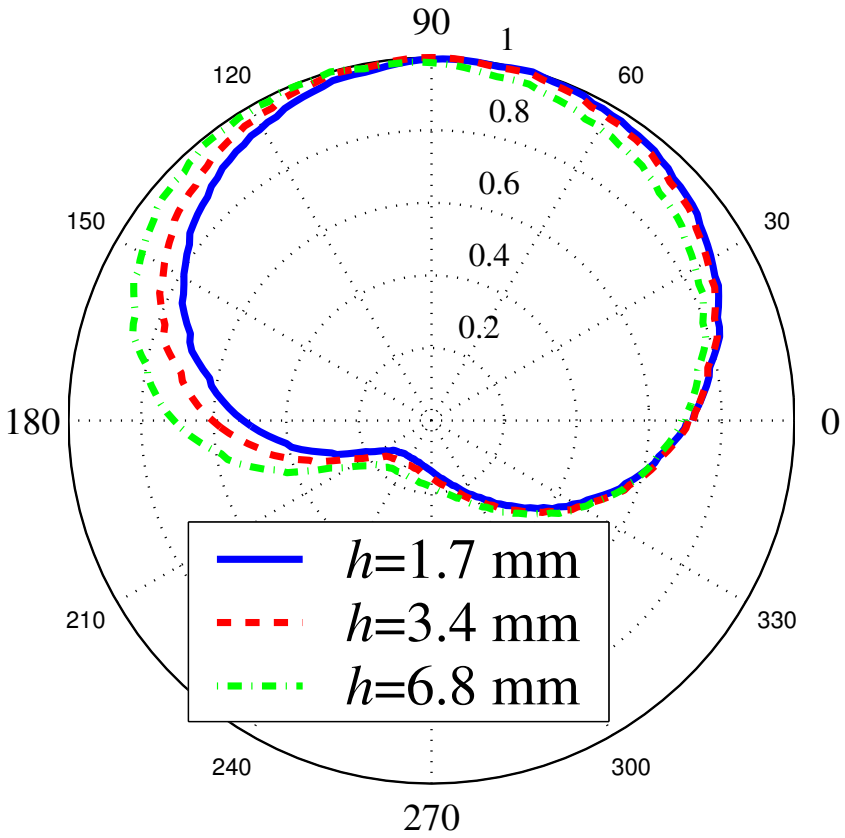

Figure 8.15: (a) Normalized near-field pattern for a one half of the folded dipole, thickness of the substrate is varied. Pattern calculated at distance $r = 3.0$ cm from the origin. Antenna is located at distance 9.0 mm from the screen.

distance between the patches, which would lead to manufacturing problems.

8.6.5 Dipole Antenna Near Impedance Surface

Let us now study a dipole antenna radiating in the vicinity of an impedance surface. The structure of the screen is similar to that presented in Figure 8.10 b). The screen size in these simulations is 33 mm $\times$ 70 mm (corresponds to 22 $\times$ 44 FDTD mesh). The other screen parameters are $D = 5$ mm, $d = 0.3$ mm. The substrate thickness will be varied. The dipole arms are 30.2 mm long (19 FDTD cells), 3.0 mm wide (2 cells), and 0.6 mm thick (the effective radius of a thin current filament is used to calculate the effective thickness of the wires), and the dipole is fed in the gap between the arms using the transmission-line feed model [78].

Voltage standing wave ratios for different substrate thicknesses are shown in Figure 8.16 a). The distance of the dipole from the screen is $d = 8.0$ mm. The resonant frequency of the antenna decreases with increasing substrate thickness, and the input impedance of the antenna approaches the characteristic impedance (50 Ω) of the feeding coaxial cable when the substrate thickness is

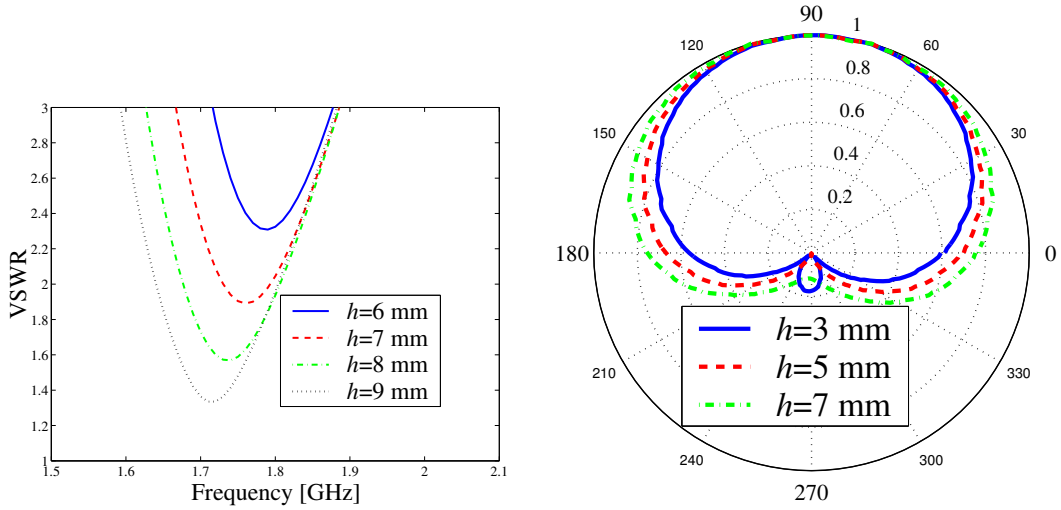

(a) (b)

Figure 8.16: (a) Voltage standing wave ratios for a dipole antenna over the impedance surface. The substrate thickness is varied, and the distance of the antenna from the screen is fixed: $d = 8.0$ mm. Two observations can be made: 1) the resonant frequency of the antenna decreases with increasing substrate thickness (increasing surface impedance), 2) the matching is better if the impedance of the surface is larger. (b) Normalized near-field patterns for a dipole over impedance surface.

increased.

The normalized patterns in Figure 8.16 b) are calculated on a circle with radius 3.0 cm from the feeding point of the dipole, in the horizontal plane. The antenna is located at distance $d = 7.5$ mm (or 5 cells) from the screen. The patterns are calculated at $f = 1.75$ GHz, and normalized to maximum values. The effect of substrate thickness is seen in the results: there are smaller fields in the back side of the antenna in the case of thinner substrate (or smaller surface impedance). Also, the pattern is broader if the impedance of the surface is larger.

Surface current distributions are shown in Figures 8.17 and 8.18. The current distributions are symmetric, and inspection of Figure 8.17 b) reveals that the maxima of J_z occur in the middle of the screen, as could be expected based on the 2D study made earlier in this chapter. The current distributions were calculated with parameters $h = 7$ mm, $d = 7.5$ mm, at frequency 1.75 GHz. More maxima and minima would be seen if the currents were calculated at resonances occurring at higher frequencies.

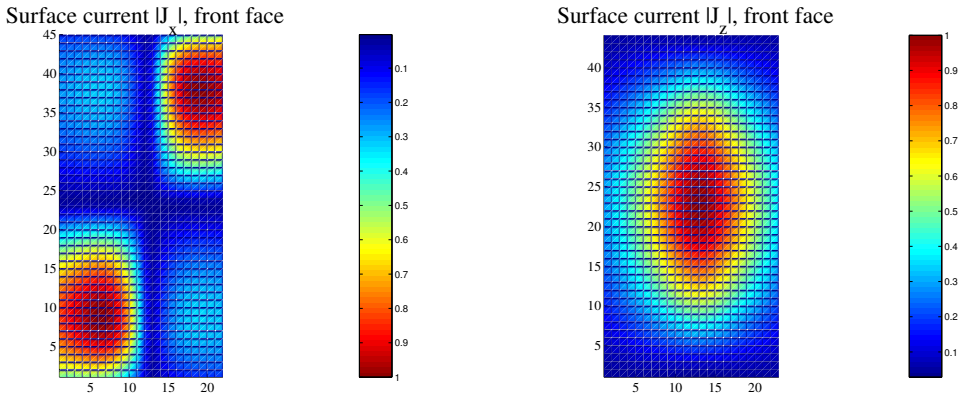

(a) (b)

Figure 8.17: (a) The magnitude of the x-component of the surface current induced on the front face of the antenna. (b) The magnitude of the z-component of the surface current induced on the front face of the antenna.

8.7 Conclusions

An FDTD model of a wire antenna near an impedance surface has been developed. We have shown that the results calculated with the proposed FDTD model compare strikingly well with the exact solution to the problem in the special case of an infinite screen when the exact solution is available. The presented FDTD model allows solving more realistic and complicated problems where the introduced impedance relation is applicable. The study of a finite-size two-dimensional model of an antenna has been made, and the results confirm theoretical predictions made on the basis of the infinite-screen model. Some 3D results were shown, where real antenna prototypes were simulated. Ideas and potential candidates for future antennas on portable devices have been established.

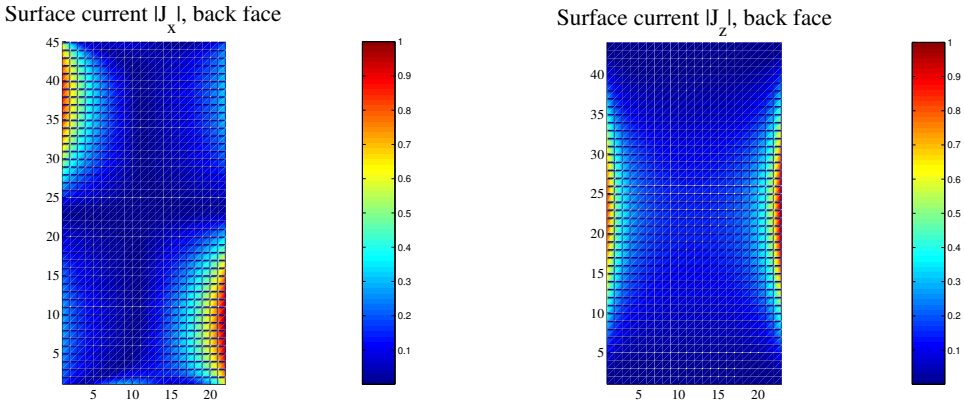

(a) (b)

Figure 8.18: (a) The magnitude of the x-component of the surface current induced on the back face of the antenna. Again, maxima occur near the corners of the screen. (b) The magnitude of the z-component of the surface current induced on the back face of the antenna.

Chapter 9

Conclusions

Several SIBC-based new FDTD models have been introduced in this thesis. The mathematical basis of each of the models has been discussed and numerical simulations have been carried out to verify the developed models.

In Chapter 2, a finite-difference time-domain model of conductors and dielectrics with nonzero conductivity using a higher order impedance boundary condition has been introduced. The advantage of the new approach compared to the previously published methods is that it takes the incidence angle into account while not making assumptions about a large conductivity of the material. The differences and the similarities to the existing methods have been discussed and the method has been validated by comparing to the analytical results for a half space excited by a line current over a wide range of conductivities.

Although the model was only verified in a two-dimensional case, it is expected that a quite similar derivation is possible in the general three-dimensional case, too. It is noticed that in a simple one-dimensional case, the proposed model does not introduce any improvement to the existing model by Maloney and Smith. A stability analysis of the proposed method was not performed. The stability limit of the proposed model may be different from that of the standard Yee algorithm, because center differences were not used everywhere in the algorithm. Due to the presence of the recursive convolution technique in the algorithm, the stability analysis may not be easy to carry out.

In Chapter 3, a new class of analytical absorbing boundary conditions has been derived and some comparisons have been made with other analytical ABC's. These new absorbing boundary conditions contain both electric and magnetic fields, and physically they are closely related to the exact surface impedance boundary condition. In the two-dimensional case, it was found that by keeping both the tangential electric and magnetic fields in the derivation, we may reduce the order of the PDE from 3 to 2 while keeping the performance of the third-order ABC. In the 3D case, we may reduce the order of the PDE by introducing two auxiliary variables that can be conveniently updated in

the standard Yee's algorithm. Also, the connection between an exact surface impedance boundary condition and the Engquist-Majda analytical absorbing boundary condition was discussed, for better understanding of the background of the new method.

An FDTD algorithm for electrically thick material coatings on ideally conducting surfaces was developed in Chapter 4. The advantages over some previous models were demonstrated, and the model was verified with many numerical examples. The most important features of the developed model are the accurate rational approximation of the impedance function, the inclusion of the angle of incidence into to model and the capability of the model to treat dispersive coatings of Lorentz, Debye, or Drude type. Alternative discretization techniques were discussed and their influence on the accuracy was noticed. The proposed higher-order model applies to dispersive coatings as well as to dielectric and conductive coatings. If the spatial derivatives are dropped out from the model, we recover a first-order model, which is still rather accurate, and has the distinct advantage of being directly applicable in a 3D situation.

The model of chapter 4 was extended in chapter 5 to apply to coatings on more general conductors. First-order model using recursive convolution technique is developed and verified. The resulting algorithm is rather general indeed: dispersive coatings on dielectric and conductive bodies can be accurately modeled with the introduced method.

An alternative technique for modeling material layers was formulated in chapter 6. The method is based on appropriate modification of the usual update equations for dispersive materials. Although the model is limited to electrically thin layers, it is seen to be more useful than the SIBC model in cases, where the layer has no metal backing. Also, electrically thin layers with multiple pole pairs are easier to handle with the subcell technique than with the SIBC method. The reason for this is that more terms in the rational approximation of the impedance function is needed when modeling layers with multiple pole pairs. However, the SIBC model is superior to the subcell model especially in the case of electrically thick dielectric and conductive coatings.

FDTD modeling of saturated ferrites was also dealt with in chapter 6. This is numerically an extremely challenging problem, since the field components orthogonal to the direction of the constant magnetization are coupled. A novel SIBC-based technique was introduced for modeling relatively thin ferrite layers on ideally conducting surfaces. Some numerical examples were given in the one-dimensional case. The proposed SIBC-based FDTD technique for ferrite layers is in principle extendable to the general 3D case. It becomes, however, increasingly complicated, and was not considered in this thesis. With some approximations, the proposed ideas might be utilized regardless of the spatial dimensionality.

The developed model could be applied to the analysis of ferrite-loaded waveguides, where the thickness of the ferrite layer is so small that direct quantiza-

tion of the fields is not a feasible approach. An alternative subcell technique was briefly discussed, and it was found to produce similar results as the SIBC model. This fact suggests that subcell-techniques, if properly constructed, may be competitive with SIBC-based techniques in the case of electrically thin layers. The advantage of the subcell techniques is that the formulation can be based on the constitutive relations.

Chapter 7 was devoted to modeling of metamaterials. As a marginal but useful contribution, a novel discretization technique for dispersive materials of Lorentz type with a single pole pair was introduced. The proposed discrete model has better stability properties than some commonly used models. The model was applied to the analysis of wave propagation and refraction phenomena in isotropic and uniaxially anisotropic metamaterials. The perfect lensing effect of a homogeneous, isotropic DNG slab predicted by some theoreticians was not observed. However, large amplitudes in the positions of expected foci were observed in the numerical simulations. No steady-state foci were found. Wave propagation in anisotropic DNG slabs was found to be in agreement with the theoretical results available in the literature.

In chapter 8, an FDTD model of a wire antenna near an impedance surface was developed. It was shown that the results calculated with the proposed FDTD model compare strikingly well with the exact solution in a one-dimensional case. Reflection coefficient from a one-dimensional interface was calculated. As a further validation, near-field patterns were calculated in a two-dimensional special case of a wire antenna over an infinite screen. Again, very good agreement with exact results was obtained.

The presented FDTD model for artificial impedance surfaces allows solving realistic and complicated problems where the introduced impedance relation is applicable. The study of a finite-size two-dimensional model of an antenna was made, and the results confirm theoretical predictions made on the basis of the infinite-screen model. Monopole and dipole antennas near impedance surfaces were numerically studied using the proposed SIBC-technique. The simulation results provide understanding how impedance surfaces change the antenna parameters and how they can be utilized in antennas.

Acknowledgements

The construction of the prototype and the assistance in the measurements of antennas by Mr. Stanislav Maslovski, Mr. Pekka Ikonen and Mr. Vasil Denchev are gratefully acknowledged.

Bibliography

[1] M.K. Kärkkäinen, S.A. Tretyakov, Finite-difference time-domain model of interfaces with metals and semiconductors based on a higher-order surface impedance boundary condition, IEEE Trans. Antennas Propag. vol. 51, no. 9, Sept. 2003, pp. 2448–2455.

[2] M.K. Kärkkäinen, FDTD surface impedance models for electrically thick dispersive material coatings, Radio Science, vol. 38, no. 3, June 2003, 16-1–16-14.

[3] M.K. Kärkkäinen, FDTD surface impedance model for coated conductors, accepted to IEEE Trans. Electrom. Compat. 2003.

[4] M.K. Kärkkäinen, S.A. Tretyakov, A class of analytical absorbing boundary conditions originating from the exact surface impedance boundary condition, IEEE Trans. Microwave Theory and Tech. vol. 51, no. 2, Feb. 2003, pp. 39–43.

[5] M.K. Kärkkäinen, Subcell FDTD modeling of electrically thin dispersive layers, IEEE Trans. Microwave Theory and Tech. vol. 51, no. 6, June 2003, pp. 1774–1780.

[6] M.K. Kärkkäinen, Numerical study of wave propagation in uniaxially anisotropic Lorentzian backward wave slabs, Phys. Rev. E 68, August 2003, 026602.

[7] J.G. Maloney, G.S. Smith, The use of surface impedance concepts in the finite-difference time-domain method, IEEE Trans. Antennas Propagat., vol. 40, no. 1, Jan. 1992, pp. 38–48.

[8] J.H. Beggs, R.J. Luebbers, K.S. Yee, K.S. Kunz, Finite-difference time-domain implementation of surface impedance boundary conditions, IEEE Trans. Antennas Propagat., vol. 40, no. 1, Jan. 1992, pp. 49–56.

[9] S. Kellali, B. Jecko, A. Reineix, Implementation of a surface impedance formalism at oblique incidence in FDTD method, IEEE Trans. Electrom. Compat. vol. 35, no. 3, Aug. 1993, pp. 347–356.

[10] K.S. Oh, J.E. Schutt-Aine, An efficient implementation of surface impedance boundary conditions for the finite-difference time-domain

method, IEEE Trans. Antennas Propagat., vol. 43, no. 7, July 1995, pp. 660–666.

[11] S. Yuferev, N. Farahat, N. Ida, Use of the perturbation technique for implementation of surface impedance boundary conditions for the FDTD method, IEEE Trans. Magnetics, vol. 36, no. 4, July 2000, pp. 942–945.

[12] N. Farahat, S. Yuferev, N. Ida, High order surface impedance boundary conditions for the FDTD method, IEEE Trans. Magnetics, vol. 37, no. 5, Sept. 2001, pp. 3242–3245.

[13] C.F. Lee, R.T. Shin, J.A. Kong, Time domain modeling of impedance boundary conditions, IEEE Trans. Microwave Theory and Tech. Vol. 40, no. 9, Sept. 1992, pp. 1847–1850.

[14] C.W. Penney, R.J. Luebbers, J.W. Schuster, Scattering from coated targets using a frequency-dependent, surface impedance boundary condition in FDTD, IEEE Trans. Antennas Propagat. Vol. 44, No. 4, April 1996, pp. 434–443.

[15] P. A. Tirkas, K. R. Demarest, Modeling of thin dielectric structures using the finite-difference time-domain method, IEEE Trans. Antennas Propag. Vol. 39, No. 9, Sept. 1991, pp. 1338–1344.

[16] J. G. Maloney, G. S. Smith, The efficient modeling of thin material sheets in the finite-difference time-domain (FDTD) method, IEEE Trans. Antennas Propagat. Vol. 40, No. 3, March 1992, pp. 323–330.

[17] R.J. Luebbers, K. Kunz, FDTD modeling of thin impedance sheets, IEEE Trans. Antennas Propagat. Vol. 40, March 1992, pp. 349–351.

[18] C.J. Railton, J.P. McGeehan, An analysis of microstrip with rectangular and trapezoidal conductor cross sections, IEEE Trans. Antennas Propagat. Vol. 38, Aug. 1990, pp. 1017–1022.

[19] L.-K. Wu, L.-T. Han, Implementation and application of resistive sheet boundary condition in the finite-difference time-domain method, IEEE Trans. Antennas Propagat. Vol. 40, June 1992, pp. 628–633.

[20] K.S. Yee, Numerical solution of initial boundary value problems involving Maxwell's equations in isotropic media, IEEE Trans. Antennas Propagat. Vol. 14, 1966, pp. 302–307.

[21] A. Taflove, M.E. Brodwin, Numerical solution of steady-state electromagnetic scattering problems using the time-dependent Maxwell's equations, IEEE Trans. Microwave Theory and Tech. Vol. 23, 1975, pp. 623–630.

[22] A. Taflove, Review of the formulation and applications of the finite-difference time-domain method for numerical modeling of electromagnetic wave interactions with arbitrary structures, Wave Motion, Vol. 10, 1988, pp. 547–582.

[23] M.I. Oksanen, S.A. Tretyakov, I.V. Lindell, Vector circuit theory for isotropic and chiral slabs, Journal of Electromagn. Waves and Applic., vol 4, no. 7, 1990, pp. 613–643.

[24] T.G. Moore, J.G. Blaschak, A. Taflove, G.A. Kriegsmann, Theory and application of radiation boundary operators, IEEE Trans. Antennas and Propagation, vol. 36, 1988, p. 1807.

[25] B. Engquist, A. Majda, Absorbing boundary conditions for the numerical simulation of waves, Math. Comput., vol. 31, 1977, pp. 629–651.

[26] Z.P. Liao, H.L. Wong, B.-P. Yang,Y.-F. Yuan, A transmitting boundary for transient wave analysis, Sci. Sin., Ser. A, vol. 27, Oct. 1984, pp. 1063–1076.

[27] A. Taflove, S. Hagness, Computational Electrodynamics, The finite-difference time-domain methed, Artech House, 2000, pp. 182, 253, 356.

[28] F.B. Hildebrand, Introduction to Numerical Analysis, McGraw-Hill, New York, 1956, pp. 378–382.

[29] M.K. Kärkkäinen, S.A. Tretyakov, 2D-FDTD modelling of wire antennas near artificial impedance surfaces, Microwave and Optical Technology Letters, vol. 34, no. 1, July 5, 2002, pp. 38–40.

[30] A. Bayliss, E. Turkell, Radiation boundary conditions for wave-like equations, Comm. Pure Appl. Math., vol. 23, 1980, pp. 707–725.

[31] A. Bayliss, M. Gunzburger, E. Turkell, Boundary conditions for the numerical simulation elliptic equations in exterior regions, SIAM J. Applied Math., vol. 42, 1982, pp. 430–451.

[32] R. L. Higdon, Numerical absorbing boundary conditions for the wave equation, Mathematics of Computation, vol. 47, 1986, pp.437–459.

[33] J. P. Berenger, A perfectly matched layer for the absorption of electromagnetic waves, J. Computational Physics, vol. 114, 1994, pp. 185–200.

[34] P.Y. Wang, S. Kozaki, M. Ohki, T. Yabe, Higher-order formulation of absorbing boundary conditions for finite-difference time-domain method, Electronics Letters, vol. 29, no. 23, Nov. 1993, pp. 2018–2020.

[35] O. Ramadan, A.Y. Niazi, Improved formulations for higher-order absorbing boundary conditions, Electronics Letters, vol. 33, no. 7, March 1997, pp. 568–570.

[36] W.V. Andrew, C.A. Balanis, P.A. Tirkas, A comparison of the Berenger perfectly macthed layer and the Lindman higher-order ABC's for the FDTD-method, IEEE Microwave and Guided Wave Lett. vol. 5, no. 6, June 1995, pp. 192–194.

[37] B.Z. Wang, Time-domain modeling of the impedance boundary condition for an oblique incident parallel-polarization plane wave, Microwave and Optical Technology Lett., Vol. 7, 1994, pp. 19–22.

[38] B.Z. Wang, Time-domain modeling of the impedance boundary condition for an oblique incident perpendicular-polarization plane wave, Microwave and Optical Technology Lett., Vol. 7, 1994, pp. 355–359.

[39] J.G. Maloney, G.S. Smith, A Comparison of Methods for Modeling Electrically Thin Dielectric and Conducting Sheets in the Finite-Difference Time-Domain Method, IEEE Trans. Antennas Propag. Vol. 41, No. 5, May 1993, pp. 690–694.

[40] D.J. Hoppe, Y. Rahmat-Samii, Impedance boundary conditions in electromagnetics, Taylor and Francis, 1995.

[41] R.J. Luebbers, K.S. Kunz, M. Schneider, F. Hunsberger, A finite-difference time-domain near zone to far zone transformation, IEEE Trans. Antennas Propagat. vol. 39, no. 4, April 1991, pp. 429–433.

[42] R.E. Collin, Foundations for Microwave Engineering, McGraw-Hill, 2nd edition, 1992, p. 93.

[43] T.G. Jurgens, A. Taflove, K. Umashankar, T.G. Moore, "Finite-difference time-domain modeling of curved surfaces", *IEEE Trans. Antennas Prop.*, vol. 40, no. 4, April 1992, pp. 357–366.

[44] G. Mur, Absorbing boundary conditions for the finite-difference approximation of the time-domain electromagnetic-field equations, IEEE Trans. Electromagn. Compat., vol. EMC-23, Nov. 1981, pp. 377–382.

[45] T.B.A. Senior, J. Volakis, Approximate boundary conditions in electromagnetics, IEE Electromagnetic Waves Series 41, 1995, pp. 263–279.

[46] R. Luebbers, L. Chen, T. Uno, S. Adachi, FDTD-calculation of radiation patterns, impedance, and gain for a monopole antenna on a conducting box, IEEE Trans. Antennas Propagat. vol. 40, No. 12, Dec. 1992, pp. 1577–1583.

[47] R.K. Mäkinen, J.S. Juntunen, M.A. Kivikoski, An improved thin-wire model for FDTD, IEEE Trans. Microw. Theory and Tech. vol. 50, no. 5, May 2002, pp. 1245–1254.

[48] I.V. Lindell, Methods for Electromagnetic Field Analysis, IEEE Press, 1995.

[49] M.K. Kärkkäinen, S.A. Tretyakov, FDTD-model of conducting structures based on a higher-order surface impedance boundary condition, Helsinki University of Technology Radio laboratory Publications, Report S 257, Digest of Technical Papers, URSI XXVII convention on radio science, Espoo, October 17.-18., 2002, pp. 59–61.

[50] M.K. Kärkkäinen, FDTD model of electrically thick material coatings based on a higher-order surface impedance boundary condition, Conference Proceedings, 19th annual review in advances in computational electrodynamics (ACES), Monterey, California, March 23–29, 2003.

[51] J.L. Young, R.O. Nelson, A summary and systematic analysis of FDTD algorithms for linearly dispersive media, *IEEE Antennas Propagat. Magazine* 43 (2001), pp. 72–80.

[52] M. Okoniewski, E. Okoniewska, FDTD analysis of magnetized ferrites: a more efficient algorithm, IEEE Microwave Guided Wave Lett. Vol. 4, No. 6, June 1994, pp. 169–171.

[53] J. A. Pereda, L. A. Vielva, A. Vegas and A. Prieto, An extended FDTD method for the treatment of partially magnetized ferrites, IEEE Trans. Magnetics, Vol. 31, No. 3, May 1995, pp. 1666–1669.

[54] F. Hunsberger, R. Luebbers, K. Kunz, Finite-difference time-domain analysis of gyrotropic media–I: magnetized plasmas, IEEE Trans. Antennas Propag. vol 40, No. 12, Dec. 1992, pp. 1489–1494.

[55] S. A. Tretyakov, Analytical modeling in applied electromagnetics, Artech House, 2003.

[56] I.V. Lindell, S.A. Tretyakov, K.I. Nikoskinen, S. Ilvonen, BW media – media with negative parameters, capable of supporting backward waves, Microw. Opt. Tech. Lett. vol. 31, no. 2, Oct. 2001, pp. 129–133.

[57] V.G. Veselago, The electrodynamics of substances with simultaneously negative values of ϵ and μ, Sov. Phys. Uspekhi, 10 (1968), pp. 509–514.

[58] P. Valanju, R. Walser, Wave refraction in negative-index media: always positive and very inhomogeneous, Phys. Rev. Lett. 88 (2002), 187401.

[59] J.B. Pendry, Negative refraction makes a perfect lens, Phys. Rev. Lett. 85 (2000), 3966.

[60] J.B. Pendry, S.A. Ramakrishna, Near-field Lenses in two dimensions, Journal of Physics, vol. 14, 2002, 8436.

[61] S. Ramakrishna and J. Pendry and M. Wiltshire and W. Stewart, http://www.arxiv.org/cond-mat/0207026, 2002.

[62] R.W. Ziolkowski, E. Heyman, Wave propagation in media having negative permittivity and permeability, Phys. Rev. E, 64 (2001), 056625.

[63] S.A. Tretyakov, S.I. Maslovski, I.S. Nefedov and M.K. Kärkkäinen, http://www.arxiv.org/cond-mat/0212393, 2003.

[64] D.R. Smith, W. Padilla, D. Vier, S. Nemat-Nasser and S. Schultz, Phys. Rev. Lett., 84 (2000), 4184.

[65] M.K. Kärkkäinen, S.I. Maslovski, Wave propagation, refraction, and focusing phenomena in Lorentzian double negative materials: theoretical and numerical study, Microwave and Optical Technology Letters, vol. 37, no. 1, 2003, pp. 4–7.

[66] N. Garcia and M. Nieto-Vesperinas, Phys. Rev. Lett., 88 (2002), 207403.

[67] M.K. Kärkkäinen, S.A. Tretyakov, S.I. Maslovski, P.A. Belov, A numerical study of evanescent fields in backward-wave slabs, http://www.arxiv.org/cond-mat/0302407, Feb. 2003.

[68] P.F. Loschialpo, D.L. Smith, D.W. Forester, F.J. Rachford, Electromagnetic waves focused by a negative-index planar lens, Phys. Rev. E, 67, 025602(R), 2003.

[69] S.A. Cummer, Simulated causal subwavelength focusing by a negative refractive index slab, Appl. Phys. Lett., vol. 82, no. 10, March 2003.

[70] X.S. Rao, C.K. Ong, Amplification of evanescent waves in a lossy left-handed material slab, http://www.arxiv.org/cond-mat/0304133, Apr. 2003.

[71] X.S. Rao, C.K. Ong, Subwavelength imaging by a left-handed material superlens, http://www.arxiv.org/cond-mat/0304474, Apr. 2003.

[72] I.V. Lindell, S. Ilvonen, Waves in a slab of uniaxial BW medium, J. of Electromagn. Waves and Appl., vol. 16, no. 3, 2002, pp. 303–318.

[73] S.A. Tretyakov, I.S. Nefedov, C.R. Simovski, S.I. Maslovski, Modelling and microwave properties of artificial materials with negative parameters, to appear in Advances in Electromagnetics of Complex Media and Metamaterials, S. Zouhdi, A. Sihvola, and M. Arsalane (editors), Kluwer, 2002, pp. 99–122.

[74] D. Sivenpiper, L. Chang, R.F.J. Broas,N.G. Alexopoulos and E. Yablonovich, High-impedance electromagnetic surfaces with a forbidden frequency band, IEEE Trans. Microw. Theory Techn., vol. 47, no. 11, 1999, pp. 2059–2074.

[75] S.A. Tretyakov, C.R. Simovski, Wire antennas near artificial impedance surfaces, Microwave and Optical Technology Letters, vol. 27, no. 1, 2000, pp. 46–50.

[76] F.-R. Yang, K.-P. Ma, Y. Qian, T. Itoh, A novel TEM waveguide using uniplanar compact photonic-bandgap (UC-PBG) structure, IEEE Trans. Microw. Theory Techn., vol. 47, (1999), pp. 2092–2098.

[77] S. A. Tretyakov, C. R. Simovski, Dynamic model of artificial reactive impedance surfaces, J. Electromagn. Waves and Applications, vol. 17, no. 1, 2003, pp. 131–145.

[78] J.G. Maloney, K.L. Schlager, G.S. Smith, A simple FDTD model for transient excitation of antennas by transmission lines, IEEE Trans. Antennas Propag., vol. 42, 1994, pp. 289–292.

[79] F. Yang, Y. Rahmat-Samii, Reflection phase characterizations of the EBG ground plane for low profile wire antenna applications, IEEE Trans. Antennas Propag. vol. 51, no. 10, Oct. 2003, pp. 2691–2703.